SCUOLA DI DOTTORATO
UNIVERSITÀ DEGLI STUDI DI MILANO-BICOCCA

Dipartimento di / Department of

FISICA

Dottorato di Ricerca in / PhD program Fisica e Astronomia Ciclo / Cycle XXIX

Curriculum in (se presente / if it is) B

Detectors and equipment for Neutrino and High Energy Physics

Cognome / Surname Cassina Nome / Name Lorenzo

Matricola / Registration number 709861

Tutore / Tutor: Gianluigi Pessina

Cotutore / Co-tutor: Marta Calvi
(se presente / if there is one)

Supervisor:
(se presente / if there is one)

Coordinatore / Coordinator: Marta Calvi

ANNO ACCADEMICO / ACADEMIC YEAR 2016/17

UNIVERSITÀ DEGLI STUDI DI MILANO - BICOCCA
FACOLTÀ DI SCIENZE MATEMATICHE, FISICHE E NATURALI
DOTTORATO DI RICERCA IN FISICA E ASTRONOMIA
CURRICULUM: FISICA APPLICATA

LORENZO CASSINA
Matr. 709861

Detectors and equipment for Neutrino and High Energy Physics

Tutor: Prof. G. Pessina
Co-tutor: Prof. M.Calvi

XXIX PHD CYCLE

DOTTORATO DI RICERCA IN FISICA E ASTRONOMIA

Introduction

It is really amazing to think that the huge variety of "things" we commonly experience is finally composed of a large empty space and few basic constituents. This astonishment motivates the physicists over more than 100 years to develop models aimed to describe new elementary particles, predicting their characteristics and interactions.

The adventure of particle physics research starts and continuously deals with the observation of reality, as summarized by A. Einstain: *"It is certainly true that principles cannot be more securely founded than on experience and consciously clear thinking."*. Thus, experiments are the reason, the source of inspiration and the last judgment of any physical model.

At the very beginning, experiments of particle physics were devoted on searching and studying electrons and protons. These particles are stable, simple to produce (electrons can be easily generated by eating up a piece of metal, while protons can be obtained by ionizing a hydrogen atoms) and pretty simple to detect. One can attract them setting up an electrostatic field produced, for instance, by charging a planar capacitance, or modify their trajectories with a magnetic field. Hence, the scale of the experiments was moderate so that the efforts of a relative small collaboration might lead to outstanding discoveries.

As often occur in science, any step forward opens further questions and asks for a deeper understanding. This driving force lets the scientist look for new particles, which are not necessary stable but typically live for a specific amount of time before decaying into lighter particles. Basically, there are three main sources of such exotic particles.

The Earth is constantly bombarded by particles (mainly protons) coming from the outer space, the so called *Cosmic Rays*. Even if it is still not fully understood what is the origin of such particles, they represent a natural and free source of signal. The primary protons interact with the atoms of the atmosphere producing a shower of secondary particles which fall down and finally reach the Earth surface. During this trip, the secondary particles usually decay into lighter products so that mostly muons and neutrinos can be collected at the ground. In addition to be free, cosmic rays has another advantage: their energy can be extremely large, as their spectrum raises up to $\sim 10^{20}$ eV, much larger than we can hope to do even with the most powerful particle accelerator currently available. On the contrary, the rate at which they interact with detectors of reasonable size is very low (for instance, the number of 1 TeV particles reaching the Earth surface is ~ 1 m^{-2}s^{-1}) and cannot be increased nor controlled.

A second elementary particle source one can use is the decay of nuclea, which naturally tend to reach the configuration maximizing the boundary energy among nucleons. When an unstable nucleus decays, it might emit neutrons, neutrinos, alfa particle (basically

a He-nucleus, i.e. a bound state of two neutrons and two protons), beta rays (actually, electrons or positrons), gamma rays (high energy photons) or protons (rare decay mode). At a first glance, using nucleus decays as source of elementary particle would lead to the same limitation as in the case of the cosmic rays, that is a low and uncontrollable production rate fixed by the intrinsic decay half-life. Nevertheless, the number of particle produced can be increased by observing large masses (up to few tons), eventually enriched with the isotope under study, for long periods (several years). In addition, the technology currently available is capable to grown high quality crystals, with outstanding levels of purity. This, combined with a series of techniques for background discrimination, allows to achieve such a sensitivity to detect few atoms out of 10^{27} and search for very rare processes. Differently from the cosmic rays, the energy of particles emitted after a nucleus decay stays below several MeV, the typical energy scale of the nucleon bounds. That is the reason why this branch of particle physics is often referred to as low energy physics.

In order to produce a high flux of particle in the energy range of GeV-TeV, one needs to look at the physics at accelerators. It basically consists of accelerating a particle beam (made of stable charge particles such as electrons, protons or even heavy ion) and making it collide against a fixed target or another beam. From such high energy collisions, the particles of the beam decompose and a huge amounts of sub-particles can be emitted. In this way it is also possible to generate secondary beams of positrons, muons, kaons, pions, neutrons or antiprotons. In general, the heavier the particle one wants to produce, the higher must be the energy of the collisions (this also explains why lighter particles were historically discovered before heavy particles). The particles produced from the collisions can be identified and studied in details and fully characterized (for instance, charge, momentum, energy can be measured with high precision). This allows to reconstruct the primary interaction process and looks for resonances and new particles immediately decaying in lighter products.

All these three sources of particles are exploited to enhance our knowledge of particle physics and check the compatibility with the expectations of the Standard Model (the theoretical framework currently accepted by the scientists) and search for effects beyond it.

My PhD work has been mainly devoted to two experiments going from particles produced in nuclear decays to the physics at colliders.

LHCb is one of the four main detectors located at the LHC collider at CERN and it is particularly designed for the research of flavor physics and effects beyond the standard model. In Sect. 2.1, the LHCb detector and its physics goals will be presented. In 2019-2020, during the Long Shutdown 2 (LS2), a whole upgrade of the detector is foreseen in order to increase the sustainable luminosity by a factor of 50. In particular, my contribution has been focused on the Upgrade of the RICH detectors, which gives funda-

mental information for the particle identification process. A more detailed description of the current LHCb RICH apparatus and the plans for its upgrade will be presented in chapter 2.

CUORE is an experiment located in the underground National Laboratory of Gran Sasso (LNGS) and it searches for the neutrinoless double beta decay in ^{130}Te exploiting a bolometric technique. A more detailed overview the CUORE experiment will be provided in Sect. 3.1. Particularly, the Milano Bicocca applied physics group is in charge of the development of the electronic system, including the power supply chain, the signal readout, amplification and filtering and the design of the hardware tools for the detector response stabilization. My contribution, mainly focused on the design, test, production and installation of such electronic system, will be presented in chapter 3.

Contents

Chapter 1

Theoretical overview

1.1 The Standard Model

The Standard Model (SM) is the theoretical framework describing the nature of particles and the interaction between them. The SM, whose current formulation was finalized in the mid 1970s, demonstrated huge and continued successes not only in explaining the experimental observations but also in providing predictions about new particles existence and properties.

The elementary constituents of the SM are either fermions, particles with half-integer spin, or bosons, particles with integer spin. According to the SM, there are four fundamental forces ruling the nature: strong, electromagnetic, weak and gravitational interaction. Since the magnitude of the gravitational force is too low to play a significant role in the elementary particle physics, it is usually neglected. Each of these forces is mediated by the exchange of vector bosons acting as force carriers, which transfer the interaction between the fermions and between each other. Eight massless gluons, each having a different combination of color and anti-color, mediate the strong interaction; two charged massive bosons, $W^{\pm}$, and a single neutral massive boson, Z^0, are related to the weak interaction; a massless photon, γ, mediates the electromagnetic force. Beside the mediator bosons, the SM includes a spin-zero particle, the Higgs boson, that allows the generation of the particle masses. Table 1.1 lists the mediator bosons for each of the main three forces and their masses.

Fermions are the constituents of all visible matter of the Universe and are divided in two categories, quarks and leptons. The SM includes six different quarks: up (u), down (d), charm (c), strange (s), top (t), and bottom/beauty (b) and the corresponding anti-quarks. Each of them might assume three different color states (red, green or blue), so that they are sensitive to the strong force. Quarks can be classified according to their fractional electric charge as up-type quarks with electric charge +2/3 (u, c, t), and down-type quarks

[1] The coupling strength depends on the energy. Consider these values as typical order of magnitude

Gauge bosons				
Force	**Boson**	**Mass [1]**	**Interacting particle**	**Interaction strength**[1]
Strong	Gluon (g)	0	Quarks and gluons	$\alpha_S \sim 1$
Electromagnetic	Photon (γ)	0	Charged particles	α_{em} =1/137
Weak	$W^{\pm}$	80.4 GeV/c^2	Quarks and leptons	$\alpha_W \sim 10^{-13}$
	Z^0	91.2 GeV/c^2		

Table 1.1: The three forces ruling the elementary particle physics and the corresponding mediator bosons.

with electric charge -1/3 (d, s, b). Quarks can be sorted in three families, and the order of the families conventionally follows the order of the quark masses, as shown in Tab.1.2. The masses of the quarks are free parameters of the Standard Model and range from a few MeV/c^2 (u and d quarks), up to about 173 GeV/c^2 for the top quark. According to the so called *color confinement* principle, color charged particles cannot be singularly and directly observed, but they gather together to form colorless group, called hadrons. There are two main classes of hadrons: the mesons (such as pions or kaons) are composed by a quark bound to an anti-quark of the same color state, while the baryons are formed by three quarks (or anti-quarks) with a different color charge. The main examples of baryons are protons and neutrons, the constituents of the atomic nuclei of the ordinary matter, which are composed by the lightest two quarks. Exotic mesons composed of a tetraquark state [2] [3] and two pentaquark states [4](exotic baryons), were also recently discovered by the Belle and LHCb collaboration respectively.

Quarks			
Generation	**Types**	**Mass**	**Electric charge**
1^{st}	u	$2.2^{+0.6}_{-0.4}$ MeV/c^2	+2/3 q
	d	$4.7^{+0.5}_{-0.4}$ MeV/c^2	-1/3 q
2^{nd}	c	1.27 ± 0.03 GeV/c^2	+2/3 q
	s	96^{+8}_{-4} MeV/c^2	-1/3 q
3^{rd}	t	173.21 ± 0.87 GeV/c^2	+2/3 q
	b	$4.18^{+0.04}_{-0.03}$ GeV/c^2	-1/3 q

Table 1.2: Classification, mass [1] and electric charge of the SM quarks.

Similar to the quarks, the leptons can also be classified in three families. Each family includes a charged lepton (e, μ, τ) and its neutral partner (ν_e, ν_μ, ν_τ), called neutrino. Neutrinos can interact only weakly, while charged leptons can interact also electromagnetically. Unlike the quarks, the lepton family number, i.e. the number of leptons belonging to each family

(L_e, L_μ and L_τ) is almost conserved. As better explained in Sect. 1.4, since neutrino oscillations have recently been observed, neutrinos do have a tiny nonzero mass and the lepton family conservation law is only approximate. However, there is still no experimental evidence of the violation of the total number of leptons ($L = L_e + L_\mu + L_\tau$). Table 1.3 lists the leptons included in the SM, pointed out their masses and family quantum numbers.

Leptons						
Generation	**Types**	**Mass**	**Electric charge**	L_e	L_μ	L_τ
1^{st}	e	511 keV/C^2	-q	1	0	0
	ν_e	< 2 eV/c^2	0	-1	0	0
2^{nd}	μ	105.66 MeV/c^2	-q	0	1	0
	ν_μ	< 190 keV/c^{2}c	0	0	-1	0
3^{rd}	τ	1.776 GeV/c^2	-q	0	0	1
	ν_τ	< 18.2 MeV/c^2	0	0	0	-1

Table 1.3: Classification, mass [1], electric charge and family quantum numbers of the SM leptons.

Despite its large success, there are fundamental physical phenomena in nature that the SM is still unable to adequately explain. For instance, the SM is widely considered to be incompatible with the current most successful theory of gravity, the General Relativity. In addition to that, cosmological observations state that only 5% of the energy of the Universe can be explained using the SM and it does not supply neither a fundamental particle that is a good dark matter candidate nor an explanation to the dark energy. Extensions to the SM are also necessary to face the problems of the Baryon asymmetry and the neutrino mass, which are better described in the next paragraphs. These shortfalls suggest that the current scheme of the SM is incomplete. The attempted confirmation of New Physics (NP) theories, which can take into account these additional phenomena, represents the driving force for experimental particle physics researches today.

1.2 Symmetries and conservation laws

The Noether's theorem states that every continuous symmetry of nature yields a conservation law or, conversely, every conservation law reflects an underling symmetry. For instance, the physics laws are symmetric with respect to translations in time and this implies the conservation of energy. Similarly, if a system is symmetric under translations in space or rotations about a point, then linear or angular momenta is conserved. Conservation of electric charge is related to the invariance of electrodynamics under gauge transformations. Beside this continuous symmetries, it is possible to define discrete symmetries described by a single (or at least countable) number of operators. Although Noether's theorem does not

hold, such symmetries represents a powerful tool to study the dynamic of particle physics processes. The most important discrete symmetries are parity (P), charge-conjugation (C) and time-reversal (T) transformations, as well as their sequential combinations CP and CPT. Table 1.4 shows the effect of such operators on some physical quantities.

Observable		**P-transform**	**C-transform**	**T-transform**
Time	t	t	t	$-t$
Position	$\vec{x}$	$-\vec{x}$	$\vec{x}$	$\vec{x}$
Energy	E	E	E	E
Momentum	$\vec{p}$	$-\vec{p}$	$\vec{p}$	$-\vec{p}$
Angular momentum	$\vec{J}$	$\vec{J}$	$\vec{J}$	$-\vec{J}$
Electric field	$\vec{E}$	$-\vec{E}$	$-\vec{E}$	$\vec{E}$
Magnetic field	$\vec{B}$	$\vec{B}$	$-\vec{B}$	$-\vec{B}$
Electric charge	q	q	$-q$	q
Baryon number	B	B	$-B$	B
Lepton number	L	L	$-L$	L

Table 1.4: Effects of parity, charge-conjugation and time-reversal transformations on some physical quantities.

The parity operator flips the sign of all the three spatial coordinates or, equivalently, allows to move from any physics state into its mirrored image. Parity is conserved by strong, electromagnetic and gravitational interaction but it is violated by the weak force. It is not a small effect and maximally appears in the neutrinos helicity (i.e the projection of the neutrino spin along its motion direction) as neutrinos always show a left-handed helicity while anti-neutrinos are right-handed. The charge-conjugation operator C flips both electric and magnetic field direction and converts each particle in its corresponding anti-particle by changing the sign of all the particle internal quantum numbers (charge, barion number, lepton number). The combination of C and P is related to an intuitive discrete symmetry: the physics law should be the same for particles and their anti-particles observed in a mirrored frame. Although all the experimental results are compatible to the CP conservation from the strong, electromagnetic and gravity interaction, it was demonstrated that the weak force violates CP [5]. It means that particles and anti-particles have a different behaviour with respect to the weak interaction. The third important discrete symmetry is the time-reversal operator T, which relates one physical process to the one running from the future to the past. Intuitively, the physics law are invariant under T transformation. So far, strong and electromagnetic force proved to conserve T, while the weak force violates such symmetry [6]. In addition to that, there is also a compelling reason to believe that time reversal cannot be a perfect symmetry of nature, which comes from the TCP theorem. Based only on the most general assumption (Lorentz invariance,

quantum mechanics and the idea that interactions are represented by fields) the TCP theorem states that the sequential combination of T, P and C operator, in any order, is an exact symmetry of any interaction. Some important implications of the TCP theorem is that every particle must have precisely the same mass and lifetime as its anti-particle. Since CP violation has been demonstrated, then there must be a compensating T violation.

1.3 Baryon asymmetry and CP violation

It is natural to assume that the Big Bang have produced an equal amount of positive and negative charged particles, as well as the same amount of matter and anti-matter. On the contrary, the Universe is mostly made out of matter, so it is likely that some physical laws have acted differently for matter and antimatter. This is the so called the baryon-antibaryon asymmetry problem.

The requirements for generating such an asymmetry from a symmetric initial state were first proposed by Andrei Sakharov in 1967 [7]. The three Sakharov conditions for baryogenesis are baryon number violation, the violation of both charge (C) symmetry and the combined symmetry of charge and parity (CP), and a departure from thermal equilibrium.

As mentioned in the previous paragraph, CP violation is related to the different behaviour of matter and anti-matter with respect to the weak interaction. Precise measurements of CP violation in the SM are crucial to further our understanding of the matter-antimatter problem. CP violation can be naturally included in the theory of weak interaction provided by the SM, in which the mass eigenstates (d, s, b) of quarks do not coincide with the quark eigenstates which participate in the weak interaction (d', s', b'). The two eigenstates are related by the so called Cabibbo-Kobayashi-Maskawa matrix (CKM-matrix), as shown in Eq. 1.1:

$$\begin{pmatrix} d' \\ s' \\ b' \end{pmatrix} = \begin{pmatrix} V_{ud} & V_{us} & V_{ub} \\ V_{cd} & V_{cs} & V_{cb} \\ V_{td} & V_{ts} & V_{tb} \end{pmatrix} \begin{pmatrix} d \\ s \\ b \end{pmatrix} \tag{1.1}$$

where the q' ($q = d$, s, b) are the quark eigenstates of the weak interaction, the q are the quark eigenstates of the mass and the V_{ij} ($i, j = 1..3$) are the elements of the CKM-matrix. It is important to note that the CKM matrix is not simply an arbitrary parametrization of physical observables but appears in the Standard Model Lagrangian.

At a first glance, the CKM-matrix is a 3×3 complex matrix, which has in general eighteen free real parameters. However, not all the elements V_{ij} are independent from each other. By construction the CKM-matrix is unitary ($V_{CKM}^{\dagger} V_{CKM} = V_{CKM} V_{CKM}^{\dagger} = 1$) which reduces the number of free real parameters to nine. One phase can be absorbed by each of the quark fields (mass- and weak-eigenstates) except for a global phase. This leaves four independent real parameters. One parametrization which remarks the magnitude of the

single matrix elements is the Wolfenstein parametrization. It consists in a series expansion of the CKM-matrix in the small expansion parameter λ ($\lambda \simeq |V_{us}|$), hence:

$$V_{CMK} = \begin{pmatrix} 1-\lambda^2 & \lambda & A\lambda^3(\rho - i\eta) \\ -\lambda & 1-\lambda^2 & A\lambda^2 \\ A\lambda^3(1-\rho-i\eta) & -A\lambda^2 & 1 \end{pmatrix} + \mathcal{O}(\lambda^4) \tag{1.2}$$

where λ , A , ρ and η are four real, independent parameters. To date, two of the CKM parameters ρ and η are very poorly determined. Furthermore, for CP violation to occur, it is mandatory the presence of a complex phase $\eta \neq 0$. As written, η only appears in V_{ub} and V_{td} terms.

A method to study the CP violation is to study the *CKM unity triangle*. As mentioned, an important constraint on the relative phases between the CKM matrix elements comes from the property that the CKM matrix is unitary. In particular, applying this condition between the first and third columns, we obtains:

$$V_{ud}V_{ub}^* + V_{cd}V_{cb}^* + V_{td}V_{tb}^* = 0 \tag{1.3}$$

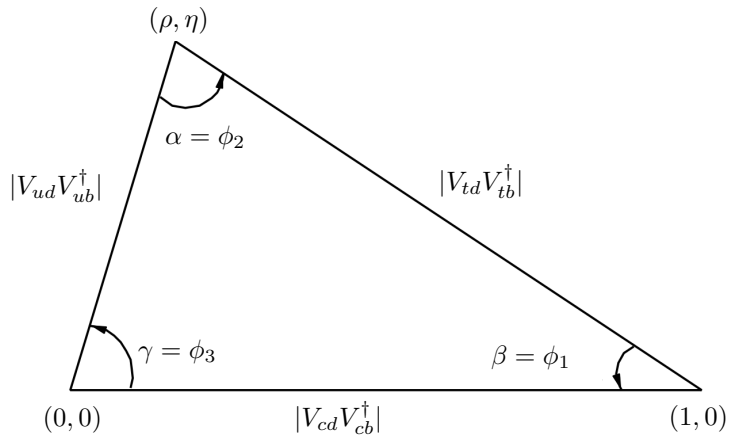

Figure 1.1: The CKM unitarity triangle with angles α, β and γ and vertices $(0,0)$, $(1,0)$ and (ρ,η).

In the complex Gauss plane, Eq. 1.3 can be depicted associating each addend to a vector. Since the vectorial sum is equal to zero, the three terms of Eq. 1.3 represents the side of the triangle shown in Fig. 1.1. Among the others one can consider exploiting the unitary of the CMK matrix, this triangle is most commonly studied because it has sides of comparable lengths (of the order of λ^3). Using the Wolfenstein parametrization (Eq. 1.2), one obtains $V_{cd}V_{cb}^* = 1$, so that one side is real and unitary. The third vertex is

located at (ρ, η). The area of the unitary triangle quantifies the amount of CP violation due to SM weak interactions in the quark sector. Precision measurements of each of the three angles and sides of the unitary triangle are necessary to test the unitary condition of Eq. 1.3. Indeed, finding that $\alpha + \beta + \gamma \neq \pi$, or that one of the sides is too long or short, would be a remarkable sign of NP and a hint of a possible fourth quark generation. To date, the γ angle is known with a poor precision and more accurate measurements are needed to search for NP. Several decays of B and D mesons are particularly interesting for such studies. For instance, $B_d^0 - \overline{B}_d^0$ mixing depends on the combination $|V_{td}V_{tb}^*|^2$ and thus provides information about the unitary triangle of Eq. 1.3. Beyond the detailed test of the CKM description of CP violation, a wide spectrum of rare B decays can be studied, yielding independent information on the CKM parameters.

Among the detectors operating at the Large Hadron Collider (LHC) at CERN, the LHCb experiment has been designed for the research of CP violation and physics beyond the Standard Model by studying rare decays of beauty and charm hadrons. A detector upgrade, whose main goal is to make the system able to work at the full luminosity provided by the particle accelerator, is planned to be installed in 2019-2020. During my PhD studies, I was involved in the development of the photosensitve plane of the upgraded Ring Imagin CHerenkov detector (RICH), crucial for particle identification. An overview on the LHCb detector, its main features and my contributions to the characterization of the new MaPMT photosensors will be provided in chapter 2. The features of the custom designed read-out electronics and my contributions to its development and optimization will be also described.

1.4 Neutrino mass and $0\nu\beta\beta$ decay

The lack of experimental evidence of right-handed (left-handed) neutrinos (anti-neutrinos) is one of the main reason why the SM classifies it as a massless particle.
This assumption is not consistent with the outcomes of the Super-Kamiokande experiment [8], that in 1998 was able to observe oscillations of atmospheric neutrinos. Such claim was confirmed in 2002 by the SNO [9], KamLAND [10] and K2K [11] experiments, which verified the neutrino oscillation hypothesis by studying solar neutrinos, nuclear reactor produced $\overline{\nu_e}$ and a man-made accelerator muon neutrino beam. Flavour oscillation is the only phenomenon which can describe the outcomes of all these experiments and explain the disappearance of both atmospheric ν_μ and solar ν_e. Indeed, the pioneering work by Gribov and Pontecorvo [12], explains how flavour conversions can arise if neutrinos are massive and mixed. All the neutrinos (ν_e, ν_μ, ν_τ) are produced or detected via weak interactions and therefore they are referred to as weak-eigenstate neutrinos (denoted as ν_α, with $\alpha = e, \mu, \tau$). In such a scenario, if we assume that neutrinos are massive, it is possible that the flavour eigenstates (states with definite flavour) are not identical to the

mass eigenstates (states which have definite mass). In general, the flavour eigenstates can be expressed as a coherent superposition of the mass eigenstate, denoted as ν_i with $i = 1, 2, 3$. Thus:

$$|\nu_\alpha\rangle = \sum_i U_{\alpha,i}|\nu_i\rangle \tag{1.4}$$

where $U_{\alpha,i}$ is the unitary leptonic mixing matrix known as the Pontecorvo-Maki-Nakagawa-Sakata (PMNS) matrix. Assuming that a given source is producing a neutrino flux of given flavour $|\nu_\alpha\rangle$ at $t = 0$, then the probability that it converts into another flavour state $|\nu_\beta\rangle$ at a given t is:

$$P_{\alpha\beta}(t) = |\langle\nu_\beta|\nu_\alpha(t)\rangle|^2 = |\sum_i \sum_j U^*_{\beta,j} U_{\alpha,i} e^{-iE_i t}\langle\nu_j|\nu_i\rangle|^2 \tag{1.5}$$

where where E_i and m_i are, respectively, the energy and the mass of the neutrino mass eigenstate $|\nu_i\rangle$. Thus the probability that a neutrino, initially in the α-flavour state, moves to the β-flavour state is not zero, but oscillates with respect to the time (or space). In addition, for ultra-relativistic neutrinos with small mass $E_i = \sqrt{p^2 + m_i^2} \simeq p + m_i^2/2E_i$. This implies that the wavelength of the flavour oscillation is proportional to $\Delta m^2_{i,j}$.
To summarize, neutrino oscillation is a phenomenon beyond the SM which proves that neutrinos are massive particles and allows to estimate the squared difference between the neutrino mass eigenstates. In particular:

$$\delta m^2_{1,2} \simeq 7.54 \cdot 10^{-5} eV^2 \ll \delta m^2_{2,3} \simeq 2.42 \cdot 10^{-3} eV^2 \tag{1.6}$$

Nevertheless, neutrino oscillations do not permit to determine neither the mass absolute value nor the *sign* of the Δm coefficients, so that two neutrino mass hierarchies can be hypothesized (direct, i.e. the neutrino mass scales proportionally to that of the charged lepton masses, or inverse hierarchy). To discriminate for the two mass hierarchies, a sensitivity of the order of 500 meV must be achieved. Furthermore, neutrino oscillations cannot tell us if the neutrino is a Dirac or Majorana (coincides with its own antiparticle). Spontaneous weak β decay can provide such information.

A nuclide can spontaneously decay, for instance via a β process, if it leads to a decrease of the (negative) binding energy, defined as:

$$-E_{binding} = \{Zm_p + Nm_n - [m(^A_Z X_N) - Zm_e]\}c^2 \tag{1.7}$$

where m_n and m_p are the neutron and proton masses, A, N and Z the mass, neutron and proton numbers of the nuclide X, respectively. If the binding energy of the son nucleus is lower than that of the mother, then the decay can occur spontaneously. A first order

approximation of the nucleus binding energy is provided by the semi-empirical Weizsäcker equation:

$$-E_{binding} = -a_v A + a_s A^{2/3} + a_c \frac{Z(Z-1)}{A^{1/3}} + a_{sym} \frac{(A-2Z)^2}{A} + \delta \tag{1.8}$$

$$\delta = \begin{cases} -a_p A^{-3/4} & \text{if both } N \text{ and } Z \text{ are even } (A \text{ is even}) \\ +a_p A^{-3/4} & \text{if both } N \text{ and } Z \text{ are odd } (A \text{ is even}) \\ 0 & \text{if } A \text{ is odd} \end{cases}$$

The various a coefficients are estimated by fitting the experimental data. Equation 1.8 estimates the binding nuclear energy by combining two simply models: the *drop model*, responsible of the first three terms, describes the classic forces acting on the nucleons, while the *shell model*, referred to the last two addenda, are related to quantum mechanic effects. In particular:

- $-a_v A$, with $a_v \sim 15.5$ MeV, is the volume factor. This binding (negative) term describes the strong force between the nucleons. Given the short range of the strong force, each nucleon is only bound to the first neighbouring nucleons, without interacting with all the others. Thus, the binding energy increases proportionally to the number of nucleons, i.e. the mass number A, proportional to the nucleus volume.

- $a_s A^{2/3}$, with $a_s \sim 16.8$ MeV, is the surface factor. This unbinding (positive) term takes into account that the nucleons at the border can be bound to a lower number of nucleons with respect to those located in the center part of the nucleus. The number of weakly bounded nucleons is proportional to the nucleus surface, i.e $A^{2/3}$.

- $a_c \frac{Z(Z-1)}{A^{1/3}}$, with $a_c \sim 0.72$ MeV, is the Coulomb factor. This unbinding term describes the energy related to the Coulomb repulsion between the protons. Each of the Z protons interacts with the remaining $(Z-1)$ protons and the main distance between these positive charge is the nucleus radius, proportional to $A^{1/3}$.

- $a_{sym} \frac{(A-2Z)^2}{A}$, with $a_{sym} \sim 23$ MeV, is called symmetry factor. This term adds unbinding contribution proportional to the square of the difference between the number of protons and neutrons. Such effect can be explain using the Pauli's exclusion principle, which states that fermions cannot stay in the same quantum-mechanical state. Thus, an equal number of neutrons and protons allows to fill in all the available lower energy levels for each nucleon family.

- δ, with $a_p \sim 34$ MeV, is usually called Pairing factor. In agreement with the Pauli's principle, two protons (or neutrons) can adjust their spins in anti-parallel directions in order to stay in degenerated energy levels. In case both N and Z are even, then the degenerated levels are filled for both nucleon families, thus minimizing the binding energy of the nucleus. On the contrary, if N and Z are odd, both families has a

nucleon with a uncoupled spin, increasing the binding energy. In case A is odd, then one nucleon family contributes to reduce $E_{binding}$, but such effect is compensated by the unbinding term of the second family, so that $\delta = 0$.

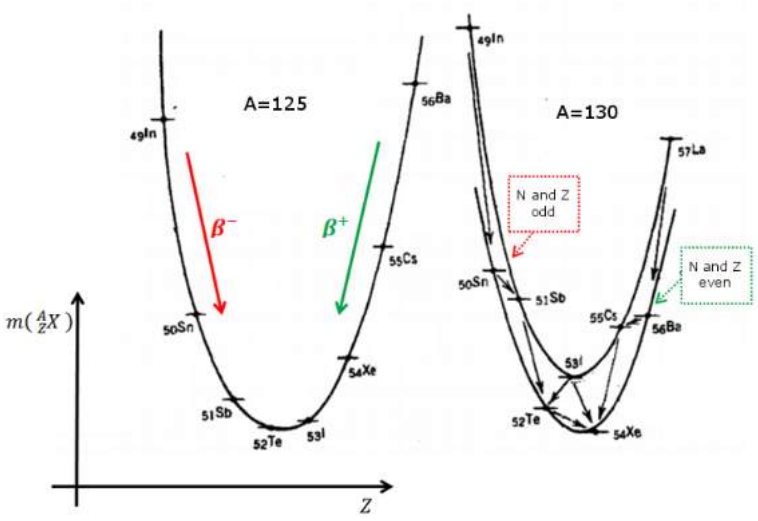

Figure 1.2: Nuclear binding energy as a function of the atomic number Z in a β decay chain. In agreement with the semi-empirical Weizsäcker equation, a parabolic trend is visible.

In the case of a β decay, where A is constant, the Weizsäcker formula states that the binding energy has a quadratic dependence with respect to Z, as:

$$-E_{binding} = \Big(\frac{a_c}{A^{1/3}} + \frac{4a_{sym}}{A}\Big)Z^2 - \Big(\frac{a_c}{A^{1/3}} + 2a_{sym}\Big)Z + \delta + cost \tag{1.9}$$

In agreement with Eq. 1.9, the binding energy of a β-decay as a function of Z describes a convex parabola, which can be eventually splits in two branches by the Pairing term in case A is even, as shown in Fig.1.2. The vertex, i.e. the minimum binding energy, represents the most stable isotope of the chain. Indeed, the isotopes spontaneously go down along the parabola and traveling upwards is kinematically forbidden. If A is even, near to the vertex might occur that $m(X(A,\widetilde{Z})) < m(X(A,\widetilde{Z}-2)) < m(X(A,\widetilde{Z}-1))$ because of the Pairing term. In such very interesting case, $X(A,\widetilde{Z}-2)$ cannot spontaneously reach the most stable isotope unless performing two simultaneous β-decays. This second order process, usually referred to as $2\nu\beta\beta$, has been observed on several isotopes, such as ^{130}Te, ^{48}Ca or ^{76}Ge, with extremely long characteristic time ($T^{2\nu}_{1/2} \sim 10^{19} \div 10^{21}$ yr). In agreement with the SM, two neutrinos are emitted and the cumulative energy spectrum of the two electrons is a continuous function extended up to the decay Q-value. Nevertheless, assuming the neutrino to be a massive Majorana particle and if the total Lepton number can be violated by the weak force, then the two neutrinos can annichilate and the full energy of the decay

transfered to the electrons. This process, forbidden in the SM, is called *Neutrinoless double beta decay* ($0\nu\beta\beta$). In the cumulative energy spectrum, such event would result in narrow peak centered at the decay Q-value. For instance, the $0\nu\beta\beta$ decay in the ^{130}Te is described as [13]:

$$^{130}\text{Te} \longrightarrow ^{130}\text{Xe} + 2e^- \qquad (\text{Q-value} = 2527.518 \pm 0.013 \text{ keV})$$

The schematic picture of the $2\nu\beta\beta$ and $0\nu\beta\beta$ decays and the expected cumulative energy spectra are depicted in Fig. 1.3.

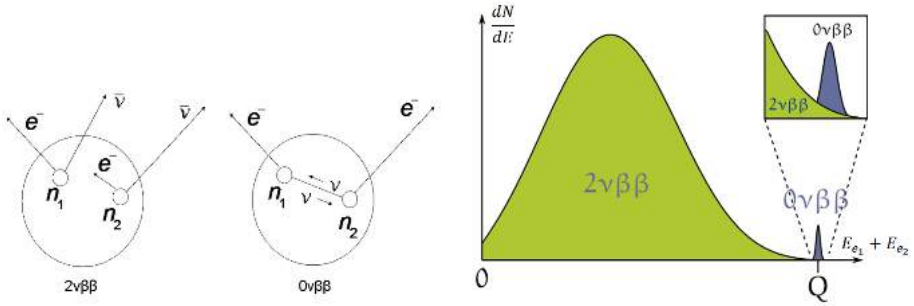

Figure 1.3: Simplified scheme of the $2\nu\beta\beta$ and $0\nu\beta\beta$ decays. The expected cumulative energy spectrum for the two emitted electrons are shown for both the $2\nu\beta\beta$ (in green) and $0\nu\beta\beta$ decay (in blue).

The $0\nu\beta\beta$ decay is strongly related to the effective mass of the electronic neutrino. Indeed, it can be demonstrated that the characteristic decay rate $\Gamma^{0\nu}_{1/2}$ is given by:

$$\Gamma^{0\nu}_{1/2} := \left(T^{0\nu}_{1/2}\right)^{-1} = G^{0\nu} \cdot \left|M^{0\nu}\right|^2 \cdot |\langle m_\nu \rangle|^2 \tag{1.10}$$

where $T^{0\nu}_{1/2}$ is the half-life of the $0\nu\beta\beta$ decay while the other factors are:

- $G^{0\nu}$ is the *phase factor* and can be exactly calculated with a multidimensional integration in the nuclear phase space.
- $\left|M^{0\nu}\right|^2$ is called *nuclear matrix factor*. Its value is model-dependent. Isotopes with large and consistent approximations of $\left|M^{0\nu}\right|^2$ between the various nuclear models are advisable in order to reduce the expected $0\nu\beta\beta$ half-life and its uncertainties.
- $|\langle m_\nu \rangle|^2$ is the *effective electronic neutrino mass*. By applying the Pontecorvo's theory, one obtains:

$$|\langle m_\nu \rangle| = \left| \sum_{i=1}^{3} U^2_{e,i} m_i \right| = \left| |U_{e,1}|^2 m_1 + |U_{e,2}|^2 m_2 e^{j\alpha_1} + |U_{e,3}|^2 m_3 e^{j\alpha_2} \right| \tag{1.11}$$

where m_i, with $i = 1, 2, 3$, are the eigenvalues of the neutrino mass eigenstates $|\nu_i\rangle$. The m_i values depend on the neutrino hierarchy mass, while $U_{e,i}$ are the Pontecorvo-Maki-Nakagawa-Sakata matrix electronic coefficients, whose complex phases are $e^{j\alpha_1}$ and $e^{j\alpha_2}$.

To summarize, the observation of the $0\nu\beta\beta$ decay would demonstrate the Majorana nature of neutrinos, represent the first evidence of Leptonic number violation and allow to define the neutrino mass hierarchy and estimate the effective electronic neutrino mass from measuring the $T^{0\nu}_{1/2}$. Because of its scientific importance, a worldwide effort is devoted to research the $0\nu\beta\beta$ decay on various isotopes, using different experimental techniques. Table 1.5 summarizes the main results obtained from the study of $0\nu\beta\beta$ and $2\nu\beta\beta$ decays [14].

Isotope	$Q_{\beta\beta}$(keV)	$T^{2\nu\beta\beta}_{1/2}$(yr)	$T^{0\nu\beta\beta}_{1/2}$(yr)	$\lvert\langle m_\nu\rangle\rvert$ (eV)
^{48}Ca	4272	$4.4^{+0.6}_{-0.5} \cdot 10^{19}$	$> 5.8 \cdot 10^{22}$	< 14
^{76}Ge	2039	$1.84^{+0.14}_{-0.10} \cdot 10^{21}$	$> 1.9 \cdot 10^{25}$	$< 0.22 - 0.66$
^{82}Se	2996	$(0.92 \pm 0.07) \cdot 10^{20}$	$> 3.6 \cdot 10^{23}$	$< 0.89 - 2.4$
^{96}Zr	3350	$(2.3 \pm 0.2) \cdot 10^{19}$	$> 9.2 \cdot 10^{21}$	$< 7.2 - 19.5$
^{100}Mo	3034.4	$(7.1 \pm 0.4) \cdot 10^{18}$	$> 1.1 \cdot 10^{24}$	$< 0.45 - 0.93$
^{116}Cd	2805	$(2.8 \pm 0.2) \cdot 10^{19}$	$> 1.7 \cdot 10^{23}$	$< 1.2 - 2.7$
^{130}Te	2527.518	$6.8^{+1.2}_{-1.1} \cdot 10^{20}$	$> 2.8 \cdot 10^{24}$	$< 0.35 - 0.77$
^{150}Nd	3367	$(8.2 \pm 0.9) \cdot 10^{18}$	$> 4.5 \cdot 10^{23}$	$< 4.8 - 7.6$

Table 1.5: The most important isotope used for the research of the $2\nu\beta\beta$ and $0\nu\beta\beta$ decay. For each nuclide, the Q-value and the decay half-life is listed [14].

One of the main factor of merit for experiments searching the $0\nu\beta\beta$ decay is the sensitivity ($S^{0\nu}$), defined as the half-life related to the minimum number of events which can be discriminated from the background at a certain confidence level, usually equal to the RMS background fluctuation. In case the target decay would not be observed, then the experiment sensitivity is lower than the target decay half-life, hence:

$$S^{0\nu} < T^{0\nu}_{1/2} = \left(G^{0\nu} \cdot \left| M^{0\nu} \right|^2 \cdot |\langle m_\nu \rangle|^2 \right)^{-1} \tag{1.12}$$

Equation 1.12 means that, if an experiment would not observe evidence of $0\nu\beta\beta$ decay, then its sensitivity represents the upper limit of the effective electronic neutrino mass. Since the background follows the Poisson statistics, it could be demonstrated that:

$$S^{0\nu} = \ln 2 \cdot \epsilon \frac{i.a.}{A} \sqrt{\frac{M \cdot t}{\Delta E \cdot B}} \tag{1.13}$$

where ϵ is the detection efficiency, $i.a.$ is the isotopic abundance of the nuclide of interest, A its mass number, M the total mass of the source under observation, t the experiment lifetime, ΔE the energy resolution at the Q-value, while the background index B is the

number background events per unit of energy, time and mass at the Q-value. In order to maximize the sensitivity, typical requirements of experiments devoted to the research of the $0\nu\beta\beta$ are:

- **High isotopic abundance**: the isotope of interest must have a reasonably high *i.a.*. Choosing an isotope with a large natural isotopic abundance would prevent the need of expensive processes of isotopic enrichment.
- **Large mass**: large scale experiments are required to push the sensitivity to extremely low neutrino masses. Worldwide collaborations are needed to deal with efforts and costs.
- **Long lifetime**: the data taking must lasts several years. Detectors and electronic systems must be reliable and extremely stable over the whole experiment lifetime.
- **Good energy resolution**: a relative energy resolution of the order of 0.1% is required. This calls for high quality crystals and low noise electronics.
- **Background minimization**: the background index should be minimized using both passive (for instance, using radiopure materials, radiation shields and developing complex cleaning procedures) and active techniques (for instance using veto detectors for cosmic rays, double read-out detectors for background recognition and developing off-line analysis tools such as the pulse shaped discrimination). Unlike the other parameters, the background index is the one which allows to improve the sensitivity by orders of magnitude. Furthermore, in zero background approximation (a single spurious count is expected in the region of interest for the whole experiment lifetime), the sensitivity rises proportionally to M and t.

During my PhD studies, I was involved in CUORE, a large scale experiment at National Laboratory of Gran Sasso (LNGS) searching the $0\nu\beta\beta$ decay in ^{130}Te using a bolometric technique. An overview of the CUORE experiment, its main features and my contributions to develop the electronics equipment used in the experiment are described in chapter 3.

Chapter 2

LHCb RICH Upgrade

2.1 The LHCb Experiment

LHCb is one of the main experiments at CERN in Meyrin, Geneva, Switzerland. The purpose of the experiment is to search for indirect evidence of new physics making very precise measurements on heavy hadron (containing charm or beauty quarks) decays, especially by looking for rare processes and CP-violating effects. LHCb experiment collects data from proton-proton collisions taking place inside the LHC (Large Hadron Collider) accelerator. The particle accelerator LHC is built inside a 26.7 km circular tunnel at a depth of about 100 m underground, between Switzerland and France. LHC is composed of two beam pipes where the proton bunches travel in opposite directions in ultra-high vacuum. The necessary centripetal acceleration is given by a system of helium-cooled superconducting bending magnets placed along the ring. The protons are focused to collide in correspondence of the four main detectors (CMS, ATLAS, ALICE, and LHCb) with a bunch crossing rate of 40 MHz (two consecutive collisions are spaced by 25 ns). The nominal peak luminosity of the accelerator is $L = 10^{34}$ cm^{-2}s^{-1}.

The LHCb experiment is dedicated to precise measurements of CP violation and rare decays of B hadrons. To achieve these goals the LHCb detector was designed to identify B hadron efficiently. The detector is configured as a single arm forward spectrometer with a forward angular coverage ranging from approximately 10 mrad to 300 (250) mrad in the bending (non-bending) plane. The detector geometry exploits the fact that, at high energies, both b and $\overline{b}$ hadrons are predominantly boosted in the direction of the initial momenta of the colliding particles, thus at small polar angles (defined with respect to the beam axis in proton-proton center-of-mass system). The angular coverage of the LHCb detector corresponds to a pseudo-rapidity of approximately $2.0 < \eta < 4.5$, where the lower limit reflects the maximum polar angle where b hadrons are produced, while the upper limit is due to the beampipe size. LHCb has operated since 2009 and during the RUN 1

(which lasted 3 years, from 2009 to 2012) collected 3 fb^{-1} with a maximum luminosity of $4 \cdot 10^{32}$ $cm^{-2}s^{-1}$ at a center of mass energy of $\sqrt{s} = 7$ TeV since 2011, $\sqrt{s} = 8$ TeV during 2012. After the Long Shutdown 1, the center of mass energy was further increased up to $\sqrt{s} = 13$ TeV and the LHCb experiment RUN 2 started from the end of 2015. In both the data taking runs, the LHCb detector operated at a nominal average luminosity of $L = 2 \cdot 10^{32}$ $cm^{-2}s^{-1}$, which is about 1/50 of the nominal peak luminosity of LHC. This choice was made to have a smaller number of interaction (usually one p-p collision per bunch crossing) for a better vertex reconstruction, which is a fundamental requirement in flavour physics. The layout of the LHCb spectrometer is shown in Figure 2.5. The right-handed coordinate system adopted has the z-axis along the beam, and the y-axis along the vertical direction. The LHCb detector is composed by several subdetectors, each of which has a specific design and is optimized to measure a different physical quantity. In the next sections, a brief overview of the LHCb detector and its various subdetectors is provided.

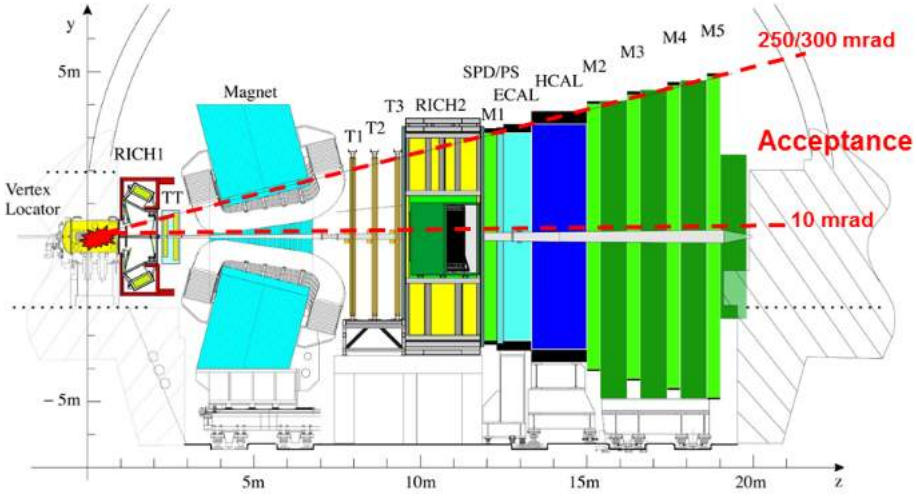

Figure 2.1: Schematic lateral view of the LHCb detector. The z-axis represents the beam direction.

2.1.1 VELO

The VErtex LOcator (VELO) [15, 16] provides precise measurements of the track coordinates close to the interaction points. This information is used to identify displaced secondary vertexes typical of b and c hadron decays. The VELO consists of a series of D-shaped planar silicon modules arranged along the beam direction. Each unit provides a two-dimensional measure of the track coordinates expressed in polar units (r is the radial distance from the beam axis and ϕ the angular displacement). r and ϕ are acquired by silicon microstrip detectors (300 μm thick) whose geometry was optimized to be sensitive

to a specific coordinate. The third coordinate (z) is provided by the knowledge of the position of each planar sensor within the VELO. In order to prevent the detector to be damaged by radiation during the beam injection and acceleration, the VELO silicon module are mounted on a retractable system which allows to keep them at a distance of 3 cm away from the beam axis. As soon as the beam is collimated and stable, the modules are moved to 8 mm from the beam axis. The VELO is capable to provide a spatial resolution in the primary vertex reconstruction of 40 μm and 10 μm in the parallel and perpendicular direction respectively. Two additional planes, located upstream of the VELO and perpendicular to the beam-line direction, constitute the pile-up detection system, acting as a trigger veto. The pile-up system also estimates the number of primary proton-proton interactions for each bunch crossing.

2.1.2 Tracking System

The trajectory reconstruction is a crucial feature necessary to identify the signatures of the decays and the particle momenta (if used with a bending magnet). Beside the VELO, the LHCb tracking system is composed by TT (Tracker Turicensis), T1, T2 and T3 tracking stations [15]. The TT is a 150 cm wide and 130 cm high planar tracking station. It is made of 4 layers of silicon microstrips and is large enough to cover the full angular acceptance of the experiment. Unlike the station TT, T1-T2-T3 are located downstream the magnet, as illustrated in Fig. 2.1. The T1-T3 are divided in two parts built with different technologies called Inner Tracker (IT) and Outer Tracker (OT). The IT [17], composed by silicon microstrip detectors, covers a 120 cm wide and 40 cm high cross shaped region in the center of the T1-T2-T3 tracking stations. The OT [18], which covers the most peripheral areas, is a drift-time detector designed as an array of individual, gas-tight straw-tube modules, composed of two staggered layers of 64 drift tubes each, filled by a mixture of Argon and CO_2. This choice ensures fast drift time (below 50 ns) and a sufficient spatial resolution (200 μm). From the position of the particle interaction in the tracking system, the trajectories of the charged particles can be reconstructed with an efficiency larger than 96% in the momentum range going from 5 GeV/c up to 200 GeV/c, and in the pseudorapidity ranging from 2 to 5.

2.1.3 Magnet

A dipole magnet [19] is used in the LHCb experiment to bend the trajectories of the traveling charged particles, thus allowing the measurement of their momenta and charge sign. Indeed, the bending of the trajectory is proportional to the electric charge of the particle and the magnetic field intensity, while a sign flip of either the charge or the field would cause an inversion of the bending direction. The magnet provides a magnetic field in the vertical direction (y-axis, referring to the notation used in Fig. 2.1) of 4 Tm integrated

along 10 m. To reduce the systematic effects of the detector, the direction of the magnetic field can be periodically flipped, so that data can be acquired with field polarity directed either upwards or downwards.

2.1.4 RICH

Particle identification (PID) is a fundamental requirement for LHCb. To this purpose, LHCb includes two RICH (Ring Imaging CHerenkov) detectors, mainly responsible for the kaons and pions identification. [15, 20]. The RICH1 detector is located upstream of the LHCb dipole magnet, between the VELO and the TT, and provide particle identification in the low momentum range (from ~ 1 to ~ 60 GeV/c) over a wide angular acceptance ranging from ± 25 mrad to ± 300 mrad (± 250 mrad), along the horizontal (vertical) direction. The RICH2 detector is located downstream of the magnet, between the last tracking station (T3) an the first muon station (M1) 2. It is capable to operate in the high momentum range, going from ~ 15 to ~ 100 GeV/c, in a limited angular acceptance ranging from ± 15 mrad to ± 120 mrad (± 100 mrad) in the horizontal (vertical) direction, large enough to cover the region where the high momentum particles are produced. A more detailed description of such apparatus will be provided in the next sections.

2.1.5 Calorimeters

The calorimeter system [15, 21] is capable to measure the transverse particle energy (E_t, defined as the energy of the particle multiplied by the sine of the angle between its momentum and the beam line), identify electrons, photons and hadrons and measure their energy and position. This system is composed by several stages: an electromagnetic (ECAL) and a hadronic (HCAL) calorimeter, a Scintillator Pad Detector (SPD) and a PreShower (PS). Both the calorimeters work exploiting the same basic operation principle: the impinging particles goes through high density material (absorber) causing a shower. The particles of the shower are collected by scintillating detectors, whose light is converted into electrical signal by a Photo-Multiplier tube (PMT). The light is driven to the PMT by means of wavelength-shifting (WLS) fibers, which also adjust the radiation wavelength to be matched to the maximum PMT quantum efficiency. The SPD and the PS are placed before the ECAL and are separated by a 15 mm lead, which is thick enough to generate electromagnetic showers but not hadronic showers. The ECAL is built from alternating 2 mm thick lead and 4 mm thick scintillating material. ECAL identifies electrons and photons end measures their energy with a resolution of the order of $\sim \sigma_E/E = 10\%/\sqrt{E}$, being E expressed in GeV. The HCAL is a similar device made of a sequence of alternating iron and scintillating tiles, behaving as absorber and active material respectively. HCAL helps in the identification of hadrons and allows to measure their energy with a resolution of $\sim \sigma_E/E = 69\%/\sqrt{E}$, being E in GeV unit.

2.1.6 Muon detector

The selection and identification of muons are fundamental requirements of the LHCb experiment as they are present in the final states of many CP-sensitive B decays and of rare B and D decays that have the potential to reveal new physics. They also help in tagging the initial flavour state of the accompanying neutral B mesons in CP asymmetry and oscillation measurements. The LHCb muon system [15, 22] is composed of five stations (M1-M5), as visible in fig.2.1. The first station M1 is placed in front of the calorimeters and is used to improve the measurement of the muon transverse momentum, useful for the trigger operation. Stations from M2 to M5 are placed downstream the calorimeters and are interleaved with iron absorbers 80 cm thick to select penetrating muons. In all the muon stations, Multi Wire Proportional Chambers (MWPC) are employed except in the inner region of station M1 where a triple-GEM (Gas Electron Multiplier) detector is used instead, in order to prevent an excessive aging of the MWPC due to the extremely high particle flux.

2.1.7 Trigger

As mentioned, the LHCb detector has been designed to operate at a luminosity of $2 \cdot 10^{32}$ $\mathrm{cm}^{-2}\mathrm{s}^{-1}$ with a bunch crossing of 40 MHz. Such huge amount of data generated by the proton-proton collisions at LHC cannot be completely stored. Furthermore, given the rareness of the events of interest, the large majority of the collisions are not useful for the experiment goals. The trigger [15, 23] is the system which fulfills the crucial task of the selection of interesting events. In particular, the 10 MHz event rate must be reduced to approximately 2 kHz to be stored for off-line analysis. The LHCb trigger is divided in two levels: the Level 0 Trigger (L0) and High Level Trigger (HLT). The former trigger is implemented in hardware and reduces the data flow from 40 MHz to 1 MHz by selecting hadrons, electrons and photons with high E_t in the calorimeters and muons with high p_t in the muon system, typical characteristic of the decay products of b or c hadrons. The L0 also uses information from the pile-up system, as veto. The HLT is implemented in software and reduces the data flow from 1 MHz to about 2 kHz. It consists of a C++ application which initially performs a partial reconstruction of the physical properties of the particles using the information from the VELO and the tracking system to confirm the L0 decision. To the remaining candidates, the HLT performs a full event reconstruction and applies a series of event selection criteria, reducing the data flow to about 2 kHz.

2.1.8 The LHCb Upgrade

The primary goal of LHCb is to measure the effects of new particles or forces beyond the Standard Model. Results obtained from data collected in 2009 show that the detector is robust capable to measure a lot of interesting channels in heavy flavour decays. Nevertheless,

a limit of about 1 fb^{-1} of data collection per year cannot be overcome without upgrading the detector. As mentioned in the first paragraph, the LHC accelerator is not the limit factor since it is able to provide luminosities up to $L = 10^{34}$ $cm^{-2}s^{-1}$, 50 times larger that currently exploited by the LHCb experiment. By reading out the detector at the bunch crossing frequency (40 MHz) and implementing a much more flexible software-base triggering strategies, a significant reduction of the statistic uncertainties can be achieved. In particular, the detector would be able to collect 5 fb^{-1} per year with an increased efficiency on triggering decays with hadronic final states. In addition, such configuration would allow to change the trigger criteria to explore different physics as LHC discoveries point us to the most interesting channels. So, the increase of the sustainable luminosity and a renewed trigger implementation would open further possibilities for interesting discoveries over a whole variety of phenomena, including searches for Majorana neutrinos, exotic Higgs decays and precision electroweak measurements.
Although the base structure of the LHCb detector will remain unchanged, the enhanced performance can be accomplished only with a complete upgrade of the read-out system. In particular, the detector read-out frequency must be increased by a factor of 40, from the current value of 1 MHz up to 40 MHz (the bunch crossing frequency). For some systems composing the LHCb detector, such large increase of the read-out frequency requires a complete renovation of both the sensors and the readout electronics. The upgrade is planned to be installed during the Long Shutdown 2 (LS2) in 2020. Afterwards, upgraded LHCb experiment will be ready to resume the data taking and start the RUN 3, at a luminosity of $L = 4 \cdot 10^{33}$ $cm^{-2}s^{-1}$ at center of mass energy of $\sqrt{s} = 14$ TeV. My contribution to the LHCb experiment has been particularly focused on the upgrade of the RICH detectors, crucial for the particle identification. In the next section a brief overview on the Cherenkov effect and on the current LHCb RICH system will be provided and finally the upgrade plan will be discussed.

2.2 Cherenkov effect

The Cherenkov effect, which brings the name from its discoverer rewarded with the Nobel Prize in 1958, consists of the emission of electromagnetic radiation by a charged particle traveling in a dielectric medium faster than the velocity of the light in that medium. The well-known Einstein relativistic theory states that the speed of light in a vacuum is an universal constant (c) and represents the maximum reachable speed. Despite this, the speed at which light propagates in a material can be significantly less than c. In particular, by the definition of the refractive index (n) of the medium where the light is propagating, the speed of the light in that medium is given by c/n. For instance, considering a typical silicate glass ($n \sim 1.4$), the speed of propagation of the light in such medium is $\sim 0.7c$ and could be exceeded by the velocity a relativistic particle.

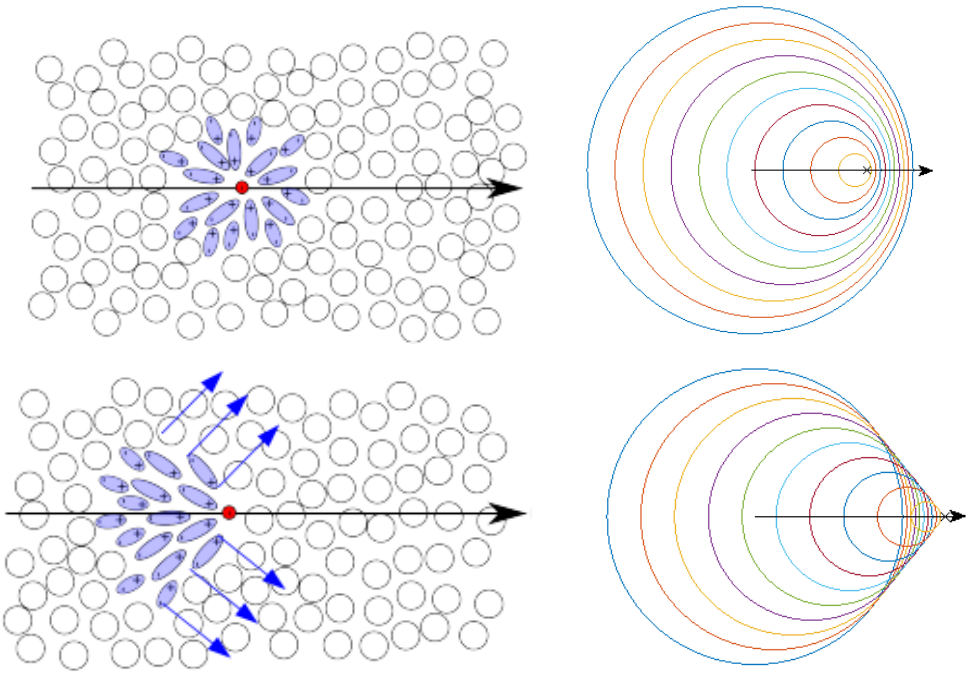

Figure 2.2: On the top line, a charged particle going through a dielectric with $\beta < c/n$. The induced dipoles are symmetric and the fronts of the emitted radiation interfere destructively: no radiation is thus emitted. On the bottom line, a charge particle traveling through a dielectric with $\beta > c/n$. The induced dipoles are asymmetric and the medium shows a local net polarization. As the dipoles relax, the fronts of the radiation interfere constructively and the Cherenkov light is emitted. On the right side, the wavelets calculating applying the Huygens-Fresnel principle in both these cases. For $\beta < c/n$, any wavefront can be recognized while, if $\beta > c/n$, the wavefront of the Cherenkov radiation consists in a cone surface.

When a charged particle passes through a medium, the particle's electric field is locally superimposed to that of the medium lattice. In particular, in the case of dielectric radiator, this time dependent local field results in a dipole momentum induced to the atoms of the medium. As the particle is gone away, the atoms relaxes to the original states and a electromagnetic radiation is emitted. In the case in which $\beta < c/n$, the induced dipoles are distributed symmetrically so that electromagnetic wavelets emitted by each of them interfere destructively and no radiation is thus generated (see Fig. 2.2). On the other hand, if the high energy particle passes through the medium with $\beta > c/n$, then the dipoles does not reach a symmetrical distribution. As the dipoles relaxes, the wavelets generated interfere constructively and the wavefront of the resulting Cerenkov radiation is emitted on the surface of a cone.

The energy spectrum of the Cherenkov radiation can be calculated from the Maxwell's

equations and is expressed by the Frank-Tamm formula:

$$\frac{d^2E}{d\omega dx} = \frac{q^2}{4\pi}\mu(\omega)\omega\left(1 - \frac{1}{\beta^2 n(\omega)^2}\right) \tag{2.1}$$

where q is the charge of the high energy particle, $\beta = v/c$ the ratio by its speed and that of the light in the vacuum, ω the angular velocity, $n(\omega)$ and $\mu(\omega)$ the refractive index and the magnetic permeability, dependent on ω, of the dielectric medium. Assuming $\mu(\omega)$ constant with respect to ω, Eq. 2.1 can be easily expressed in term of number of photons emitted per unit length and wavelength. Considering that $E = Nh\nu$ and $\nu = \omega/2\pi = \beta c/\lambda$, one obtains:

$$\frac{d^2N}{d\lambda dx} \propto \frac{q^2}{\lambda^2}\left(1 - \frac{1}{\beta^2 n(\lambda)^2}\right) \tag{2.2}$$

Neglecting the refractive index spread as a function of the radiation wavelength, the photon production yield linearly increases with the thickness of the Cherenkov radiator and is inversely proportional to the square of the radiation wavelength. In particular, the Cherenkov photons are typical emitted into the optical domain and the radiation increases in the violet-ultraviolet range. In addition, Eq. 2.2 states that the Cherenkov spectrum only depends on the charge and the speed of the high energy particle, so that the radiation spectra of electrons, pions, protons or kaons are identical at a given β. This characteristic can be easily deduced considering the particle as source of radiation and applying the Huygens-Fresnel principle. Each point of the particle trajectory behaves like an electromagnetic source, which propagates isotropically in the medium with a speed of c/n, while the particle moves with a speed $v = \beta c$. The wavefront can be geometrical calculated as the line tangent to all of the wavelets emitted by all the punctual sources. By using this procedure, one can built the plots in Fig. 2.2, right column. It can be clearly observed that, if $\beta < c/n$, then there is no line tangent to all the wavelets, compatible with the expectations of destructive interference between them. On the other hand, if $\beta > c/n$, then the envelop of the wavelets results in a cone whose vertex is centered in the particle position. Moreover, the angle of the Cherenkov cone can be easily deduced from its geometrical construction.

Referring to Fig. 2.3, let consider a particle moving from A to B with $\beta > c/n$ and project the motion on the plane which the particle's trajectory belongs to. Called t the time interval in which the particle moves from A to B, than ABC is a right-angle triangular whose hypotenuse is $\overline{\text{AB}} = \beta ct$ represents the particle trajectory while the $\overline{\text{AC}} = ct/n$ cathetus is the motion of Cherenkov photon. Note that this formula assumes that the particle moves with a uniform motion, although it loses energy to induce the dipoles, sources of the radiation. This approximation is good since the energy lost by the particle via Cherenkov effect is negligible ($\sim 0.1\%$) with respect to that due to atom ionization. Finally, the ABC triangle is right-angle as $\overline{\text{AC}}$ is the radius of the Huygens-Fresnel circular

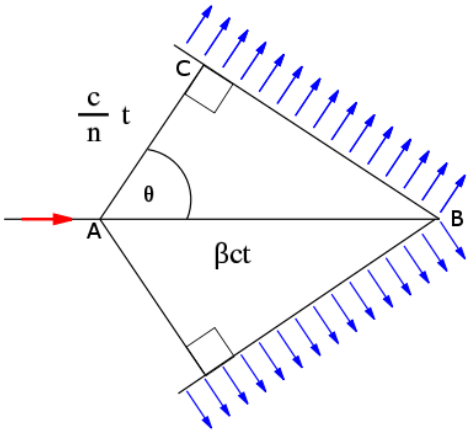

Figure 2.3: Geometrical scheme of the Cerenkov cone emission, projected on the plane hosting the particle's trajectory.

wavelet centered in A and $\overline{\mathrm{BC}}$ is built as a tangent to this circumference. Hence, from the definition of the trigonometric functions, one obtains:

$$\cos\theta = \frac{\overline{\mathrm{AC}}}{\overline{\mathrm{AB}}} = \frac{1}{n\beta} \tag{2.3}$$

or, equivalently:

$$\theta = \cos^{-1}\left(\frac{1}{n\beta}\right) \tag{2.4}$$

Equation 2.4 implies that the Cherenkov angle θ only depends on the refractive index of the dielectric medium (function of the radiation wavelength) and the particle speed. This means that the velocity of the particle can be measured from the Cherenkov angle irrespective of particle charge, mass or type, just knowing the medium refractive index. Since the cosine codomain is limited to 1, Eq. 2.3 implies that $\beta \geq 1/n$ is the condition ensuring the Cherenkov angle is well defined. In addition, given that $\beta \leq 1$ by definition, the maximum Cherenkov angle saturates to $\theta = \cos^{-1}\left(\frac{1}{n}\right)$. The medium refractive index plays a crucial role to the operation of a RICH system.

2.3 The LHCb RICH detector

In order to fulfill the task of particle identification (PID) and, particularly, discriminate kaons from pions over a wide momentum range (from 1 to 100 GeV/c), the LHCb detector is equipped with two RICH stations. The RICH is a detector which uses Cherenkov radiation, emitted when a particle traverses a proper radiator with speed higher than speed of light in that medium. Since, according to Eq. 2.4, the Cherenkov radiation is emitted with a characteristic angle θ which depends on the speed of the particle irrespective

of the particle momentum p, its mass can be determined if θ and p are independently measured. Indeed, exploiting the natural unit measurement base (i.e. $c = 1$ and $\beta = v$), the particle momentum can be expressed as $p = \gamma\beta m$, where γ is the Lorentz factor defined as $\gamma = \frac{1}{\sqrt{1-\beta^2}}$. Using this convention, Eq. 2.4 becomes:

$$\theta = \cos^{-1}\left(\frac{\sqrt{p^2+m^2}}{np}\right) \tag{2.5}$$

Equation 2.5 explicits the dependence of θ from the particle mass m and the possibility to deduce m by measuring n, p and θ. In order to do that, a noticeable variation of θ as a function of m is necessary to provide a good discrimination between particles, for a given values of p and n. In particular, from Eq. 2.5, one can calculate:

$$\frac{\delta\theta}{\delta m} = -\frac{m}{\sqrt{(p^2+m^2)\left[(n^2-1)\,p^2-m^2\right]}} \tag{2.6}$$

Since $\gamma^2 = \frac{m^2+p^2}{m^2}$, one obtains:

$$\frac{\delta\theta}{\delta m} = -\frac{1}{\gamma p\sqrt{n^2-1-\left(\gamma^2-1\right)^{-1}}} \tag{2.7}$$

The square root of Eq. 2.7 is well-defined as long as $n^2-1-\left(\gamma^2-1\right)^{-1} > 0$. This condition is equivalent to require that $\beta > 1/n$, which is the usual condition that makes particles emit Cherenkov radiation. If the detector deals with ultra-relativistic particles ($\gamma \gg 1$), then the term $\left(\gamma^2-1\right)^{-1}$ is negligible and Eq. 2.7 can be simplified in:

$$\lim_{\gamma\gg 1}\frac{\delta\theta}{\delta m} = -\frac{1}{\gamma p\sqrt{n^2-1}} \tag{2.8}$$

If $p \gg 1/\left(\gamma\sqrt{n^2-1}\right)$ then $\delta\theta/\delta m \sim 0$, which implies that the Cherenkov angle is substantially independent of the particle mass. Indeed, at extremely high momenta the Cherenkov angle is saturated to the value $\theta = \cos^{-1}\left(n^{-1}\right)$, condition that prevent us to measure the particle mass and perform the PID. Otherwise, if $p \sim 1/\left(\gamma\sqrt{n^2-1}\right)$, then an observable variation of θ can be detected and PID accomplished. Thus, the detector Cherenkov radiator must be optimized to provide a good distinction between particles in the desired momentum range. In particular, the higher the particle momentum, the closer to unity must be n. Furthermore, the closer to 1 is n, the less Cherenkov photons are produced (Eq. 2.2) and the smaller is the Cherenkov angle emission (Eq. 2.4). The criticalness of the radiator justifies the need of two RICH stations with different Cherenkov media in order to be sensitive over the full momentum range ($0-100$ GeV/c). The RICH 1 detector, located upstream the magnet, identifies charged particles in the low and medium momentum range (from 1 to 60 GeV/c, approximately), using silica aerogel ($n = 1.01$) and fluorobutane (C_4F_{10}, $n = 1.0014$) as radiators and covering the full LHCb angular acceptance. The RICH 2 detector, located downstream of the magnet, contains a carbon tetrafluoride

gaseous radiator (CF_4, $n = 1.00048$) and provides PID in the high momentum range (from approximately 15 to 100 GeV/c) in a acceptance limited to the low-angle region (where high momenta particles are produced). A schematic view of the two LHCb RICH stations is shown in Fig. 2.4.

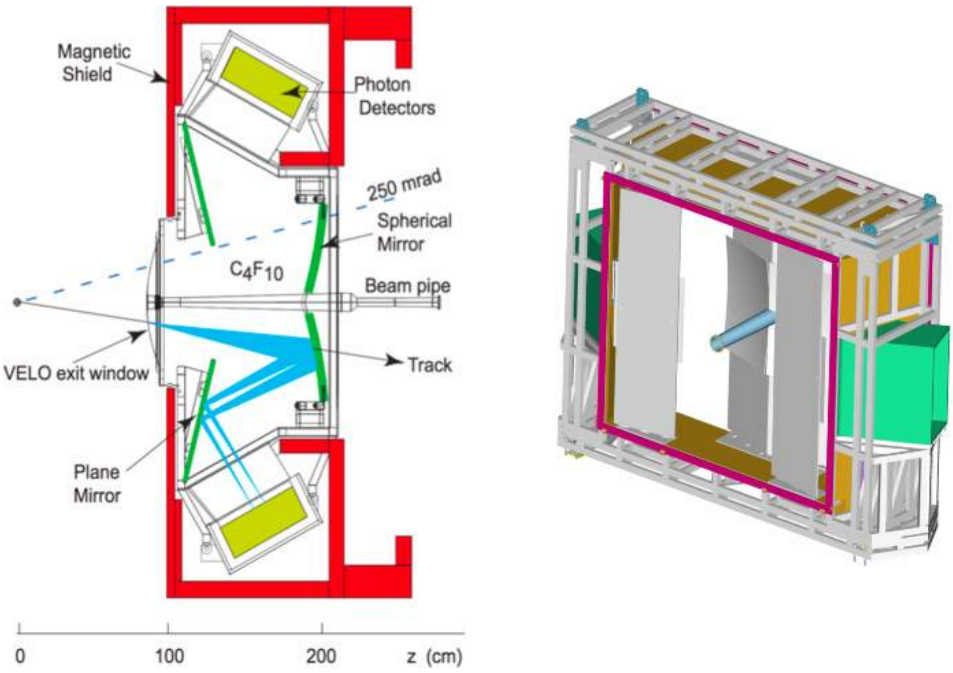

Figure 2.4: Schematic view of the LHCb RICH 1 (on the left) and RICH 2 (on the right) detector.

The structure of the two stations is similar. The high energy particles enter in the detector vessel, enclosing the gaseous radiator, and emit Cherenkov photons with the characteristic emission angle with respect to the momentum direction. Since the radiation is isotropically emitted in the plane perpendicular to the particle motion, the photons are emitted on the surface of the a cone. The Cherenkov light is reflected by a spherical mirrors towards a plane mirror, finally driving the radiation to the photon detector planes located outside the spectrometer acceptance. The curvature of the spherical mirror has been studied to focus the Cherenkov radiation to the photosensitive plane, so that the hitmap of the photons emitted by each particle describes a circular trace representing the base of the Cherenkov cone. Neglecting all the detector non-idealities, the radius of such circle only depends on the known focal length of the spherical mirrors and on the Cherenkov emission angle. The photon hit positions, for each target particle, is fitted with a circular function. The radius of the trace is thus measured and the Cherenkov angle is finally calculated. By combining such information with the momentum and charge sign measured by the tracking and magnet systems, it is possible to determine the particle species [20]. In order

to accomplish the PID, an overall event log-likelihood algorithm is employed, where all tracks in the event and in both RICH detectors are considered simultaneously. At the starting point, all particles are assumed to be pions, since they are the most abundant particles in proton-proton collisions. Then, for each track, the mass hypothesis is changed to electron, muon, kaon and proton. The one which gives the largest increase in the event likelihood is set as preferred value of the mass hypothesis for that track. The typical hitmap acquired by the photosensors and the measured Cherenkov angle as a function of the momentum are shown in Fig. 2.5. This figure also shown the PID performance achieved by the LHCb RICH detectors during the RUN 1 [20].

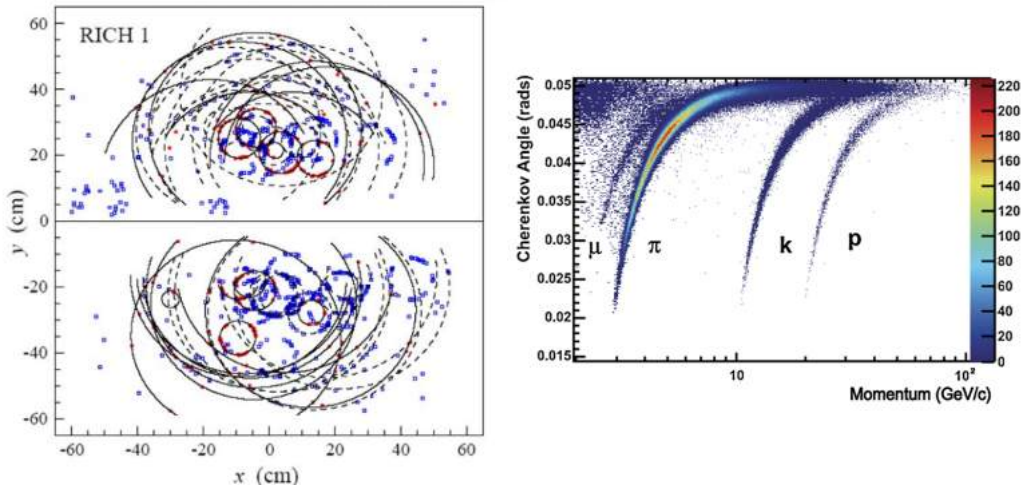

Figure 2.5: On the left, a typical event hitmap observed at the LHCb RICH system. The circular lines fitting the detection point are the results of the Cherenkov ring reconstruction. This lead to a particle identification over a wide momentum range, as shown in the right plot.

The ~ 2.9 m^2 photosensitive surface needed for the total RICH system of the current LHCb detector is composed of a matrix of Hybrid Photon Detector (HPD) operating at room temperature. The circular-shaped entrance window, made of quartz to be transparent to UV radiation, hosts the photocathode which converts the impinging photons into electrons via photoelectric effect (single photon sensitivity ensured at wavelengths ranging from 200 nm to 600 nm). Thanks to the low working function of the photocathode, the photoelectrons usually have enough energy to escape from it inside the device vessel, in deep vacum condition. An intense electrical field (~ 20 kV) accelerates the photoelectrons for ~ 10 cm towards the anode, consisting of a Silicon pixel array (1024 pixels per device, 2.5×2.5 mm^2 pixel size). When the photoelectrons hit the anode, they have enough energy to start a multiplication cascade, so that ~ 5000 electrons per photon are collected at the output. Given the relative small gain of the HPD, a low-noise pre-amplifier circuit has to be placed as near as possible to the anodes. The front-end electronics is bump bonded to

the Si pixel array, thus it is embedded in the HPD enclosure. The electronics has been designed to operate with a maximum read-out frequency of 1 MHz. Since the gain of the HPD is achieved in a single step, the fluctuation of the collected charge is usually lower than the electronic noise and the typical spectra show peaks related to the different photon multiplicity. Furthermore, the HPDs ensure a good gain uniformity between the various pixels.
Several parameters have to taken into account which can spoil the spatial resolution and, consequently, the PID performance accomplished by the RICH system.

- **Mirror aberrations**: during the reconstruction procedure, all the photons are assumed to be emitted from the midpoint of the particle trajectory inside the RICH vessel. However, since the optical system of the RICH is non-ideal, the parallel wavefronts of the Cherenkov light emitted from the traveling particle are not perfectly focused on the photosensitive plane. Thus, the position where the photon hits the sensor shows a residual dependence from the photon emission point. As a consequence, aberrations of the lens might add a contribution reducing the spatial resolution.

- **Photon emission position**: as mentioned, the all the photons are assumed to be emitted from the midpoint of the particle trajectory inside the RICH vessel. As the RICH system is enclosed in an iron magnetic shield, the trajectory is assumed to be the linear segment linking the positions detected by the tracking system place upstream and downstream the RICH. The spatial resolution of the tracking system results in a photon emission point uncertainty and, consequently, affects the Cherenkov angle reconstruction.

- **Chromatic dispersion**: the refractive index of the medium is not constant since depends on the unknown wavelength of the radiation. As the Cherenkov light spectrum is characterized by a continuous function, then the Cherenkov angle depends on the wavelength of the photon. In particular, the variation of n (for the radiator of interest, CF_4 and C_4F_{10}) as a function of the radiation wavelength is more remarkable in the near UV region.

- **Pixel size**: the pixel size represents the geometrical capability of sensor to discriminate for two adjacent positions. Photons synchronously hitting the photosensors with a distance lower than the pixels size cannot be separated.

- **Cross-talk among pixels**: this effect consists in the sharing of the signal between two adjacent pixels. This issue, to which both photosensors and read-out system might contribute, usually results in the synchronous counts of two spatially-correlated pixels. Since the signal of the photon cannot be discriminated to the cross-talk signal, this effect leads to an uncertainty of the photon detection position.

- **Number of photons**: the Cherenkov angle is measured from ~ 30 photons per event produced in RICH 2 by the traveling particle. In particular, the Cherenkov angle resolution improves proportionally to the square root of the number of detected photons. High quantum collection and detection efficiency can enhance the PID performance.

- **Dark counts**: spurious counts (for instance, due to thermally generated cascade) are usually less critical than cross-talk since these event are not spatially correlated with the photon signals. Nevertheless, the dark count rate must be kept low to simplify the reconstruction procedure and ensure a fast likelihood calculation.

The LHCb RICH system has been able to provide an excellent PID capability during the experiment RUN 1, as visible in Fig. 2.5 [20]. Nevertheless, the performance of the current RICH system do not match with the requirements for the upgraded LHCb detector.

2.4 The Upgraded LHCb RICH detector

In order to exploit the whole luminosity provided by the LHC accelerator, an upgrade of the LHCb detector is planned in order to increase the read-out frequency to 40 MHz. As mentioned in the previous section, the currently used HPDs is equipped with an embedded front-end electronics operating at 1 MHz. Furthermore, the much higher event rate expected in the RUN 3 can cause issues related to the radiation tolerance of the silicon device (pixellated array and front-end chip). The upgraded system has to cope with a much higher occupancy, defined as the ratio between the rate of event per pixel and the read-out frequency. Although the overall structure of the RICH system will remain unchanged, the following improvements are planned:

- **Mirror focal length**: keeping the photosensors in the current position, the expected occupancy level in the hottest RICH 1 region at the enhanced luminosity would overcome 100%, so that it cannot be sustained by the system. A method to reduce the occupancy to reasonable value would be to use much smaller pixels, but this solution leads to an extremely high channel density and to much higher costs. On the other hand, the same effect can be obtained using a larger focal length. The photosensitive plane must be moved backwards to match with the new focal length. In this case the photons are distributed over a larger surface, reducing the number of hits per channel. Adjusted optical system and renewed mechanics for the photosensitive planes are planned.

- **Aerogel removal**: unlike the first design of the detector, which also exploited a solid radiator made of Aerogel, the current RICH 1 uses the only C_4F_{10} radiator. Such improvement will be maintained also in the upgraded detector as the relatively

large refractive index of the Aerogel is not compatible with the new requirements due to two main concerns. Firstly, the larger focal length and the new position of the photosensitive plane prevent the Aerogel Cerenkov radiation to be entirely contained inside the photosensitive area. There is neither room nor further founds to significantly enlarge the photosensitive plane dimension to match with the Aerogel signal. In addition, the large number of Cherenkov photons produced by the Aerogel contributes to further increase the occupancy, thus stressing the system and making the likelihood calculation to long to be exploited for the new on-line software trigger. As a consequence, the Aerogel has been removed. As drawback, the RICH system is less sensitive in the very low momentum range (under $\sim$ 10 GeV/c). In order to compensate for this effect, other techniques, such as the TORCH detector [24, 25], have been proposed for the upgraded phase.

- **Renewed photosensitive plane**: the HPDs cannot operate at 40 MHz read-out frequency so that they are removed. The photosensitive plane will be composed of Multi-Anode PhotoMultiplier Tube (MaPMT) coupled with an external custom front-end electronics, sustaining the 40 MHz read-out rate. Mechanics, magnetic shielding, high and low power suppliers, cooling system and whatever is related to the Cherenkov photon detection system must be adjusted to interface with the new sensors and electronics.

The photosensitive planes of the RICH detector are designed with a modular structure where the smallest units are called Elementary Cell (EC). Two EC models were designed: EC-R houses four 1×1 inch^2 MaPMTs (the Hamamatsu R13742 MaPMT, a customization of the R11265 tube), whereas the EC-H houses a single 2×2 inch^2 MaPMT (the Hamamatsu R13743 MaPMT, a customization of the R12699 tube). Both MaPMTs models are 64 channel, 8×8 pixallated square device. The whole upgraded RICH system will be composed of $\sim$700 EC-R covering the RICH 1 and the central part of the RICH 2 photosensitive planes, while $\sim$400 EC-H will be used in the peripheral areas of the RICH 2 detector (as shown in Fig. 2.6), where larger pixel size can be used since the occupancy level is lower and the spatial resolution is not limited by the photodetector granularity. This design ensures significant reduction of the costs with a negligible degradation of the overall PID performance. The final system will consist of $\sim$3100 MaPMTs and $\sim 2 \cdot 10^5$ channels.
An isometric view of a half-mounted EC-R for the upgraded LHCb RICH detector is shown in Fig. 2.8. The incoming Cherenkov photons produced by a particle moving faster than light in the dielectric gas radiator hit the MaPMT surface. The photodetectors are mounted in a custom support, called baseboard (BsB), which hosts the voltage divider biasing the sensors (HV$\sim$ 1 kV) and provides a cross-shaped thermal mass, which behaves as a low thermal impedance path driving the heat dissipated by the divider towards the metallic structure surrounding the EC. The photocathode of the MaPMT converts the

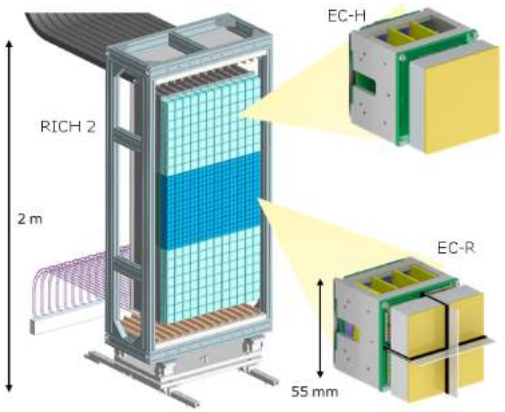

Figure 2.6: Schematic view of the LHCb Upgraded RICH 2 photosensitive plane. The EC-R, also used in whole RICH 1 system, populates the central region of the RICH 2 detector, where high occupancy is expected. In the peripheral areas the EC-H cells are used instead, since large pixel size do not affect the overall PID capability.

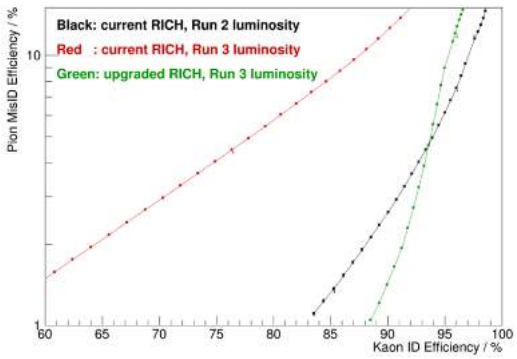

Figure 2.7: Simulated PID performance of the LHCb RICH system. The pion misidentification rate is shown with respect to the kaon identification efficiency is shown at the luminosities expected in the LHCb RUN 2 ($L = 2 \cdot 10^{32}$ cm^{-2}s^{-1}) and RUN 3 ($L = 4 \cdot 10^{33}$ cm^{-2}s^{-1}). The upgraded RICH system ensures performance as good as the current system at luminosity 50 times larger.

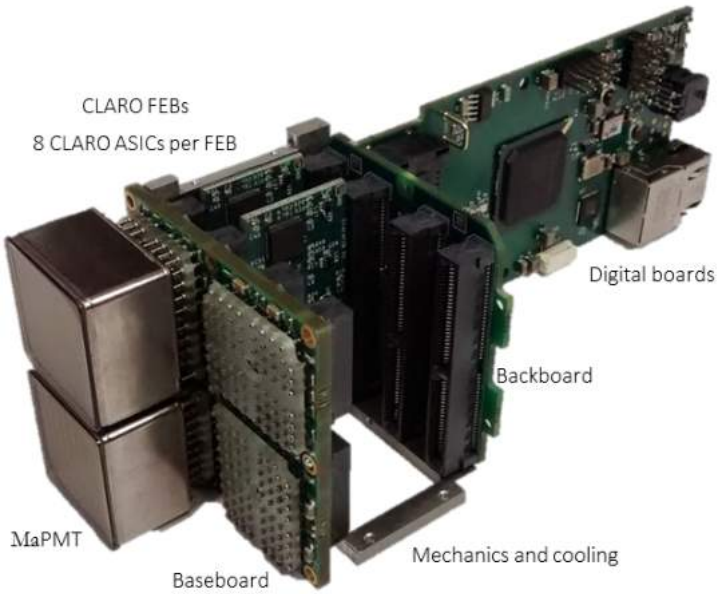

Figure 2.8: Half-instrumented EC-R

incident photons into electrons via the photoelectric effect, and the electrical signal is then amplified by a 10-stage dynode chain, so that $\sim 10^6$ electrons per photon are collected at each anode. The electric signal is transmitted through the BsB to the front-end board (FEB), each hosting 8 read-out ASICs, called CLARO, specifically developed for this purpose. The CLARO [26] is a 8-channel chip designed in 0.35 μm CMOS technology from AMS[1] able to provide a digital pulse if the integrated charge collected at the MaPMT anode is larger than a settable trigger threshold. This pulse, interpreted as the detection of a photon hitting the pixel under study, passes through the backboard and reaches the digital board[2] (DB). The core of the DB is a FPGA capable of collecting the CLARO signals, sending the data out of the detector, configuring the operational parameters of the chip and interfacing to the remote control. Finally, the metallic structure surrounding the cell is coupled to the cooling system allowing the system to operate close to room temperature.

During the PhD, my contribution was particularly devoted on the characterization of the MaPMT and the development of the CLARO ASIC. In Sect. 2.5 and Sect. 2.6 the study on the Hamamatsu R11265 and R12699 MaPMT will be shown. The obtained results guided the LHCb RICH Upgrade collaboration to choose such devices as photosensors to be used in the renewed detector design. In Sect. 2.7 the CLARO chip and the choices guided the EC layout design will be presented. In Sect. 2.8, the procedures for the EC calibration are presented. During these years, the whole system performance has been periodically tested at CERN using a high energy beam to produce Cherenkov photons. The results obtained at such beam tests, useful to characterize the full system in a experimental condition similar to those expected in the final environment, are shown in Sect. 2.9.

2.5 R11265 MaPMT Characterization

Recently, Hamamatsu started to produce the new R11265 multi-anode photomultiplier tube (Fig. 2.9). It is a 64-channel (8×8) pixel device with an active area of 23×23 mm^2 and a pixel size of approximately 2.9×2.9 mm^2 which is able to detect single photons. A very small inactive border around the device ensures a total active area coverage of about 77%, while the MaPMT square cross-sectional geometry allows for a close packing ratio (approximately 90%). This value is much larger than the coverage area facor of $\sim 70\%$ accomplished with the HPDs, given their circular cross-sectional geometry.

These features make the R11265 particularly tailored for an application in high energy physics, such as in the LHCb RICH system. In order to fulfill the requirements of such an application, the MaPMTs must add a minimal noise contribution with respect to the

[1] Austria Micro Systems, website `http://ams.com`

[2] The final design of the DB is currently in development. The DB shown in Fig. 2.8 is a preliminary version.

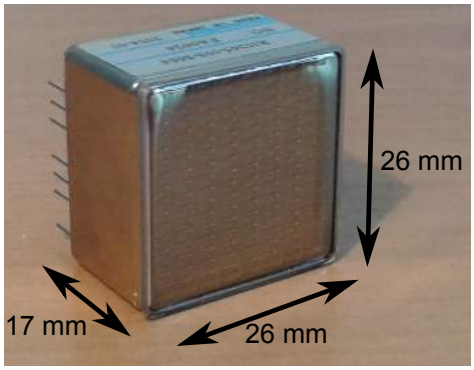

Figure 2.9: A picture of the Hamamatsu R11265 MaPMT and its outer dimensions. The active area is 23×23 mm^2 (declared by Hamamatsu).

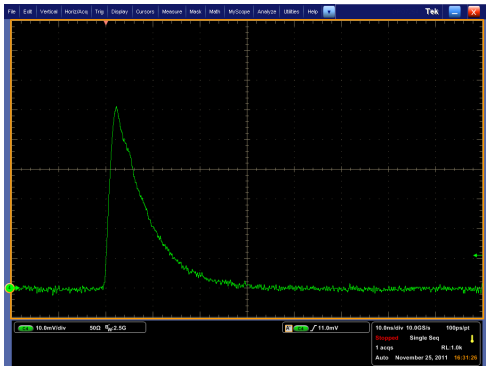

Figure 2.10: A typical single photon signal acquired by the Tektronix DPO7254 oscilloscope.

signal rate and a adequate cross-talk between neighbouring pixels. In addition to that, the photodetectors must not be affected by the magnetic field or, otherwise, external magnetic shields have to be developed. Considering, for instance, the upgraded RICH detector of LHCb, a magnetic field up to 30 G (3 mT) could be present on the photosensitive plane. Note that, previously, two different tubes made by Hamamatsu have been characterized by the INFN Milano Bicocca group to verify their compliance with the LHCb RICH requirements:

1. the H9500 was rejected because of a non-negligible cross-talk between pixels and was not designed for single photon signal [27].

2. the R7600 which gives good performance for single photon detection [28], but has poor coverage area.

The new R11265 MaPMT is similar to the R7600 but has an improved sensitive area. In order to fully characterize the device, different features were considered; for each of them, the description of the setup conditions and the results obtained are described. In section 2.5.1 the studies of the gain variation, anode uniformity, dark current, bias voltage divider, cross-talk, quantum efficiency and temperature behaviour are presented. In section 2.6.3 the measurements of the device inside a magnetic field and aging monitoring are described.

2.5.1 General features

The setup used to measure the basic characteristics of the tubes is the same as described in [28]. All the MaPMT pixels, except those under study, were covered with a black mask and black tape. A commercial blue LED was biased with a very small current so that

only few photons per second were generated. An optical fiber was positioned laterally to the LED and a small fraction of photons were brought to one pixel of the MaPMT, so that only that pixel was illuminated in each measurement. The black mask behaved also as a mechanical support for the optical fiber. The illuminated spot was a circle of 1 mm diameter, given by the dimensions of the optical fiber, centered on the MaPMT pixel. The anode current signal was read-out using a commercial wide bandwidth current feedback operational amplifier (CFOA) [29]. It produced an output voltage signal whose amplitude was proportional to the integrated input charge (Fig. 2.10). Finally, after acquiring this signal by a Tektronix DPO7254 fast oscilloscope, we were able to determine the signal amplitude and plot the single photon spectrum.

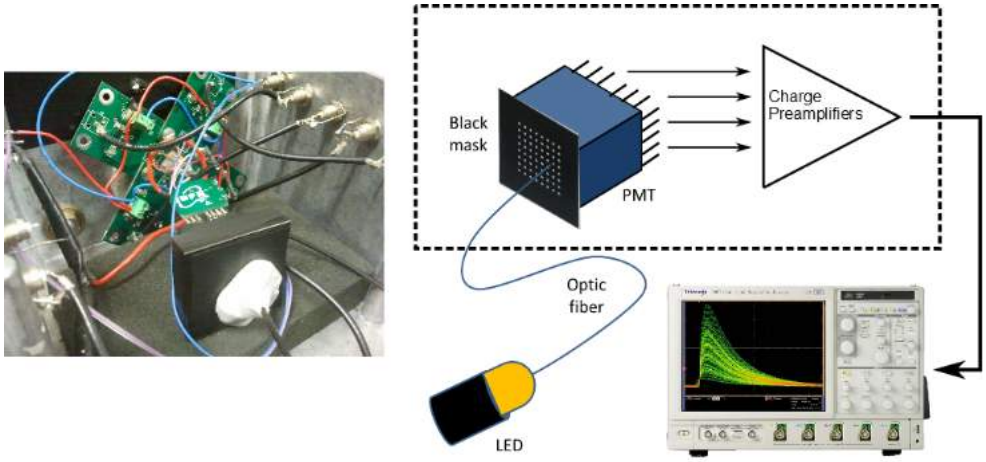

Figure 2.11: Schematic picture of the setup developed for the standard characterization of the R11265 MaPMT. The photons produced by a LED operating in single photon regime are brought to the pixel under study by means of an optical fiber (circular section, diameter of 1 mm). A black mask and a black tape cover all the other pixels, preventing from their illumination. The MaPMT output signal is read-out by a charge sensitive preamplifier circuit and finally acquired by a Tektronix DPO7254 fast oscilloscope.

2.5.2 Gain Variation and Anode Uniformity

The MaPMT gain and the anode uniformity were measured at different bias voltages in order to compare them with the Hamamatsu datasheet. During these tests the standard bias divider with a 2.3-1.2-1-...-1-0.5 ratio from the first dynode to the last was used. Excellent single-photon response is observed in almost all channels and only few channels show a bad single-photon peak resolution (Fig. 2.12). A MaPMT-to-MaPMT (Fig. 2.13) and channel-to-channel variation in gain is measured up to a factor of three. In order to equalize the response, the channels to channel mismatch can be corrected by adjusting the MaPMT voltage supply and the gain or the threshold of the front-end electronics [26], as

shown in Sect. 2.8. A uniformity table is provided by Hamamatsu for every tube. For one of the devices tested at -900 V it is shown in Fig. 2.14 (left). The numbers represent the relative gain of each pixel, the highest being 100.

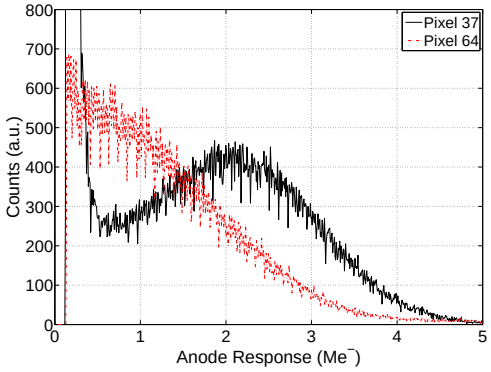

Figure 2.12: Single photon spectra for pixel 37 and 64 (MaPMT SN-ZN0702 biased at -1050 V.)

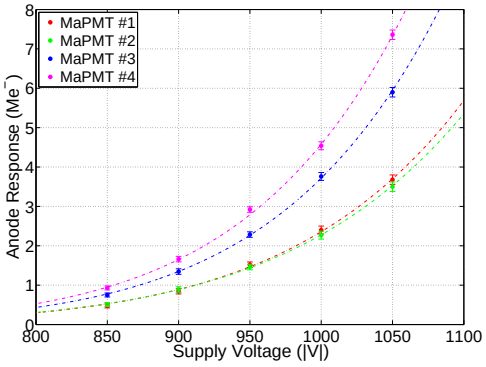

Figure 2.13: The single photon response versus the MaPMT bias voltage for the pixel with the maximum gain in each tube.

This measurement was performed by Hamamatsu with a continuous light source and thus the numbers reported represent the contributions from quantum efficiency, collection efficiency and gain. Figure 2.14 (right) shows the comparison of the spectra of different pixels, obtained with the setup previously described. The spectra are obtained with single photon signals and are normalized to the number of entries. The gain spread between different pixels is clearly visible. Almost all the pixels match the uniformity table, except for few of them (for example pixel 5). The gain spread among pixels is about 2.3 to 1 for this device.

2.5.3 Dark current

The photodetector dark current is measured at room temperature by recording the events above a threshold of 300 ke$^-$. Four MaPMTs have been tested in similar conditions and they showed the same behaviour. Each MaPMT is left in darkness for about two hours and after that the dark signal rate is below 5 Hz per pixel, or about 60 Hz/cm^2, for almost all anodes. Only few channels showed a slightly higher rate. The distribution of dark signals is acquired and compared with the spectra obtained turning on the LED. Figure 2.15 shows the two spectra, normalized to the same number of counts in the single photon region: the spectra are very similar.

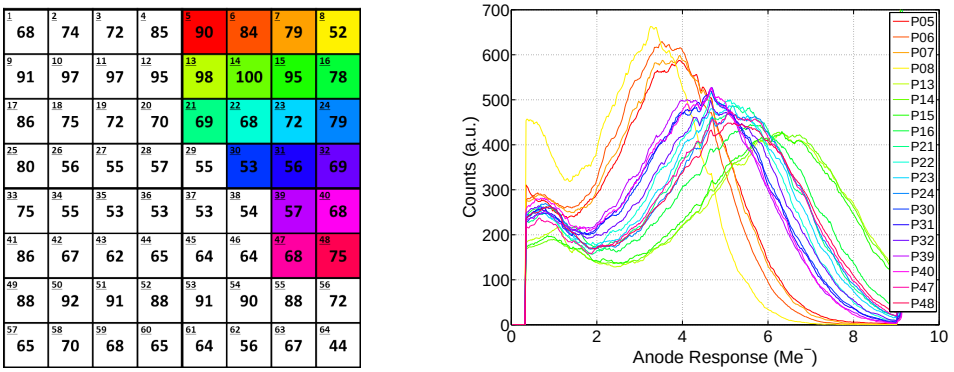

Figure 2.14: Pixel-to-pixel gain spread relative to the MaPMT SN-ZN0170. On the left, the uniformity table provided by Hamamatsu. On the right, the single photon spectra for some pixels highlighted with the corresponding colors (bias voltage equal to -950 V).

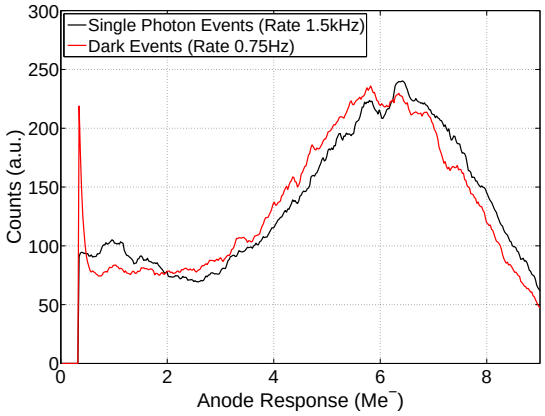

Figure 2.15: Comparison between the single photon spectra for dark and single photon events (MaPMT SN-ZN0170 biased at -950V).

2.5.4 Bias Divider

The standard bias divider proposed by Hamamatsu splits the high voltage between dynodes with a 2.3-1.2-1-...-1-1-1-0.5 ratio. This configuration allows to obtain a mean gain of about 2 Me^- at -1000 V supply voltage (Fig. 2.16) and ensures a good linearity. From the device specifications, the maximum anode output current should be mantained below 100 μA. In the region of the LHCb RICH with a high occupancy, this limit value could be easily exceeded unless operating with a gain lower than 1 Me^-. If this is obtained only by lowering the high voltage, also the collection efficiency may decrease. For this reason we have tested a different bias divider (2.8-1.5-1-...-1-1.3-3.3-0.5) that provides an overall gain lower than the standard bias divider keeping the voltage unchanged at the first

stages, as summarized in table 2.1. In this way the detection efficiency and in particular the photoelectrons collection efficiency is not affected. Note that this second bias divider has been also designed to increase the voltage at the last stage in order to maximize the electron collection just before the anode pins. Both the dividers have not been optimized independently, but they have been suggested by Hamamatsu. For all the following tests, the standard bias divider was used.

Bias Divider	Standard		Customized	
Stage	Ratio	$\|\Delta V\|$	Ratio	$\|\Delta V\|$
K - P	15	1000	18.4	1000
K - Dy1	2.3	153	2.8	152
Dy1 - Dy2	1.2	80	1.5	81
Dy2 - Dy3	1	67	1	54
Dy3 - Dy4	1	67	1	54
Dy4 ... Dy9	1	67	1	54
Dy9 - Dy10	1	67	1	54
Dy10 - Dy11	1	67	1	54
Dy11 - Dy12	1	67	1.3	71
Dy12 - G.R.	1	67	3.3	179
G.R. - P	0.5	33.5	0.5	27

Table 2.1: Table of the high voltage distribution ratio for the standard and customized bias divider (designed by Hamamatsu).

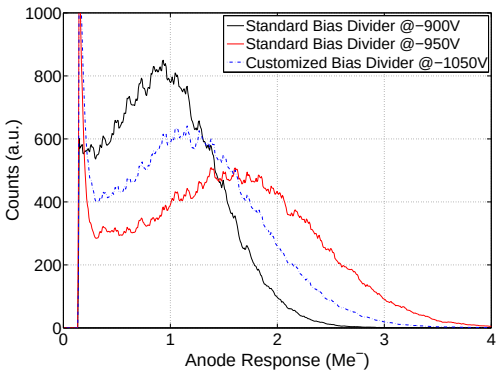

Figure 2.16: Comparison between the single photon spectra acquired using the two different voltage dividers (MaPMT SN-ZN0170).

2.5.5 Cross-talk

A small cross-talk level is required for application in the LHCb RICH, because cross-talk can bias the photon counting and the ring reconstruction. This measurement was performed covering all but one pixels of the MaPMT with a black mask and black tape. Only one pixel was illuminated with the LED and the acquisition was triggered by this channel. In order to avoid the electronic read-out contribution, the input stray capacitance was minimized connecting the MaPMT anodes to the preamplifier with independent, very short coaxial cables. In Fig. 2.17 a single photon event and the coincident cross-talk events on the neighbouring pixels are plotted. They show a small oscillation with a period of about 4 ns which is probably induced through the dynode bias.
Although the shapes of the induced signals and the main signal are very different, only their amplitudes are taken into account in order to quantify the cross-talk level. The results are summarized in Fig. 2.18, which shows the distributions of the cross-talk amplitude normalized with respect to the main signal amplitude for four tested pixels. For instance, in the top-left plot the LED illuminates the pixel 7 and the cross-talk signals on pixels 8, 15 and 16 are simultaneously recorded. As it can be observed, the cross-talk level depends on the mutual position of the pixels. Indeed, the cross-talk level rises up to $\sim 7\% - 8\%$

along the vertical direction while it amounts to $\sim 3\% - 5\%$ in the other directions.

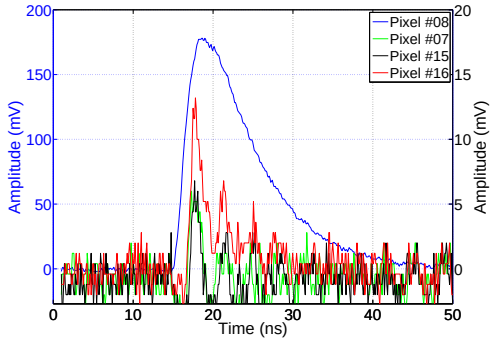

Figure 2.17: A single photon event (left y-axis) and in coincidence the neighbouring pixel events (right y-axis), magnified by a factor of 10.

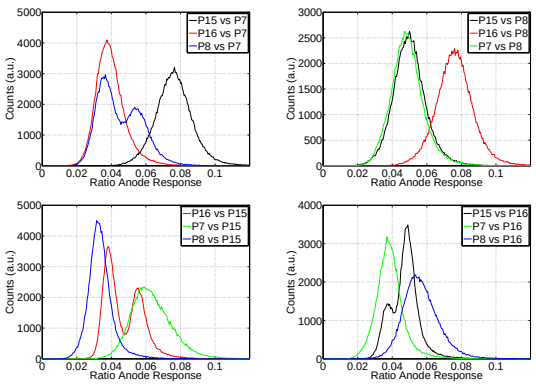

Figure 2.18: Distribution of the ratio between the amplitude of the cross-talk signals and main signal.

2.5.6 Temperature Dependance

The MaPMT response as a function of temperature has been studied. This is important for correlating the characterization in the laboratory with the final experimental environment. The setup to perform these measurements was the following: the MaPMT with its read-out electronics was put in a climatic chamber (Votsch VC 4018), working in the range $-30\,^{\circ}$C to $50\,^{\circ}$C. The behaviour of the electronic read-out chain as a function of the temperature was previously studied, in order to separate its contribution to the measurement. Cherenkov light was simulated with a commercial blue LED located outside of the climatic chamber at constant temperature. Two features of the MaPMT were studied: the single photon spectrum and the rate of dark signals.

The measurements show a decrease of the gain increasing the temperature (Fig. 2.19), which can be explained by the reduction of the mean free path of the secondary electrons inside the dynodes. This behaviour is well known and studied ([30], [31] and [32]) and it can be summarized as follows. The photoelectron energy does not change with temperature, because it is determined only by the electric field between dynodes. Thus, fixing the bias voltage, the electrons hit the dynode with similar energies and predominantly interact with it by electron-electron interactions, which have a negligible dependence on the temperature. Thus, irrespective of the temperature, the incident electrons penetrate the dynode for approximately the same length, exciting the same number of secondary electrons. These particles have a low kinetic energy so that they manly interact with phonons. This interaction has a strong temperature dependence and the mean free path of electrons inside the dynode decreases by increasing the temperature. Therefore, a smaller number of

electrons is able to escape from the dynode surface and takes part in following multiplication steps. The global result is a gain decrease. Figure 2.19 shows that the gain depends on the temperature quite linearly and the reduction slope is of about 5500 $e^-/°C$. Assuming 30 °C as reference value, a gain variation of about 0.3% per °C is expected.

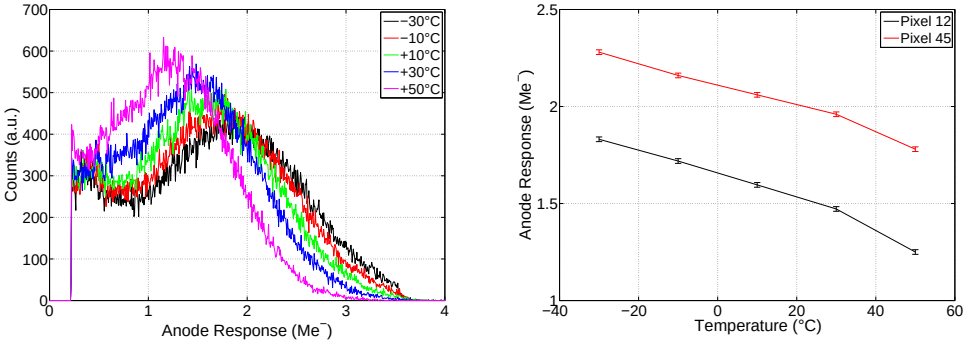

Figure 2.19: Spectrum of single photon events (left) and gain (right) as a function of temperature (Pixel 12 and Pixel 45, MaPMT SN-ZN0170 biased at -850 V).

The second feature studied is the temperature dependence of the dark current (Fig. 2.20). The rate of noise signals increases greatly with temperature (the dark signal rate at 50 °C is about 30 times larger than the one at −30 °C). The reason of this phenomenon is that, increasing the temperature, the number of electrons which have enough thermal energy to escape from the dynodes or the photocathode surface and generate a multiplication process increases. In first approximation, at room temperature the dark event rate increases quite linearly with the temperature, as it can be seen in Fig. 2.20 (right).

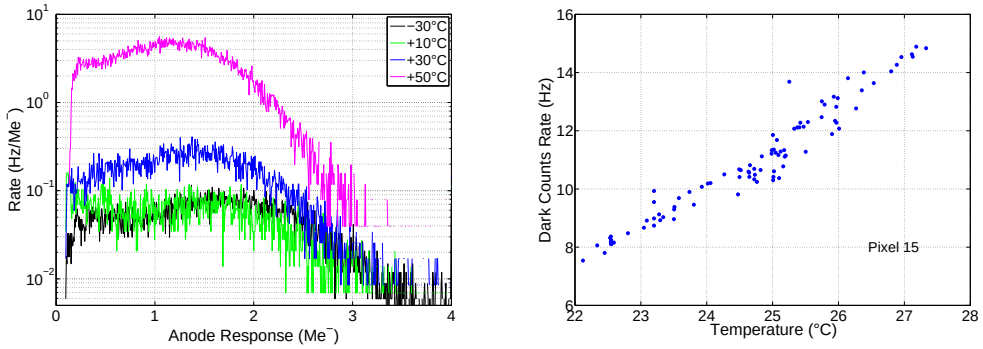

Figure 2.20: Spectrum (left) and rate (right) of dark signals as a function of temperature (Pixel 12 and Pixel 15, MaPMT SN-ZN0170 biased at -850 V).

2.5.7 Quantum efficiency

The photocathode quantum efficiency (QE) is defined as the probability to trigger a photoelectron emission when a single photon hits the photocathode. This is a very important parameter to be maximized in photon counting application and when the MaPMT operates in single photon regime. The QE mainly depends on the material that the photocathode consists of, its thickness and the wavelength of the incoming radiation. In the studies following described, the QE estimation is affected by the entrance window transmittance, defined as the ratio between the intensity of of the light passed through the window with respect to the incident light intensity.

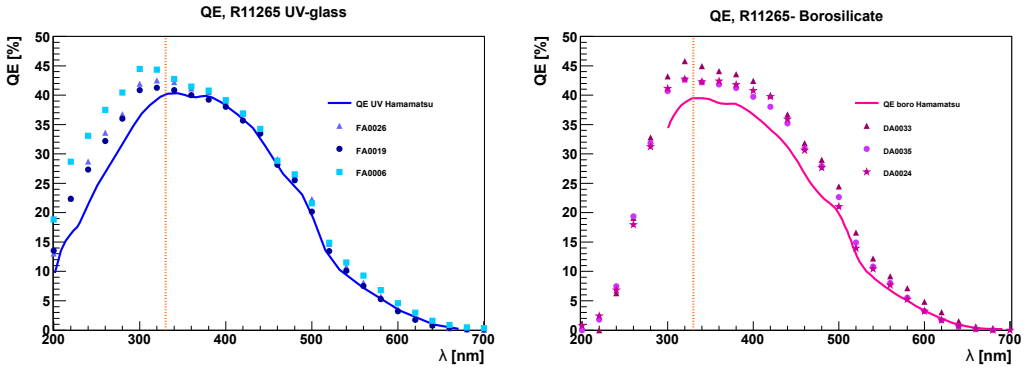

Figure 2.21: Quantum efficiency of the superbialkali photocathode of the R11265 as a function of the radiation wavelength for entrance window made of UV (on the left) and borosilicate (on the right) glasses.

A dedicated setup for the measurement of the MaPMT QE has been set up at CERN. The stable reference light of a sodium lamp is guided into a light-tight box hosting a monochromator which allows to select, from remotely, the desired wavelength in a wide range (from 200 nm up to 800 nm) with a precision of 2 nm. The resulting monochromatized light beam passes through an output slit and finally reaches the chamber where the photosensor is located. The slit size can be adjusted to regulate the light intensity. The MaPMT under test is placed on an aluminum support mounted on a trail, so that the photosensor can be moved out off the light beam. Except for the photocathode, all the dynodes of the MaPMT under test are shorted to ground. The photocathode is biased at $\sim -200 \div -150$ V and the photocathode current is measured using a Keithley 6-digit multimeter, sensitive to few tens of pA currents. The cathode biasing voltage has been gradually increased in order to be sure to collect all the photoelectrons emitted from the photocathode towards the first dynodes. Since the MaPMT is optimized to operate in single photon regime, it cannot sustain large photocathode currents. In particular, the resistivity of the photocathode prevent us to operate at currents larger than 10 nA. A calibrated photodiode can be moved along the trail in front of the monochromatic beam to measure

the light intensity. In order to obtain reliable results and maximize the signal-to-noise ratio, the reference photodiode must be exposed to an illumination much larger the maximum level sustainable by the MaPMT. Calibrated light filters, from Kodak, are thus used to attenuate the light source intensity by a factor of $5 \cdot 10^3$ when the MaPMT is exposed to the light beam. Since the photocathode emits a single photoelectron per converted photon, the QE of the tube can be obtained as:

$$QE = \frac{I}{eR} = \frac{I}{e}\frac{E_\gamma}{\varepsilon P_\gamma} \tag{2.9}$$

where I is the photocathode current read by the multimeter (once subtracted the dark current contribution), e is the electron charge and $R = E_\gamma/\varepsilon P_\gamma$ is the photon hit rate. Note that the incident light power P_γ is measured by the calibrated photodiode, the filter attenuation factor ε is known and the single photon energy $E_\gamma = hc/\lambda$ is fixed by the selected radiation wavelength λ. As mentioned, this measure gives the QE only if an ideal entrance widow is assumed (transmittance 100%). However, the entrance window can be much lower than 1, since borosilicate glass is opaque when operating in the UV region. Figure 2.21 shows the obtained results superimposed to the reference value provided by Hamamatsu, using several R11265 MaPMT equipped with a superbialkali photocathode. The plots show the outcomes for devices with the standard borosilicate glass entrance window (on the left) or the UV-glass (on the right). As it can be observed and in agreement with the expectations, the maximum QE value of $40\% \div 45\%$ is reached around $320 \div 400$ nm, just before the UV domain. The effects of the UV-glass are evident for wavelength ranging for 200 nm to 300 nm, where the borosilicate glass transmittance steeply decreases to zero. The higher QE in the UV region is not the reason why the LHCb RICH Upgrade group opted to use the UV glass entrance window. Indeed, the refractive index of the gas radiator of both the RICH detectors increase quite abruptly in the UV domain. So, even detected a larger number of photons, the spatial resolution is spoiled because of the larger chromatic dispersion of the refractive index. In order to avoid such issue, a proper coating layer covers the RICH upgrade mirrors preventing the UV photons to be reflected towards the photosensitive plane. Nevertheless, UV-glass is still the preferred choice as it ensures better performance in term of radiation tolerance.

2.5.8 Behaviour in critical environment condition

The performance of the R11265 tube was investigated also in case it has to operate in critical environment conditions, such as under the action of a magnetic field or during long time operation at intense light exposure. These tests are particularly important in case the R11265 will be employed in application such as the LHCb RICH detector where a fringe magnetic field up to 30 G is expected and the photosensor is supposed to withstand the intense illumination of the most central zone for about ten years. In the

next paragraphs the investigations about the behaviour of the R11265 as a function of a longitudinal magnetic field up to 100 G are shown. In the last paragraph a quantitative estimation of the aging effects (gain loss, photocathode efficiency deterioration and dark current increase) is illustrated.

Behaviour in magnetic field

If the photomultipliers have to work in magnetic field it is important to know their behaviour and eventually be shielded with a high permeability material (such as Skudotech® or MuMetal®).

Setup

The response of photomultiplier can be sensitive to a magnetic field because it might induce some electrons to change their trajectory from one dynode to the following one. As far as a transversal magnetic field (perpendicular to the tube axis) is concerned, the metallic layer covering the MaPMT lateral surface behaves by itself as a shield, thus the effects are usually negligible up to 100 G and more. The main effects are induced by a longitudinal magnetic field (parallel to the tube axis), as already demonstrated in [28]. The studies were made with a R11265 MaPMT placed in a longitudinal magnetic field produced by a solenoid (Fig. 2.22). An automatic system, made of custom MATLAB® scripts, changed the current flowing in the solenoid in order to obtain fields ranging from 25 G to 100 G. The field magnitude was measured with a Hirst GM04 gaussmeter.
A commercial blue LED, which was biased with a very low voltage so that it operated in single photon region, illuminated the 32 tested pixels. The MaPMT was biased at -1050 V at an average gain of about 2.5 Me^-/photon. The MaPMT signal was amplified using a classic charge sensitive preamplifier circuit and finally acquired by a DT5720 CAEN Desktop Digitizer[3] fixing a threshold of $\sim$60 ke$^-$. Although all the measurements were performed at room temperature, with a maximum range of 1°C, small fluctuations are expected between different acquisitions. For this reason in order to check the system stability, three zero field observations were performed at the beginning, in the middle, and at the end of the run.

Measurements without the magnetic shield

The spectra acquired for 4 pixels are shown in Fig. 2.23. The central pixels turn out to be quite insensitive to a weak magnetic field, while significant single photon spectra deformation is observed for the peripheral pixels.

[3]The DT5720 is a 4 channel 12 bit 250 MS/s Desktop Waveform Digitizer with 2 Vpp single ended input. The DC offset is adjustable via a 16 bit DAC on each channel in the ± 1V range.

Figure 2.22: A picture of the setup used for the tests of the R11265 MaPMT in magnetic field.

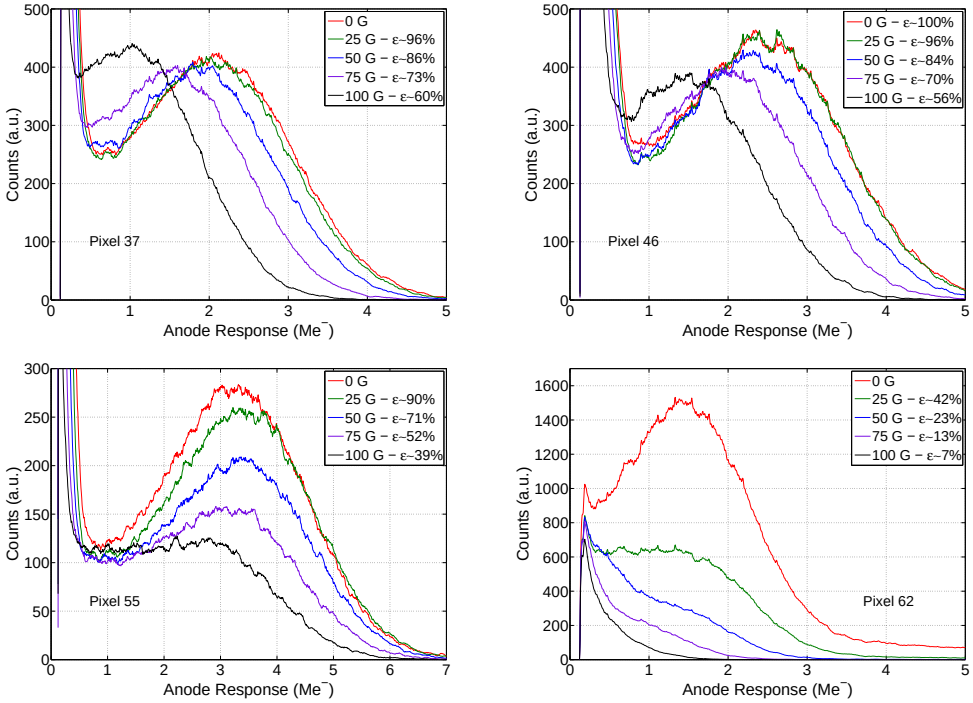

Figure 2.23: Each graph shows the superposition of single photon spectra acquired under the action of different longitudinal magnetic fields values. The two upper plots refer to pixels located in the central part of the MaPMT while the two lower plots correspond to pixels in the peripheral region (MaPMT SN-ZN0702 biased at -1050V.)

If we define the efficiency ϵ as the rate of events whose amplitude is larger than the noise level (fixed at 0.2 Me^-), then for the most external pixel (pixel 62 in Fig. 2.23) the efficiency at 25 Gauss is less than half with respect to the one measured without

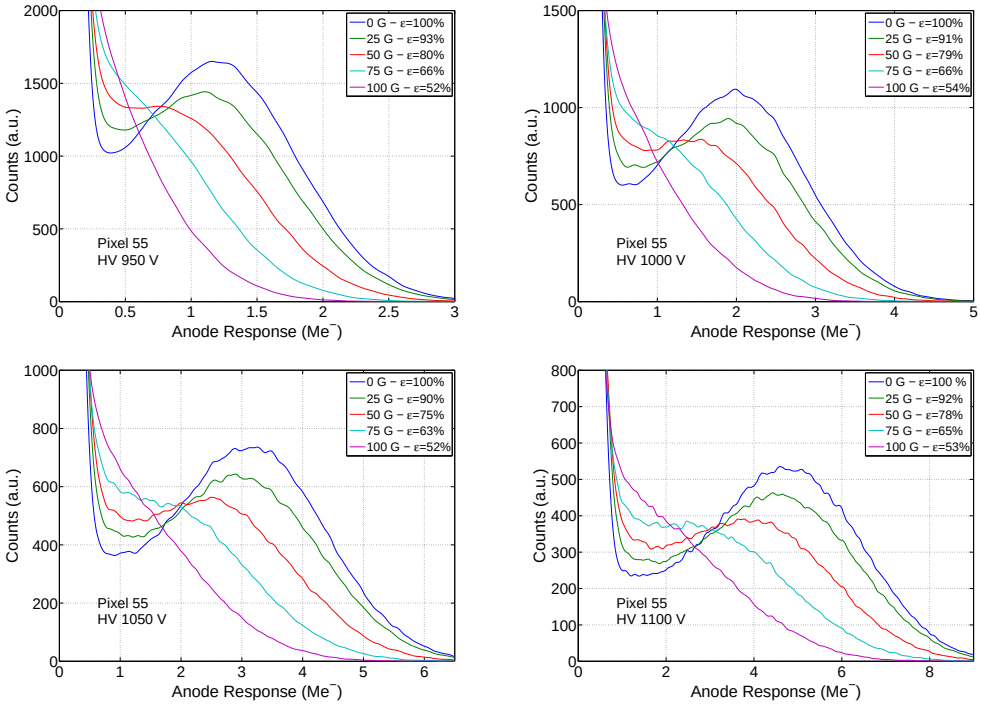

Figure 2.24: Each graph shows the superposition of single photon spectra acquired under the action of different longitudinal magnetic fields values. All the plots refer to the pixel 55 located near the side of the device. The data were acquired biasing the MaPMT (FA0019) at a bias voltage that ranges from -950 V to -1100 V moving from the top-left picture to the bottom-right one.

magnetic field. Considering a more intense field, large distortion can also be observed for central pixels, while for the peripheral ones the single photon peak almost merges with the pedestal. The results suggest that these devices need to be shielded to work properly in a magnetic field.

Note that this effect was found to be almost independent on the bias voltage and on the average gain of the MaPMT. As it can be observed in Fig. 2.24, no significant variation of the photon detection efficiency is visible increasing the bias voltage from -950 V to -1100 V.

Tests and optimization of shielding configuration

In light of the results shown in the previous paragraph 2.5.8, a magnetic shielding is necessary to preserve a good response at the peripheral pixels. The main parameters which have to be considered to obtain an effective shielding are its material, the geometrical shape, the thickness and the length of its protrusion from the photocathode surface. In order to absorb a static magnetic field, high permeability materials are needed.

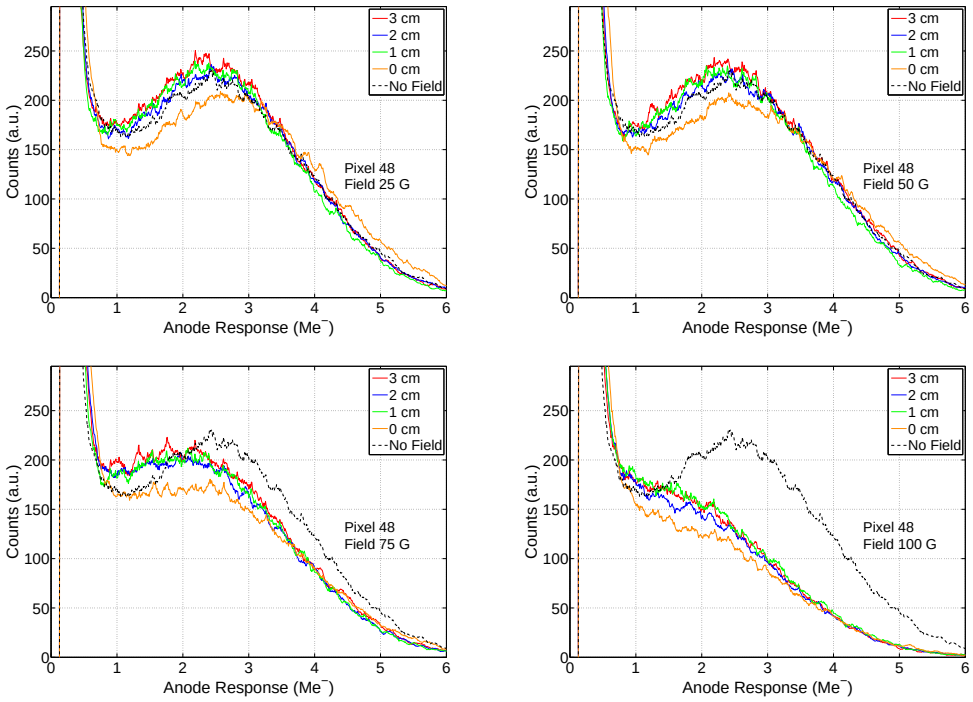

Figure 2.25: Each graph shows the superposition of single photon spectra acquired with the MaPMT R11265 (ZN0702) under the action of a longitudinal magnetic field using shields which differ in the protrusion length. All the plots refer to the pixel 48, located on the side of the device. The magnetic field ranges from 25 G to 100 G and increases moving from the top-left to the bottom-right graph.

For all the measurements described in this section, the shields were made of 200 μm thick Skudotech® (produced by SELITE), material with a nominal maximum permeability[4] of $3.27 \cdot 10^5$. This material was chosen also for its flexibility, so different shapes can be easily obtained and the thickness of the shield can be increased by wrapping multiple Skudotech® layers around the tube. Other high permeability materials, like the MuMetal® (maximum magnetic permeability value[5] $\sim 2 \cdot 10^5$), can be appropriate shields. By the way, the MuMetal® is used around the HPD detectors currently employed in the LHCb RICH. In all the measurements, the Skudotech® sheet was wrapped around the lateral surface of the MaPMT and protruded, by different lengths, from the photocathode window.
The wrapping did not cover the tube pins at the back. The thickness and the protrusion lengths are the parameters to be optimized. In principle the more the shield protrudes, the more it is effective. The drawback is that the protrusion limits the angular acceptance of the photons to be detected. Figures 2.25 and 2.26 show the effects of shields with different protrusion lengths. Note that all these shields were made by a single wrap of 200 μm thick

[4]Further informations: http://www.bmtel.it/Skudotech.pdf
[5]Further informations: http://www.mushield.com/material-specs.shtml

Skudotech®, so they differ only in their length.

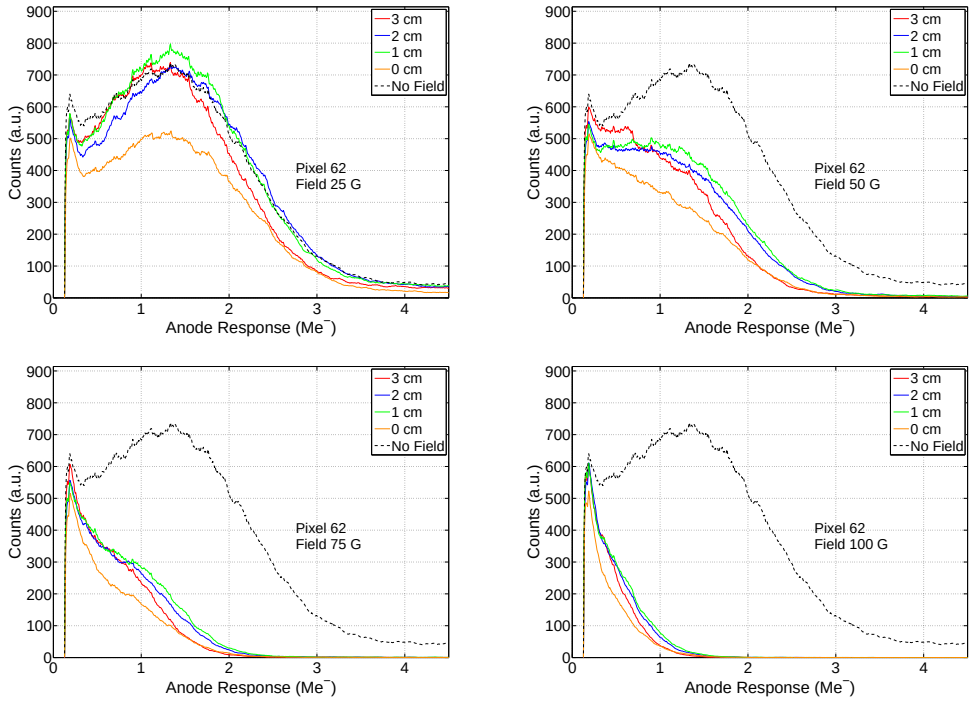

Figure 2.26: Each graph shows the superposition of single photon spectra acquired with the MaPMT R11265 (ZN0702) under the action of a longitudinal magnetic field using shields which differ in the protrusion length. All the plots refer to the pixel 62, located on the side of the device and next to the bias voltage pins. The magnetic field ranges from 25 G to 100 G and increases moving from the top-left to the bottom-right graph.

Figure 2.25 shows the single photon spectra acquired on the pixel 48 (located on the side of the MaPMT) as a function of the longitudinal magnetic field, from 25 G to 100 G. The shield which does not protrude from the surface (0 cm) is not able to properly absorb the magnetic field and its effectiveness is inadequate even at 25 G. All the other shields are more effective and show similar performance. In particular, the spectra distortions are critical only in case of magnetic field larger than 50 G. Figure 2.26 shows the same results for the pixel 62, located just next to the bias voltage pins. In this case, the magnetic field can even turn the pixel efficiency to zero, since the single photon peak is not resolved from the pedestal above 50 G. Although both these pixels, 48 and 62, are located on the side of the device, their performance is quite different. In order to recover the signal in each pixel, properly shielding all of them, the worst cases must be taken into account. For the central pixels, the effects of the magnetic field are much less dramatic.

Another important conclusion from Fig. 2.25 and 2.26 is that, irrespective of the protrusion

length, the shield efficiency decreases in case of field larger than 50 G. This is a typical behaviour of the ferromagnetic material whose relative permeability, as a function of the magnetic field, initially increases, then reaches a maximum value and finally decreases. Indeed, over a critical value, field generated within the magnetic shield causes the relative permeability to asymptotically approach unity. This behaviour is known as saturation effect and it causes the loss of the shield efficiency at stronger field. The critical value over which the shield saturates depend on the material of the shield itself (generally, the higher is the permeability, the weaker is the saturation field), its shape and thickness. Hence, in order to obtain good shielding performance at 50 G, we tested thicker shields made of multiple Skudotech® wraps. Figure 2.27 shows the results obtained for pixel 61 (an extremely sensitive pixel which represents one of the worst case observed) using single, double and triple Skudotech® wraps, corresponding to 200 μm, 400 μm, 600 μm thickness. In all these cases, the protrusion length was fixed at 1 cm.
One single Skudotech® wrap properly absorbs a magnetic field up to 25 G and the saturation effect is not reached. Under the action of 25 G, neither significant spectra distortion nor photon detection efficiency loss are visible. At 50 G the single wrap shield is saturated and its efficiency degraded. The double wraps shield works satisfactorily: the efficiency increases to about 95 % and the spectra distortions become negligible. At stronger field (up to 75 G) also the double wraps shield becomes inadequate and three wraps seem to be necessary.

To summarize: the effects of a magnetic field on the performance of a R11265 MaPMT was thoroughly investigated. We studied a longitudinal magnetic field up to 100 G. The performance deterioration seems not to be correlated with the bias voltage and the pixel gain. While central pixels proved to be almost unaffected, the peripheral pixels turned out to be very sensitive to a longitudinal magnetic field. Thus, 200 μm Skudotech® shields were tested which wrapped the lateral surface of the device protruding from the photocathode. About 1 cm of protrusion and 2 wraps proved to be adeguate to be sure that even the worst pixels works properly up to 50 G.

Magnetic shield for the EC

The goal of these measurements is to test the R11265 performance under the action of a longitudinal magnetic field using a single shield wrapping the whole Elementary Cell instead of each device of the matrix (Fig. 2.28). Besides the practical advantages, a single shield would ensure a lower shading of the MaPMTs and a larger photon angular acceptance as well. Figure 2.29 shows the custom 2×2 socket developed by the Ge-INFN group for the R11265 MaPMTs. The devices are oriented in order to satisfy a radial symmetry with respect to the center of the socket, so that pixel 1 is near the center of the EC for each MaPMT, as well as pixel 64 is always located at the corner

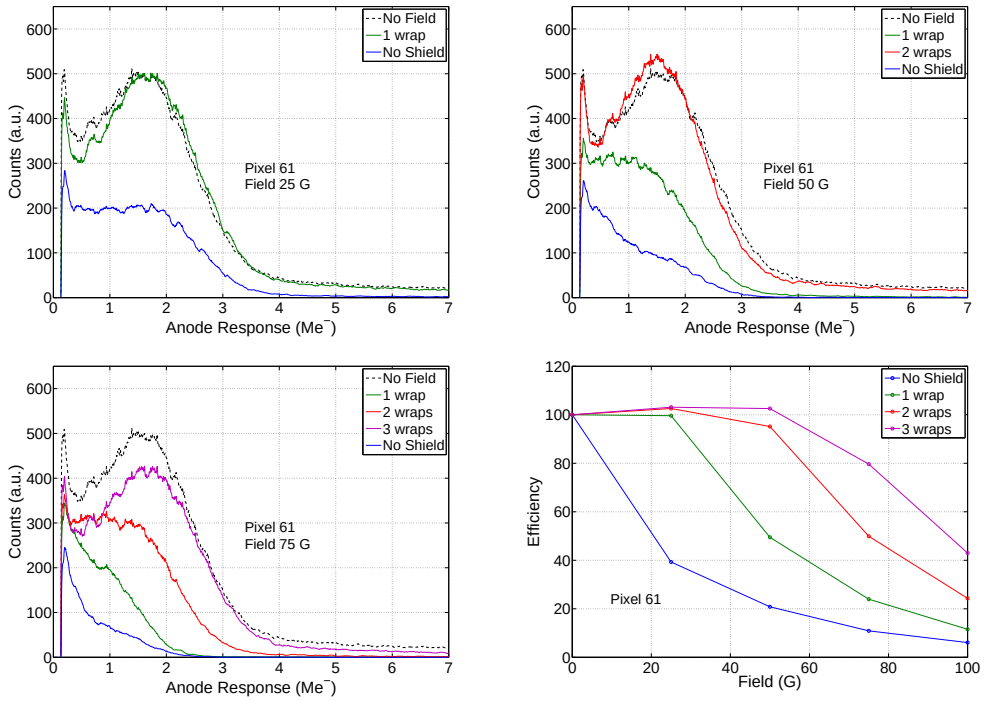

Figure 2.27: In the first three pictures, the single photon spectra acquired with the MaPMT R11265 (ZN0702) are shown. They are obtained using shields with different thickness. The longitudinal magnetic field ranges from 25 to 75 Gauss. The bottom-right plot shows the photon detection efficiency, defined as the relative rate of events whose amplitude is larger than the noise level ($2 \cdot 10^5$ e^-), as a function of the magnetic field.

of the matrix (Fig. 2.29). Thanks to the radial symmetry, each R11265 MaPMT is perturbed by a longitudinal magnetic field independently on its position inside the matrix. For instance, pixel 64 is always in the corner of the cell and just near to the shield, so that both the longitudinal magnetic field and the shield will act in the same way on all these pixels of the cell for each tube. Thus, we can restrict to study only one R11265 MaPMT of the matrix and extend the results to the other MaPMTs of the Elementary Cell.

The setup is the same used for the single device characterization and previously described. The whole MaPMT matrix was wrapped by a single Skudotech® layer protruding ~ 1 cm from the photocathode surface (Fig. 2.28). Following the expected mechanical constraints, the anode pins were not shielded.

Figure 2.30 shows the single photon spectra obtained for four pixels at various magnetic field values. Most of the pixels behave similarly to pixel 48 (top-right plot): the distortions are negligible and no loss of efficiency is observed in these pixels even at 25 G. In agreement with what obtained from the characterization of a single device, the most sensitive pixels

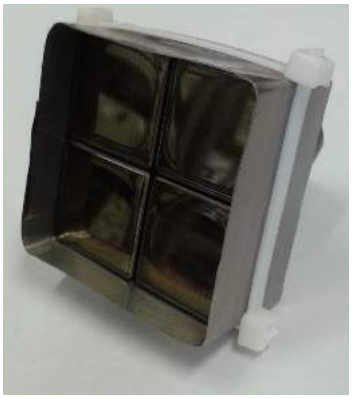

Figure 2.28: The matrix studied in Milano Bicocca Labs. The orientation of the four R11265 MaPMTs was set in agreement with the custom 2 × 2 socket developed for the RICH upgrade [24]. The shield wrapping the whole matrix was made of a single Skudotech® layer which protrudes ∼ 1 cm from the photocathode surface.

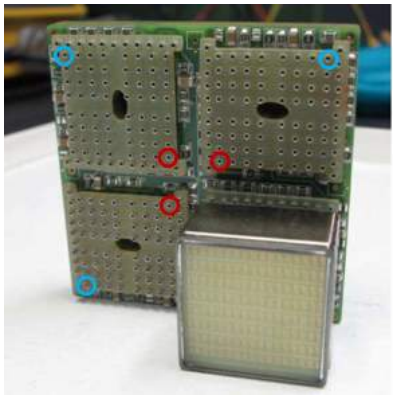

Figure 2.29: The custom 2 × 2 socket which represents the Elementary Cell (EC) for the RICH upgrade [24]. The red and blue circles indicate the pixel 1 and pixel 64 positions respectively.

turned out to be those near the biasing high voltage pins (i.e. pixels 1 to 8 and 56 to 64). The shield works satisfactorily so that the loss of efficiency at 10 G becomes almost negligible (∼ 2%), while it rises to ∼ 20% at 25 G. It was also demonstrated during the characterization of a single R11265 MaPMT that thicker shields can be used in order to achieve a more effective absorption of the external magnetic field.

Instead of wrapping each EC with the magnetic shield, a similar configuration can be obtained by using a "cross-shaped" shield. As soon as a large number of cells are mounted to built the RICH photosensitive plane, 2×2 device matrix will be wrapped by a high magnetic permeability material. This alternative shielding configuration, shown in Fig. 2.31 right side, ensures the same performance as that wrapping the full cell (in Fig. 2.31 left side). Since this second shielding option tuned out to be easier to assemble, it represents the current choice for the final detector setup.

2.5.9 Aging Test

It is well-known that long periods of light exposure may deteriorate the MaPMT nominal performance on three different aspects. First, the DC-gain of the tube could decrease due to the wear of the multiplication dynodes. Second, the photocathode efficiency may decrease, and an increasing number of incident photons may not produce any photoelectron,

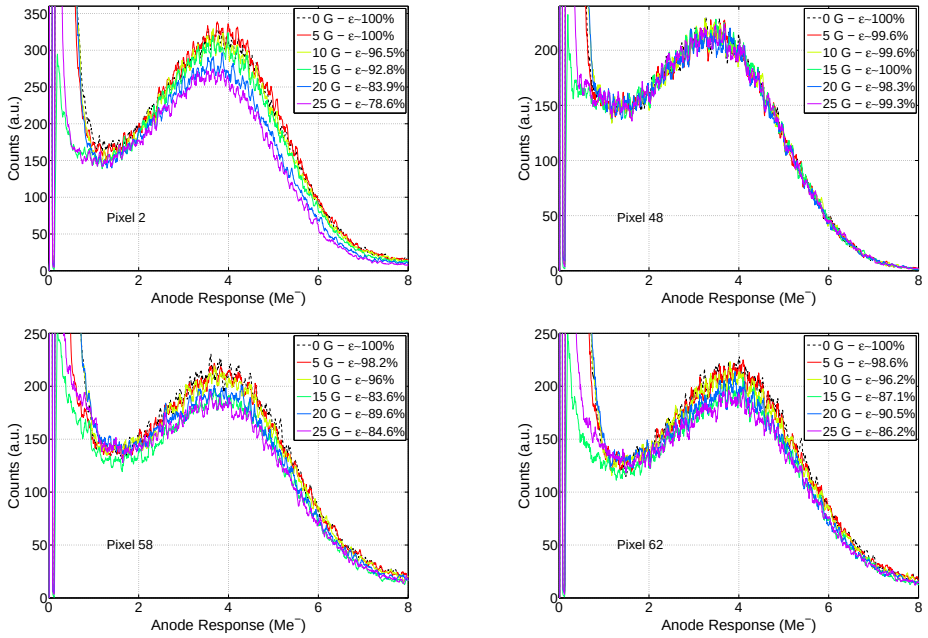

Figure 2.30: Each graph shows the superposition of single photon spectra acquired under the action of a longitudinal magnetic field. The plots show the results for four pixels of one of the tubes of the matrix cell. The shield wrapping the whole matrix was made of a single Skudotech® layer which protrude 1 cm from the photocathode surface. Pixels 2, 58 and 62, located just on the side of the biasing high voltage pins, represent the worst case conditions.

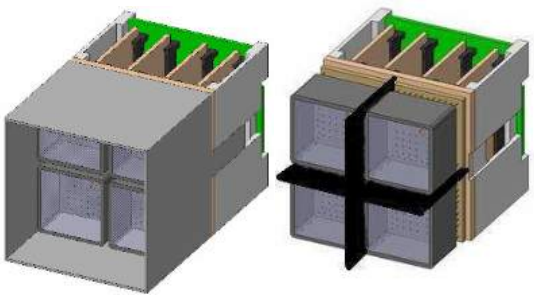

Figure 2.31: Two options evaluated to shield the R11265 MaPMT of RICH 1 detector.

remaining therefore undetected. Finally, the dark current might increase, due to incident radiation which causes the photocathode and dynodes deterioration. The aim of the tests described in the following section is to quantitatively estimate the aging effects of the R11265 MaPMT. We have fixed the measurement time to 3000 hours[6].

[6]This is equivalent to two years of LHCb RICH operation considering that the average effective LHCb operation time over 2011 and 2012 amounted to about 1500 hours per year. (https://lhc-statistics.web.cern.ch/LHC-Statistics)

Setup

In order to observe the aging effects, a long time exposure has to be performed. This requires a setup as automatic as possible able to manage the MaPMT measurements, to check the system stability and to acquire single photon signals. Such system was arranged by developing custom scripts in MATLAB®. Eleven pixels of a R11265 MaPMT were tested so far and they were illuminated using a commercial blue LED. A PbF_2 crystal covered with a black tape was placed in front of the photo sensors, as shown in Fig. 2.32. A window in correspondence to the read-out pixels was opened on the tape to let the LED light to pass. No optic fiber was used for coupling the LED to the MaPMT so that the pixels were aged with different light exposures (from few tens of nA to about 5 μA).
The system supervised the measurement acquiring the DC aging current values for all pixels every five minutes by recording the voltage dropped across a 1 $M\Omega$ resistor with a Keithley 2700 Multimeter (Fig. 2.32). The LED was biased using a Agilent E3631A which was adjusted to keep the aging current stable in one pixel (channel 4) used as the reference. Furthermore, temperature and humidity near the MaPMT were continuously monitored and the temperature was kept stable at 24 degrees using some power resistors located on the black box surface. This configuration prevented any MaPMT gain variation due to temperature fluctuation. Finally, the MaPMT bias voltage was periodically measured and fixed at a suitable value which guarantees an adequate gain of about $2 \cdot 10^6$ electrons per photon.
Figure 2.33 shows the pixels position and a table giving the measured relative average DC aging current, I_{DC}, and the expected occupancy percentage ϑ. These values are related by the following equation:

$$\vartheta = \frac{I_{DC}}{R_p \cdot G \cdot e} \tag{2.10}$$

where R_p is the proton-proton collision rate, G is the pixel gain and e is the electron charge.
Considering that the LHC is expected to produce 40 million proton-proton collisions per second ($R_p \simeq 40$ MHz) and the gain and the DC aging current were measured for every pixel, the occupancy levels ϑ can be easily calculated. The measured currents correspond to an occupancy level of the pixels ranging from 0.1% to about 38%, while the maximum expected in the LHCb RICH is 25%.

Aging measurements

Every four hours, the system stops the slow control, decreases the LED bias voltage and starts the waveform acquisition. Each observed pixel was connected to a standard charge sensitive preamplifier circuit and the shaped signals, over a fixed threshold of 0.2 Me^-, were acquired by three 4-channel ADCs CAEN Desktop Digitizer DT5720. For each trigger a 1 μs waveform was acquired and saved. The off-line analysis calculated the events rate

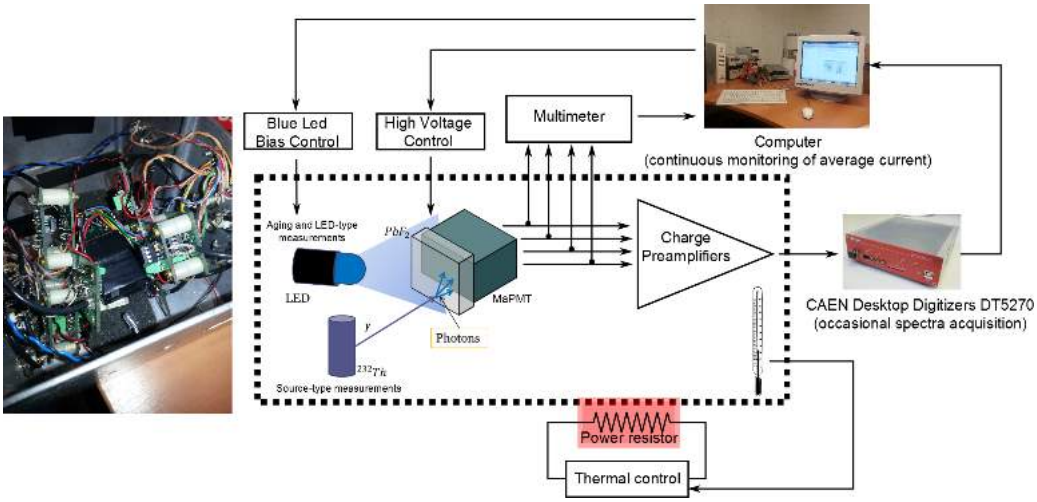

Figure 2.32: Schematic picture of the fully automatic system developed for the aging test. The MaPMT is covered by a black tape and only a small window leaves the LED light pass. A PbF_2 crystal is located in front of the MaPMT and allows to acquire source-type measurements. For each channel, the single photon signal is read out using a charge sensitive preamplifier circuit and acquired by a CAEN Desktop Digitizer. The slow control unit records the DC current and supervises the test ensuring the stability of the high voltage, of the LED supply and of the temperature.

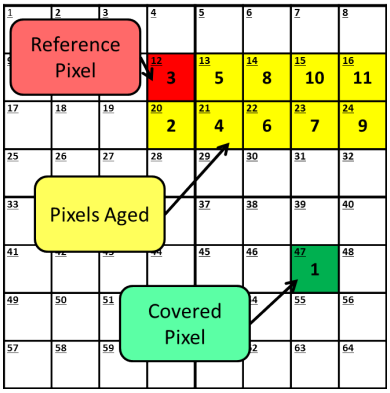

	MaPMT SN-0707		
CH	$I_{DC}(\mu A)$	$G(\cdot 10^6)$	$\vartheta(\%)$
1	0.02	1.54	0.19
2	0.05	1.29	0.65
3	0.18	2.08	1.35
4	0.18	1.40	2.03
5	0.57	2.09	4.28
6	0.57	1.26	7.05
7	0.95	1.36	10.9
8	1.91	2.06	14.5
9	1.63	1.33	19.1
10	2.93	2.00	22.9
11	4.91	2.02	38.0

Figure 2.33: Left: Schematic front view of the MaPMT. Right: Table of the studied pixels with the relative DC aging current, gain and occupancy level.

and the signal amplitude as the difference between its maximum and the baseline. Three different single photon measurements were performed.

1. In the LED-type measurement, the LED was biased for about five minutes at a very low voltage so that it operated in a single photon regime compatible with the acquisition rate and the signal to noise ratio. This data allowed to obtain for every pixel the single photon spectrum and to estimate the gain loss from the peak position

variation.

2. The Noise-type measurement was performed turning off the LED for half an hour and acquiring dark signals.

3. Once per month, a Source-type measurement was performed to qualitatively observe the aging effects on the photocathode efficiency. In this case the LED was turned off for about two hours and a ^{232}Th γ-source was used to produce Cherenkov photons in the PbF_2 crystal placed in front of the MaPMT, acting as a Cherenkov medium. Hence, in the Source-type measurement, the photon production rate is constant, depending only on the source activity. If the photocathode looses efficiency due to aging, i.e. some photons do not produce any photoelectron, then a signal rate reduction would be observed.

System stability performance

Before starting the aging measurements, the stability of the single photon acquisition chain was checked for three days. Several LED-type measurements (one run every two hours) were performed keeping on the device but without aging it. As expected, all the spectra from each channel were perfectly superimposed (an example is shown in Fig. 2.34). Also few Noise-type measurements were acquired to define precisely the MaPMT starting conditions before its aging. The stability of the aging process conditions was also continuously monitored. Figure 2.35 shows the MaPMT bias voltage. As it can be observed, the maximum variation observed was 50 mV at -1000 V (0.005%). The temperature control worked efficiently and ensured a maximum variation of about 0.05 °C. Finally, the DC current of the reference pixel (channel 4) versus time is plotted in Fig. 2.35 (right): it was kept stable at 0.180 μA with a maximum variation of about 5 nA ($\sim$3%) adjusting the LED bias voltage.

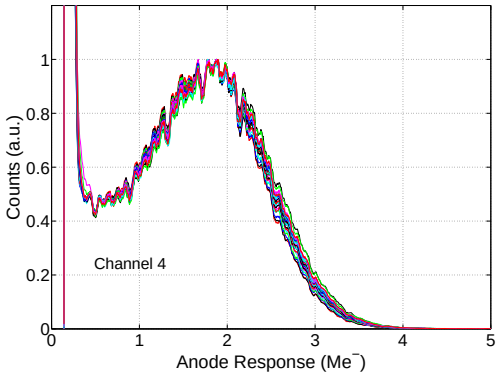

Figure 2.34: Pre-aging spectra, good superposition.

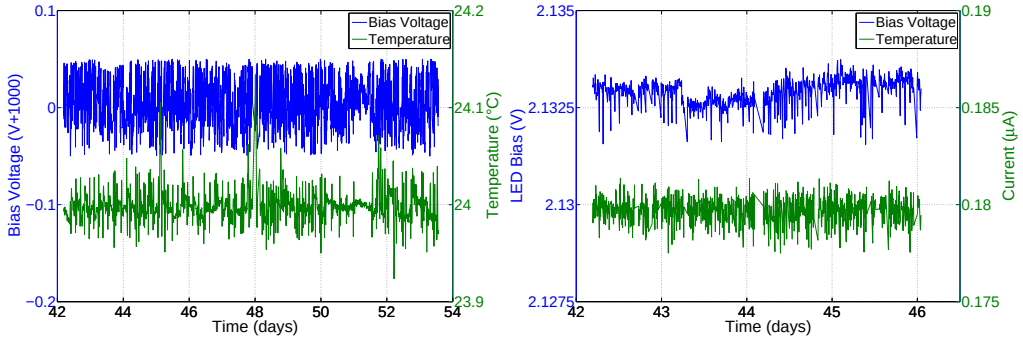

Figure 2.35: The system stability versus time. Left: high voltage and temperature. Right: LED bias voltage and DC current in the reference channel 4.

Results

Figure 2.36 shows the results concerning the gain variation due to the aging for most of the observed pixels. Note that the live-time takes into account only the effective period of LED illumination. More than 600 acquisitions were performed over more than 3000 hours. For each acquisition, the gain of each pixel was obtained from the acquired spectra by measuring the energy of the single photon peak. A whole day of illumination turned out to be necessary for stabilizing the MaPMT response, so the percentage gain variation is evaluated considering the gain value at 24 hours as the starting point condition.

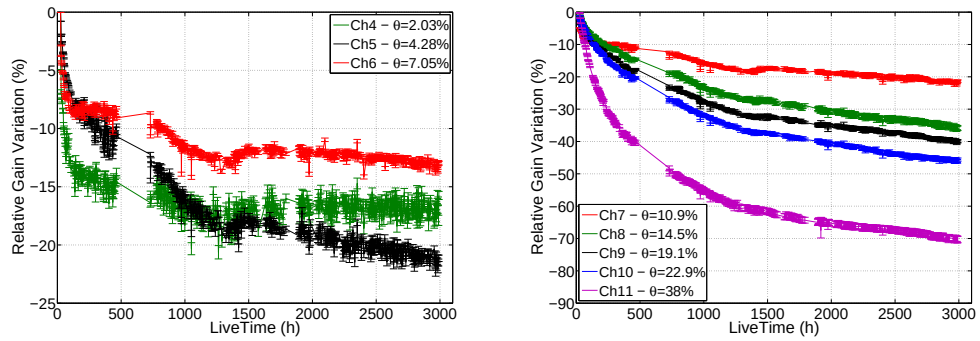

Figure 2.36: Gain variation (in %) versus live-time for some of the tested pixels (SN-ZN0707). Left: The pixels with an occupancy lower than 10%. Right: The pixels with an occupancy higher than 10%

The gain loss seems to strongly depend on the DC aging current, or equivalent, on the occupancy level ϑ. In particular, the pixels with a DC current lower than 1 μA ($\vartheta \lesssim 10\%$) have a similar behaviour shown in Fig. 2.36 (left). An initial sharp linear decrease can be observed, followed by a plateau reached after about 1200 hours of LED illumination. The gain loss for these pixels can be assessed at about 12-22%. On the other hand, the

gain loss of the most illuminated pixel (channel 11) falls down to about 60% after only 1200 hours (see Fig. 2.36 right). Roughly, this decrease can be observed also for the other channels with a DC current larger than 1 μA ($\vartheta > 10\%$). After about 1200 hours, the gain variation reduces, then remaining more stable.

Although the gain loss is higher than expected, even the most illuminated pixel ensures a single photon gain larger than 0.7 Me^- after the aging and the single photon peak is still clearly resolved from the pedestal (Fig. 2.38). The standard method to compensate the aging effect is to increase the bias voltage. As Fig. 2.37 shows, increasing the high voltage by only 25 V (from -1000 V to -1025 V at 1917 hours) a gain loss of 10-15% was compensated for almost all the channels.

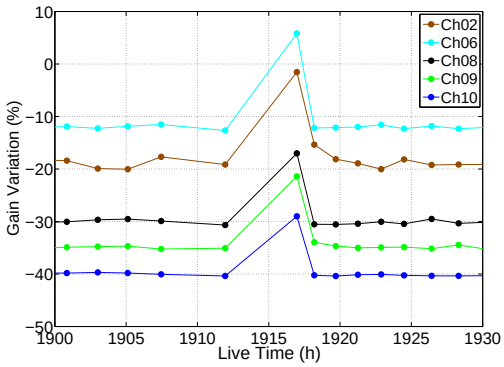

Figure 2.37: The gain loss decreases by about 10-15% increasing the bias voltage, from -1000V to -1025V at 1917 hours (SN-ZN0707).

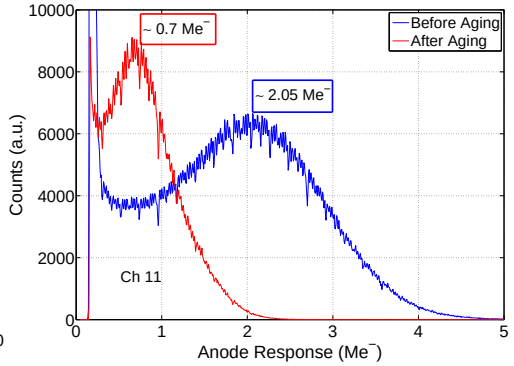

Figure 2.38: Single photon spectra acquired in the most illuminated pixel (channel 11) before and after the aging.

Since the gain loss has been much larger than the expectations, two more recently produced R11265 MaPMT (belonging to the FA series, serial code FA0025 and FA0026) were tested keeping almost unchanged the abovementioned setup conditions. All the 12 pixels under test were illuminated with a similar light exposure (11.2 % $\leq \theta \leq$ 21.9 %) which corresponds to the maximum integrated current sustainable by the tube (100 μA). The gain variation as a function of the LED illumination time can be observed in Fig. 2.39 (FA0025) and Fig. 2.40 (FA0026, tested for $\sim$ 1300 hours). As expected, all the channels show a similar behaviour. As soon as the FA0025 MaPMT is illuminated (Fig. 2.39), an initial sharp gain loss by several percentage points can be observed (within $\sim$ 150 hours of LED illumination). After that, the gain starts to increase almost linearly and with a similar slope for all the observed channels ($\sim$ 50 ppm/h). Although in the last section of the tests some setup failures occurred, the trends seems to be maintained until $\sim$ 3000 hours. A very similar behaviour can be also observed in Fig. 2.40, referred to the FA0026 MaPMT. After the first several hours, a linear gain recovery is noticeable for all the tested pixels

and this trend is compatible with the one previously described for the FA0025 MaPMT. It can be noticed that some pixels show a final gain larger than the starting value, while others have not recovered the initial performance completely. Anyway, the average gain variation over the observed pixels turns out to be negligible (lower than 1%).

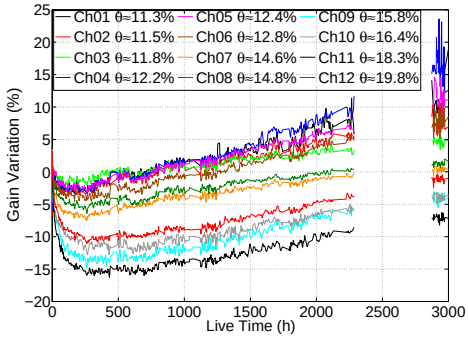

Figure 2.39: Gain variation (in %) versus the illumination period for the third tested MaPMT (FA0025).

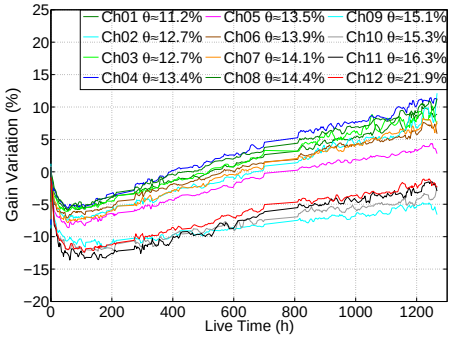

Figure 2.40: Gain variation (in %) versus the illumination period for the fourth tested MaPMT (FA0026).

Summarizing, the first tests showed a gain loss higher than the expectation. However, even the most illuminated pixel ensured a single photon gain larger than 0.7 Me^-/photon after the aging and the single photon peak could be still clearly resolved from the pedestal. The standard method to compensate such an aging effect is to increase the bias voltage. It turned out that increasing the high voltage by only 25 V (from -1000 V to -1025 V at 1917 hours) a gain loss of 10-15% could be compensated for almost all the channels. On the other hand, the last measurements suggested that the latest generations of the R11265 (the FA series) better sustains long period of light exposure, even when operating at the maximum integrated current. It was observed a gain increase during the device aging. According to the manufacturer, this is not an unusual effect and it can be ascribed to the spread of the thickness of the Cesium layer grown on the dynode surfaces between different devices.[7]. MaPMTs belonging to the same production batch are expected to have similar aging performances.

Figure 2.41 shows the results of the Noise-type measurements. The initial software threshold over which the events are integrated is fixed as the half of the single photon peak energy, but then it is adjusted taking into account the gain loss obtained by the LED-type measurements. The dark signal rate exhibited a quite similar behavior for all the observed pixels. In particular, the dark signal rate seems not to significantly depend on the aging. In the Source-type measurements, the rate of the Cherenkov photon produced in the PbF_2 is measured. Similarly to the Noise-type measurements, the trigger threshold is

[7] Confidential information provided by the manufacturer

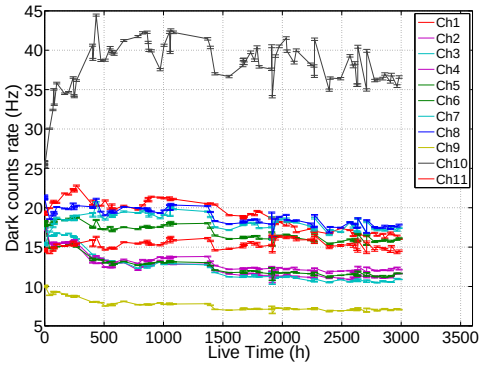

Figure 2.41: The dark signal events rate for all pixels as a function of live-time.

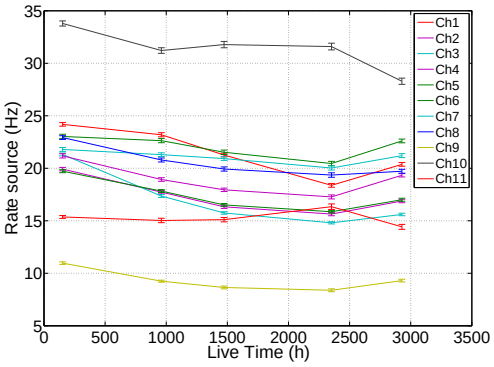

Figure 2.42: Source event rate as a function of the aging live-time.

adjusted according to the gain loss. The dark signal contribution is then subtracted in order to estimate the source events rate. Since this setup condition ensures a constant photon production rate of about 20 Hz, if a deterioration of the photocathode efficiency happens, then the observed rate should decrease. Such a measurement does not mean to be a precise study of the photocathode response, but only a qualitatively observed behaviour. As Fig. 2.42 shows, in almost all the pixels the rate decreases by few Hz after ∼3000 hours of LED illumination. This suggests that the MaPMT might be affected by a photocathode degradation which would reduce the photon detection efficiency by 5-10%. Further investigations are necessary for a more precise estimation of this effect.

2.6 H12700 and R12699 MaPMT Characterization

The H12700A-03-M64 Multi-Anode PhotoMultiplier Tube is a novel 64-channel, 52 × 52 mm^2 square pixelated device produced by Hamamatsu (Fig. 2.43). It consists of a 8×8 pixel matrix (6×6 mm^2 each) able to detect single photons, amplifying the signal through a 10-stage dynode chain. The H12700 MaPMT can be equipped with a borosilicate or UV glass entrance window coupled with a bialkali photocathode so that a spectral response ranging between 300 - 650 nm or 185 - 650 nm respectively is obtained, with a maximum quantum efficiency of ∼33%[8] at about 350 nm. A socket, provided by Hamamatsu as standard and embedded with the H12700 MaPMT (Fig. 2.44), connects the anodes to the output pins and includes the HV divider. Note that all the measurements described below were acquired using such an embedded voltage distribution ratio: 2-1-1-...-1-1-0.5[9]. A second tube version is also available, called R12699-03, which has the same structure as

[8] Reference value provided by the manufacturer.
[9] Standard configuration suggested by the manufacturer.

the H12700 except for the absence of the socket. In this case, the output pins are connected directly to the anodes and the HV bias of the dynodes was provided by a custom-made passive voltage divider.

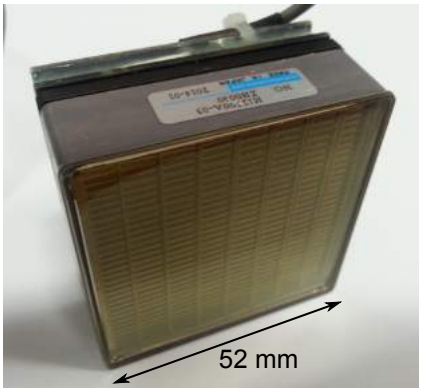

Figure 2.43: Front view of the Hamamatsu H12700 (serial code: ZB0030, produced in January 2014).

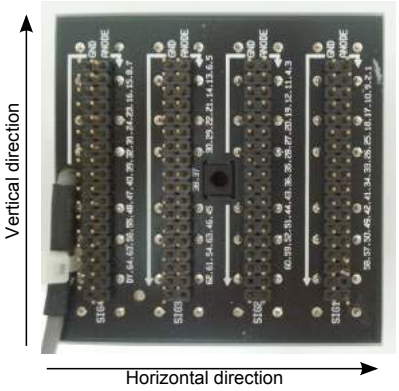

Figure 2.44: Back side of the H12700. The output pins of the socket embedded with the MaPMT are visible. The convention used to indicate the horizontal and vertical directions is shown.

Among the multi-channel photodetectors, the H12700 stands out for its large effective active area[8] (48.5 × 48.5 mm^2) while the very small inactive border around the device and the MaPMT square cross-sectional geometry allows for a close packing ratio (∼87% [8]). These features, together with the nominal low dark counts contribution and the moderate cross-talk between neighbouring pixels, make the H12700 particularly suitable for applications in RICH detectors.

The baseline tube chosen for the upgraded LHCb RICH detector is the R11265 MaPMT [24] which ensures an excellent spatial resolution thanks to the small pixel size (2.9×2.9 mm^2). Nevertheless, in the peripheral areas of the RICH 2 detector the spatial resolution is mainly limited by the chromatic dispersion of the refractive index of the Cherenkov medium (CF_4), by the uncertainties affecting the reconstructed track position from which the photons are emitted and by the aberration of the focusing mirrors [20]. In those areas, devices with larger granularity such as the H12700 can be used without affecting the overall PID performance of the system. This choice reduces the number of devices and channels with a consequent lower cost.

Five devices have been tested (three H12700 and two R12699 MaPMTs), each equipped with a UV glass entrance window and bialkali photocathode and the outcomes are shown. In section 2.6.1 the studies of gain variation, anode uniformity, dark current and pixel collection efficiency are presented. The cross-talk signal induced between neighbouring pixels was investigated in depth and the results are presented in section 2.6.2. Section 2.6.3

describes the characterization of the tube in the critical environment conditions expected in high energy physics applications such as the temperature dependence of gain and noise, the deterioration of the photodetector performance due to an external static magnetic field and the gain variation caused by the device aging after a long period of intense light exposure.

2.6.1 Standard characterization

This section is devoted to the measurements of the basic parameters characterizing the operation of the H12700 and R12699 MaPMTs in single photon detection regime. The following results were achieved by illuminating uniformly the device under test with a commercial blue LED biased with a very small current so that it produced only few tens of photons per second. A photon reaching the photocathode and converted into one photoelectron via photoelectric effect starts the 10-stages multiplication process on the dynodes so that a final charge of the order of few Me^- is collected at the anode. This signal is integrated by a charge sensitive preamplifier (standard current integrator circuit based on an AD9631 voltage feedback operational amplifier, by Analog Devices) producing an output voltage signal proportional to the total input charge, recorded by a CAEN Desktop Digitizer DT5720[10]. Unless otherwise noted, the tests were performed at room temperature and biasing the device at HV=1050 V using the voltage divider recommended by Hamamatsu (voltage ratio distribution: 2-1-1-...-1-1-0.5). In Fig. 2.45 the superposition of typical single photon spectra from different pixels of a H12700 MaPMT (serial code: ZB0030) are shown. All the pixels, except pixel 57[11] (see Fig. 2.47), are able to detect single photon signals with the single photon peak well resolved with respect to the pedestal. The low amplitude peaks just above the pedestal (centered at $\sim 20\%$ with respect to the single photon peak position) could be interpreted as a non ideal electron paths along the multiplication chain, such as photoelectrons skipping the first dynode, or photons that are converted into electrons at the first dynode stage. As will be described in section 2.6.3, this peak becomes higher in the presence of an external magnetic field which affects the ideal trajectory of the secondary electrons moving from one dynode to the next. The anode uniformity can be estimated from Fig. 2.45 as the ratio between the single photon peak position in each pixel with respect to the pixel with the maximum gain. The typical gain spread among pixels amounts to a factor 2-2.5 at most, in agreement with the uniformity tables provided by Hamamatsu. At 1050 V, the H12700 under investigation provides a typical gain of ~ 3.5 Me^-/photon. Similar gains and spreads were observed also in the

[10] The DT5720 is a 4 channels 12 bit 250 MS/s Desktop Waveform Digitizer with 2 Vpp single ended input. The DC offset is adjustable via a 16 bits DAC on each channel in the $\pm$ 1V range.

[11] Pixels 57 shows a dark counts rate higher than 1 kHz, so that the single photon peak could not be studied with the described setup (maximum single photon production rate of ~ 1 kHz per pixel). As declared by Hamamatsu, this anomalous value is due to a manufacturing defect. No other tested device shows analogous behaviour.

other tested devices.

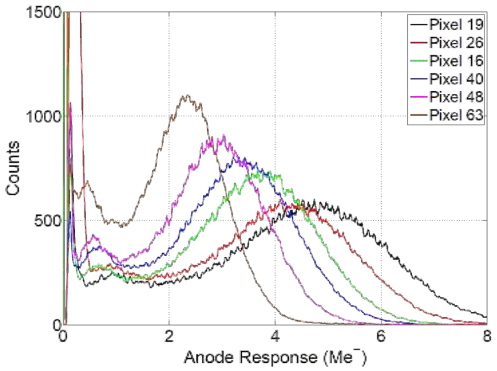

Figure 2.45: Superposition of single photon spectra acquired on different pixels of the H12700 MaPMT (serial code: ZB0030) biased at 1050 V. Note that pixels 19 and 63 are the ones with the maximum ($\sim$ 4.9 Me$^-$) and minimum ($\sim$ 2.4 Me$^-$) gain respectively. For the pixel numbering, see Fig. 2.47.

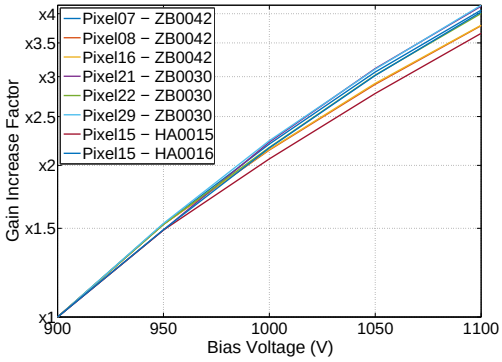

Figure 2.46: Gain increase factor (in logarithmic scale) measured on several pixels of two H12700 (serial codes: ZB0030 and ZB0042) and R12699 (serial codes: HA0015 and HA0016) MaPMTs as a function of the biasing voltage ranging from 900 V to 1100 V.

By measuring the single photon peak position at different biasing voltages, it is possible to determine how the gain of the photodetector scales as a function of the HV. Figure 2.46 shows the increase of the gain with respect to the HV value ranging from 900 V to 1100 V for several pixels of the four MaPMTs. It is observed that the gain at HV=1100 V is $\sim$3.5-4 times larger than that at 900 V. These scaling values do not depend on the MaPMT model or on the pixel absolute gain, as expected.

The dark current, i.e. the charge collected at the anodes due to spurious electron emission from the photocathode or the dynodes, represents an important figure of merit of the MaPMT. The dark current is usually quoted as the overall DC anode current measured keeping the MaPMT in the dark. For the studied MaPMTs the dark current at room temperature ranges from $\sim$ 0.5 nA to $\sim$ 3.5 nA, values lower than the typical value declared by the manufacturer (6 nA).

In case were the photodetector used in applications which require single photon sensitivity in all the pixels, it is interesting to measure the rate of spurious counts triggered in each channel above a defined threshold. Thus, the MaPMT dark current was also measured at room temperature by recording the rate of events with an amplitude larger than 1 Me$^-$ (average position of the valley between the pedestal and the single photon peak, as visible in the spectra in Fig. 2.45). Figure 2.47 shows the dark event rate measured for all the pixels of a tested device. The dark event rate turned out to be really low ($\leq$ 15 Hz per pixel or, equivalently, $\leq$ 40 Hz/cm^2) for most of the pixels. Few of them have a larger

dark current (up to several tens of Hz) and pixel 57 is the only one with an extremely high dark event rate ($\sim$ 1.4 kHz).

1 12	2 18	3 14	4 16	5 35	6 17	7 17	8 16
9 6	10 10	11 21	12 18	13 16	14 13	15 12	16 11
17 20	18 13	19 4	20 4	21 34	22 35	23 2	24 3
25 11	26 10	27 3	28 2	29 43	30 43	31 1	32 2
33 2	34 2	35 1	36 1	37 2	38 1	39 3	40 5
41 2	42 2	43 2	44 2	45 2	46 2	47 4	48 4
49 11	50 8	51 6	52 5	53 14	54 13	55 9	56 12
57 1430	58 25	59 13	60 15	61 115	62 42	63 11	64 38

Figure 2.47: Dark event rate (in Hz) measured for the H12700 MaPMT pixels over a 1 Me^- amplitude threshold (H12700 MaPMT, serial code: ZB0030).

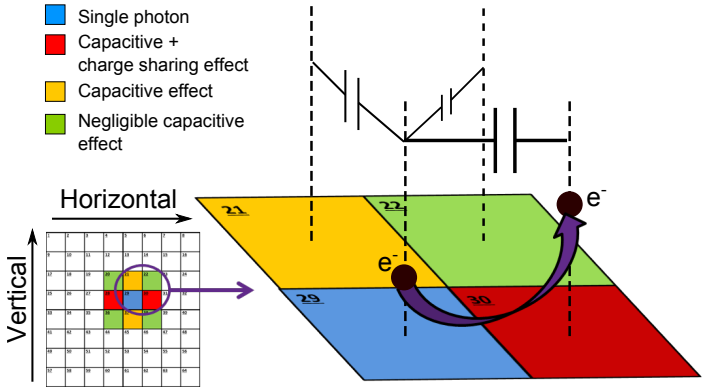

Figure 2.48: Schematic representation of the different sources of cross-talk usually affecting a MaPTM. This scenario is compatible with the results of the cross-talk measurements.

2.6.2 Cross-talk and charge sharing

A photon hitting a pixel induces a signal in the neighbouring pixels so that they could trigger an event despite being in the dark. This undesired effect is called cross-talk and is caused by different mechanisms, as schematically represented in Fig. 2.48.
A first cross-talk contribution (CT_{bias}) is due to the signal injected through the voltage divider biasing the dynodes unless properly filtered. A second contribution comes from the stray capacitance between neighbouring pixels which results in an AC coupling between the anode pins. This contribution ($CT_{coupling}$) causes not only spurious signals, but it also reduces the single photon signal amplitude at high frequency, as part of the charge deviates from the original path. Note that, in addition to the intrinsic contribution of the photodetector, the $CT_{coupling}$ also depends on the possible stray couplings between the electrical paths driving the signal from the input nodes to the read-out electronics. This suggests that not only particular care must be applied in the design and layout of the front-end circuit, but also that the socket embedded with the H12700 MaPMT could introduce an additional contribution, as it will be shown later. The waveform of the signals due to CT_{bias} and $CT_{coupling}$ is expected to have a bipolar shape. Furthermore, the charge sharing can be considered as a cross-talk source ($CT_{sharing}$), since it causes effects similar to $CT_{coupling}$, but with a different signal shape. The charge sharing is a statistical process which takes place whenever an electron deviates from its path during multiplication, starting a new avalanche in the neigbouring channel. Note that $CT_{sharing}$

gives a negligible contribution unless it starts from the first dynode stages; if the charges are shared only at the the first dynode, then the amplitude of the induced signal is expected to be independent of the gain of the reference pixel. Otherwise, if the charge sharing occurs at few initial dynodes, then the amplitude of the induced signal is proportional to the gain of the inducing pixel. Anyway, what matters for our investigations is that, differently to the previous contributions, the signals due to $\mathrm{CT}_{sharing}$ have the same shape as the main signal, so that they can be discriminated from that due to $\mathrm{CT}_{coupling}$.

The cross-talk effect is estimated by measuring the cross-talk ratio distribution. The cross-talk ratio is the cross-talk signal amplitude divided by the corresponding source signal amplitude, both calculated as the difference between the maximum of each signal and its baseline. Since, independently on the sources, the cross-talk signal amplitude is expected to be proportional to the inducing signal amplitude, this distribution should exhibit peaks centered on the values characteristic of the cross-talk source. These measurements were performed illuminating the whole MaPMT with a blue LED operating in single photon regime and acquiring a cluster of four contiguous pixels simultaneously. The cross-talk signals were discriminated off-line considering the coincidences with single photons hitting the adjacent pixel with signal amplitude larger than 100 ke^-. A pulse shape analysis is also performed in order to discriminate between unipolar ($\mathrm{CT}_{sharing}$ contribution) and bipolar (CT_{bias} and $\mathrm{CT}_{coupling}$ contributions) signals. Note that the front-end preamplifier was kept as close as possible to the device under test (pins connected with $\leq$ 10 cm widely separated unshielded copper wires), minimizing the loss of the signals on the stray capacitance of the wires connecting the anodes and the read-out system. In the following, a pair of side-by-side pixels is defined as *horizontally oriented* if the numbers of the pixels are consecutive (see Fig. 2.48) and consequently comes the definition of *vertically oriented* pixels.

Figure 2.49 shows the cross-talk ratio distribution measured by illuminating pixel 16 with single photons and acquiring the induced signals on pixels 8 (*a*, vertical direction) and 15 (*b*, horizontal direction). In Fig. 2.49.a, an asymmetric peak centered at ∼1.3% and extending up to ∼3% is visible on pixel 8. The behaviour is different for the induced signal on pixel 15 (Fig. 2.49.b, horizontal direction). In the horizontal direction, two peaks are clearly resolved, one located at around 3% and a second peak at about 7%. The signals which populate the two regions have different waveforms, as shown in Fig. 2.50. The waveforms of the $\sim$ 3% cross-talk events (Fig. 2.49.a) have a bipolar shape, while the ones corresponding to $\sim$ 7% cross-talk events (Fig. 2.49.b) have a single polarity since they always stay above the baseline level[12].

Another interesting aspect found in these tests is that both cross-talk behaviours coexist

[12] As far as the cross-talk ratio distribution of pixel 8 is concerned, Fig. 2.49.a, a prevalence of unipolar shaped waveforms can be seen in the asymmetric high-amplitude ratio tail with respect to the bipolar shaped signals mostly populating the main peak. However, the two contributions are not easily separated.

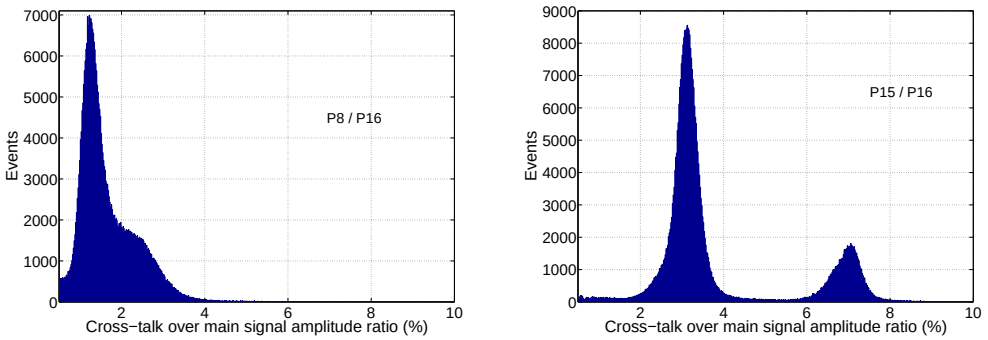

(a) (b)

Figure 2.49: Cross-talk amplitude distribution of a Hamamatsu H12700 (serial code: ZB0030), obtained illuminating pixel 16 with single photons and acquiring the cross-talk signals on pixels 8 (a) and 15 (b).

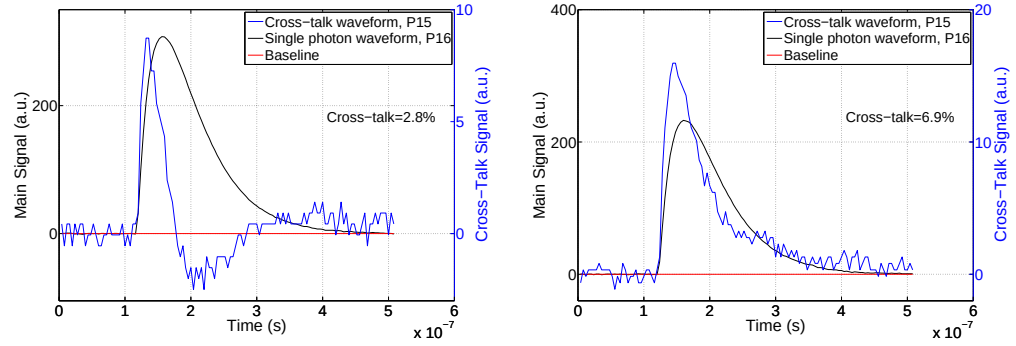

(a) (b)

Figure 2.50: The typical cross-talk waveforms acquired on pixel 15 induced by a single photon event occurred on the adjacent pixel 16 (horizontal direction). On (a), the typical bipolar shape of the $\sim 3\%$ cross-talk events. On (b), the single polarity cross-talk signal. Note that the main signal (black line) and the cross-talk (blue line) are plotted in two different scales.

for all amplitudes of the main signal, as shown in Fig. 2.51, where the cross-talk amplitude on pixel 15 is plotted as a function of the single photon signal amplitude on pixel 16. Two different linear trends can be seen, with a slope equal to $\sim 3\%$ and $\sim 7\%$ respectively. Both lines span from reference signal amplitude of about $\sim$100 ke$^-$ to several Me$^-$. Hence, independently of the main signal amplitude, both high-level and low-level cross-talk events are present.

Figure 2.52 shows the single photon spectrum acquired on the reference pixel 16 over a threshold of 1 Me$^-$. The probability that these events could induce cross-talk signals

larger than 100 ke$^-$ in the neighbouring pixels is quoted (in percentage unit) in the table shown in the top-right corner. As it can be observed, the probability of inducing cross-talk signal over threshold is of the order of $\sim 10\%$ along the vertical direction (pixels 8 and 24) where the $\mathrm{CT}_{coupling}$ contribution dominates. Such value is compatible to the one obtained assuming that the mean amplitude of the cross-talk signals due to $\mathrm{CT}_{coupling}$ is $\sim 2\%$ of the inducing signal amplitude. In this case, only events larger than 5 Me$^-$ (orange area in Fig. 2.52) induce cross-talk over a 100 ke$^-$ threshold. The same mechanism causes few induced pulses also along diagonal direction (pixels 7 and 23), even if they occur with a much lower probability. On the other hand, the $\mathrm{CT}_{sharing}$ contribution is responsible of larger cross-talk signals. Assuming that the average cross-talk amplitude ratio on the horizontal direction amounts to $\sim 5\%$, then 2 Me$^-$ collected at the pixel 16 anode are enough to induce cross-talk over the selected threshold on pixel 15 (ocher area in Fig. 2.52). This estimation is compatible to the observed probability ($\sim 65\%$) that single photon signals larger than 1 Me$^-$ on pixel 16 cause cross-talk 100 ke$^-$ threshold on pixel 15.

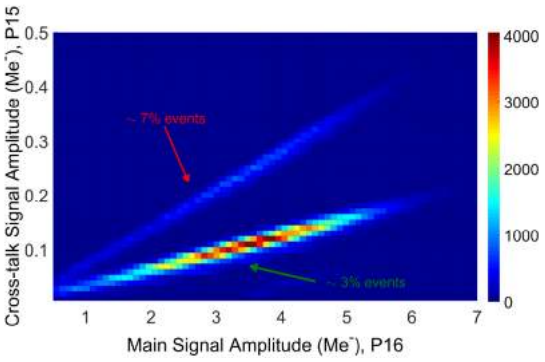

Figure 2.51: Cross-talk on pixel 15 versus single photon signal amplitude on pixel 16.

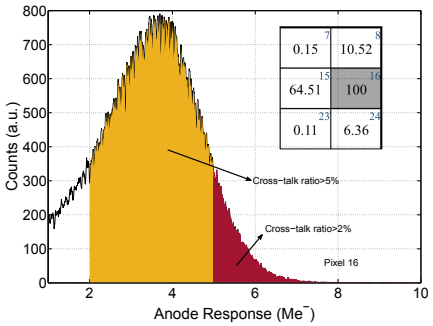

Figure 2.52: Single photon spectra acquired in pixel 16 over a 1 Me$^-$ threshold. The table shows the probability (in %) to see a cross-talk signal above 100 ke$^-$ threshold in all the neighbouring channels around around pixel 16. The pixel numbers are reported in blue in the top-right corner.

In summary, the cross-talk results indicate an unexpected asymmetry between contiguous pixels located on rows or columns. Illuminating with single photons a pixel used as reference, the neighbouring pixels along the vertical direction show a cross-talk dominated by CT_{bias} and $\mathrm{CT}_{coupling}$ contributions, with an amplitude distribution centered at $\sim 1.3\% - 3\%$. Also along the diagonal direction a small coupling between neighbouring pixels is expected.

However this turned out to be a negligible effect.

The cross-talk level between horizontally contiguous pixels deserves more attention. In addition to the previous behaviour, a second gaussian-like peak centered at $\sim 4-7\%$ is visible in the cross-talk amplitude distribution. These two peaks are the result of the combination of the $\mathrm{CT}_{coupling}$ and $\mathrm{CT}_{sharing}$ contributions. Similar outcomes were observed in all the tested pixels of two devices for each MaPMT type (H12700, serial codes: ZB0030 and ZB0042; R12699, serial codes: HA0015 and HA0016). While the double peak structure in the cross-talk ratio distribution was systematically observed along the horizontal direction, the peaks heights differ between pixel pairs and, in first approximation, the probability of charge sharing events ranges from $\sim 25\%$ up to $\sim 50\%$. This value strongly depends on the position where the inducing photon hits the reference pixel.

As described above, the uniformity of response of the pixel was studied dividing the pixel area in a 3×3 matrix of $\sim 1.5 \times 1.5$ mm^2 regions using a mask. Each region can be individually illuminated by means of a 1 mm diameter optical fiber fastened to the mask. For example, using pixel 43 as reference, the cross-talk signal is acquired on both horizontal (pixel 42) and vertical (pixel 35) directions. Figure 2.53 shows the obtained results. Along the horizontal direction, two peaks are clearly resolved if the photon hits the A-areas, located at 0.75 mm from the borderline between pixel 43 and 42. In agreement with the previous measurements, the low-level and high-level cross-talk peaks are populated by bipolar (star marker in Fig. 2.53) and unipolar (circular marker) shaped signals respectively. In this case, about $\sim 60-70\%$ of single photons induce charge sharing. On the other hand, if the photon hits the B-areas (2.25 mm away from the borderline), a negligible charge sharing is observed since the cross-talk amplitude distribution results in a single low-level gaussian peak.

In first approximation, assuming the probability of inducing charge sharing to be 65% in the first 2.25 mm from the borderline ($\sim 37\%$ of the whole pixel area) and negligible in the other regions of the pixel, $\sim 24\%$ of photons would cause charge sharing in the horizontal direction. This coarse estimation is consistent with the results previously shown.

Similar considerations can be made in the vertical direction (pixel 35). In this case, the two peaks are not well-separated and the charge sharing due to photons hitting the 1-column only causes an asymmetric tail ranging from $\sim 1\%$. to $\sim 3\%$. In case of uniform illumination in the pixels, the $\mathrm{CT}_{coupling}$ dominates the cross-talk amplitude distribution.

As mentioned above, the stray capacitance of the electrical links driving the signal from the anodes to the read-out electronics has to be minimized as it contributes to the $\mathrm{CT}_{coupling}$ effect. In this regard, the socket embedded in the H12700 MaPMT could also add a non-negligible effect. In order to highlight this contribution, pixel 15 of a tube (serial code: ZB0042) was uniformly illuminated and the cross-talk ratio distribution was acquired in the neighbouring pixels with the usual setup. The obtained results are shown in Fig. 2.54. While the lower amplitude peak of pixel 7, 14 and 23 are centered at $\sim 1\%$, higher values

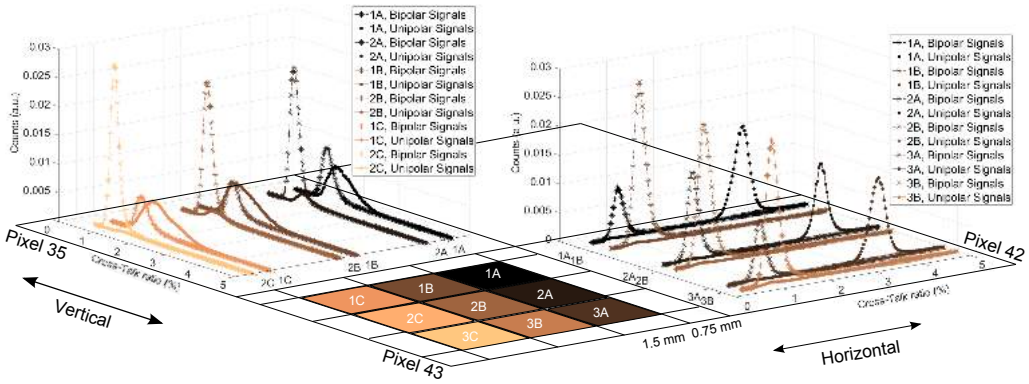

Figure 2.53: Cross-talk amplitude distribution induced on pixel 42 (horizontal direction) and 35 (vertical direction) by a single photon hitting pixel 43 in different 1.5×1.5 mm^2 areas (R12699 MaPMT, serial code: HA0015). Different markers are used for the distributions populated by unipolar (circular) or bipolar (star) shaped cross-talk signals. The plots are colored according to the position where the inducing photon hits the reference pixel.

($\sim 3\%$) are observed in pixels 8 and 16, located close to the biasing high voltage pins. Later, the socket equipping the device was unsoldered and the measurements were performed on the same pixels keeping unchanged the setup. This second cross-talk amplitude distribution is reported in Fig. 2.55. It can be observed that the distributions of the pixels not contiguous to the biasing pins remains almost unchanged. Moreover, the lower amplitude peak of pixels 8 and 16 are now centered at $\sim 1.5\%$, similar to all the other tested pixels. This suggests that the socket standardly provided by Hamamatsu is responsible of an extra capacitive coupling to the biasing nodes which doubles the bipolar shaped cross-talk signal amplitude of the pixels located near those pins.

Besides cross-talk, there is another known mechanism that could induce spurious signals in photomultipliers, by generating delayed afterpulses following the main signal. The MaPMTs can be affected by two types of afterpulses. The first occurs due to the elastic scattering electrons produced at the first dynode which cause small amplitude signals following the main one with a very short delay (several nanoseconds to several tens of nanoseconds). In our measurements, the anode current is integrated with a time constant of the same order and an acquisition window which lasts ~ 500 ns per signal (see Fig. 2.50). Therefore, this class of afterpulses is triggered together with the corresponding main signal without significantly affecting the amplitude of the signal of interest, causing marginal effects. A second category of afterpulses is due to ion feedback which induces high amplitude signals delayed by several hundreds of nanoseconds to over a few microseconds. This kind of afterpulses is expected to be larger than single photon signals so that these two contributions can be easily separated. We treated them similar to high amplitude

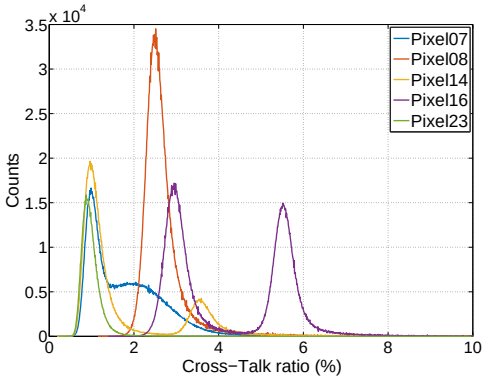

Figure 2.54: Cross-talk ratio distribution measured on the neighbouring channels of the uniformly illuminated pixel 15 (H12700 MaPMT, serial code: ZB0042). The socket provided by Hamamatsu is connected and operating.

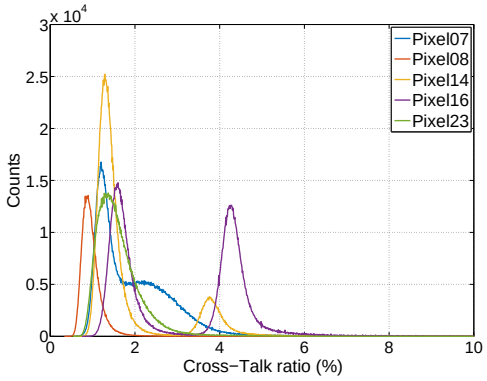

Figure 2.55: Cross-talk ratio distribution measured on the neighbouring channels of the uniformly illuminated pixel 15 (H12700 MaPMT, serial code: ZB0042). The socket provided by Hamamatsu is unsoldered and the biasing voltage is provided with a custom-made passive voltage divider (standard voltage ratio).

dark events, since we were not able to discriminate these two effects. Although our setup (based on single photons emitted at random by a DC-biased LED) is not able to quantify the afterpulse probability for the present device, it is expected to be below 5% for a PMT with a good quality vacuum, as explained in [33].

2.6.3 Behaviour in critical environment condition

As mentioned, the features of the H12700 and the R12699 MaPMTs make them tailored for the application in the RICH 2. Unlike the RICH 1 system, located near the bending magnet, a negligible magnetic field is expected in the RICH 2 detector. Despite this, the photodetector performance has been characterized with respect to the magnetic field and the obtained results are following described. In addition to that, the MaPMTs are sensitive to the operating temperature which can alter the gain and cause a dark current increase. In the case of LHCb RICH upgrade, the photosensor is expected to withstand the intense illumination of up to $\sim 10^6$ photons per pixel per second in the most illuminated detector areas.

2.6.4 Behaviour in magnetic field

In principle the performance of a photomultiplier tube is affected by an external magnetic field since it might induce some electrons changing their trajectory starting from the

photocathode. According to the results already obtained studying the R7600 [28] and the R11265 [34] MaPMTs, the main effects are caused by a longitudinal magnetic field (parallel to the tube axis and perpendicular to the photocathode surface). In a very conservative approach, the tube performance was tested under the action of a magnetic field up to 100 G produced by a solenoid. As usual, the single photons were produced using a commercial blue LED and the output signals were amplified with a charge sensitive preamplifier and acquired by a CAEN Desktop Digitizer. Figure 2.56 shows the single photon spectra observed on various pixels at different magnetic field intensities.

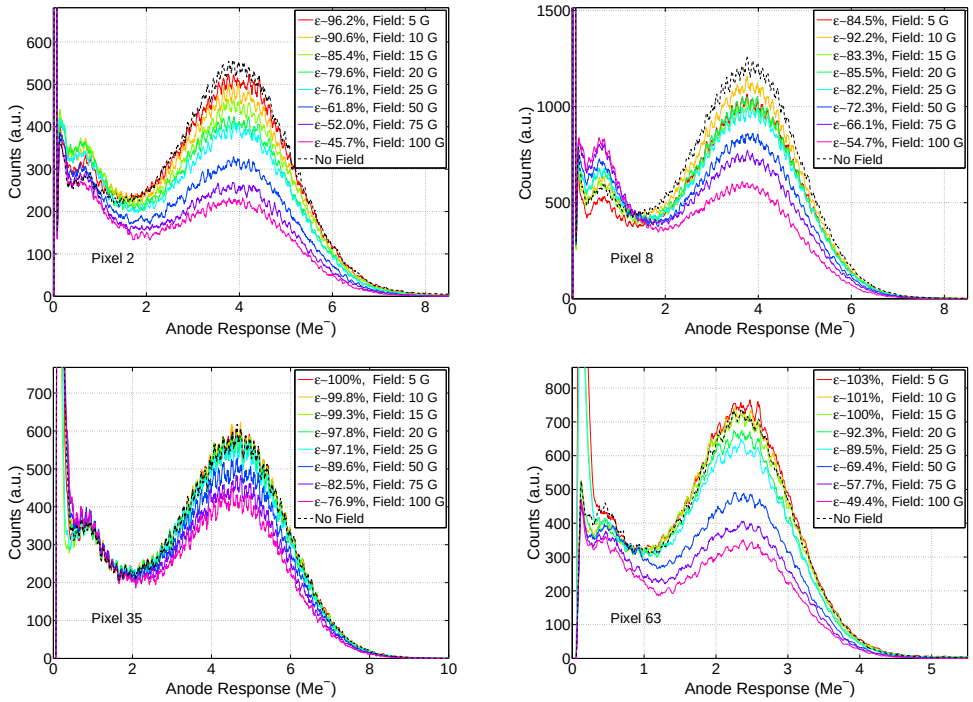

Figure 2.56: Superposition of single photon spectra acquired under the action of different longitudinal magnetic fields. The top plots and the bottom right one refer to pixels 2, 8 and 63 respectively, located in the external region of the MaPMT, near the biasing high voltage pins. The bottom left plot shows the results in the central pixel 35. No high magnetic permeability material was used to shield the photon detector (serial code: ZB0030, HV= 1050 V).

The central pixel 35 is quite insensitive to the external magnetic field since significant degradation of the spectra is visible only for fields higher than 25 G. Defining the efficiency ϵ as the number of events with an amplitude larger than 1 Me^- divided by the one triggered above the same threshold without the magnetic field, the loss of efficiency at 25 G is almost negligible ($\sim 3\%$). On the contrary, the pixels located in the peripheral area of the photon detector and near the HV pins turned out to be more sensitive. As Fig.

2.56 shows, the loss of efficiency at 25 G measured on pixel 63 is more than 10%. An even more critical behaviour is visible in pixels 1 to 8. In this case, the loss of efficiency rises to 20-25% at 25 G. The number of events in the single photon peak decreases significantly even for weaker fields.
As expected, the events affected by a non-ideal electron path along the multiplication chain happen more frequently if an external magnetic field is applied. This effect is clearly visible from the number of events at ~ 0.7 Me$^-$, which increases with the field intensity. In order to recover the nominal performance of these peripheral pixels, the photodetector was wrapped in a high magnetic permeability material to absorb the field. In particular, the performance of the H12700 was studied in presence of a longitudinal magnetic field up to 100 G while shielding the device with one layer of Skudotech wrapping the MaPMT lateral surface.

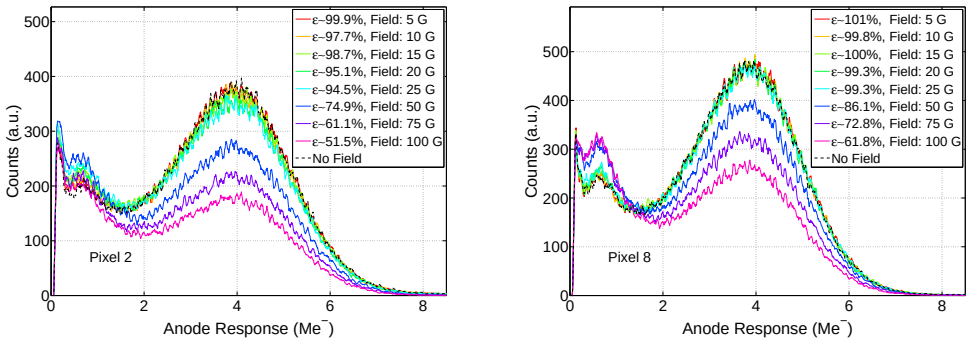

Figure 2.57: Superposition of single photon spectra acquired under the action of different longitudinal magnetic fields. A single Skudotech layer (thickness ~ 200 $^-$m) wraps the H12700. The left and right plots refer to pixels 2 and 8 respectively, which represent the worst case condition since they are located near the biasing high voltage pins (serial code: ZB0030, HV= 1050 V).

The shield protrudes by 1 cm from the photocathode surface, while the anode pins were kept uncovered. Figure 2.57 shows the results of these measurements for two of the most sensitive pixels. It can be noticed that the efficiency is almost fully recovered at moderate magnetic field intensities (≤ 25 G), and the loss of efficiencies reduces at most to $\sim 5\%$. Also the spectrum distortions previously observed (see Fig. 2.56) are recovered if a magnetic shield is used. In presence of fields larger than 25 G, a single Skudotech layer saturates and loses its efficiency.

2.6.5 Temperature dependence

The behaviour of the MaPMTs under investigation was studied with respect to the effects of a temperature variation. Indeed, increasing the operating temperature, the MaPMT gain decrease while spurious dark counts get more frequent. The setup to perform these

measurements was the same used for the characterization of the R11265 MaPMT: the photosensor and the read-out electronic circuitries were put in a climatic chamber (Votsch VC 4018) operating at a temperature ranging from 10 °C to 50 °C. The single photon signal was provided by a commercial blue LED located outside of the climatic chamber and operating at constant temperature.

Figure 2.58 shows the superposition of single photon spectra acquired in the same pixel at different temperature. As it can be estimated from the single photon peak position, the gain reduces with increasing the temperature, analogously to that observed in the R11265 tubes ([34]). Indeed the mean number of secondary electrons emitted from each dynode reduces with the temperature, with a consequent gain decrease. From Fig. 2.58 it is possible to estimate that the gain reduction as a function of the temperature is quite linear in the range of interest and the characteristic slope amounts to about -10 ke$^-$/°C or 0.25 %/°C.

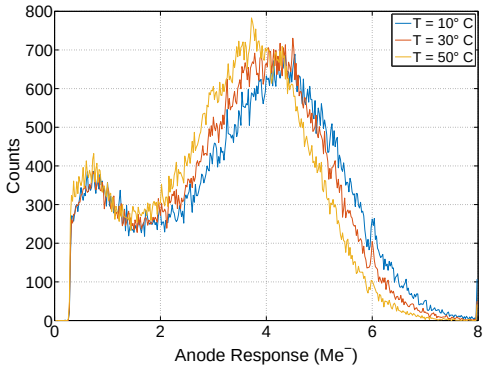

Figure 2.58: Single photon spectra as a function of temperature (H12700 MaPMT, serial code: ZB0030, Pixel 15, HV= 1050 V). The gain variation can be estimated from the single photon peak position.

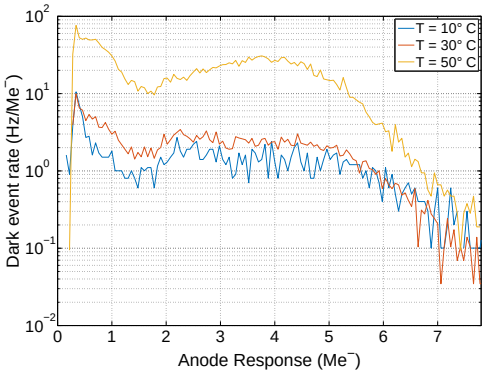

Figure 2.59: Dark rate spectra, in logarithmic scale, as a function of temperature (H12700 MaPMT, serial code: ZB0030, Pixel 15, HV= 1050 V).

Another parameter that strongly depends on temperature is the dark current. Indeed, the rate of noise signals increases greatly with temperature as shown in Fig. 2.59 where dark counts spectra acquired at different temperature are superimposed with a logarithmic scale. The reason of this phenomenon is that, increasing the temperature, the number of electrons which have enough thermal energy to escape from the dynodes or the photocathode surface and generate a multiplication process increases. In particular, the dark counts rate at 50° C above 1 Me$^-$ is more than an order of magnitude larger than that at 10° C.

2.6.6 Aging Test

Long periods of light exposure cause MaPMT aging and will therefore deteriorate the device's initial performance. This critical condition is common in high energy physics applications where the device must withstand extremely high photon rates for thousands of hours. Typical effects due to the aging of the device are the reduction of the photocathode efficiency, the dark count rate increase and the variation of the gain of the tube. From the experience gained during the characterization of the R11265 MaPMT [34], the most critical effect due to the aging is the gain loss caused by the deterioration of the dynodes which change the mean number of secondary electrons emitted.
In order to make a quantitative estimation of how much the gain is affected by aging, a fully automatic system was set up to age a H12700 and a R12699 MaPMTs. A commercial blue LED illuminated the device under test, causing a stable aging current. Periodically, the LED biasing voltage was turned down so that it operated in single photon regime. The single photon signals from the tested pixels were amplified by charge sensitive amplifiers and acquired with three DT5720 Desktop Digitizers (CAEN). The gain loss was evaluated by measuring the single photon peak position over several thousand hours of effective LED illumination. A slow control system continuously monitored the DC aging current in all the device and ensured the temperature stability by adjusting the heat injected by four power resistors. This prevents the temperature variation to affect the gain of the photosensor during the measurement. Further details on the setup conditions and the analysis can be found in [34].

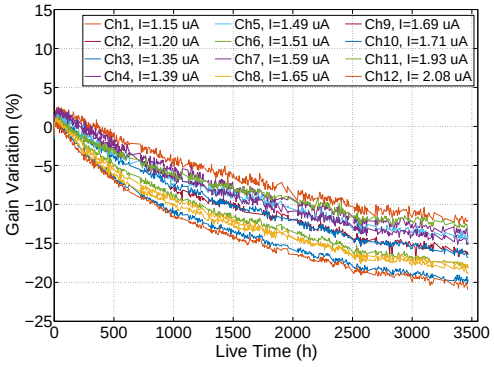

Figure 2.60: Gain variation (in %) versus the illumination period for the tested H12700 MaPMT (serial code: ZB0030, HV= 1000 V, T= 24.5° C).

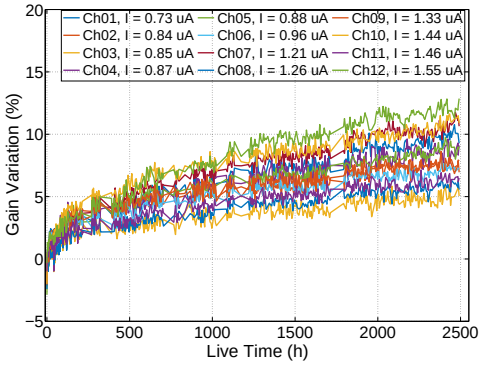

Figure 2.61: Gain variation (in %) versus the illumination period for the tested R12699 MaPMT (serial code: HA0016, HV= 900 V, T= 25° C).

As mentioned above, two MaPMTs have been tested (one H12700, serial code: ZB0030, and one R12699, serial code: HA0016) and the gain variation as a function of the effective LED illumination period are shown in Fig. 2.60 and Fig. 2.61. The gain loss is calculated

as the percentage variation of the single photon peak position with respect to the value measured at the beginning in each pixel, after keeping the device in the dark for 24 hours and illuminating it for one hour.

Referring to Fig. 2.60, the illumination level was set in order to induce an initial integrated current over the anodes of $\simeq 94$ μA, similar to the maximum value sustainable by the tube according to the manufacturer specifications (100 μA). Such an intense illumination, roughly equivalent to a single photon rate of few MHz per pixel, was chosen because it is similar to the current value standardly used in this test by the manufacturer. All channels are observed to have a similar trend and the gain loss after 3500 hours ranges from $\sim 13\%$ down to $\sim 20\%$. The slope of the curves gradually decreases with the LED illumination period and becomes almost flat above ~ 2800 hours. In particular, the gain loss in the last ~ 700 hours of LED illumination is of the order of 1% and comparable with the measurement uncertainties. In this plateau region the performance of the photodetector can be assumed stable.

Figure 2.61 shows the result of the same measurement performed on the R12699 MaPMT, serial code HA0016. The device was biased at HV= 900 V with a consequent reduction of the initial anode current to ~ 40 μA. The absolute gain variation decreases with respect to the one observed in the former tube. This suggests that the gain variation is related to the integrated DC current which is responsible of the deterioration of the dynodes and depends on the illumination level and the average gain of the device.

What stands out comparing the two measurements is that the two photodectors show opposite trends. Indeed, the gain of all the observed pixels of Fig. 2.61 increases with the illumination period in contrast with what observed in the other device (Fig. 2.60). This strange behaviour was already exhibited by some R11265 samples, as presented in [35]. Hamamatsu ascribes this to the spread of the thickness of the Cesium layer grown on the dynode surfaces[13].

According to our observations, the absolute gain variation amounts at worst to $\mid \Delta G \mid \simeq 20\%$ after 3000 hours of high intense illumination (equivalent single photon rate of few MHz per pixel). Finally, note that, as the device reaches gain stability, its overall variation can be compensated by adjusting the high voltage biasing the MaPMT, as shown in [34].

2.7 The CLARO chip

The front-end electronics specifically designed to read the signals of the RICH MaPMTs is based on a integrated circuit named CLARO. The CLARO chip is a 8 channel custom designed ASIC realized in 0.35 μm CMOS technology from Austria Micro Systems (AMS)[14]. Such a relatively aged and inexpensive technology can still meet the LHCb requirements

[13] Confidential information provided by the manufacturer

[14] AMS website: http://asic.ams.com

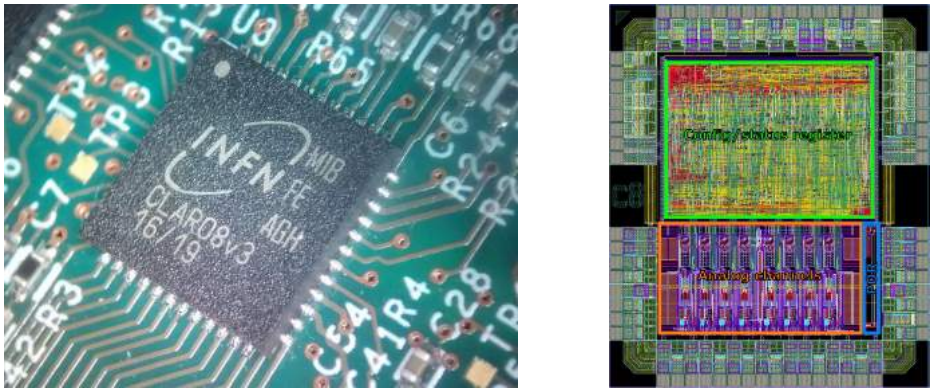

Figure 2.62: A picture of the CLARO ASIC in packaged (on the left) and die (on the right) format. In the latter figure, the digital and analog blocks are pointed out. (Courtesy of C. Gotti)

in terms of wide-bandwidth and low power, also ensuring a very high yield and a good tolerance to radiation. A picture of the CLARO ASIC is shown both in the QFN56 package and die format in Fig. 2.62. As it can be observed, the input pins (located on the bottom pads row) are connected to the analog block processing the signal. In order to minimize the coupling at the input nodes, the input pads has been alternated with grounded pads. The chip is also equipped with a configuration register that store and manage the operating parameters of each channels and allow the user to enable/disable the various features developed for test, calibration and debug purpose. The output pads, where the fast discrimination signal is generated, are located on the top pin row Fig. 2.62, as far as possible to the sensitive input pins in order to avoid self-induced disturbance injection. For the same reason a great care was taken to properly ground the ASIC bulk and, in general, to the grounding configuration of the EC.

The analog chain of the CLARO chip is essentially composed of an input Charge Sensitive Amplifier (CSA) and a Discriminator, as shown in Fig. 2.63. When a photon hits the MaPMT surface, a photoelectron is emitted from the photocathode starting the charge multiplication process. The collection time of the photodetector is very small, of the order of 1 ns. Thus, the typical signal at the anode consists of a ~ 1 Me^- current pulse, injected at the input node of the CLARO. The CSA integrates the current pulse and provides an exponentially shaped voltage signal, whose amplitude is proportional to the charge collected at the input. The rise time constant of the CSA is of the order of ~ 1 ns and is proportional to the input capacitance, while the fall time constant amounts to few ns, large enough for an effective integration of the fast pulses but short enough to sustain high rates without pile-up. The CSA is DC-coupled to a discriminator stage which provides a digital pulse if the signal at its input crosses a adjustable threshold level. The typical pulse provided at the CLARO output in case an event has been triggered, in shown in

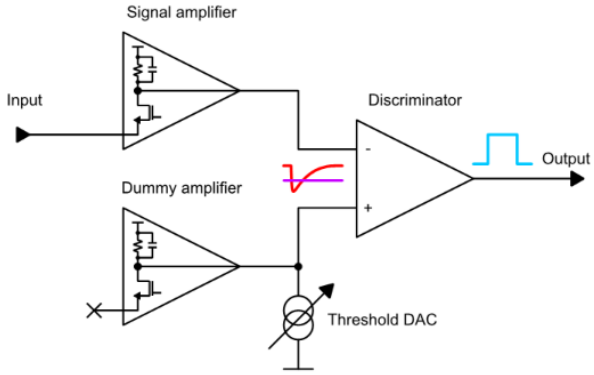

Figure 2.63: Simplified electrical scheme of the CLARO analog block.

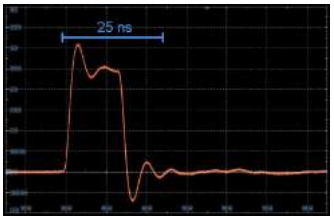

Figure 2.64: Tipical output signal (in time domain) provided by the CLARO. The baseline is completely restored in 25 ns.

Fig. 2.64. The FWHM of the digital output signals is lower than 25 ns so that photon counting rates up to 40 MHz can be sustained avoiding pile-up, as required for the RICH upgrade. Despite its wide bandwidth, the CLARO must ensure a low power consumption in order to minimize the heat injection in the most illuminated areas of the RICH detector, avoiding the need for a dedicated cooling system in such a closely packed system. Except during the chip configuration procedure, the digital register is static and does not dissipate power. The consumption of the analog block increases proportionally to the output load capacitance (typical value $C_L = 30$ pF) and the photon detection rate ($R = 10$ MHz at the maximum foreseen occupancy of $\theta = 25\%$). The total power consumption of a CLARO ASIC is described by:

$$P = P_0 + RC_L V_{CC}^2 \tag{2.11}$$

where $P_0 = 1$ mW is the power consumption in idle mode and $V_{CC} = 2.5$ V is the CLARO power supply positive rail. According to Eq. 2.11, the power consumption of a chip amounts to $\sim$ 2.5 mW at most. This contribution is completely negligible with respect to that consumed across the voltage divider biasing the MaPMT ($\sim$ 1 W), so no additional heat is injected from the read-out electronics towards the photosensors. Since the response of the MaPMT pixels typically differs in gain by a factor of three and strongly change as a function of the HV biasing voltage, as shown in Sect. 2.5 and Sect. 2.6, the CLARO must be able to operate in a wide input current range and provide feature to compensate for the photosensor non-uniformities. The input CSA of each channel is equipped with an adjustable attenuation factor settable through the digital configuration register over 4 values, 2-bit (1, 1/2, 1/4, and 1/8, all expressed in V/V unit). Thus, the amplifier input dynamic ranges up to 5 Me^- (millions of electrons) for attenuation 1 V/V up to 40 Me^-

at 1/8 V/V. Furthermore, the trigger threshold can be adjusted over 64 values, 6-bit, by changing the current injected by the DAC into the positive terminal of the output discriminator (see fgi.2.63). In particular with 1 V/V (1/8 V/V) input attenuation, the trigger threshold resolution is 30 ke^- (240 ke^-) in a range of 2 Me^- (16 Me^-). The analog block includes also a dummy amplifier with consists of a CSA ideally identical to that used to amplify the signal but with a floating input. In case no current is generated from the threshold DAC current source, the output value of the dummy amplifies compensate any offset of the input CSA allowing its DC coupling to the discriminator stage. Moreover, the symmetrical configuration obtained using the dummy amplifies improves the Power Supply Rejection Ratio (PSRR) performance of the ASIC.

As mentioned, the CLARO is equipped with a digital configuration register, which can be set and read using a SPI-like protocol. Each channel is provided with a 12-bit configuration register through which the attenuation and trigger threshold values can be adjusted independently. This register also allow to enable/disable a desired channel, translate the threshold by half range to compensate for negative offset (as better described in next section), enable/disable the trigger threshold hysteresis and allow the injection of test pulse for debug purpose. The digital block manages also global features, useful for the debug, calibration and monitoring of the chip. As well-know, integrated circuit are sensitive to the effects of the environment radiation due to the energy it delivers inside the silicon die generating electron-hole pairs. In particular, not scaled integrated circuits are more sensitive to the Total Ionising Dose (TID), which is the total dose collected by the circuit during its operating life. The major effect related to the TID is the shift of the CMOS gate threshold voltage caused by the holes trapped in the gate oxide. This effect leads to an increase of the leakage current and a change of the working point of the transistors composing the circuit. Scaled technologies are most affected by Single Event Effects (SEEs), statistical events which can abruptly modify the chip behaviour. For instance, one bit of a configuration register can be flipped because of the electrical pulse induced by the electron-hole pairs produced by a interacting ionising particle (Single Event Upset effect, SEU). In addition, Single Event Latch-up (SEL), which is the inadvertent creation of a low-impedance path between the power supply rails, can be triggered by an ionising particle on the parasitic structure formed by the PN-junctions defining the N-MOS and P-MOS transistors. In case of SEL, the ASIC would stop to operate and absorb a lot of power, which can even lead to the chip destruction. For middle-scaled technology such that used for the CLARO design, the TID mostly affect the analog block, whereas cares to the SEEs must be taken for the digital block. Table 2.2 reports the maximum particle fluency and TID level expected in ten years (10^7 seconds per year, 50 fb^{-1} of total integrated luminosity) of RICH operation during RUN 3.

In order to guarantee a reliable operation in the LHCb environment, the CLARO must be tolerant to the radiation collected in 10 years of system operation. The digital block was

Detector	1 MeV n_{eq} (cm^{-2})	High energy hadrons ($E > 20$ MeV) (cm^{-2})	Dose (krad)
RICH 1	$1.53 \cdot 10^{12}$	$5.75 \cdot 10^{11}$	100
RICH 2	$7.75 \cdot 10^{11}$	$2.5 \cdot 10^{11}$	40

Table 2.2: Radiation collected in 10 years of LHCb operation during the RUN3 [36]. Note that the tests as been performed adding an addition safety factor of 2.

fabricated using a radiation-hard design [37] [38] which ensures the immunity to SEL. In addition to that, the configuration registers are protected from SEU by adopting a triple modular redundancy architecture, so that an eventual bit flip in one module are compared by a voter to the same bit of the other two modules and the error is immediately and automatically corrected [36]. Note that the digital block also includes a SEU correction counter to monitor the operation of this active protection. The radiation test campaign, performed by the INFN-Fe group, demonstrated that the trigger threshold drifted by $\sim 5\%$ (few equivalent DAC step), without any relevant noise or power consumption increase, after 200 krad (20 years of LHCb operation). Moreover, only ~ 3.5 SEU per chip were observed, all of which can be corrected by the voter, while no SEL were detected [36].

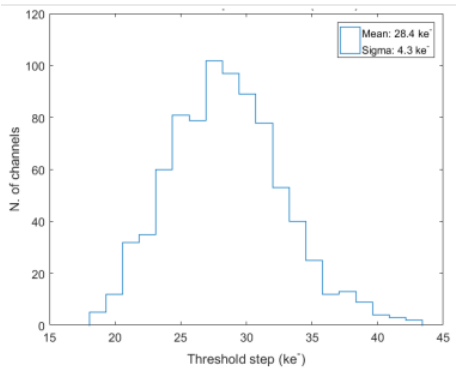

Figure 2.65: DAC threshold step distribution at attenuation 1 V/V, measured on the full CLARO pre-production. The nominal design value is 30 ke^-, in agreement with the experimental result: $\Delta Q = (28.4 \pm 4.3)$ ke^-. In general, mismatches between the CLARO channels cause a spread of the trigger threshold step of 20% RMS, independently of the attenuation value.

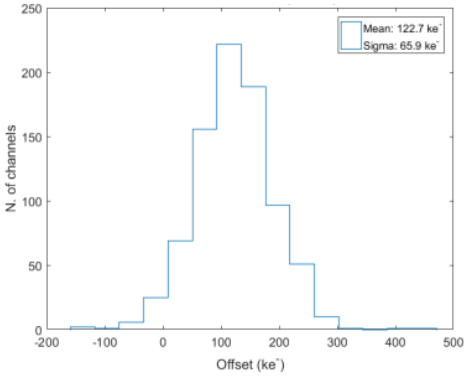

Figure 2.66: Offset distribution at attenuation 1 V/V, measured on the full CLARO pre-production. A mean offset of $Q_0 = (127 \pm 66)$ ke^- was observed. In general, mismatches between the input and dummy CSAs can cause an offset of $Q_0 = 1.5\Delta Q$, independently of the attenuation value.

Ideally, in typical 1 V/V attenuation condition, the CLARO should provide an adjustable trigger threshold step of 30 ke^- ranging from 0 to 2 Me^-. Nevertheless, the fabricating process does not guarantee the achievement of high accuracy since the transistor dimensions have a poor level of precision (typical tolerance of few tens of percent). As a consequence, setting the same threshold code in all the system channels, the threshold value expressed in equivalent electrons changes from channel to channel. In addition to that, mismatches can cause asymmetries between the input and dummy CSAs, so that the input terminals of the discriminator have a different value even when no current is generated from the threshold DAC. The effective threshold step amplitude (ΔQ) and the offset (Q_0) have been characterized on a large number of CLAROs belonging to the pre-production run. Figure 2.65 and 2.66 shows the distribution of the obtained results concerning the threshold step and the offset respectively. As it can be observed, the mean threshold step is in agreement with the expectation. The distribution can be approximated to a Gaussian function whose standard deviation is 20% of the mean value. A similar behaviour was observed measuring the offset distribution. In order to study negative offsets, the CLARO configuration register provides a flag so that the zero DAC level corresponds to the threshold number 32. In this way, the user can set a negative threshold level of 32 equivalent step at most and investigate the offset close to ground rail. The obtained results show a positive average offset whose RMS value is 1.5 times the trigger threshold resolution ($Q_0 = 1.5\Delta Q$). All the mismatches between the electronic channels are superimposed to the non-uniformities between the various pixels of the MaPMT. In order to compensate for both effects, two calibration procedures have been developed to characterize the electronic chain and the MaPMT pixel. The calibration principles and th obtained outcomes are described in the next section. Note that periodic calibration can also compensate for the threshold drifts due to the collected TID.

2.8 The Elementary Cell design and calibration

Each digital pulse provided at the CLARO output is recorded by the DB. This event might be from a photon emitted by a particle crossing the detector faster than the speed of light in the detector radiator or from a noise source. The system is only capable to provide a 1-bit digital information per channel, so the signals of interest cannot be distinguished from spurious counts once they are triggered by the CLARO discriminator. However, the effects of the different sources of noise could be interpreted as a Cherenkov photon event only if the spurious counts cause signals larger than the CLARO trigger threshold. The MaPMT performance and the design of the EC were specifically characterized to ensure a good separation between the signal of interest and spurious counts.
Beside the choices made for the system design, a great improvement of both signal detection efficiency and spurious counts rejection can be achieved by a proper setting of the trigger

threshold. Figure 2.67 shows a typical single photon spectrum of a MaPMT pixel. Assuming that the pedestal is only populated by spurious events while the single photon peak contains the signal of interest, the noise rejection and the signal detection efficiency as a function of the trigger threshold level (express in terms of equivalent electrons) are superimposed in blue and orange respectively. By setting the trigger threshold in the valley between the two peaks, efficiencies of the order of 95% can be obtained for both the signal detection and the noise rejection. Given the non-uniformity of the anode responses, the mismatches between the electronic channels and the steepness of the curves of curves in Fig. 2.67 around the optimal value, it follows that such performance can be achieved only with a pixel-by-pixel calibration. Being able to calibrate the ECs in the final full-mounted RICH system, would allow to periodically calibrate the system and correct for drifts due to MaPMT aging or threshold variation because of the collected TID.

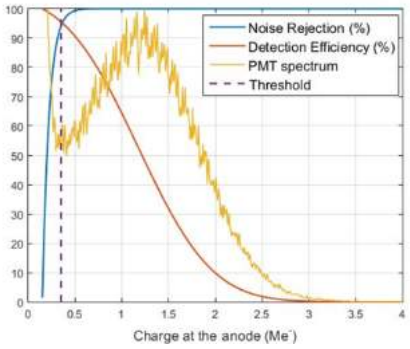

Figure 2.67: Typical single photon spectrum (yellow), light signal detection efficiency (orange) and dark counts rejection efficiency (blue) as a function of the signal amplitude. The dashed line shows the trigger threshold

EC design

The main sources of spurious events in the LHCb RICH application are the spontaneous electron emission from either photocathode or dynodes via thermionic effect, the charge sharing effect between neighbouring pixels and the cross-talk due to the capacitive coupling between adjacent anodes. As shown in Sect. 2.5 and Sect. 2.6, dark counts due to thermionic emission from dynodes usually result in low amplitude signals, mainly located in the pedestal peak, and thus rejected by a proper trigger threshold setting. On the other hand, any electron emitted from the photocathode is amplified by the dynodes chain in the same way as the photon signal, so that these two contributions cannot be discriminated. At room temperature the dark count rate of the MaPMTs is of the order of $\leq$100 Hz/cm^2, totally negligible if compared to the signal rate ($\sim$10 MHz/pixel). The thermionic dark rate increases exponentially with the operating temperature, according to Richardson's

law (as shown in Sect. 2.5 and Sect. 2.6). So cooling is required. This constraint guided the design of BsB (equipped with a cross-shaped thermal mass) and CLARO (extremely low power consumption). Such design makes the MaPMTs operate at 20-25 °C so that the thermionic emission rate is negligible with respect to the signal rate.
Charge sharing and cross-talk would induce spurious signals correlated with the Cherenkov photon signal rate. To ensure the rate of counts due to these effects is negligible, the amplitude of the induced signal must be lower than the trigger threshold in the associated pixel. As described in Sect. 2.6, the largest cross-talk signals are caused by the sharing of the charge among adjacent pixels during the multiplication chain. In this case, the amplitude of the cross-talk signal is ∼5% of the height of that due to an event. Given these results, in the worst case condition, assuming the trigger threshold in each pixel of an EC has been set in the valley between the pedestal and the single photon peak, only 1% of the single photon signals is expected to be large enough to induce a triggered spurious event in the associated pixel.
The effects described above are ascribed to the photosensors. However, the amplitude of the cross-talk signal is also proportional to the stray capacitance between neighbouring electronic channels and to the CLARO input impedance. It is also important to keep low the input capacitance to ground since the electric noise and the rise time of a CSA increase proportionally to it. Hence, the length of the electrical path connecting the MaPMT anodes to the CLARO input should be as short as possible. This consideration guided the choice to keep the number of channels per chip low, so that shorter connections, with a stray inter-channel capacitance of ∼0.2 pF, can be used. The baseboard (BsB) was also designed to fulfill this requirement and contributes ∼0.2 pF to the total capacitance between neighbouring channels. The contribution of the CLARO is expected to be negligible. Summarizing, the total capacitance between the inputs is of the order of ∼0.5 pF. The total input capacitance to ground was measured to be ∼ 10 pF, given by the sum of three components (BsB, FEB and CLARO), contributing to about 2.5-3 pF each. Another parameter that has to be taken into account is the input impedance of the CLARO to which the cross-talk is proportional. For this reason, the ASIC was designed to have an input impedance of ∼ 100 Ω at low frequency, raising to ∼1 kΩ at high frequency. The goodness of the design choices has to be tested in a complete EC system. In particular, cross-talk probability and eventual effects of large noise were studied in a realistic operating condition, during the beam tests (see 2.9).

EC calibration

Two procedures have been designed to characterize and calibrate each channel of the EC. These procedures can be easily automatized and can be run in parallel on all the channels of the RICH detector, greatly reducing the time needed to perform the full system calibration.

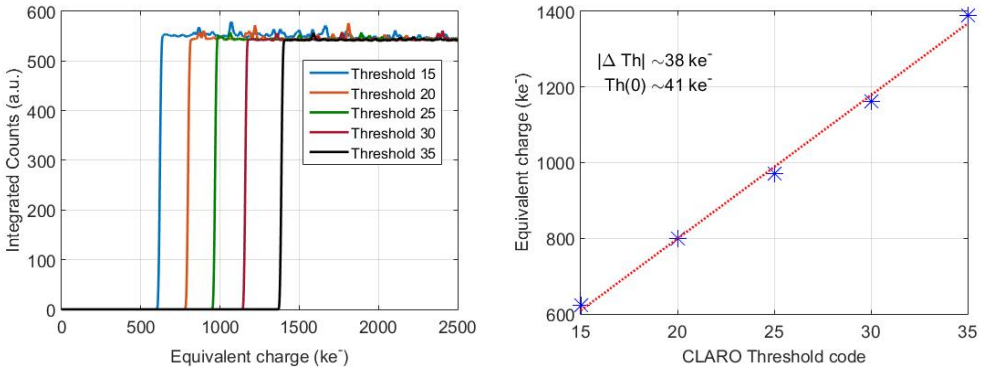

Figure 2.68: Procedure for the CLARO channel calibration, called *DAC scan*. On the left, the S-curves acquired by measuring the counting rate at a fixed threshold as function of the input signal generated by the DAC. Measuring the transition point at various threshold levels, the trigger step amplitude and the CLARO offset can be measured.

The first process, developed for the conversion of the trigger threshold levels into equivalent input electrons, is called *DAC scan* since it exploits an 10-bit Digital-to-Analog converter currently located on the EC backboard. Note that, in the final setup, a DAC output of the GBT-SCA chip mounted on the PDM-DB will be used instead. The DAC can deliver a settable DC value loading a 640 fF capacitor embedded in the CLARO chip. As the capacitance discharges, a known amount of charge (given by $Q(e^-) = CV/q$, where $C = 640$ fF, V the DAC voltage and $q = 1.6 \cdot 10^{-19}$ C) is injected at the CLARO input. Equivalently, the DAC voltage will determine the amplitude of the test signal with a conversion factor of 1 Me^-/250 mV. The calibration pulse delivery can be triggered via SPI (by setting a dedicated bit of the global configuration register) or giving an external trigger pulse at a dedicated CLARO pad. The configuration register of each channel is also equipped with a dedicated bit to disable the test pulse injection on a specific channel. Moreover, a global flag can be used to prevent the test pulse injection from either internal or external trigger.

The *DAC scan* calibration procedure follows these steps. After fixing the trigger threshold one wants to calibrate, the number of trigger events are measured as a function of the charge provided at the input. Ideally, if the charge is lower than the chosen trigger threshold, no events are counted by the CLARO. By gradually increasing the DAC signal, a larger amount of charge can be injected into the system; as soon as the calibrating signal is larger than the trigger threshold, then all the input pulses are counted. The number of triggered events as a function of the calibrating signal amplitude of an ideal system describes a step function. The electric noise of the real apparatus makes the calibrating pulse amplitude and trigger threshold fluctuate, so that the step curve is smoothed and results in the so

called S-curve (shown in Fig. 2.68, left side). The transition point of the S-curve gives the trigger threshold position express in equivalent input electrons, while the slope of the curve is related to the noise.

By repeating the procedure on all (or several) threshold values, one can correlate the threshold number to the corresponding equivalent charge. This relationship describes the linear trend reported in Fig. 2.68, right side. The slope of this line represents the average threshold step (nominally 30 ke^- at attenuation 1 V/V), while the y-intercept gives the offset. The gain and threshold step of each channel can be calibrated with a precision better than 20% at $\pm 3\sigma$, that is the spread in the value of the test capacitor. The residual spread is more than one order of magnitude smaller than the gain spread between MaPMT pixels. Note that such procedure allows also to check the linearity of the CLARO response on the whole dynamic. The procedure can be applied at various attenuation factor. By comparing the threshold step at different attenuation levels, the actual attenuation coefficient can also be measured. In summary, all the parameters describing the response of each CLARO channel can be studied without the need of any additional setup, thus allowing to use this method even in the full-system configuration.

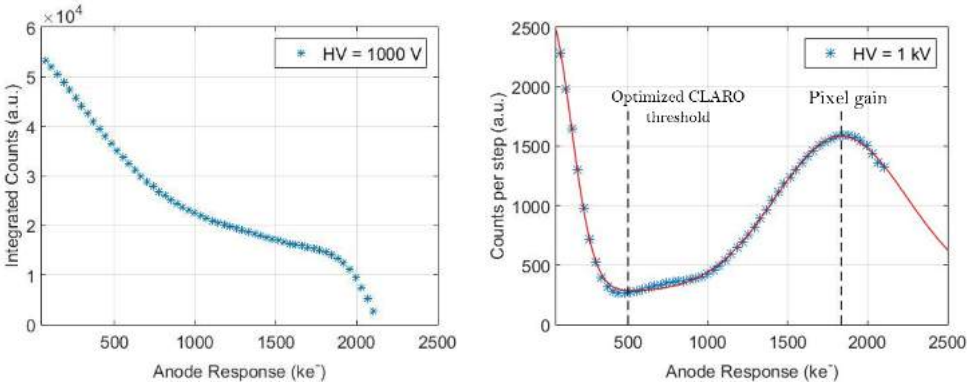

Figure 2.69: Procedure for the MaPMT calibration, called *Treshold Scan*. Providing a stable illumination level, the photon counting rate is measured increasing the trigger threshold. The curve shown on the left can be acquired. Taking the derivative of such curve, the single photon spectrum, shown on the right, can be measured. The gain and the position of the valley between the single photon peak and the pedestal can be measured for each anode.

The second calibration process is the *Threshold Scan* which gives the possibility to acquire single photon spectra in each MaPMT pixel, so measuring the gain of each MaPMT channel and allowing to optimize the CLARO trigger position. This procedure usually relies on a stable illumination level, so that the MaPMT is working in single photon regime with a stable rate of events in each pixel. Note that blue LEDs are available inside the

current LHCb RICH vessel for test and calibration purpose. A similar apparatus, able to illuminate all the sensitive pixels, is planned for the upgraded RICH detector. The MaPMT must be biased at the same level planned for the usual operation. Turning on the stable light source illuminating the MaPMT, the triggered photon rate is acquired as a function of the trigger threshold spanning the full system dynamic (30 ke^- step, 0-2 MeV range, for attenuation 1 V/V) or, the desired region of interest. The plot shown in Fig. 2.69 (left side) is thus acquired. Taking the derivative of such curve and flipping the sign, one obtains the single photon spectrum shown on the right side. Note that the x-axis can be expressed in e^- unit if the threshold values were previously calibrated with a DAC scan. The single photon spectrum allows to measure the gain of each pixel from the single photon peak position. In addition to that, the location of the valley between the pedestal and the single photon peak can be measured. As mentioned, this information is essential to properly adjust the trigger threshold in order to maximize the signal detection and spurious rejection efficiencies and, thus, compensate for the gain spread between pixels and devices.

2.9 Test-beam results

In order to test the full EC system in a more realistic environment condition, periodic studies of the EC operation in beam tests were performed. Unless otherwise noted, the results are referred to the measured acquired in Autumn 2014, since that was the test in which I was particularly involved to set up the system and, also, to the data analysis. The major part of the setup described has not been changed during subsequent beam tests, so that the results reported are similar to those obtained in more recent measurements.

Figure 2.70: Picture of the planoconvex lens used as Cherenkov radiator for the beam tests.

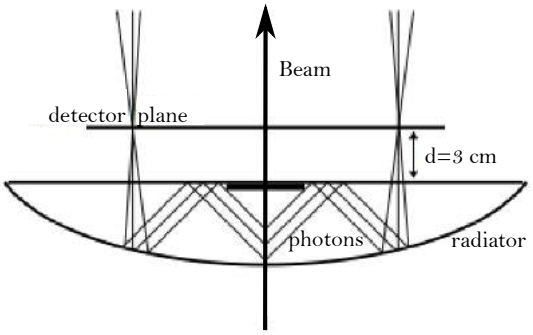

Figure 2.71: Scheme of the Cherenkov photon trajectories inside the radiator lens.

The beam used for the EC tests is provided by the Super Proton Synchrotron (SPS)

facility, North Area of the Prevessin site at CERN. A high energy beam, with well-defined momentum, mainly composed of 180 GeV/c protons and pions was used. The beam provides $\sim 10^6 \div 10^7$ particles per spill. The particles traverse scintillators that provide the trigger to the EC acquisition system. A telescope made of 8 planes of Timepix3 silicon pixel sensors [39,40] were used to reconstruct the trajectories of the particles. Downstream the tracking telescope, the beam passes through a light-tight box containing a planoconvex lens (shown in Fig. 2.70), in which Cherenkov photons are emitted. The radius of the lens has been measured to be $R = (144.6 \pm 0.1)$ mm and a thickness at the center of (27.0 ± 0.1) mm. A reflective annulus layer, 20 mm wide, was deposited on the spherical surface. Particles enter the lens at the middle of the spherical side producing Cherenkov photons which are reflected at the rear flat surface due to total internal reflection, as reported in Fig. 2.71. The photons are reflected again by the thin reflective layer deposited onto the spherical surface and exit from the lens at the flat surface. The photons are thus focused by the spherical lens to the photodetector plane, about 3 cm distant from the lens output surface. According to the simulation, the expected Cherenkov ring radius is ~ 60 mm with a spatial resolution of 0.6 mm, limited by the optical system and the MaPMT pixel size. Note that, given the large refractive index of the radiator ($n \sim 1.4$), the Cherenkov angle is always equal to the maximum saturated value $\theta = acos^{-1}(n^{-1})$; the test is intended to study the EC system and not to discriminate protons from pions. Two EC prototypes are located symmetrically, left and right of the beam center, along the horizontal diameter, so that only two arcs of the Cherekov ring can be detected. A picture of the setup used in the test-beam is shown in Fig. 2.72.
Only four of the available 8 MaPMT sockets were instrumented.

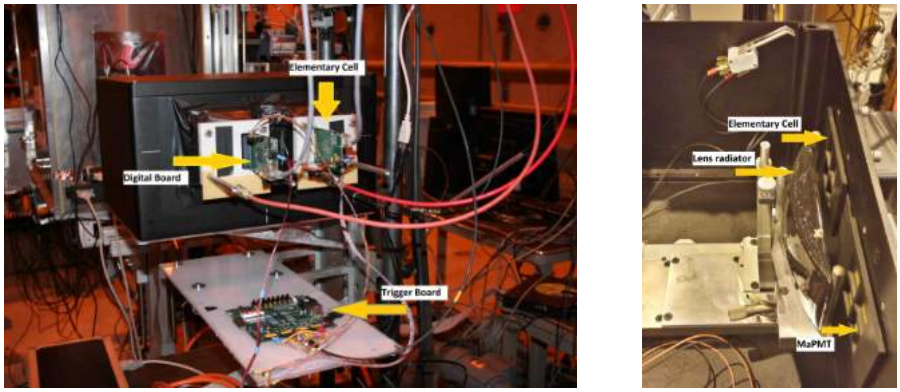

Figure 2.72: External and internal view of the box installed in the testbeam experimental area. Two half-populated ECs (2 MaPMTs and 128 channels each) are used.

The digital outputs of the CLARO are connected to a FPGA on the Digital Board (prototype), collecting events in response to triggers. The DB formats the data into multi-

event packets (MEP) and transmits them via Gbit Ethernet to a PC where they are saved. The Gbit Ethernet links are also used to configure the FPGA on the DB and the CLARO chips. The control of the data aquisition (DAQ) system is achieved using a Graphical User Interface (GUI). The GUI manages configuration parameters for the EC (such as the CLARO chip thresholds and attenuations) and provides run control functions. Triggers can be generated externally by beam particles (exploiting the scintillator detector place up and downstream the telescope tracking) or by an internal pulser. Triggers are only sent when the gate signals of all connected DBs are asserted in order to prevent buffer overflow at high trigger rates. One of the trigger outputs is sent to the beam telescope trigger board to provide synchronisation between the two systems.

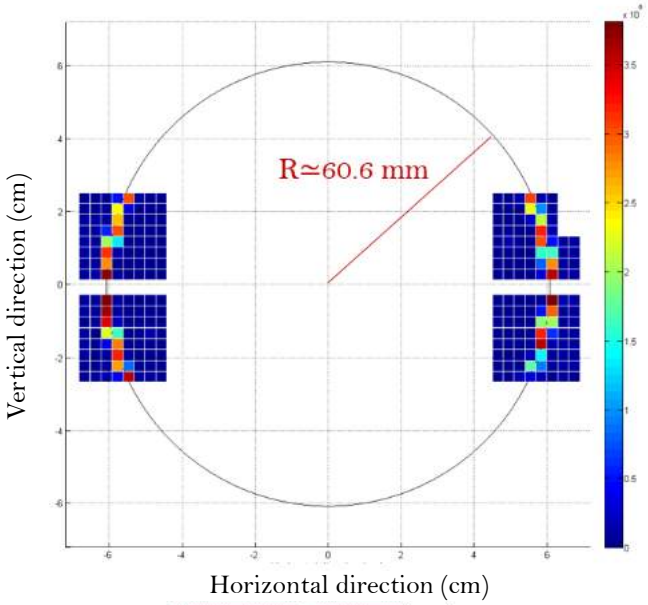

Figure 2.73: Cherenkov ring observed during the beam test. The plot is obtained integrating 10^5 events collected.

The system proved to be capable to detect Cherenkov photons. Figure 2.73 shows the Cherenkov ring obtained by superimposing the signals acquired in $\sim 10^5$ events. As it can be seen, the radius of the Cherenkov ring was measured to be $\simeq 60.6$ mm in agreement with that expected from the simulation. The circular fit superimposed to the measured data was obtains by minimizing the circle-to-data distance weighted by the number of hits per pixel, assuming a uniform distribution inside the pixel. A second analysis method to estimate the Cherenkov radius and the spatial resolution of the system exploits the saturation of the Cherenkov angle emission. In this case, each particle provides the same circular trace. The radius can be estimated separately for each triggered event and its distribution can be computed. In the case of saturated emission angle, the radius estimation

uncertainty is expected to be dominated by statistical effects. Figure 2.74 shows the results: a normal Gaussian trend describes the radii distribution. The center of the Gaussian function represents the average radius value (similar to the one shown in Fig. 2.73) while its width is the spatial resolution. A good spatial resolution of ~ 0.5 mm was achieved. Similar spatial resolution values can be obtained measuring the position of the beam center along the x-axis, while the position of the ECs with respect to the ring limits the resolution achievable on the y-axis as the ring is almost vertically oriented.

The EC calibration procedures have also been tested. The *DAC scan* process was executed to calibrate the CLARO trigger thresholds, for the attenuation value of 1 V/V. In addition to that, inside the light-tight box, a commercial blue led was placed and exploited to perform the *threshold scan* procedure. Single photon spectra in all the tested pixels were measured and the gain of each channel could be measured and turned out to be comparable to the reference values provided by the manufacturer. Furthermore, the CLARO trigger threshold of each channel was located in the valley between the pedestal and the single photon peak. In such configuration, the photon detection efficiency can be estimated by measuring the number of photons per event detected and comparing the experimental value with the expected value ($N_\gamma = 13.1 \pm 2.9$ photons per event detected in total to the whole system). The distributions of the number of hits per event is in agreement with the expectation, as reported in Fig. 2.75.

In the recent beam test of mid2016, the complete EC assembly allows us to measure the cross-talk probability and evaluate if the electronics chain causes an appreciable contribution to increase the unavoidable cross-talk due to photosensors (charge sharing effect). This can be done by looking at pairs or clusters of neighbouring active pixels during the same event in a region of the MaPMT far from the Cherenkov ring. Indeed, as the illumination rate of pixels off-ring is less than 1% of the total events and the dark count rate is extremely low, the probability of accidental coincidence between two neighbouring off-ring pixels is negligible. For these reasons, the coincidences are attributed to cross-talk. Using the binary data from the read out system it is not possible to distinguish which of the two neighbouring pixels induced cross-talk on the other, thus the number of cross-talk events was evenly split between the two pixels. Based on these assumptions the probability that the i-th pixel induces a cross-talk event on a neighbouring j-th pixel can be calculated as $P_{i \to j} \simeq (N_{ij}/N)/2$ where N_{ij} is the number of events where both i and j pixels are on and N is the number of events where at least i is on. The same calculation is done exchanging pixel j with pixel i, and the final cross-talk probability is the mean value of the two evaluations. Such analysis is extended to all the off-ring pixels, so that the cross-talk probability distribution shown in Fig. 2.76 was measured. The mean cross-talk probability is below 1%. As explained in Sect. 2.8, such contribution is compatible with that expected from the charge sharing effect. This implies that the electronics chain add a negligible contribution, proving the goodness of the design choices.

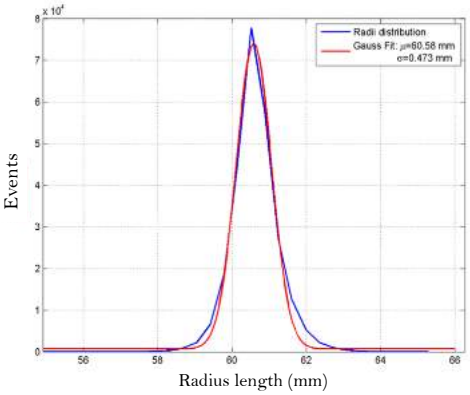

Figure 2.74: Cherenkov radius distribution, computed by fitting the Cherenkov ring for each triggered event. The ring radius is $R = (60.58 \pm 0.47)$ mm, in agreement with the simulation.

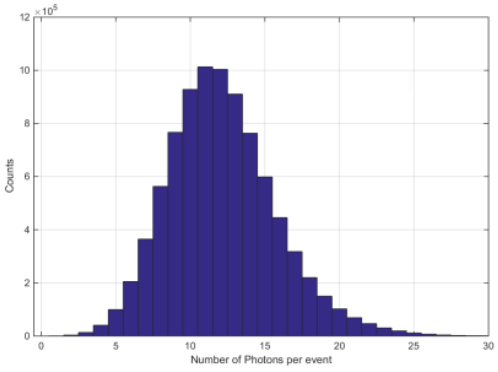

Figure 2.75: Distributions of the number of hits per event integrated in all the four MaPMTs.

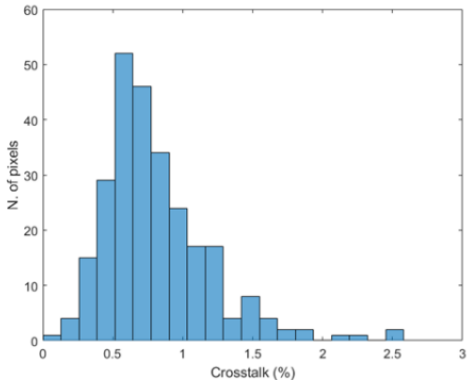

Figure 2.76: Cross-talk probability distribution calculated on all the off-ring pixels (preliminary results, beam test of 2016).

Being available a larger number of ECs, the beam tests of 2016 allowed to study the power supply system, the operating temperature of the various EC components, the cooling system performance and the optimization of the grounding reference for an increasing number of cells. The EC-H was also set up and satisfactorily tested. Lot of data, essential for the complete characterization of the system, have been acquired and the analysis is still ongoing. Further beam tests are foreseen to characterize the system even at the highest trigger rate condition.

Chapter 3

The CUORE Experiment

3.1 The CUORE Experiment

CUORE (*Cryogenic Underground Observatory for Rare Events* [41]) is a large scale experiment that searches the neutrinoless double beta decay $0\nu\beta\beta$ decay in ^{130}Te using a bolometric technique. As described in chapter 1, the experimental observation of such rare decay would represent the first experimental evidence of leptonic number violation, demonstrate the Majorana nature of the electronic neutrinos and allow to estimate the effective mass of the electronic neutrino and the neutrino mass hierarchy. In order to push the experiment sensitivity to explore the inverted hierarchy neutrino mass region, which corresponds to a sensitivity of $|\langle m_\nu \rangle|$ smaller than 50 meV, large mass and long live-time observations are needed. The CUORE detector will consist of an array of 988 TeO_2 bolometers arranged in a cylindrical configuration of 19 towers, each made from the assembly of 4 columns of 13 crystals each, so that a single tower hosts 52 cubic bolometers, $5 \times 5 \times 5$ cm^3 each. The excellent performance of such crystals was already demonstrated by the pilot experiment CUORICINO [42–46]. Reproducibility was tested, the pulses amplitude was in agreement with the thermal model and the energy resolution of $\simeq 1$ keV FWHM for low energy gamma peaks and $\simeq 8$ KeV FWHM at the 2615 keV background Tallium γ line was achieved [43].

3.1.1 Experiment location

CUORE is one of the experiment located at the underground National Laboratories of Gran Sasso (LNGS, L'Aquila, Italy). In particular, the cryostat hosting the CUORE bolometers is placed in the LNGS Hall A, a cave with a length of about 100 m and height above 18 m, for an overall volume exceeding 180000 m^3 (Fig. 3.1). These laboratories are situated at 150 Km North-East of Rome and are directly accessible by means of the 10 km highway tunnel passing through the Gran Sasso mountain. This unique characteristic makes feasible

to pick large experimental setup underground. The average dolomitic rock covering the experimental area is 1400 m, or 3700 m.w.e. (meter water equivalent). In the experimental area, the measured fluxes of muons, γ-rays and thermal neutrons are: $\Phi_\mu = (1.5 \pm 0.06) \cdot 10^{-6}$ $\mathrm{sr^{-1}s^{-1}cm^{-2}}$ [47, 48], $\Phi_\gamma \sim 1$ $\mathrm{s^{-1}cm^{-2}}$ [49] and $\Phi_n = (1.08 \pm 0.02) \cdot 10^{-6}$ $\mathrm{s^{-1}cm^{-2}}$ [50].

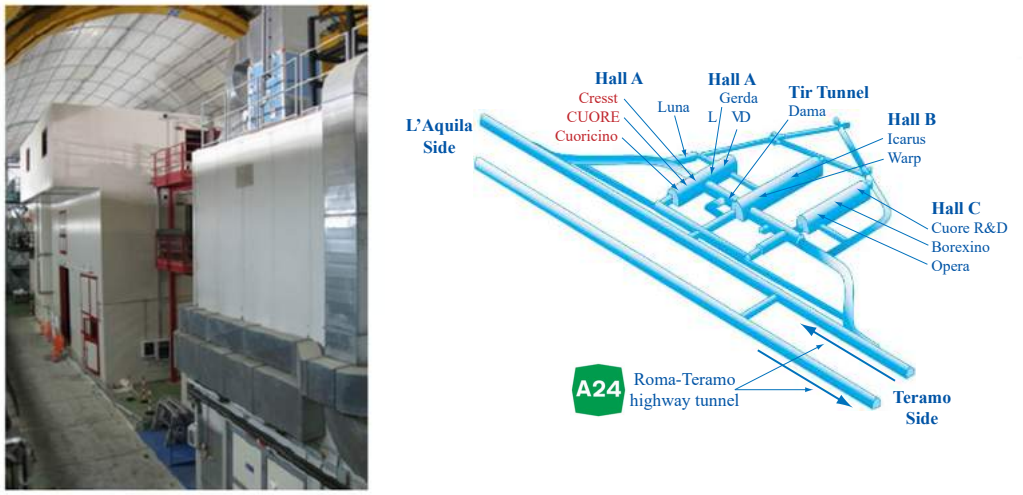

Figure 3.1: LNGS location and a picture of the CUORE hut.

3.1.2 Bolometer technique

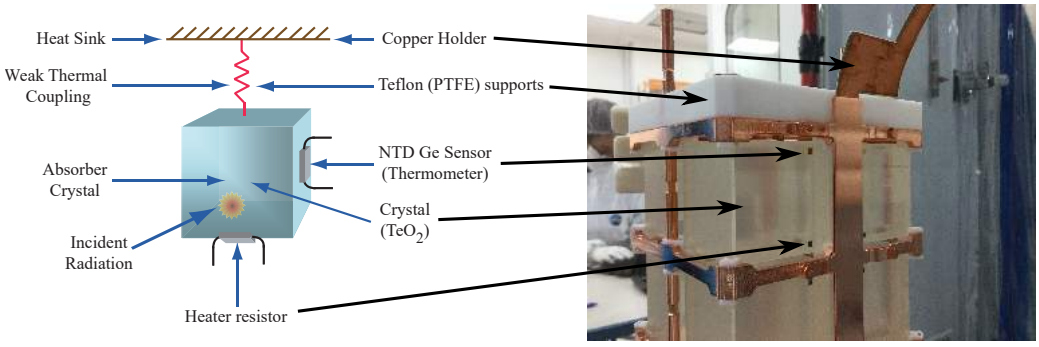

Figure 3.2: Simplified scheme and a picture of a bolometer CUORE detector. The sensitive crystal is weakly coupled to the thermal bath through an insulating Teflon frame. The NTD thermistor and the heater resistor are also pointed out.

The use of bolometers as rare events detectors for the double beta decay measures, was firstly suggested by Professor E. Fiorini in 1984 [51]. Bolometers are low temperature calorimeters where the energy released in the absorber crystal by an interacting particle is converted into phonons and detected as a temperature increase. Unlike the widely used spectroscopic technique based on the detection of the energy converted into excitations and

ionization of the detector atoms, which roughly corresponds to the 30% of the whole energy released by the impinging particle, the bolometers are sensitive to the phonon channel. This is a great advantage since in principle bolometers can absorb the phonons ($E_{ph} \sim 1$ μeV at the operating temperature of 10 mK) produced both from the primary interaction and from the relaxing of the ionizing channel, being sensitive to the whole energy delivered (assuming that no electric field for the charge collection is applied and neglected radiative emission). The base blocks composing a bolometer detector are shown in Fig. 3.2. The sensitive crystal, made of TeO_2, is weakly thermally coupled to the reference thermal bath by means of supports made of Teflon. This reference allows to restore the bolometer baseline temperature after each event, but is weak enough to let the detector heating up after a particle interaction. The thermal conductivity of such supports is labeled as G. In order to detect the thermal increase due to an interaction, each bolometer must be equipped with a sensor able to convert the temperature increase into a detectable electric signal. CUORE employs Neutron Transmutation Doping (NTD) thermistor, whose operating principle is described in the following sections. A heater resistor is also thermally coupled to the bolometer and, as described in detail in section 3.5, allows to provide a reference signal for the detector response stabilization.

There are two main advantages which make bolometers particularly suitable for the search of $0\nu\beta\beta$ decay:

- **Excellent energy resolution**: bolometers achieves an excellent intrinsic energy resolution with respect to that of most particle detectors [52]. The thermal energy of a solid crystal can be expressed in terms of quantum particles, the phonons, each having an energy $E_0 = k_B T$, where k_B is the Boltzmann's constant and T the temperature of the crystal. At usual temperature, we can associate a phonon to each atomic oscillation mode with respect to its equilibrium position. At macroscopic level, it is useful to define the crystal thermal capacitance C as the ratio between the crystal energy and its temperature, so that $E = CT$. The thermal energy of the crystal fluctuate due to the Poisson statistics regulating the number N of excited phonon ($N = E/E_0$), so that the relative standard deviation is approximated by $dE/E \sim 1/\sqrt{N}$. Thus:

$$dE \sim \frac{E}{\sqrt{N}} = \sqrt{EE_0} = \sqrt{CK_B}T \tag{3.1}$$

  Equation 3.1 states that the thermal energy of an absorber shows an intrinsic and irreducible fluctuation proportional to the crystal temperature and to its thermal capacitance. As a consequence, to enhance the energy resolution, it is necessary that the absorber operates at deep cryogenic temperature, close to 10 mK. Moreover, if the absorber is insulating, diamagnetic and dielectric, then its thermal capacitance rapidly

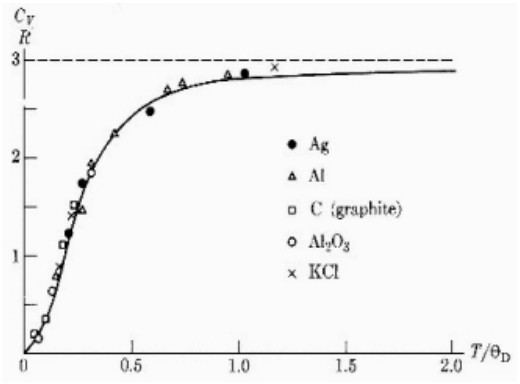

$$C(T) = k_B N_T \frac{12\pi^4}{5}\left(\frac{T}{\theta_D}\right)^3$$
$$k_B = \text{Boltzmann constant}$$
$$N_T = \text{Total number of atoms} \qquad (3.2)$$
$$\theta_D = \text{Debye temperature}$$

Figure 3.3: Thermal capacitance of several materials as a function of temperature. The Debye law well fits the experimental data.

decreases close to zero for temperatures lower than the so called Debye temperature θ_D, characteristic of the absorber material. Indeed, the thermal capacitance of such materials as a function of the temperature (for $T < \theta_D$) follows the Debye low, reported in Eq. 3.2 and Fig. 3.3.

Cryogenic temperature allows to accomplish energy resolutions of few keV (similar to that achieved by CUORICINO [43]) since the thermal capacitance reduces to few tens of pJ per mole. Note that, unlike the usual solid state detectors, the energy resolution does not depend on the interacting particle energy. Indeed, a particle of energy $E = 1$ keV causes a temperature increase of the order of few μK with a energy fluctuation of $dE = \sqrt{E_0 E} = \sqrt{k_B T E} \sim 30$ meV, totally negligible compared to intrinsic energy resolution of the bolometer.

- **Wide choice of materials**: as mentioned, the absorber material does not need to satisfied any particular requirements, unlike solid state detector which must be made of semiconductors. In principle, any insulator with a good thermal conductivity can be used as sensitive detector in a bolometer measurement. This wide versatility is very important in the case of $0\nu\beta\beta$ research since it can allow to develop architectures where the signal source coincides to the detector. Such configuration maximize the detection efficiency with respect to the geometrical acceptance. Moreover, a cross check between bolometers made of different compounds and decaying via various $0\nu\beta\beta$ channels can be performed. A description of the isotope selection criteria is provided in the next section.

- **Active area**: in principle a bolometer does not have dead layers, so that the whole detector area is fully sensitive.

The bolometer response is well described considering an equivalent electric circuit where the thermal power is depicted as an electrical current and the temperature (referred to

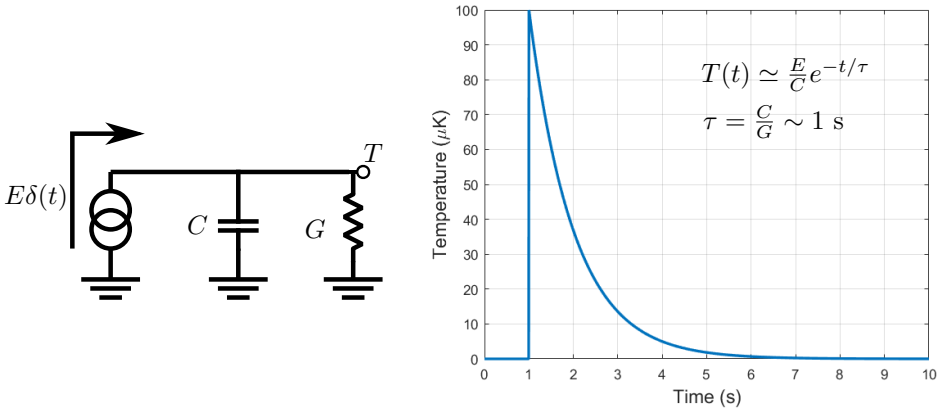

Figure 3.4: Equivalent electric circuit simulating the bolometer response. Ground reference is the thermal bath, C the crystal thermal capacitance, G the thermal conductivity to the thermal bath and the $\delta(t)$) current source represents the thermal power injected by an interacting particle. A typical temperature pulse as a function of time is depicted on the right.

the thermal bath baseline value) is the voltage drop with respect to ground. In such a parallelism, the response of a bolometer can be easily studied by schematizing the detector as a thermal capacitance (C) in parallel to a weak thermal conductance (G) with respect to the thermal bath (ground). An interacting particle releases in a very short time a certain energy E, so that, in time domain, the signal thermal power at the input of the equivalent circuit is $P(t) = E\delta(t)$. The bolometers behaves like an integrator circuit and the temperature signal shows a typical exponential shape with an amplitude equal to E/C and a slow thermalizing tail whose characteristic time is $\tau = C/G$. As a rule of thumb, the CUORE macro-bolometers work at the baseline temperature of $T_0 \sim 10$ mK, condition in which they have a thermal capacitance $C \sim 1$ nJ/K and a thermal conductance to the thermal bath $G \sim 1$ nW/K. This means that an interacting particle releasing $E = 1$ MeV to the bolometer would cause a temperature pulse of ~ 100 μK. The baseline temperature is recovered with a characteristic time of the order of $\tau \sim 1$ s. In this evaluation the effect of the electrical power on the time evolution of the signal has been neglected.

3.1.3 Isotope choice

A figure of merit of the bolometer technique consists in the wide versatility, so that various materials fulfill the experimental constraints in term of low thermal capacitance and good thermal conductivity. The choice of the isotope under study is aimed to the maximization of the experimental sensitivity, as described in chapter 1, Eq. 1.13. Several features have to be taken into account and guided to the choice of the ^{130}Te as good candidate for the research of the $0\nu\beta\beta$ decay, following listed:

- **Isotopic Abundance**: the sensitivity of a $0\nu\beta\beta$ experiment (except those that can be treated as zero-background experiment) is proportional to the square root of the number of nuclei candidate to decay, i.e. to the square root of the detector's mass multiplied by the isotopic abundance of the candidate. In small scale experiment, the natural isotopic abundance can be increase undergoing the crystal to a very expensive enrichment procedure. Nevertheless, the costs would be hardly affordable for large scale experiments such as CUORE. It is thus important to select an isotope with high natural isotopic abundance in order to avoid the need of enrichment procedures. The isotope ^{130}Te is an optimal choice since its isotopic content in natural tellurium is i.a = 34.50% [53].

- **Transition energy**: the Q-value of the $2\nu\beta\beta$ decay is very important parameter because of its relation with the natural radioactivity background. In the case of the ^{130}Te, the $2\nu\beta\beta$ decay is described by the following transition:

$$^{130}\text{Te} \rightarrow ^{130}\text{Xe} + 2e^- + 2\overline{\nu} \;\rightarrow\; Q = (2530.3 \pm 2.0)\,\text{keV} \tag{3.3}$$

  The Q-value of ^{130}Te is located in a clean energy windows, between the photoelectric peak and the Compton edge of the 2615 KeV line of ^{208}Tl produced by the natural ^{238}U decay chain.

- **Phase space**: the parameter $G^{0\nu}$ is the element of phase space of the transition. This represents the pure kinematic contribution to the decay process and can be exactly calculated with a multidimensional integration in the nuclear phase space. For a $0\nu\beta\beta$ decay, $G^{0\nu} \propto Q^5$, so the higher is the Q-value, the bigger is the probability for the decay to occur. The quite high $0\nu\beta\beta$ Q-value of the ^{130}Te contributes to enhance the experiment sensitivity.

- **Nuclear dynamics**: as shown in the previous chapters, the life time for $0\nu\beta\beta$ decay is inversely proportional with the matrix elements $|M^{0\nu}|^2$, whose values are model dependent and different from one nuclide to another. In most of the nuclear models used to compute the matrix elements (for example RQRPA and QRPA methods [54, 55]) the nuclear structure factor of ^{130}Te is reasonably high and larger than that of other competitive nuclide, such as ^{76}Ge.

Despite all these positive features, pure tellurium is not the best choice to perform a bolometric experiment. Instead of it, CUORE opted to use crystals made of Tellurium dioxide. This choice was motivated by the following considerations:

- **Debye temperature**: Tellurium is a metalloid, so that its thermal capacitance does not scale proportionally to T^3. On the contrary, TeO_2 crystals, being dielectric and diamagnetic material, have only the lattice to contribute to the specific heat, so that

the thermal capacitance obeys to the Debye law. Moreover, the Debye temperature θ_D of the tellurium dioxide is higher than of pure Te and so, at the same temperature, the former has a lower specific heat according to Eq. 3.2. Hence, higher pulses and better signal-to-noise ratios can be achieved [56].

- **Mechanical properties and radiopurity**: although pure Te has poor mechanical properties and breaks after few thermal cycles, large crystals of TeO_2 can be grown with excellent mechanical properties. In addition to that, an excellent radiopurity can be accomplished even in large scale experiments. In particular, the CUORE crystals has a level of impurities of ^{232}Th and ^{238}U lower than 1 pg/g.

- **Compound mass**: the tellurium dioxide mass is dominated by the tellurium, which contributes by about 80% to the overall crystal mass. Thus, the choice of using TeO_2 crystals instead of pure Te absorber does not causes a dramatic reduction of the effective mass under study.

3.1.4 Thermistor operation

The phonon sensors are devices thermally coupled to the bolometer which are responsible to collect the phonon and convert them into the electric signal to be amplified, filtered and acquired. In order to be sensitive to the small temperature increase due to a single particle interaction and ensure an adequate energy resolution, the phonon sensors must show a steep slope of their resistivity as a function of the temperature at the working point. There are two main phonon sensor classes: the *Transition Edge Sensors* (TES) and the *Semiconductor Thermistors* (ST). The latter sensor is easier to use since it can be glued to the bolometer without the need of complex serigraphy process, as requested in the case of TES. STs are intrinsically slow, so that they are sensitive mainly to thermal phonons.
The sensors used for CUORE are Neutron Transmutation Doping Germanium thermistor (NTD-Ge thermistor). Such fabricating technique, consisting in irradiating the whole Germanium wavers with thermal neutrons at a nuclear reactor in order to induce nuclear reactions and creates dopant inside the Germanium. The concentration and the dopant distribution can be controlled by changing the flux of the neutron irradiation. This technique allows to accomplish an uniform dopant distribution down to the atomic level. A doped semiconductor near absolute zero can behave as insulator or a metal, depending on whether the level of implanted dopant is larger than a critical concentration. Around such doping level, the operating regime is called *metal-insulator transition region* (MIT) [57]. At the baseline temperature ($T \sim 10$ mK) and for semiconductors doped slightly below the MIT level, the resistivity of the thermistor strongly depends on the temperature, as the electric conductance is allowed by charges migrating from one impurity site to the

others via phonon mediated tunnel effect (hopping phenomenon [58, 59]). In particular, the thermistor resistance as a function of the temperature can be expressed as:

$$R_{bol}(T) = R_0 e^{\sqrt{\frac{T_0}{T}}} \tag{3.4}$$

where R_0 and T_0 are parameters depending on the doping concentration.

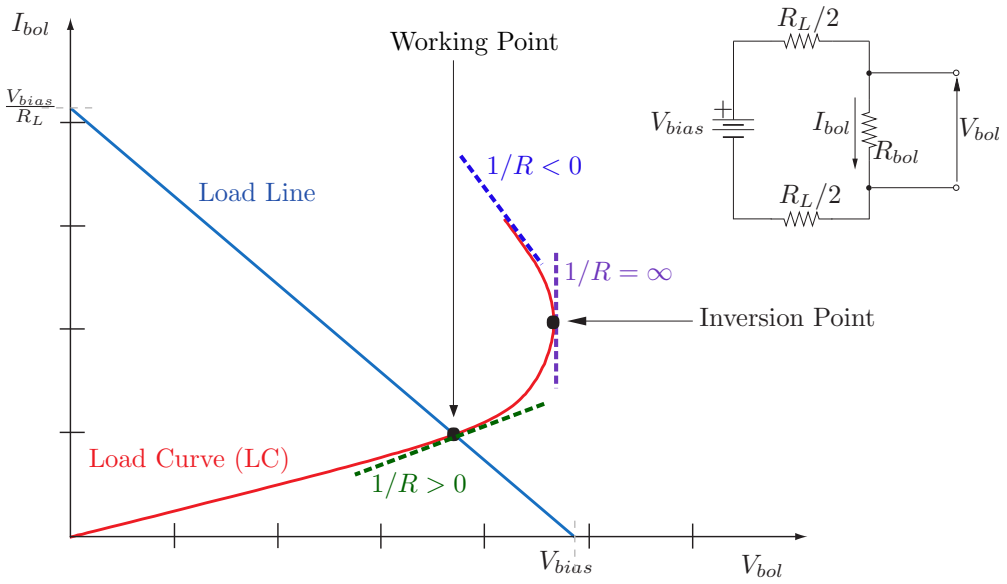

Figure 3.5: NTD thermistor characteristic curve (load curve). The working and inversion point are pointed out. The working point is given by the intersection between the NTD load curve and the constant current injected from the biasing system.

It is important to stress that, being a semiconductor resistor, the NTD resistance increases going to lower temperatures, i.e. $R_{bol}(T)$ has a steep negative slope. The temperature pulse due to a particle absorbed into the bolometer, can be measured as a dynamic reduction of the R_{bol}. In order to measure it, one cannot fix the voltage drop across the NTD and read a current variation (as usually happens for solid state detector) but, instead, one must force a stable current flowing through the NTD and measure the voltage drop, proportional to the dynamic resistance value. The thermistor dissipates power, given by the product between the current I_{bol} flowing through it and the voltage drop V_{bol} across it. Moreover the temperature of the thermistor, in equilibrium with that of the bolometer, is intentionally allowed to change, as a very small thermal conductance G to the heat sink is provided. Thus, unless for a negligible power dissipated in the thermistor, R_{bol} depends on the base operating temperature T, the static biasing working point (which contribute to increase the working temperature by $I_{bol}V_{bol}/G$) and on the dynamical variation of the

power consumed due to the particle signal. The electrical and thermal properties of the bolometer are thus closely related with a mechanism known as *electrothermal feedback* [60]. The dynamic NTD impedance as a function of the working point due to the electrothermal feedback is shown in Fig. 3.5, usually referred to as load curve. As the thermistor has a negative thermal coefficient, a stable working point is reached by biasing it with a constant current, since a larger value for R_{bol} would result in a larger power dissipation $R_{bol}I_{bol}^2$ by the bias current and the consequent larger temperature forces a smaller value for R_{bol}. If, on the contrary, the thermistor would be biased with a constant voltage, then the sign of the electrothermal feedback results to be positive, making the working point unstable. The easiest way to implement the current generator biasing the NTD is using a stable voltage reference V_{bias} and a couple of matched loading resistors $R_L \gg R_{bol}$. As shown in Fig. 3.5, the NTD working point is given by the intercept of the load curve to the load line.

3.2 Overview of the electronic system

My PhD work has been mainly focused on the hardware and firmware design, production, optimization and test of the CUORE electronic system. In particular, my contribution has been specifically devoted to the production of the HUB mediating the communication between the slow control and the electronic system, the managing of the DCDC power supply system, the development of a digital board to protect and monitor the linear power supplier and the study and design of the calibrating pulser board. These works will be presented in the next sections. In order to better understand the context in which such devices are expected to work, a brief overview of the electronic system used in the CUORE experiment is provided.
Beside the pulser calibration board (described in Sect. 3.5), the electronics of CUORE [61–64] is composed by three main parts, following presented. The whole system is fully configurable by remotely via optical fibers and equipped with monitoring and debug tools to trace back the status of each board. These features are extremely useful in large scale experiment because they give the possibility to develop automatic scripts for the system configuration and monitor.

3.2.1 Power supply chain

The primary goal of the power supply chain [65] is to provide stable and low noise reference voltage levels biasing the rest of the system. The chain consists of three stages, as shown in Fig. 3.6:

- **AC/DC converter**: the first stage of the power supply chain exploits 5 commercial Lambda programmable AD/DC converters, from TDK. This commercial device, directly connected to the 230 V, 50 Hz AC power source, is able to provide a stable

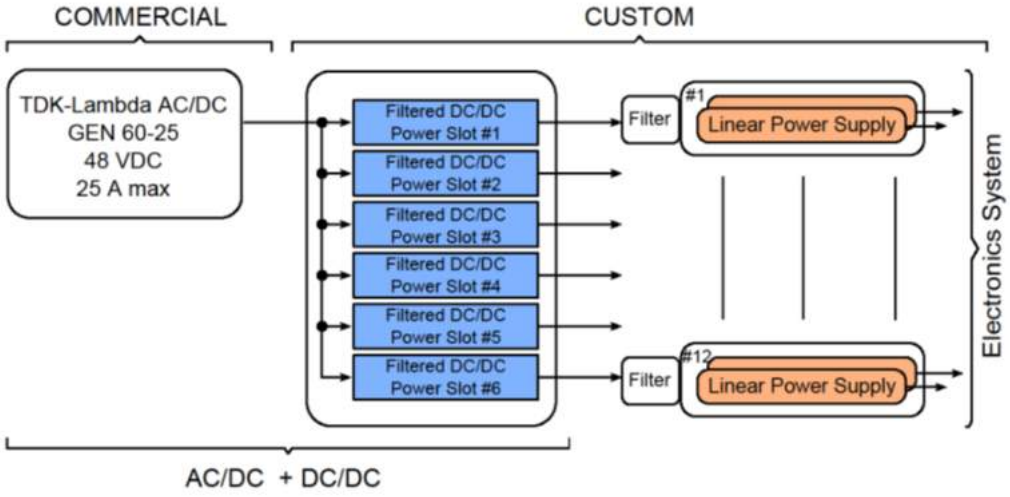

Figure 3.6: Scheme of the power supply chain of the CUORE experiment.

48 V DC voltage level, up to 25 A and moderate ripple noise ($\sim$ 60 mVpp). In order to prevent long-term issue (i.e to increase the mean time between failures, MTBF), the suppliers are maintained at about half of the maximum power suggested by the manufacturer. The four devices can be daisy chained and controlled from the slow control system by means of a commercial USB-to-Serial optical decoupler. Each AC/DC converter supply a whole DC/DC cage. The AC/DC boards are placed on the top of two racks in the CUORE hut, 2nd floor, above the DC/DC converters, outside the Faraday cage.

- **DC/DC converter**: the second stage of the power supply chain is the DC/DC board, specifically designed in the Milano Bicocca University for the use in the CUORE experiment. Every DC/DC can convert the 48 V input (from the AC/DC) into 3 programmable floating channel outputs. The first two channels represent a differential reference pair able to provide the analog power to bias either the Bessel filters ($\pm$12 V) and the linear power suppliers ($\pm$9 V). The third channel is used to generate the single-ended digital power ($\pm$6 V). Each DC/DC is equipped with an additional digital board based on the use of the LPC2368 ARM7 micro-controller, from NXP. The additional board mediates the communication to the slow monitoring system (via CAN bus protocol), is capable to set and measure the output voltage delivered by each channel and the operating temperature. The micro-controller iteratively adjusts the desired output voltage in order to ensure the best accuracy. The DC/DC are hosted by 4 cages, of 5 board each, located in the CUORE hut, 2nd floor, outside the Faraday cage. The DC/DC outputs are connected with a 10 m, double shielded power supply cable driving the bias toward the front-end boards, inside the Faraday cage. Such a long cable has a non-negligible inductance ($\sim$ 10 μH)

which is energized during the usual operation. In case of sudden and unwanted shorts at the end of the connection cable, the energy stored in the inductance discharges causing large overvoltages (up to 80 V) that might damage the apparatus. To prevent this issue and absorb the dangerous energy eventually injected in case of shorts, low-pass filters are set up just before the linear power supply. The AC/DC, DC/DC and filter chain, has a remarkably low noise performance: a clean noise spectrum, with no peaks due to the switching frequency and a RMS value of ~ 40 μV from 10 Hz to 100 MHz was measured. Such results can be achieved for all the boards over the entire production lot.

- **Linear Power Supply (LPS)**: the linear power supply board is fed by the DC/DC analog output signal and provides the reference voltage used to bias the NTD thermistor. Extremely low noise, minimal thermal drift, high reliability and over-power protections are the most important features that the LPS must fulfill. A pair of boards, located at the front-end cage side, are used to bias a complete front-end crate. In order to minimize noise injection through the power supply rails, two Linear Power Suppliers are also used to bias the pulser boards. More details about the LPS board are provided in section 3.4.

Two 2231A-30-3 power suppliers, from Keithley, are also available to provide an auxiliary ± 30 V power rail to the front-end boards. This device are remotely controllable from the slow control system through two USB-to-Serial optical decouplers and are located near the AC/DC converters. These additional power sources are used to bias the front-end output buffers at the highest detector biasing levels. Since their are not used as reference signals, the performance of such commercial devices are good enough to match the experimental constrains.

3.2.2 Front-End Boards

The front-end board is responsible of three main tasks:

- **Detector bias**: as mentioned, since the thermistor resistance decreases with respect to the operating temperature, then a stable working point can be reached by biasing the detector with a fixed current flowing through it. The circuity designed for the thermistor bias is shown in Fig. 3.7. The reference ± 5 V level, provided by the LPS, feeds an output buffer stage. Exploiting the auxiliary power provided by the 2231A-30-3 Keithley suppliers, the bias can be increased up to 30 V. This voltage signal is converted into the desired fixed output current by the output resistive load, that can be set to $R = 5 + 5$ GΩ or $R = 30 + 30$ GΩ. In both cases, $R \gg R_{bol}$ so that the bias circuit well approximates an ideal DC current source. Moreover, the wide current range available allows to accommodate for the large mismatches between

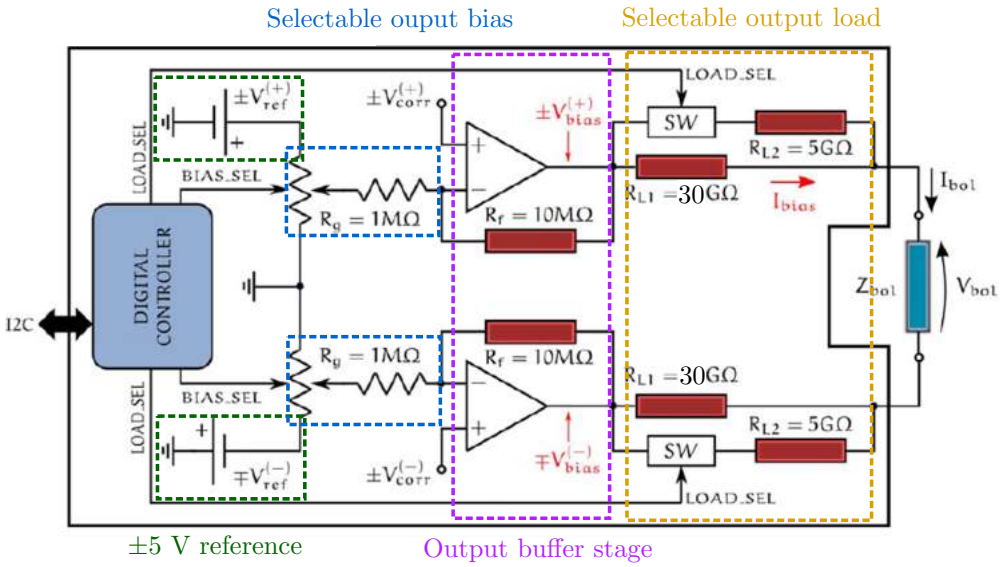

Figure 3.7: Simplified scheme of the circuitry devoted to the detector bias (front-end board).

the thermistor characteristic curves. In order to compensate for possible mismatches between the positive and negative side, the output pin polarities can be inverted in order to flip the bias current direction. The average result is independent of any eventual offset, which can thus be measured and compensated in each channel. The buffer outputs can also be disconnected from the detector and referred to ground by means of a 2 MΩ resistor at both inputs. This feature is particularly useful to test and calibrate the preamplifier performance

- **Voltage pre-amplification**: the pre-amplification stage [66] is mounted on a dedicated PCB placed upon the front-end board, very close to the input pins. This stage consists on a fully differential voltage sensitive pre-amplifier (DVP) based on a JFET input differential pair DC coupled to the NTD thermistor. Compared to a single-ended configuration, the amplifier noise increases by a factor 40%. On the other hand, common mode noise, is largely suppressed since it induces the same signal at both inputs. In addition, the fully differential configuration is effective in the suppression of the cross-talk induced among neighbouring channels, due to the capacitive coupling between the adjacent electrical paths of the flat cable driving the signal from the NTD to the front-end. The JFETs and their working point were studied and optimized to minimize the series and parallel noise contribution, especially in the low frequency bandwidth of interest (from 1 to few tens of Hz) [67]. In particular, the typical input referred white noise amounts to ~ 3.5 nV/$\sqrt{\text{Hz}}$. Also the low frequency noise is extremely low and typically amount to less than 7

nV/$\sqrt{\text{Hz}}$ at 1 Hz. Thus, the average RMS noise (up to 120 Hz) referred to the input is less than 40 nV/$\sqrt{\text{Hz}}$. The preamplifier gain can be set to $\sim$ 30 V/V or $\sim$ 200 V/V, so that the relative weight of the second stage noise contribution is less critical with respect to the pre-amplification stage. The DVP gain must show a high thermal stability, since any drift of the gain, would result in a bolometer baseline shift that would be wrongly interpreted as a bolometer operating temperature variation. A circuit, based on a diode that serves as a thermometer and a 8-bit trimmer (coarse correction) and a 12-bit ADC (fine correction), has been developed to compensate for the thermal drifts. Each pre-amplification underwent a thermal calibration. The outcomes were saved into the on-board EEPROM memory. The firmware exploits them to compensate for the thermal drift and keep it below 170 nV/°C.

- **Variable gain amplification**: the outputs of the pre-amplifier in connected at the differential inputs of the programmable gain amplifier (PGA), which is the second stage of the analog signal processing chain. The gain of this stage can be selected from 1 V/V up to 4096 V/V with 12 bits of resolution.

Each front-end board hosts 6 independent channels, so that 170 cards are required to read the 988 CUORE bolometers. The boards are divided in 14 card cages, each hosting 13 front-end boards at most and 2 LPSs. 2 cages compose a front-end tower and the 7 needed towers, 5 of which host also the pulser board cages, are placed on the top of the cryostat close to the connections coming from the link to the detectors. In order to prevent that low frequency electromagnetic interference (especially the 50 Hz from the main line) deteriorates the noise performance of the apparatus, a Faraday cage made of Skudotech (a very high permeability metal alloy) has been designed to contain the whole front-end circuitry. The cage has been designed and tested to reduce the 50 Hz electromagnetic field by 2 orders of magnitude.

3.2.3 Bessel Boards

The differential signal processed by the front-end board is driven at the input of the the Bessel filter board the last analog amplifying stage. Each board hosts 12 fully differential channels, so that 7 card cages each equipped with 13 boards at most were set up to read all the CUORE channels. The Bessel board crates are located outside the Faraday cage, in two cabinets close to the DAQ system. Since the specification about the noise and stability of the power supply are much less critical than that of the front-end circuit, then the Bessel board are powered directly from the DC/DCs. The custom designed CUORE Bessel boards consists of a six-pole active low-pass filter which shows a roll-off of 120 db/decade. Since macro-bolometers are slow detectors, the primary aim of the Bessel board is to optimize the signal bandwidth to the range of frequency of interest and cutting-off all those frequencies which contribute to spoil the noise performance. In this way, the signal-to-noise

ratio is maximized. Moreover, the Bessel board also acts as anti-aliasing filter placed at the downstream of the analog signal processing and just before the digitalization system. The Bessel filter was chosen since it maximally preserves the wave shape of filtered signals in the passband. A n-order Bessel low-pass filter is characterized by the following transfer function:

$$H(s) = \frac{\theta_n(0)}{\theta_n(\frac{s}{\omega_0})} \qquad \text{where} \qquad \theta_n(x) = \sum_{k=0}^{n} \frac{(2n-k)!}{(n-k)!\,k!} \cdot \frac{x^k}{2^{n-k}} \tag{3.5}$$

where $\theta_n(x)$ is a *reverse Bessel polynomial* and ω_0 is the cutoff frequency. The six-poles filter is implemented as a cascade of three 2-poles filters, properly tuned to obtain the desired overall transfer function. Likewise all the other electronic cards of CUORE, the Bessel board is equipped with a micro-controller responsible to enable/disable the filter, select the cut-off frequency among 4 available values (from 15 to 120 Hz, 4 Hz step) and overview the board operation. The filtered differential signal is finally ready to be continuously acquired by the commercial DAQ system, from National Instrument, and stored for the off-line trigger and analysis.

3.3 Remote Control Communication

As briefly introduced in the previous sections, the whole electronic apparatus was designed to be fully monitored and settable from a remote slow control system. The communication between each device and the central slow control system is based on a 100 kbit/s CAN (Controller Area Network) bus protocol. The CAN is a multi-master serial bus designed to allow the communication between two or more devices (called nodes) sharing the same two-wire line. All the nodes are able and allowed to send and receive messages to/from the bus, but not simultaneously. Each node is uniquely defined with a 11 (standard) or 29 (extended) bit identifier (ID). Each CAN message is tagged by a ID preceding the payload and coinciding to the ID of the node involved in the communication. The ID also represents the priority of the message. In the CUORE experiment, the extended CAN ID is used and its value is defined from the typology and location of the device sharing the bus, as shown in Fig. 3.8. Beside the ID, each CAN message is composed of a 8-byte payload and several control bits for the node synchronization and for checking the signal integrity.
The choice to use the CAN bus protocol has been guided by several features following listed:

- **Minimum number of connections**: a single bus can be shared by a large number of components. There is no need to set up a dedicated line for each device, so that the number of connections and cable are minimized. This is not only a practical benefit, but it also reduces the magnitude of the mechanical vibration induced by

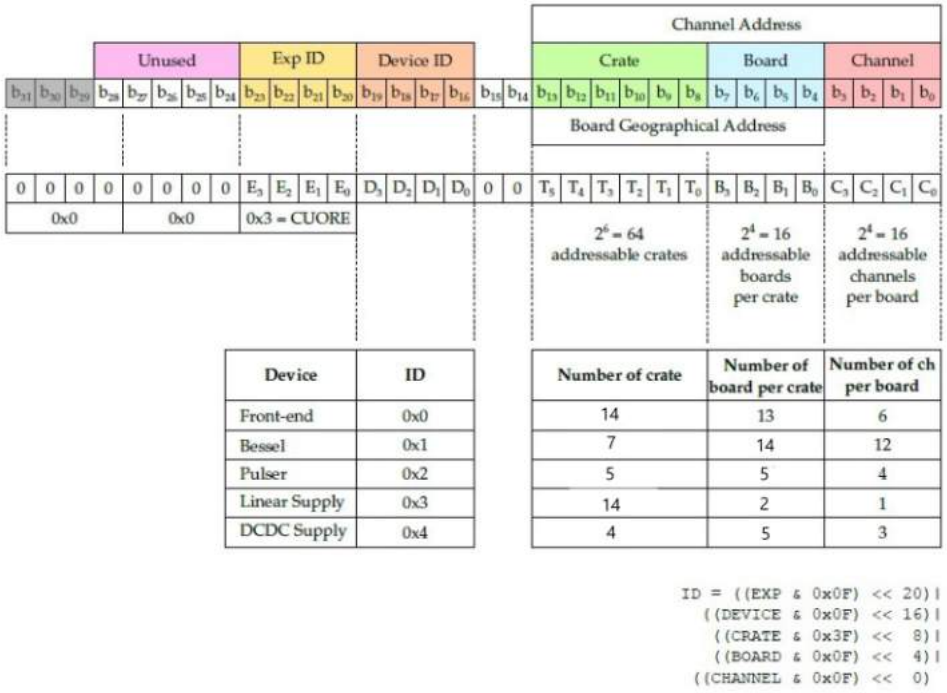

Figure 3.8: Convention used in the CUORE experiment to set the CAN bus ID of each electronic board. The 29-bit extended identifier gives information about the typology and the position of the desired component.

this cable and injected disturbances if picked up by the most sensitive component (connection to the cryostat, front-end input).

- **Flexibility**: the CAN protocol, which was originally developed for the automotive sector, is internationally standardized in DIN ISO 11898. This wide success among different industrial applications proves its high flexibility and capability to interface with different systems. For instance, if an additional node should be added during the data taking, then it can be simply connected to the bus during the usual operation without affecting all the other devices.

- **Reliability**: the CAN bus architecture was studied to ensure the maximum data integrity. Some advantages are the fault tolerance, the resistivity to radiation and electromagnetic disturbances, the presence of an internal fault counter and tools useful for the error type identification and for the error handling. For instance, each node of the bus checks the message integrity and override the *Acknowledge bit* to point out any error detection.

All the boards belonging to the CUORE CAN network satisfies these additional conventions:

- **Power down mode**: all the digital components rely on a reference clock, whose fast and steep transitions cause disturbances to the low noise analog electronics. In the power noise spectrum, these effects usually result in narrow peaks centered to the clock period (several MHz) and thus out of the bandwidth of interest. Nevertheless, if lot of clocks are simultaneously enabled, their interference can also causes low frequency noise spoiling the performance of the system. To prevent such issue during the data taking, the digital blocks of all the CUORE devices are capable to switch off the clocks, going in power down mode, and turn them on only in case of effective need. In particular, if the slow control does not send any communication, all the boards goes in power down mode. In case a message is present on the bus, the boards automatically turn on, check the message ID and its integrity, eventually execute the command and reactivate the power down mode.

- **Additional communication rule**: as mentioned, the CAN message is basically composed of a 29-bit ID and a 8-byte payload containing the data. The ID, set as described in Fig. 3.8, uniquely identifies a message from/to a specific node, so that the board is designed to always returns back responses with its specific ID. In order to make the slow control sure that a message has been correctly delivered through the bus and processed by the target board, the electronics was designed to answer back a response to any valid message. The first byte of the payload data, whose meaning usually depends on the board typology, is a flag that identifies a specific functionality. All the further parameters are stored in the other 7 available bytes. All the electronic boards have been designed to answer back keeping unchanged the command flag byte. All these additional rules allow the slow control to mange the electronics using parallel and asynchronous treads, giving back traces to the check the outcomes.

- **Nope function**: this function is identified by setting to 0 the command flag and foresees a null response from the board (all the payload bytes set to zero). This function is implemented in all the CUORE electronics. The Nope function is of great utility to check the capability of a board to see and process data through the bus. Moreover, a Nope message is sent just before each command in order to power up the desired node and be sure that it is ready to process any subsequent command. This procedure ensure high reliability in the message delivery.

The standard CAN bus link is realized using a pair of DB9 male connectors bringing the two-wire signal (CAN-H and CAN-L), the reference power supply ($V_{CAN} = 5$ V) and the reference ground. As all these signals are connected between all the nodes of the bus, two undesired effects have to be considered. The CAN power and ground is very noisy, not only during the communication process, but because they are shared with the slow control system, i.e. the computer system. If not properly decoupled, this can cause deterioration

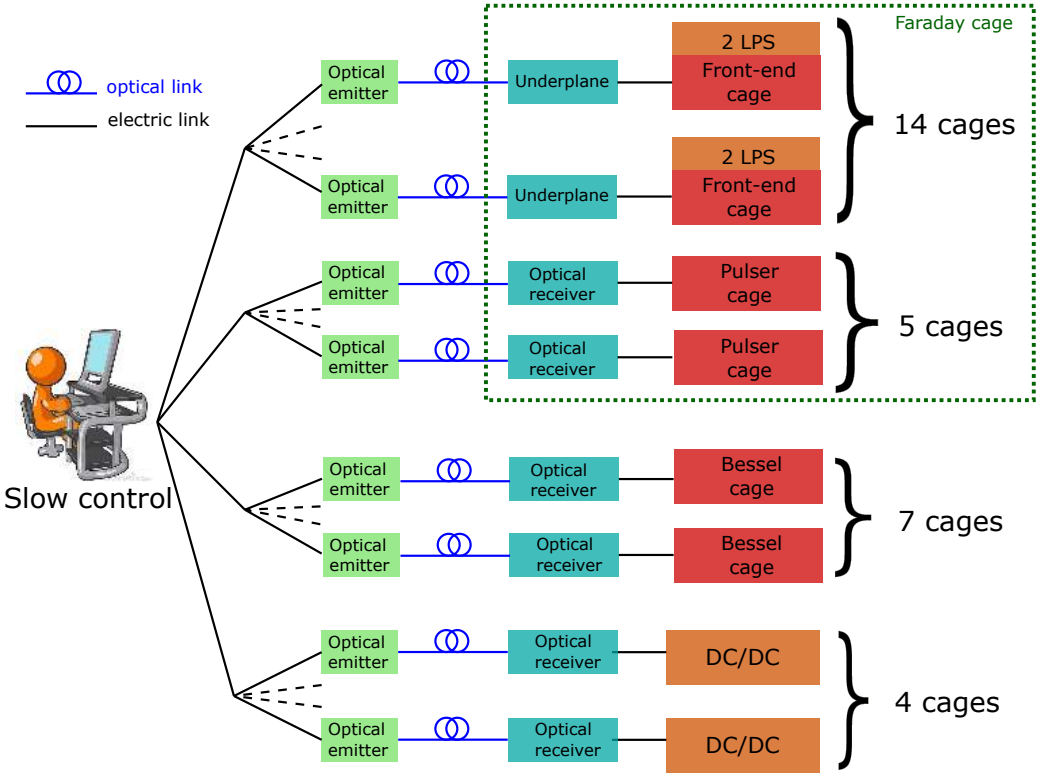

Figure 3.9: Schematic view of the slow control system designed for the CUORE experiment. As it can be seen, the remote control is optically decoupled to the various electronic devices by means of the HUB board.

of the performance of the entire system. Similar issues are expected to be induced even by the CAN-H and CAN-L nodes. The second undesired effect is related to the power down modality. In case a message is present on the bus, each node powers up and turns the clocks on in order to be able to read the massage and checks for its ID. Thus, if all the nodes are connected to a single CAN bus line, then all the devices powers up at each message. Moreover, a too large number of nodes can cause problems to the bus termination resistance, due to the non-infinite input impedance of each node.

In order to prevent such issues, a custom CAN bus HUB was designed. The core of the board consists in a LPC1768 ARM Cortex-M3 micro-controller, from NXP, which mediates between a standard electrical CAN bus line and an optical link pair. In particular, each HUB is devoted to the communication with a specific card cage from which inherits the CAN identified, except for the Device-ID byte[1] (bit 16-19, as pointed out in Fig. 3.8) which is incremented by 5 unit. The HUB divides the main CAN bus into different subsystems

[1]In the case of the HUB board, the Device-ID byte of can CAN ID is obtained as the value of the corresponding device typology plus 5. Thus, the Device ID byte of the HUB devoted to the communication with the front-end board is 5, with the Bessel filters is 6 and so on.

(CAN bus segments) and acts as an active ID filter, so that each message at the input is forwarded to the output only if it concerns the corresponding subsystem branch. The accepted CAN ID can be easily set by means of the on-board 8-bit dip switch. As a result, the electronics are not involved in the CAN communication unless the message is directed to one board of the same card cage, reducing the problem of undesired power up[2]. In addition, each CAN bus segment has an independent resistor termination and a low number of nodes, avoiding the problem of signal reflection along the bus. Another feature of the HUB is that it optically decouples the signal coming from the slow control system to that driven to the electronics board, as shown in Fig. 3.9. In particular, the HUB can work as an optical emitter which reads the standard electrical CAN message from the slow control and converts it into an optical signal driven to the electronics by means of a ~ 10 m optical fiber pair. The same HUB board can also be configured as optical receiver mounted close to the electronic devices, in order to convert back the input optical signal to the standard electrical message. Beside the electrical isolation from the noisy slow control system, the optical fibers ensure simple handling and lower vibrations as their are much lighter than the electrical DB9 connection. Finally note that such architecture is totally transparent from the point of view of the slow control system.
About 30 HUBs have been designed and tested. The optical emitters are placed in three boxes hung up at the CUORE hut, 2nd floor, near the AC/DC and DC/DC cages (see Fig. 3.10). The optical receivers, instead, are located at the side of the corresponding crate.

3.4 Linear Power Supply

The CUORE experiment requires electronics with exceptionally low noise and a very good stability versus time and temperature in order to maintain high performance over several years of data taking. Such requirements apply not only to the front-end circuit, but also to the detector biasing circuits. As shown, the performance of the NTD biasing circuits strongly depends on that of its reference input voltage. A good control of the quality and precision of the power supplies and reference voltages is mandatory to this purpose. This is the reason why the power supply consists in three stages of which the linear power supply [68] (LPS) represents the last node. The circuit supplies precise, stable, and low noise voltages biasing the front-end electronics and the pulse generator boards. The frequency range of interest with the CUORE macro-bolometers extends from DC up to a few kHz. Particular care was therefore given to the minimization of low frequency noise contributions and of all sources of drift or instability. The LPS, shown in Fig. 3.11, is composed by both an analog and a digital circuit. My work has been mainly devoted to the digital block.

[2]For debug purpose, the CAN ID filtering feature can be bypassed. If so, each message at the HUB input is forwarded at the output.

Figure 3.10: Some pictures of the HUB board. On the top-left, the HUB during the tests at the Milano Bicocca Labs. The top-right picture shows the HUB mounted as optical-to-electrical converter for a DC/DC supplier cage. On the bottom, the boxes hosting all the electrical-to-optical CAN converters which mediates the communication towards all the other devices.

Figure 3.12 exhibits a simplified scheme of the analog circuit. The external bias is filtered by a diode bridge in order generate a rectified positive voltage even if the polarity of the input bias is incorrect. This reference allows the digital board to operate and supply an input decisional block which monitors the input bias. If the input voltages are of the correct polarity, correct range and symmetrical with respect to ground, then the analog block is energized.

The positive 2.5 V reference is generated by a set of four LTC6655 voltage regulators,

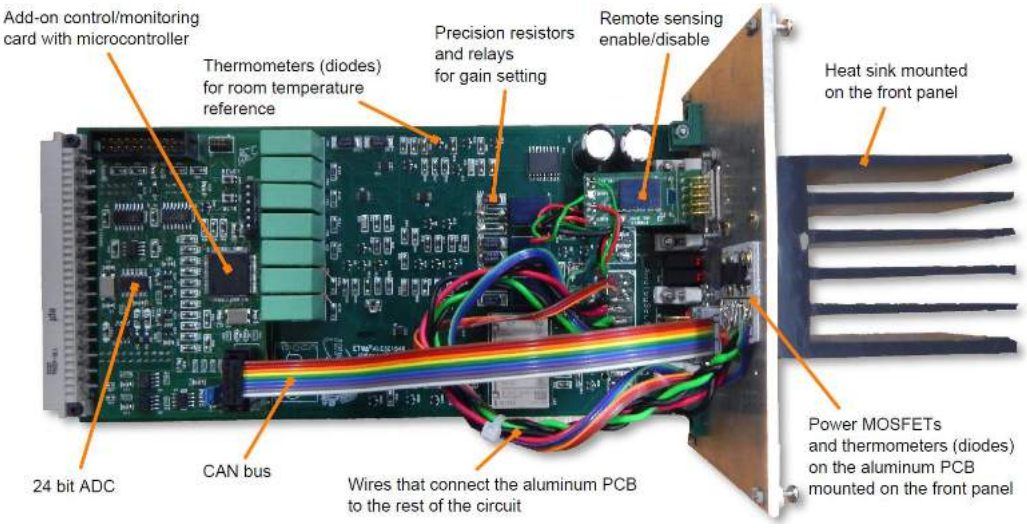

Figure 3.11: The linear power supply designed for the CUORE experiment.

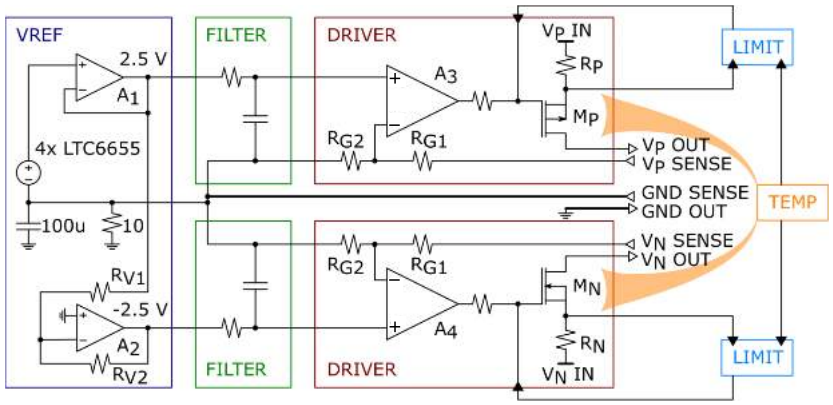

Figure 3.12: Simplified scheme of linear power supply design.

from Linear Technology, connected in parallel to take their average output voltage and to reduce their noise by a factor of two. Two ADA4084 operational amplifiers, from Analog Devices, are used in non-inverting (A_1) and inverting (A_2) unity gain buffers to generate ± 2.5 reference voltages. These signals are filtered by a passive low-pass filter and used to feed the adjustable gain output drivers. The R_{G1} and R_{G2} resistors are made by a set of high precision SMR1DZ metal foil resistors, from Vishay, with an absolute precision of ± 100 ppm and thermal drift of ± 0.2 ppm/°C. The R_{G1} and R_{G2} values, whose ratio defines the gain of the driver stage, can be adjusted by managing bistable dual relays that ensure a negligible series resistance. Thus, the LPS output voltage can be set in the range ± 3.75 V to ± 12.5 V, delivered at the output by a power MOSFET (the AUIRFR5505 and AUIRFR024N from International Rectifier, for the positive and negative output respectively). In order to avoid the voltage drop due to the series resistance of the

output wires at high currents, the driver block feedback loop is usually remotely closed shorted the OUT and SENSE node at the load side. Also the ground reference is connected to the load with two wires, GND SENSE and GND OUT. The latter is used to carry the load current while the former is the precise reference of the VREF, FILTER, and DRIVER blocks. The R_P resistors sense the current delivered at the outputs and enable the limit blocks. They act as current-controlled voltage source pulling up the gate of M_P (or down the one of M_N) for currents larger than 6 A, breaking the driver feedback loop. Despite this limit, the output transistors might work in unsafe condition if their power consumption is high enough to cause overheating. This condition can be established in case of shorts at the output so that the limit current is delivered at the maximum V_{DS}. A foldback protection circuit has been designed to modulate the maximum output current as a function of the power dissipation of the output MOSFETs, proportional to their working temperature. The voltage drop of two forward biased diodes are monitored to measures their working temperature, assumed to be equal to the output MOSFETs thanks to the proper board layout. Thus, the larger the power consumption of the output drivers, the lower the maximum allowed current delivered at the outputs. This protection makes the MOSFETs always operate in safety condition and ensures that the 6 A current limit is automatically and gradually restored as soon as the output short is solved. Further on-board diodes are used to sense the LPS working temperature and provide a signal proportional to it. A proper fraction (α) of such signal is injected to the output drivers to compensate for the LPS thermal drift, already in the ppm/°C range thanks to the choice of components used in the circuit. The α coefficient is adjusted board-by-board performing a thermal drift calibration. The architecture just described, allows the LPS to reach remarkably performance to all the boards of the lot. In particular, the measured noise amounts to 50 nV/$\sqrt{\text{Hz}}$ at 1 Hz and 20 nV/$\sqrt{\text{Hz}}$ white, mostly uncorrelated between the positive and negative outputs. The resulting total noise from each output between 0.1 Hz and 10 Hz is 125 nV RMS (0.8 μVpp). If a bandwidth up to 100 Hz is considered, the total noise is 240 nV RMS, or 1.6 μVpp. In addition to that, the thermal stability of the order of few ppm/°C is reduced to lower than $\pm$1 ppm/°C adjusting the α thanks to the thermal calibration produce [68].

A add-on digital block, visible in Fig. 3.11, completes the design of the linear power supply. This circuit is mounted on a dedicated PCB placed on the rear side of the LPS card and biased by the rectified positive voltage, so that the digital circuit fully works even in case of flipped input bias. The core of the digital block is the LPC1768 ARM Cortex-M3 micro-controller, from NXP, which is capable to manage the communication with the slow control system via CAN bus protocol, monitor the operation of the analog circuitry and drive the relays to define the R_{G1} and R_{G2} values, thus setting the voltages provided at the LPS outputs. 16 different nodes can be measured by multiplexing them at the inputs of a dual differential channel 24-bit AD7732 Analog-to-Digital converter, form Analog Devices.

Further 8 nodes can be acquired by the 12-bit ADC embedded into the micro-controller. This features not only gives the possibility to fully check the status of the LPS from remote, but also behaves as an additional active protection. As mentioned, the foldback protection reduces the maximum deliverable current in case of transistor overheating, which usually occurs in case of shorts at the LPS ground. This can be due to permanent unwanted connections or transient issues that lasts few seconds or less. The digital block is capable to discriminate and trigger the former errors and deactivate the LPS to prevent circuit overstress. Figure 3.13 shows the output positive voltage, the output current, and the temperature of the output transistor M_P versus time, while the output was repeatedly shorted to ground. The curves were acquired exploiting the add-on digital monitoring system.

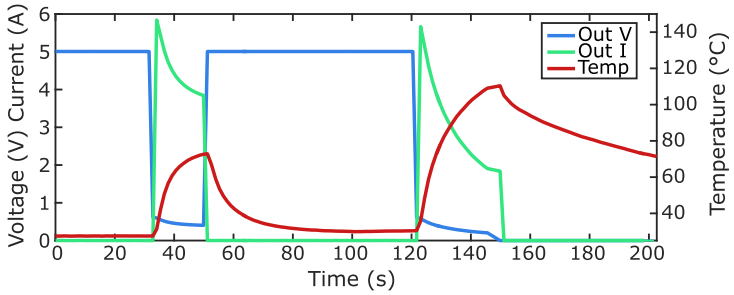

Figure 3.13: Linear power supply output voltage, current and temperature as a function of time during the tests about the foldback and digital protection system. (Courtesy of C. Gotti)

At the beginning of the measurement, the circuit was operating without any load, so that the output voltage is 5 V and no current is delivered. In this condition, the operating temperature of M_P stays close to the room temperature. After about 30 s the output was shorted to ground. The peak current is 6 A at first, but as the temperature of M_P increases, the output current promptly reduces to lower values. The slope of the current decrease depends on that of the temperature increase, which is slowed by the heat sink coupled to M_P. At $\sim$ 50 s the short was removed: the current falls back to zero, while the temperature of the output transistor relaxes to lower values. At about 120 s the heat sink was removed and the output was shorted again to ground. The evolution is similar to the first time, aside from the fact that the temperature is now rising faster, since the heat sink was removed. While all this happens, the micro-controller on the digital board is monitoring the voltages and currents. Its firmware has been designed to cut off the output in case of permanent problem, i.e if the short condition lasts for more than an adjustable duration, set to 30 s. At this point the output stays disabled until the user sends a proper command to micro-controller (via CAN bus) to restore the usual operation. In agreement with this procedure, at about 150 s the micro-controller cut-off the LPS output: both voltage and current go to zero and the temperature slowly decreases.

3.5 Pulse generator board

In order to be sensitive to the temperature increase induced by the interaction of impinging particle, the bolometers of CUORE need to operate close to 10 mK. However, the cryogenic system allowing to operate at such extremely low temperatures shows intrinsic instabilities which can spoil the energy conversion gain and the energy resolution. It is mandatory to develop a system to stabilize the detector response or, at least, to correct its instabilities. This procedure must be effective along the whole data taking, which is supposed to last several years without human intervention. A way to achieve this goal is to periodically deliver a fixed and known amount of energy to the bolometers, inducing a response as similar as possible to that of a particle interaction. This technique allows to monitor the pulse amplitude variations during the data taking and correlate these variations to the detector baseline level, proportional to the bolometer temperature. Off-line, it is finally possible to correlate the temperature variation to the gain drift and compensate the energy conversion. A common way to inject a known amount of energy to the detector is by using a γ source, that emits monochromatic particles absorbed by the bolometers. These signals result in a narrow peak in the energy spectrum centered at a fixed energy only dependent on the decay mode. These peaks are absolute reference allowing the energy spectrum calibration. Another advantage of such solution is that the detector response is identical to the response to the events of interest. On the contrary, a natural source of energetic particles permanently left close to the measurement apparatus, would increase the radioactive background spoiling the overall experiment sensitivity. A second method to accomplish the bolometer response stabilization foresees the use of a resistive heater glued on the bolometer crystal, across which a Joule pulse is delivered. As will be demonstrated in the following sections, the energy injected to the bolometer by a single calibrating pulse is expressed by the following equation:

$$E = \alpha \frac{V^2 T}{R} \tag{3.6}$$

where V and T are the pulse amplitude and width, R the resistance of the heater and α a constant which relates the power consumed on the resistor and that injected to the bolometers. A merit of this solution is the complete control of the pulse generation procedure, since the generated pulse rate, amplitude and width can be tuned as desired. Moreover, this solution do not cause a background increase, preventing the deterioration of the experiment sensitivity. The relationship between the Joule power dissipated across the heating resistor and the energy measured strongly depends on the thermal coupling between the crystal and the heating resistor. The thermal coupling is not known a priori and significantly differs from crystal to crystal. For this reason, this method cannot be an absolute reference and needs an initial calibration of each channel. Nevertheless, a very accurate stabilization can be achieved if the calibrating pulse parameters are maintained

extremely stable over long periods of operation.
The solution adopted in the CUORE experiment exploits both approaches: the radioactive source is used to periodically calibrate the system, while the heating source is used to stabilize it during the long data taking periods. The detector baseline is used to monitor the operating temperature of the bolometers. On the other hand, the heating pulses are used to monitor the gain, by measuring their amplitudes as a function of the temperature. This allows to establish the dependence between the gain and temperature and rescales the responses of the bolometers to the initial calibration values. In this way the energy resolution is maintained at its optimum value for the entire data taking between the γ calibration procedure, that will take place about once per month. A similar procedure was satisfactorily implemented and tested in the pilot experiment CUORICINO [69]. The good results obtained in the CUORICINO experiment by implementing a similar calibration and stabilization technique as that described for the CUORE experiment are shown in Fig. 3.14. As it can be observed, the energy dispersion due to the operating temperature instabilities and the consequent fluctuations of the energy conversion factor, responsible of the bad energy resolution of the red peak, can be recovered using the reference signal generated by the pulser board.
In the next sections the hardware and firmware design choice (Sect. 3.5.1), the stability performance reached after the thermal drift compensation (Sect. 3.5.2) and the studies of the effects limiting the pulser board energy resolution (Sect. 3.5.3) will be presented.

3.5.1 Design choices

The CUORE experiment consists of 988 TeO_2 bolometer crystals, gathered in 19 towers of 4 columns and 13 floors each. As mentioned, beside the NTD thermistor for the signal measurements, each bolometer is equipped with a glued heater resistor, thermally coupled to the detector. At the baseline temperature, the typical heater resistance amounts to about $R_H = 300$ kΩ. Each pair of terminals of the heater resistor is connected to the pulse generator boards by several meters long wires, ensuring the maximum thermal decoupling between the detector and the electronic system, operated at room temperature. All the 13 heaters belonging to the same column are connected in parallel, so that the total resistor loading the pulser outputs is of the order of $R = R_H/13 = 25$ kΩ. This nominal values is not homogeneous among the columns, as variations by a factor of 2 are expected.
To achieve the best performance in terms of detector response stabilization, the signal injected through the pulser board must be as similar as possible to that induced by an interacting particle. The response of a bolometer can be easily studied by schematizing the detector as a thermal capacitance (C) in parallel to a thermal conductance (G) with respect to the thermal bath (i.e. the ground reference, as shown in Fig. 3.4). As an impinging particle interacts in the sensitive volume, it injects a power impulse into the thermal capacitance causing a proportional increase of the bolometer temperature, read with the

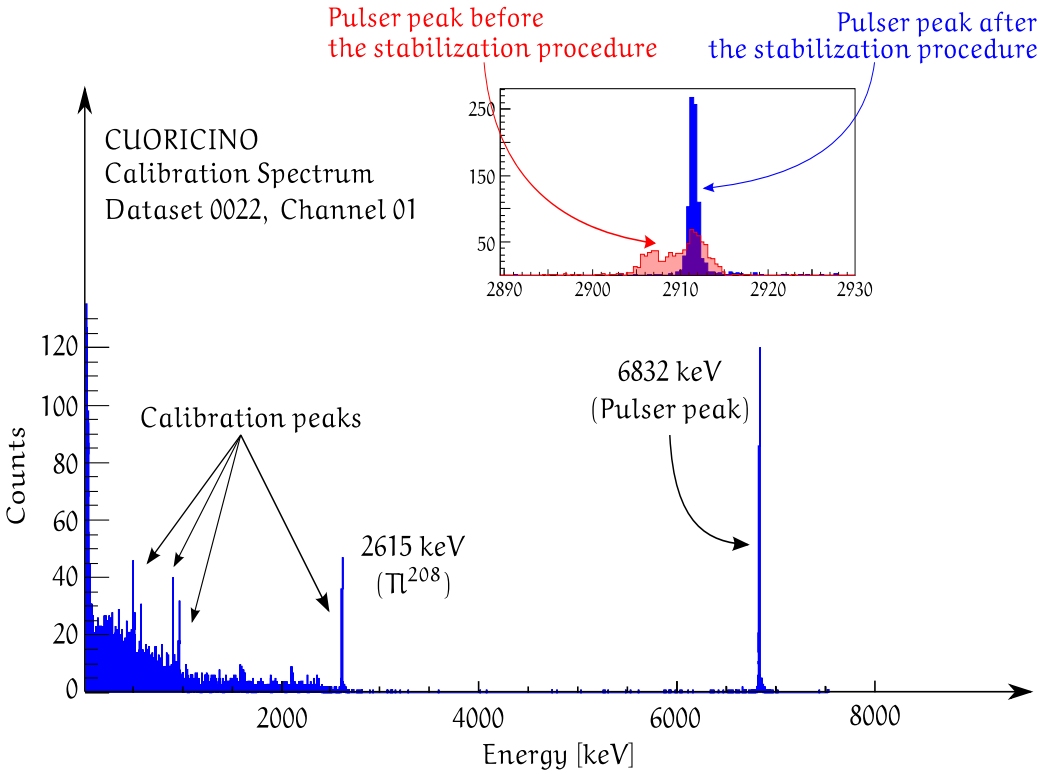

Figure 3.14: Energy spectrum acquired in the CUORICINO experiment. In the upper plot, the improvements in the energy resolution after the calibration procedure is clearly visible. (Courtesy of A. Giachero)

NTD thermistor. The over-temperature relaxes to the baseline temperature by thermalizing via the thermal conductance (G). Using the typical formalism developed for the study of electronic circuits, the particles acts as an impulsing current source driving the low pass filter composed by the thermal capacitance and conductance. In this parallelism with the electronics, the temperature variation (K) is associated to the voltage signal. The transfer function of the bolometer is thus described by the following equation:

$$B(s) = \frac{1}{G}\frac{1}{1+s\tau_B} \simeq \frac{1}{sC} \tag{3.7}$$

where the last approximation follows from $\tau_B = C/G \gtrsim 500$ ms much larger than the frequencies of interest. In this case, the transfer function of the bolometer behaves like an ideal integrator, in which the output temperature, in time domain, coincides to the integral of the total power delivered to the detector.

A first example of the system response is the signal induced by a interacting particle. In time domain, the power injected consists in a δ-like pulse whose amplitude is equal to the energy (E) released in the bolometer by the particle. The time evolution of the detector response can be calculated as the inverse Laplace transform of the product between the

constant input signal in frequency domain $E(s) = E$ and the bolometer transfer function (Eq. 3.7). Thus:

$$K(t) = \mathscr{L}^{-1}\{E(s)B(s)\} = \frac{E}{C}e^{-t/\tau_B} \tag{3.8}$$

A second interesting example is the case of a calibrating pulse injected by the pulser board, consisting in a voltage drop across the heater resistor. In time domain, the ideal voltage pulse is well described by a rectangular shaped power signal:

$$P(t) = P_0[\theta(t) - \theta(t-T)] \;\; \rightarrow \;\; P(s) = \frac{1 - e^{sT}}{s} \tag{3.9}$$

where $P_0 = V^2/R$ is the power dissipated across the heater resistor R, calling V and T the calibrating pulse amplitude and width respectively. In time domain, the bolometer response is:

$$K(t) = \mathscr{L}^{-1}\{P(s)B(s)\} = \alpha\frac{P_0}{G}\left[1 - e^{-t/\tau_B} - \theta(t-T)(1 - e^{\frac{-t+T}{\tau_B}})\right] \tag{3.10}$$

where α is the constant introduced in Eq. 3.6. Assuming $T \ll \tau_B$, we can divide Eq. 3.10 in three different regions:

$$K(t) = \begin{cases} \frac{P_0}{G}[1 - e^{-t/\tau_B}] \sim \frac{P_0}{C}t & \text{if } t < T \ll \tau_B \\ \frac{P_0}{G}[e^{-\frac{t-T}{\tau_B}} - e^{-t/\tau_B}] \sim \frac{P_0 T}{C} & \text{if } T < t \ll \tau_B \\ \frac{P_0}{G}[e^{-\frac{t-T}{\tau_B}} - e^{-t/\tau_B}] \simeq \frac{P_0 T}{C}e^{-t/\tau_B} & \text{if } T \ll \tau_B \leq t \end{cases}$$

At the very initial time ($t < T \ll \tau_B$), the bolometer temperature increases linearly with respect to the time as long as heating power is delivered. The maximum temperature is reached at $t = T$ and the thermal pulse amplitude is proportional to the total energy collected by the bolometer (P_0T). This temperature is maintained until the bolometer starts to thermalize at the baseline temperature by dissipating the heating power to the thermal bath through the thermal conductance ($T \ll \tau_B \leq t$). Similarly to the particle, the heating power injected by the pulser is integrated by the bolometer as long as the power is delivered by pulses much shorter than the detector time constant. Summarizing, the maximum temperature increase of the bolometer can be described by the following equation:

$$K_{max} \propto E \propto \int_0^{\tau_B} P(t)dt \tag{3.11}$$

In the case of an ideal square Joule puses, with V and $T \ll \tau_B$ the pulse amplitude and width respectively, Eq. 3.11 becomes:

$$E[eV] = \eta\frac{V^2 T}{e\varepsilon^2 R} \tag{3.12}$$

where $\varepsilon \simeq 200$ is the amplitude attenuation factor (obtained, as will be shown, with a ultra-stable output voltage divider), $R \sim 25$ kΩ the resistance of the heater and e the electron charge. $\eta \sim 20\%$ is the thermal coupling coefficient which represents the ratio between the power injected into the detector and that dissipated across the heater resistor. As mentioned, this constant changes from crystal to crystal, requiring for an initial calibration.

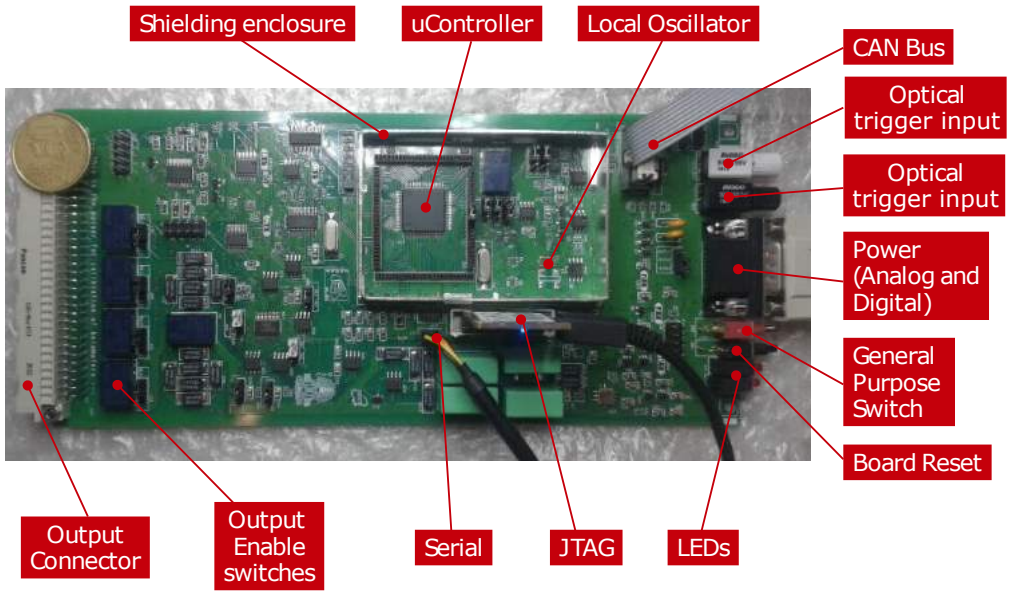

Figure 3.15: A picture of the layout of the CUORE pulser board. The main functional components are pointed out.

The pulser board has been specifically designed to provide calibrating pulse ensuring an outstanding stability and pulse repeatability in time and with respect to the operating temperature variation, large flexibility, high reliability, features for diagnostic and debug and an optical line to provide an optional external trigger. The CUORE pulser board, designed in the INFN Milano Bicocca Laboratories, is shown in Fig. 3.15. It consists of a four layer Printed Board Circuit hosting a Cortex M3 LPC1768, 32-bit micro-controller, from NXP, managing several external peripherals and communicating via a CAN bus protocol to the CUORE slow control system. The board has 4 four output channels able to independently provide squared calibrating pulse. As mentioned, all the heater resistors of a CUORE detector column are connected in parallel to a pulser output. Since each CUORE tower is composed of 4 columns, a single pulser board supplies a complete CUORE tower, so that 19 boards are necessary to calibrates all the 988 bolometers. These boards are arranged in 5 crates hosting 4 boards each. The crates are placed at the top of the front-end electronic tower, inside the Faraday cage, at the top of the CUORE cryostat.

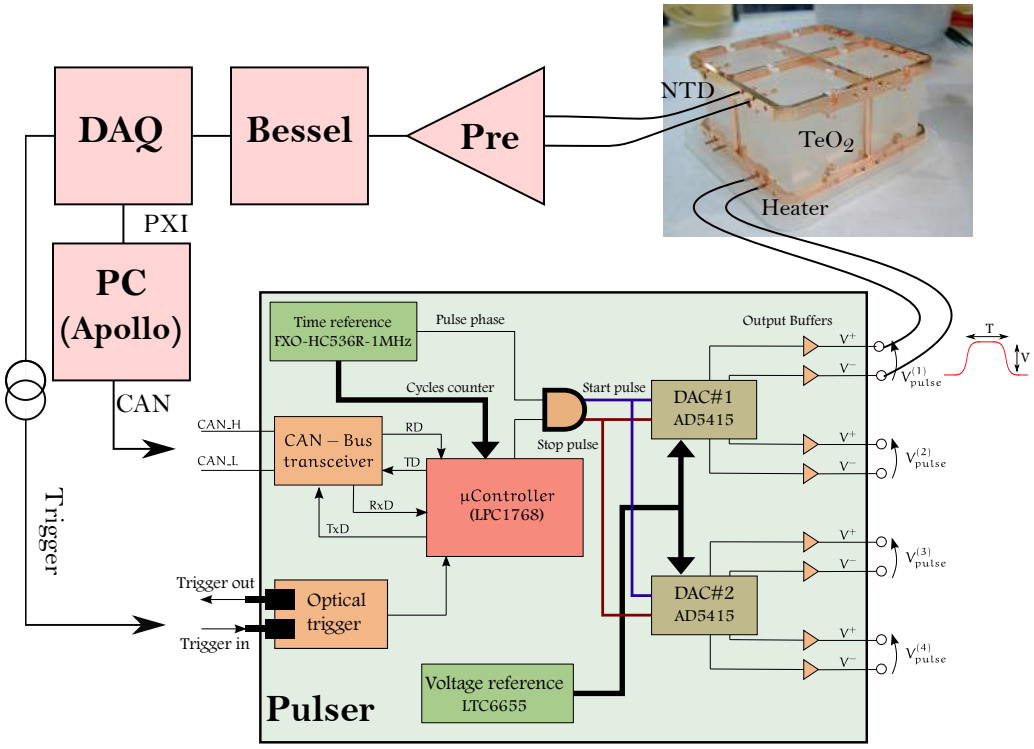

Figure 3.16: Simplified scheme of the CUORE pulse generator board. The main blocks of the DAQ and slow monitoring system are also reported.

Figure 3.16 shows the main blocks composing the pulse generation chain. The high precision square pulse is driven inside the cryostat and reaches the heater resistors glued on the bolometers. The thermal power injected induces an increase of the temperature of the bolometer, according to Eq. 3.10. This signal is converted to a voltage step across the NTD thermistor, amplified by the front-end electronics feeding the Bessel filters. The signal is finally acquired by the DAQ system and stored for the off-line analysis. As mentioned, the pulser board operating parameters can be remotely controlled through the optically decoupled CAN connection using the APOLLO software from the slow control system. In order to easily tag the calibrating pulse before their storage and prevent synchronization issues, it is convenient that the DAQ system triggers the generation of the pulse so that the pulse itself can be tagged. Thus, the DAQ provides a digital TTL transition which is converted to an optical pulse, driven to the pulser board front panel, hosting an optical receiver triggering the pulse generation. The optical trigger is daisy chained among the 19 boards, so that a unique optical connection from the DAQ system (outside the Faraday cage) to the pulsers is enough to provide the trigger to the whole system. To summarize, the slow control communicates via CAN-bus to the desired pulser board and sets the pulse parameters and the columns to be calibrated, while the effective pulse generation is triggered from the DAQ board.

Figure 3.16 also exhibits the main blocks used to generate the calibrating pulse. In order to obtain precise pulse transitions, the pulser board is equipped with the FXO-HC536R oscillator, a very accurate device able to provide a 1 MHz reference clock with a declared phase stability of ±25 ppm. This time reference is connected at the input of the LPC1768 micro-controller which can enable or disable the clock source and count its cycles. The first order estimation of the pulse width is obtained simply by converting the desired duration in terms of equivalent clock cycles (i.e. as an integer multiple of the 1 μs time unit). However, the timing performance of the micro-controller is not good enough to directly trigger the pulse transitions. The voltage generator is driven by a fast flip-flop (the NC7SV74 from Fairchild Semiconductor) connected to both the micro-controller and the reference oscillator. The micro-controller acts as a gate: when the gate is closed, the flip-flops maintained the output voltage generator in reset mode. The gate is opened as soon as the micro-controller clock cycles counter matches with the target value (i.e. the pulse coarsely lasts as desired). Being the gate opened, the flip-flop triggers the pulse transitions at the first reference clock rising edge. Using such architecture, the timing performance only depends on the precise clock reference and the fast flip-flop performance, independently of the pulse width. In particular, the phase stability of the generated pulse coincides to that of the reference clock. The outcomes of the timing performance characterization in term of temperature stability and random fluctuations will be shown in Sect. 3.5.2 and Sect. 3.5.3 respectively. Finally note that the boards is equipped with three clocks which serves as reference for the pulse timing, for the micro-controller operation and for the on-board Analog-to-Digital (ADC) converter. In order to prevent that the fast transitions of the clocks could introduce high frequency disturbances induced by the associated electromagnetic field, all these noisy components are enclosed inside a grounded metallic box acted as a local mini-Faraday cage shields (see Fig. 3.15).

The output voltage generator system is based on the very precise and low noise voltage reference LTC6655, from Linear Technology, as shown in Fig. 3.16. This component generates a 5 V voltage reference ensuring an outstanding thermal stability (few ppm/°C) and a negligible sensitivity to the humidity level, thanks to the LS8 hermetic package. In order to reduce its noise contribution by a factor of 30%, two components are connected in parallel and averaged, so that the resultant value is used to feed the AD5415, a 12-bit, dual channel Digital-to-Analog converter (DAC) from Analog Devices. Coupled with low noise and high precision OPA140 operational amplifier, from Texas Instrument, the DAC can be schematize as a settable resistor, ranging from 10 kΩ to an open circuit, as shown in Fig. 3.17. Since R_{D1} amounts to 10 kΩ and the OPA140 is used in inverting configuration, this architecture deliver a negative voltage level ranging from ground to $-V_{REF} = -5$ V. This signal is also driven at the input of a second inverting unity gain amplifier, which allows

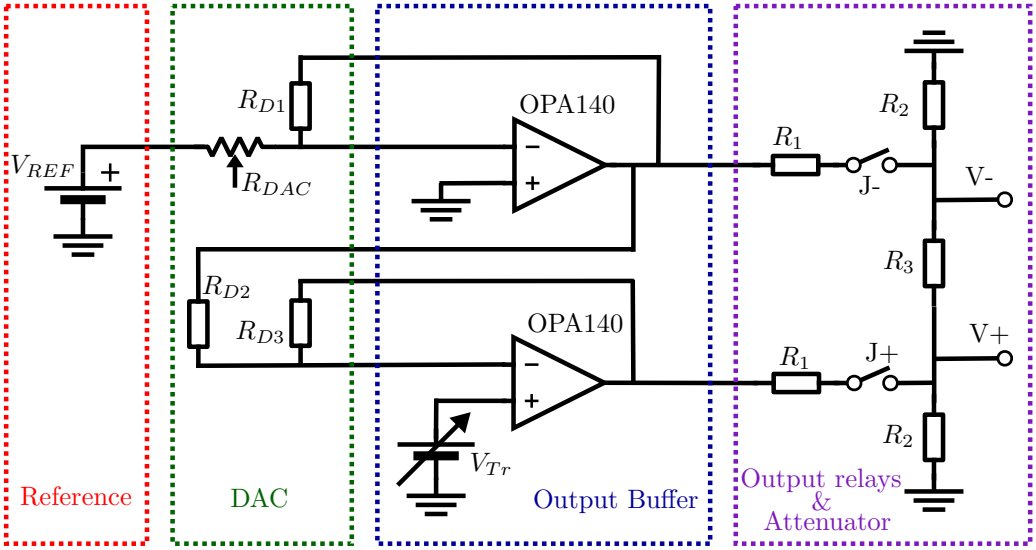

Figure 3.17: Simplified schematic of a pulser board channel

to obtain a positive voltage ranging from ground to $V_{REF} = 5$ V. A differential signal up to 10 V can thus be supplied at the outputs. Note that the positive terminal of this second inverting amplifier is not referred to ground but to a variable voltage, controlled by a 8-bit potentiometer. As shown in the next section, this component can add a proper offset at the positive node to compensate for the thermal drift of the voltage generation chain. The differential voltage is driven to the output stage, composed of a dual channel bistable relay (the TQ2-L2, from Panasonic) and an ultra-stable voltage divider, which attenuates the signal by a factor of $\varepsilon = 201$, down to suitable energy levels. Each of the two channels of the DAC is connected to two independent output stages, so that 4 channels are available in total. The choice to avoid solid state relays has been guided to the minimization of their series resistance, which usually show a poor thermal stability deteriorating the performance of the whole system. The drawback of using mechanic relays is that some disturbances can be induced at the nearby outputs by the magnetic energy released by the coil during the relay transition. In particular, neglecting the R_1 and R_2 resistors, the eventual disturbances are injected to the heater resistors and leading to a very poor pulse energy resolution. In order to avoid such problem, the $R_1 = 50\ \Omega$ and $R_2 = 500\ \Omega$ are placed at the relay output fulfilling two goals: absorb to ground any disturbances induced by the magnetic coils and give a ground reference to the heater resistor when the relays are opened. The thermal calibration procedure and performance achieved in term of temperature stability and noise injection will be shown in Sect. 3.5.2 and Sect. 3.5.3 respectively.

The pulser board is also able to deliver a constant voltage level at the output and, eventually, superimpose pulses over it. The capability of providing an adjustable static

level can be exploited to inject a settable DC power inside the cryostat. In particular a proportional–integral–derivative (PID) controller has been set up to read the actual cryostat temperature and properly adjust the power injection to compensate for thermal drifts usually occurring in bolometer experiments. A 24-bit, dual differential channel, AD7732 Analog-to-Digital converter, form Analog Devices, is used to measure the external node one would stabilize. By means of a 8 channel multiplexer, the second ADC channel can be used to remotely monitor all the voltage references and the output signals delivered by the DAC. The pulser board is also equipped with peripheral and features useful for debug purpose. Finally, the board is provided with a embedded 32-Kbit serial I^2C bus EEPROM, the M24C32 from ST. This memory stores the board identifier, its location in the CUORE setup and all the characteristic parameters used for the thermal drift compensation.

3.5.2 Thermal stability

As mentioned, the pulser board has been designed to provide a reference signal that mimics the interaction between a series of monochromatic impinging particles and the bolometer detector. In the energy distribution spectrum, such events results in a gaussian shaped peak whose center is located at the mean energy delivered by the particles, while the peak width only depends on the detector energy resolution. In order to reproduce this scenario using a series of Joule pulses, one must be able to deliver monochromatic signals with an energy fluctuation much lower than that of the detector. If the average energy supplied to the system changes in time, then the corresponding peak loses its gaussian symmetry and provokes a systematic uncertainty in the detector response calibration. On the other hand, energy fluctuations would cause a poor energy resolution, as described in Sect. 3.5.3, so that a larger number of pulses would be necessary to obtain a reliable average energy.
The thermal drift is the most important parameter that has to be taken into account to ensure the pulser stability. Indeed, the CUORE Faraday cage hosting the pulser boards is not equipped with any thermalising system in order to avoid the injection low frequency disturbances. Slow temperature drifts are expected in the experimental operation so that the pulser operation should be stable irrespective of them. According to Eq. 3.12, three pulser parameters plays an important role in the energy delivery: the pulse width (T), dependent on the on-board reference oscillator, the voltage level produced at the DAC output (V) and the attenuation factor of the output divider (ε). In particular, from Eq. 3.12, the energy drift with respect to the temperature variation is:

$$\frac{dE}{EdK} = 2\frac{\partial V}{V\partial K} + \frac{\partial T}{T\partial K} - 2\frac{\partial \varepsilon}{\varepsilon \partial K} \tag{3.13}$$

where K is the operating temperature. In the next sections each contribution will be presented separately. A thermal calibration procedure, presented in section 3.5.2, was

developed to mitigate such drifts in the temperature range going from 20°C up to 60°C. The obtained results will be shown.

Pulse width stability

As mentioned, the pulse width depends on the FXO-HC536R reference oscillator. In particular, if the clock period changes as a function of the operating temperature, then the pulse energy drifts proportionally. The clock reference drift cannot be directly compensated, but the system is designed to over-compensate the pulse amplitude in order to take it into account. Thus, it is important to characterize the pulse width stability on each board to achieve the best performance. The pulse width thermal drift was measured using a Rohde&Schwarz RTO1044 oscilloscope. This system exploits the HD option, that allows to acquire the pulser signals with 14 equivalent bit precision, 100 MHz bandwidth, in a settable voltage range and reach a time resolution few tens of picoseconds ($\sim 10^7$ sampled point in the acquired window). The pulser board has been tested in climatic chamber which increases the operating temperature from 20°C to 60°C, with a constant slope of 0.1°C per minute. Such slow temperature increase ensures that the pulser board is in thermal equilibrium with respect to the environment during all the measurement. Every 5°C, a series of pulses (amplitude 5 V, width 1 ms, no attenuation) were delivered by the pulser under test. The oscilloscope acquires both positive and negative polar pulses, calculates the differential signal of interest, triggers on the rising edge and measures the pulse width from the delay between the points where the differential signal crosses a threshold placed at half of the pulse amplitude on the rising and falling edges. The system is fully automatized and repeats this procedure delivering 10^3 identical pulses for each temperature. These events are collected into a histogram, fitted with a Gaussian function, as shown in Fig. 3.18.a. The pulse width as a function of the temperature can be obtained as the mean value of the Gaussian fit for each sequence of pulses. The typical pulse width thermal drift is shown in Fig. 3.18.b.
The outcomes show that the pulse width slightly increases with the temperature. The clock thermal drift is almost linear, with a typical slope of $0.3 - 0.4$ ppm/°C. Only small deviation from this trend was observed at the highest temperatures ($K \geq 50$°C). Each pulser board used in CUORE was characterized with respect to the pulse width thermal drift and linear slope coefficient is stored in the on-board EEPROM.

Voltage stability

The output voltage level is obtained feeding the AD5415 DAC with a 5 V reference voltage provided by the LTC6655 linear regulators. As a consequence, the voltage level stability depends on the thermal stability of both components. According to the datasheets provided by the manufactures, the voltage drift can be ascribed to several causes, following described.

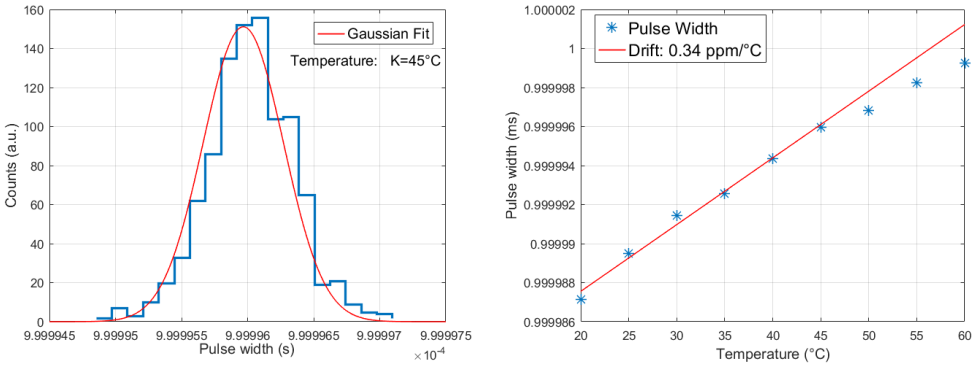

(a) (b)

Figure 3.18: Pulse width thermal stability: on the left, the pulse width distribution acquired at 45°C. The average pulse width is given from the Gaussian center. On the right, the pulse width with respect to the temperature. The typical pulse width drift amounts to $0.3 - 0.4$ ppm/°C.

- **Operation temperature dependence**: the voltage provided by the reference changes with respect to the component temperature. This drift is component dependent, non linear and generally shows a minimum drift around $K \sim 35$ °C. The manufacturer quotes the voltage regulator thermal drift to ± 2 ppm/°C. In addition to this the DAC response depends on the operating temperature in a complex and non linear way. The DAC gain variation with respect to the temperature is quoted to be ± 5 ppm/°C, full range scale. These effects dominates the overall voltage instability.

- **Long-term drift**: the voltage reference shows a variation as a function of the operational time. Long-term drift cannot be extrapolated from accelerated high temperature testing since this erroneous technique gives drift numbers that are wildly optimistic. The only way long-term drift can be determined is to measure it over the time interval of interest. This characteristic prevent us to measure and compensate for this effect. To mitigate it, the pulser board is equipped with voltage reference in LS8 package, whose long-term drift is quoted to be ± 20 ppm/$\sqrt{\text{kHr}}$. Since this effect is proportional to the square-root of the time, its contribution becomes lower after long period of operation.

- **Thermal hysteresis**: the thermal drift of the voltage reference is not only proportional to the actual temperature, but also depends on whether the temperature is increasing or decreasing. This phenomenon is called thermal hysteresis and is particularly deleterious in case of fast temperature changes. In worse case condition, the thermal hysteresis might result in a instability of the order of 30 ppm. Although

the CUORE environment is not equipped with active system to keep the operating temperature stable, the environment temperature is expected to slowly change during the data taking, thus mitigating the hysteresis effects.

- **Mechanical strains**: temperature increase causes the expansion of all the metals composing the pulser board. In particular, large ground or power supply planes would be affected by such effect. The mechanical stress caused by soldering parts to an expanding printed circuit board may cause the output voltage to shift and the temperature coefficient to change. Proper layout technique help to mitigate this second order effect.
- **Humidity**: with changes in relative humidity, plastic packaging materials absorb water and change the amount of pressure they apply to the die inside. Considering the voltage reference, this strain can cause slight changes in the output of a voltage reference, usually of the order few tens of ppm. To prevent such effect, the voltage reference is packaged in the hermetic LS8 enclosure, so that humidity negligibly contribute to the drift. Residual second order effects can be ascribed to the mechanical stress applied to the voltage reference by the printed circuit board material which may absorb water. Proper board materials and layout are thus essential.

The voltage drift as a function of temperature has been measured placing the pulser board in the VOTSCH VT-7004 climatic chamber. The environment temperature is increased linearly from 20°C to 60°C, with a slope of 0.1°C per minute. Such slow temperature increase ensures that the pulser board is in thermal equilibrium during all the measurement. During the temperature cycle, the remote control makes each pulser channel generate a static voltage level (from 1 V to 10 V, 1 V step), measured with the 3706A Multimeter, from Keithley, kept at room temperature . Such multimeter is able to measure with extremely high accuracy and stability the voltage delivered from the pulser board, so that even small drifts can be observed.
Figures 3.19 shows the measured thermal drift as a function of temperature. The drift behaviour significantly changes as a function of the amplitude delivered. In particular, at lower amplitudes (Fig. 3.19.a) the contribution of the voltage reference is largely attenuated and the DAC thermal drift dominates the overall instability. On the other hand, at larger output amplitudes (Fig. 3.19.b) the plot changes since the relative contribution of the voltage reference increases while the DAC contribution does not change. In this condition the voltage shows a negative slope below ~ 35 °C, while a positive drift at larger temperatures. The typical voltage drift order of magnitude amounts to several ppm/°C.

Output voltage divider stability

The signal produced from the Analog-to-Digital converter is buffered to the heater resistor after being attenuated by mean of a output voltage divider. As it can be easily calculated

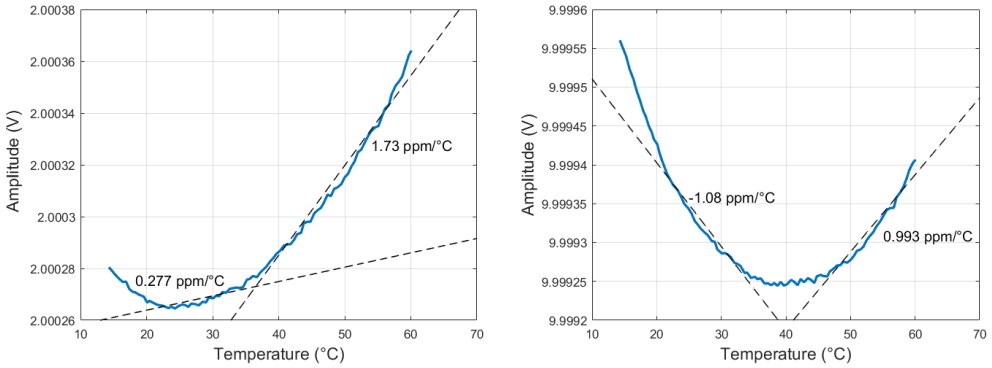

(a) (b)

Figure 3.19: Intrinsic (non-compensated) pulse amplitude thermal drift. The plot are shown for low (2 V, on the left) and high amplitudes (10 V, on the right).

applying the Kirchhoff's circuit laws and referring to the schematic shown in Fig. 3.17, the attenuation coefficient ε of the voltage divider is given by:

$$V+ - V- = \varepsilon V_{in} \simeq \frac{R_2 R_3}{R_1(2R_2 + R_3)} V_{in} \tag{3.14}$$

The approximation used to deduce Eq. 3.14 exploits that $R1 = 5\ \text{k}\Omega \gg R_2 = 500\ \Omega$, so that $R_1 /\!/ R_2 \sim R_2$. In order to ensure the maximum thermal stability of the voltage divider coefficient, SMR1DZ ultra-high precision foil resistors, from Vishay, are used to implement R_1 and R_2. Such components are quoted to have a thermal stability of $\frac{\partial R_1}{R_1 \partial K} = \frac{\partial R_3}{R_3 \partial K} = 0.1$ ppm/°C. As will be shown soon, the thermal stability of R_3 is less critical, since it contributes only by the 5% to the total resistance to ground. Thus, R_3 was chosen to ensure a thermal stability of R_3 $\frac{\partial R_2}{R_2 \partial K} = 5$ ppm/°C. From Eq. 3.14, the contribution of each resistor can be expressed taking the partial derivatives with respect to the temperature variation:

$$\frac{d\varepsilon}{\varepsilon dK} = \frac{\partial \varepsilon}{\partial R_1}\frac{\partial R_1}{R_1 \partial K}\frac{R_1}{\varepsilon} + \frac{\partial \varepsilon}{\partial R_2}\frac{\partial R_2}{R_2 \partial K}\frac{R_2}{\varepsilon} + \frac{\partial \varepsilon}{\partial R_3}\frac{\partial R_3}{R_3 \partial K}\frac{R_3}{\varepsilon} \tag{3.15}$$

By calculating the various partial derivatives, one obtains:

$$\frac{d\varepsilon}{\varepsilon dK} = -\frac{\partial R_1}{R_1 \partial K} + \frac{\partial R_2}{R_2 \partial K} + \frac{\partial R_3}{R_3 \partial K} - \frac{1}{2R_2 + R_3}\left(2\frac{\partial R_2}{\partial K} + \frac{\partial R_3}{\partial K}\right) \tag{3.16}$$

By substituting the expected thermal coefficients for each resistor and considering that $R_2 = 10R_3$, one obtains:

$$\frac{d\varepsilon}{\varepsilon dK} = \frac{1}{21}\left(\frac{\partial R_2}{R_2 \partial K} - \frac{\partial R_3}{R_3 \partial K}\right) \leq 0.3\ \text{ppm/°C} \tag{3.17}$$

Thanks to the performance of the components chosen to realize the output voltage divider, the thermal stability of the attenuation factor has been kept remarkably small and within the experimental goal.

Total drift

Although the thermal drift depends on a lot of different effects combined in complex and non linear way, the intrinsic pulse energy stability is of the order of several part per million per Celsius degree. Such good performance are ensured by the hardware choice which guided the pulser board design. Nevertheless, most of the thermal drift can be compensated by injecting a correcting voltage level (V_{tr}) into the positive output buffer (see Fig. 3.17). This voltage can be adjust with a resolution of few μV by managing the on-board 8-bit AD5263 digital potentiometer, from Analog Devices. Given the complex dependence of pulse energy from temperature, the drifts must be empirically measured on each board to be compensated. An automatic system has been set up to calibrate each CUORE pulser board. The calibration procedure follows these steps:

- Since the thermal drift due to the voltage chain and the time reference is expected to be very small by design (of the order of several ppm/°C), the drift cannot be observed if further attenuated by the output voltage divider. Hence, the voltage divider is disconnected during the calibration procedure and its contribution will remain uncompensated.

- The clock thermal drift is measured for each board in the temperature range from 20°C to 60°C. The pulse width drift is assumed to be linear and the slope coefficient is measured and store in the pulser EEPROM memory. Such value is used to properly under-compensate the pulse amplitude in order to correct for the clock thermal drift.

- The board is kept turned on for one day at controlled temperature to reduce long-term drift contribution. During this period, the digital potentiometer is calibrated and its average step is recorded in the on-board EEPROM. Moreover the pulser baseline is measured and the potentiometer is initially set to compensate for the initial offsets. Baseline offsets lower than 1 μV are achieved even without enabling the attenuating voltage divider.

- The voltage thermal drift is measured as explained in Sect. 3.5.2 for each board in the temperature range from 20°C to 60°C, for output levels ranging from 1 V to 10 V, 1 V step. For each amplitude level, the output voltage drift measured every 5°C of temperature variation is recorded in the on-board EEPROM. Assuming that in each temperature segment the voltage drift can be consider linear, the EEPROM values allows to reconstruct the uncompensated voltage drift for each amplitude.

- The direct voltage drop of two on-board diodes are measured during the temperature cycle. The direct voltage drop of a PN-junction linearly decreases by about -2 mV/°C. The diode calibration results are stored in the on-board EEPROM memory. After the calibration, the measurement of the diode voltage drop by means of the on-board ADC allows to measure the board operating temperature with a precision of ~ 1 °C.

- The thermal calibration is completed. During the calibration pulse delivery, the micro-controller automatically measures the actual operating temperature from the thermometer diodes and recalls from the EEPROM the drift empirically measured at that temperature and for the desired signal amplitude. The potentiometer sets a proper correcting voltage (V_{tr}) so that both the pulse amplitude and width thermal drift are compensated. In particular, from Eq. 3.13, the compensating voltage V_{tr} added at the pulser output is given by:

$$V_{tr} = -2\frac{\partial V}{V\partial K}\Big|_{K_\alpha} - \frac{\partial T}{T\partial K}\Big|_{K_\alpha} \tag{3.18}$$

  where K_α is the actual temperature. All the factors are known from the calibration procedure.

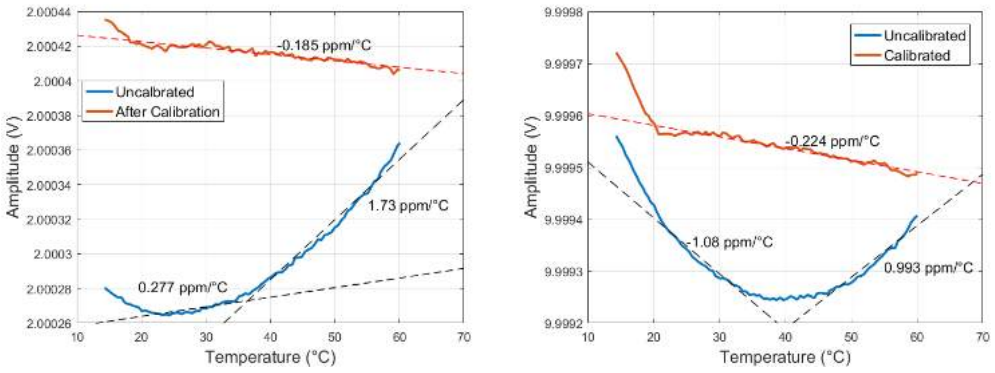

(a) (b)

Figure 3.20: Intrinsic (non-compensated) and corrected (compensated) pulse amplitude thermal drift, in blue and orange respectively. The plot are shown for low (2 V, on the left) and high amplitudes (10 V, on the right). The drift is properly over-compensated to correct for the pulse width instability.

Figure 3.20 shows the voltage thermal drift compensation performance obtained for both low (Fig. 3.20.a) or high (Fig. 3.20.b) output levels. Note that the voltage drifts is deliberately under-compensated, so that the effect of pulse width linear and positive thermal drift coefficient is also compensated. As expected, the thermal compensation is

effective in the temperature range from 20°C to 60°C. The vertical separation between the two curves is adjusted to compensate for any initial offset so to keep the zero-amplitude level as close as possible to the ground reference.
The calibration procedure allows to reduce the thermal drift of the pulse energy by an order of magnitude, i.e. at the level of ~ 0.1 ppm/°C. The thermal calibration procedure turned out to be very effective for all the CUORE pulser board, as shown in Fig. 3.21. The residual thermal drift coefficient distribution is obtained by measuring it in both the DAC outputs on all the 23 CUORE pulser board (20 planned to be used plus 3 boards for spares), for a total of 46 calibrated channels. Since the contribution of the voltage reference changes its polarity around 35-40 °C, the intrinsic thermal drift coefficient distribution is shown considering separately the results obtained at lower or higher temperature range domain. As it can be observed, the intrinsic thermal drift coefficient is $\sim \pm 5 - 6$ ppm/°C. As shown in Fig. 3.21.b, the residual thermal drift coefficient is $\sim \pm 0.3$ ppm/°C, more than an order of magnitude lower than the performance measured before the calibration.

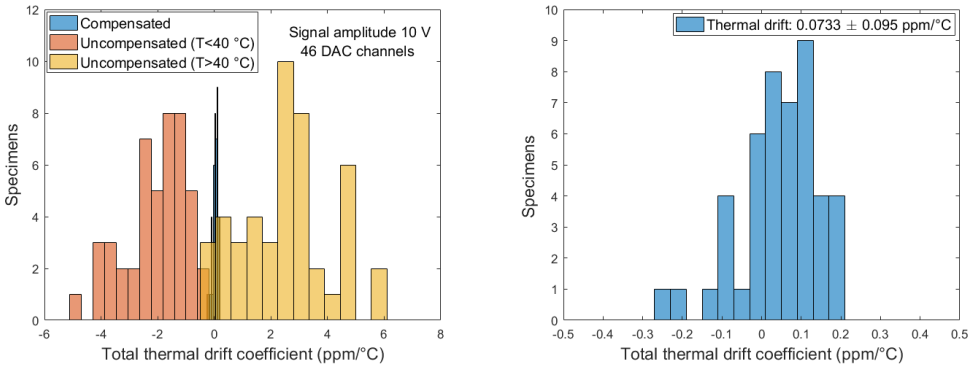

(a) (b)

Figure 3.21: Efficacy of the thermal drift correction on the whole pulser board lot. Plot (a) shows the superposition of the intrinsic thermal drift distribution at low ($T < 40°$ C, orange histogram) and high temperature ($T > 40°$ C, yellow histogram). The blue histogram is the residual thermal drift distribution of the same board after performing the thermal drift compensation. Plot (b) shows the same result for the compensated board. The residual drift is off the order of 0.1 ppm/°C.

3.5.3 Energy resolution

Beside the calibrating pulse stability, the pulser must maximize the reproducibility of the calibrating pulses. Indeed, considering a sequence of identical pulses, any amplitude or width fluctuation with respect to their nominal value would result in a random variation of the energy delivered to the bolometers and, consequently, in the deterioration of the

energy resolution of the calibrating peak in the acquired energy spectrum. In principle, this effect can be mitigate by sending a large number of calibrating pulses and taking the average energy provided by each pulse. However, a similar procedure is clearly troublesome and, for practical reasons, cannot be pursued in a large scale experiment such as CUORE. On the other hand, if the fluctuation of the energy supplied by identical calibrating pulses is much lower than the intrinsic bolometer resolution (few keV), then the the pulser board negligibly contribute to the final peak energy resolution. In this case, the energy resolution of the calibrating peak would allow to evaluate the intrinsic resolution of the detector and thus similar to the detector baseline resolution.
Concerning the contribution of the pulser board, the fluctuation of energy delivered is due to the stochastic variation of the pulse amplitude (V) and width (T). From Eq. 3.12, the energy fluctuation can be express as:

$$\frac{dE}{E} = 2\frac{dV}{V} + \frac{dT}{T} \tag{3.19}$$

where dV is the effective electric noise, dT the fluctuation of the pulse width. The contribution of these two sources of uncertainty will be studied separately in the next sections.

Electric noise effects

The main source of energy fluctuation can be ascribed to the electric noise of the pulser board which generates random additional power heating the bolometers. Since the effects of the electric noise on the edges of the pulse will be studied in the next section, the following dissertation is based on the assumption that the calibrating pulse is ideally rectangular. The noise injection from the pulser is due to two different effects: the output buffer noise, acting from the output relays connection to their release, and the noise of the reference voltage, which has to be taken into account only during the pulse delivery. Although the delay between the relay transition and the pulse generation can be remotely increased for debug purpose, by default the output relays are set 5 ms before the pulse generation and completely released 5 ms after the pulse falling edge. A typical pulse is at least 10 times shorter as its width ranges from about 100 μs up to 1 ms, so that each pulse delivery lasts about 10 ms independently of the energy injected. When the relays are released, the pulser outputs are totally disconnected from the heater resistor so that no further noise can be inject to the bolometers. Any power from the pulser boards is delivered in bunches of 10 ms each.
Since the relays are connected to the heaters for a period much shorter than the detector response ($\tau_B =\gtrsim 500$ ms), the total energy supplied by each pulse to the target bolometer can be calculated by taking the integral of the total power dissipated across the heater (as shown in Eq. 3.11). Assuming to connect the output relays at $t = 0$, in time domain the

voltage supplied by the n-th calibrating pulse at the output of the pulser can be expressed as:

$$\begin{aligned} V_n(t) = {} & B_n(t)[\theta(t) - \theta(t - T_1)] \\ & + [V + P_n(t)][\theta(t - T_1) - \theta(t - T_2)] \\ & + B_n(t)[\theta(t - T_2) - \theta(t - T_3)] \end{aligned} \tag{3.20}$$

where $B_n(t)$ and $P_n(t)$ are the n-th voltage noise sample superimposed to the baseline level and the pulse respectively, V and $T = T_2 - T_1$ the amplitude and width of the ideal square pulse, $T_1 \sim 5ms$ the relay setting time before the pulse generation and T_3 the instant of the relay disconnection ($T_3 - T_2 = 5$ ms). Basically, the pulser is connected to the heater at $t = 0$ but, because of the setting time of the mechanic relay, the pulse is generated 5 ms later. During this period the noise of the baseline ($B_n(t)$), due to the output buffers, is injected to the bolometers. Such contribution is taken into account in the first line of Eq. 3.20. At $t = T_1$ the calibrating pulse is generated till $t = T_2$. In this case, superimposed to the pulse amplitude, the noise $P_n(t)$ due to the buffers and the voltage reference must be considered (as expressed in the second line of Eq. 3.20). Between T_2 and the instant of the relay release (T_3) only the baseline noise contribution has to be taken into account (third line of Eq. 3.20).

The electric noise randomly changes the effective power delivered to the bolometer, which causes a statistical fluctuation of the corresponding energy detected among namely identical pulses. Providing a sequence of N identical pulses, the mean energy delivered is:

$$\overline{E}[eV] = \lim_{N\to\infty} \frac{1}{N} \sum_{n=1}^{N} \int_0^{\tau_B} \frac{\eta}{e\varepsilon^2 R} V_n(t)^2 dt \tag{3.21}$$

Substituing Eq. 3.20 in Eq. 3.21 we obtain:

$$\begin{aligned} \overline{E}[eV] = \frac{\eta}{e\varepsilon^2 R} \lim_{N\to\infty} \frac{1}{N} \sum_{n=1}^{N} \Bigg(& \int_{T_1}^{T_2} V^2 dt + \int_{T_1}^{T_2} P_n^2(t) dt \\ & + 2\int_0^{T_1} B_n^2(t) dt + 2V \int_{T_1}^{T_2} P_n(t) dt \Bigg) \end{aligned} \tag{3.22}$$

The electrical noise is a random and stationary effect whose statistics is described by a gaussian distribution centered at the zero baseline with a standard deviation equal to $\sigma = dP_{RMS}$. Hence:

$$\lim_{N\to\infty} \frac{1}{N} \sum_{n=1}^{N} \int_{T_1}^{T_2} P_n(t) dt = \lim_{N\to\infty} \frac{1}{N} \int_0^{NT} P_n(t) dt = 0 \tag{3.23}$$

where the first equivalent exploits the stationary property and the second one the zero mean value of $P_n(t)$ for long time of integration. Thus, Eq. 3.22 becomes:

$$\overline{E}[eV] = \frac{\eta}{e\varepsilon^2 R}\left[V^2 T + dP_{RMS}^2 T + 2dB_{RMS}^2 T_1\right] \tag{3.24}$$

Providing a large number of pulses, the peak acquired by the bolometer energy spectrum distribution is centered at $\overline{E}$, which is the sum of the energy provided by an ideal calibrating pulse and the root mean squared noise multiplied by the noise duration. Since, as will be shown soon, $dB_{RMS}/V < dP_{RMS}/V \leq 10^{-4}$, the power injected by the pulse is at least 8 order of magnitude larger than that ascribed to the noise. Thus, the noise contribution to the average calibrating energy is of the order of 0.01 ppm and thus can be totally neglected.

It is more interesting to evaluate the noise contribution to the intrinsic energy resolution of the pulser peak, in order to compare it with respect to the detector intrinsic resolution. The variance of the energy delivered after N identical pulses affected by electrical noise is defined as:

$$dE^2[eV] = \lim_{N\to\infty} \frac{1}{N} \sum_{n=1}^{N} \left(\int_0^{\tau_B} \frac{\eta}{e\varepsilon^2 R} V_n(t)^2 dt - \overline{E} \right)^2 \tag{3.25}$$

Thus:

$$\begin{aligned} dE^2[eV] = \left(\frac{\eta}{e\varepsilon^2 R}\right)^2 \lim_{N\to\infty} \frac{1}{N} \sum_{n=1}^{N} \Bigg(& \int_{T_1}^{T_2} P_n^2(t)dt + 2\int_0^{T_1} B_n^2(t)dt \\ & + 2V\int_{T_1}^{T_2} P_n(t)dt - dP_{RMS}^2 T - dB_{RMS}^2 T_1 \Bigg)^2 \end{aligned} \tag{3.26}$$

Since, as mentioned, the pulse amplitude is about 4 orders of magnitude larger than the voltage noise, the variance is largely dominated by the term $2V\int_{T_1}^{T2} P_n(t)dt$. Hence, assuming $V \gg P_n \geq B_n$ we obtain:

$$dE^2[eV] = \left(\frac{\eta}{e\varepsilon^2 R}\right)^2 \lim_{N\to\infty} \frac{1}{N} \sum_{n=1}^{N} \left(2V\int_{T_1}^{T_2} P_n(t)dt \right)^2 \tag{3.27}$$

Similar to the previous calculations, we can use the noise stationarity and exploit that it does not change under translations in time. Thus:

$$dE^2[eV] = \left(\frac{\eta}{e\varepsilon^2 R}\right)^2 \lim_{N\to\infty} \frac{1}{N} \sum_{n=1}^{N} \left(2V\int_{0}^{T} P_n(t)dt \right)^2 \tag{3.28}$$

In order to solve the integral factor, we consider $P_n(t)$ as the inverse Fourier transform of its $\hat{P}_n$ coefficients, whose dimension is V/Hz. In particular:

$$\begin{aligned} \int_0^T P_n(t)dt &= \int_0^T \left(\frac{1}{2\pi} \int_{-\infty}^{+\infty} \hat{P}_n(\omega) e^{i\omega t} d\omega \right) dt \\ &= \int_0^T \left(\frac{1}{\pi} \int_0^{+\infty} \hat{P}_n(\omega) e^{i\omega t} d\omega \right) dt \end{aligned} \tag{3.29}$$

The last equation exploits that $\hat{P}_n(\omega) = \hat{P}_n{}^*(-\omega)$, following by the real domain of $P_n(t)$. Considering the white noise contribution inside the bandwidth of the pulser (named $\omega_P = \tau_P^{-1}$), we can consider $\hat{P}_n$ independent of ω and neglect all the noise contribution due to frequencies larger than ω_P. Thus:

$$\begin{aligned}\int_0^T P_n(t)dt &= \frac{1}{\pi}\int_0^T \left(\int_0^{\omega_P} \hat{P}_n e^{i\omega t}d\omega\right) dt \\ &= \hat{P}_n \frac{1}{\pi}\int_0^{\omega_P} \left(\int_0^T e^{i\omega t}dt\right) d\omega \\ &= \hat{P}_n \frac{1}{\pi}\int_0^{\omega_P} \frac{2}{\omega} sin(\frac{\omega T}{2}) e^{i\omega T/2} d\omega\end{aligned} \tag{3.30}$$

The last integral cannot be analytically calculated since its antiderivative cannot be expressed in terms of elementary functions. To obtain a first order estimation, we shall consider two limit cases which make easier the resolution of Eq. 3.30. In particular:

$$\begin{aligned}\omega \gg T^{-1} \rightarrow \ & \frac{sin(\omega T/2)}{\omega} \sim 0 \\ \omega \ll T^{-1} \rightarrow \ & \frac{sin(\omega T/2)}{\omega} \sim \frac{T}{2} \ \text{ and } \ e^{i\omega T/2} \simeq 1\end{aligned} \tag{3.31}$$

Hence, the integrand differs from zero for those frequencies whose period is much larger than the pulse width. On the contrary, larger frequencies gives a negligible contribution since their effects averages to zero during the pulse delivery. Thus:

$$\int_0^T P_n(t)dt \sim \hat{P}_n \frac{1}{\pi}\int_0^{1/T} 2\frac{T}{2} d\omega = \frac{\hat{P}_n}{\pi} \tag{3.32}$$

And finally:

$$\begin{aligned}dE^2[eV] &= \left(\frac{\eta}{e\varepsilon^2 R}\right)^2 4V^2 \lim_{N\to\infty} \frac{1}{N}\sum_{n=1}^{N} \frac{\hat{P}^2}{\pi^2} \\ &= \left(\frac{\eta}{e\varepsilon^2 R}\right)^2 4V^2 \frac{\overline{\hat{P}_n^2}}{\pi^2}\end{aligned} \tag{3.33}$$

The $\hat{P}$ coefficients can be calculated using the Parseval's theorem:

$$\begin{aligned}\frac{1}{2\pi}\int_{-\infty}^{+\infty} |\hat{P}_n|^2 d\omega &= \int_{-\infty}^{+\infty} |P_n(t)|^2 dt \\ \frac{1}{\pi}\int_0^{\omega_P} |\hat{P}_n|^2 d\omega &= \int_0^T |P_n(t)|^2 dt\end{aligned} \tag{3.34}$$

Considering the mean values, Eq. 3.34 implies:

$$\frac{\omega_P}{\pi}\overline{\hat{P}^2} = dP_{RMS}^2 T \tag{3.35}$$

Substituting Eq. 3.35 in Eq. 3.33, we obtain:

$$dE^2[eV] = \frac{4}{\pi}\left(\frac{\eta}{e\varepsilon^2 R}\right)^2 \frac{V^2 T dP_{RMS}^2}{\tau_P} \tag{3.36}$$

so that:

$$\left(\frac{dE}{E}\right)^2 = \frac{4}{\pi}\frac{dP_{RMS}^2}{V^2 T \tau_P} \propto \overline{E}^{-1} \tag{3.37}$$

Since the relative resolution is inversely proportional to the square root of the pulse energy, the signal to noise ratio increases at higher energies. Moreover, in first order approximation and as far as the voltage noise is concerned, the pulse resolution does not depend on the pulse amplitude or width, whatever combination of V and T has been chosen.
Note that, since $(dE/E)^2 = 4(dV/V)^2$, we obtain that:

$$dV^2 = \frac{1}{\pi}\frac{\tau_P}{T} dP_{RMS}^2 = \frac{1}{\pi}\frac{\omega_N}{\omega_P} dP_{RMS}^2 \tag{3.38}$$

It means that the effective voltage noise (dV) does not coincide with the RMS value calculated over the whole pulser bandwidth (dP_{RMS}), since the high frequency noise is filtered by the bandwidth of the delivered pulse. Indeed, Eq. 3.38 implies that the effective noise bandwidth does not extends up to the output stage bandwidth ($\omega_P = \tau_P^{-1} \simeq 10^6$ Hz), but it is limited by the calibrating pulse width ($\omega_N = T^{-1} \simeq 10^3 - 10^4$ Hz). This effect reduces the effective noise by at least two orders of magnitude with respect to the RMS noise measured from a static DC level.

Let us calculate the expected RMS noise to be substituted in Eq. 3.38. Figure 3.22 shows the most important sources of noise that have to be taken into account.
The first contribution is due to the 5 V reference regulator and the low noise, high precision, OPA140 operational amplifier (U_1) buffering this reference value. These contributions are depicted as voltage sources named e_{REG} and $e\pm$ at the input nodes of U_1. As mentioned, two LTC6655 linear regulator are used in parallel in order to reduce their noise contribution by $\sim 30\%$. From the noise declared by the manufacturer, the total white noise of the reference block amounts to $e_{REF} \sim 100$ nV/$\sqrt{\text{Hz}}$. The reference voltage is filter by a RC low-pass filter ($R = 50\ \Omega$, $C = 10\ \mu$F, cut-off frequency $f \sim 300$ Hz) which makes the reference white noise negligible over few hundreds Hz. The high frequency white noise of the voltage reference stage is dominated by the buffer contribution ($e_+ = e_- = 5$ nV/$\sqrt{\text{Hz}}$). At the negative output V_-, the noise of the reference block (e_{REF}) depends on the R_{DAC} adjustable resistor (from 10 kΩ up to an open circuit) or, equivalently, to the output voltage level. In particular:

$$e_{REF}\Big|_{V-} = \begin{cases} \frac{|V_-|}{V_{REG}}\sqrt{e_+^2 + e_-^2 + e_{REG}^2} = 0 - 100\ \text{nV}/\sqrt{\text{Hz}} & \text{if } f < 300Hz \\ \frac{|V_-|}{V_{REG}}\sqrt{e_+^2 + e_-^2} = 0 - 7\ \text{nV}/\sqrt{\text{Hz}} & \text{if } f > 300Hz \end{cases} \tag{3.39}$$

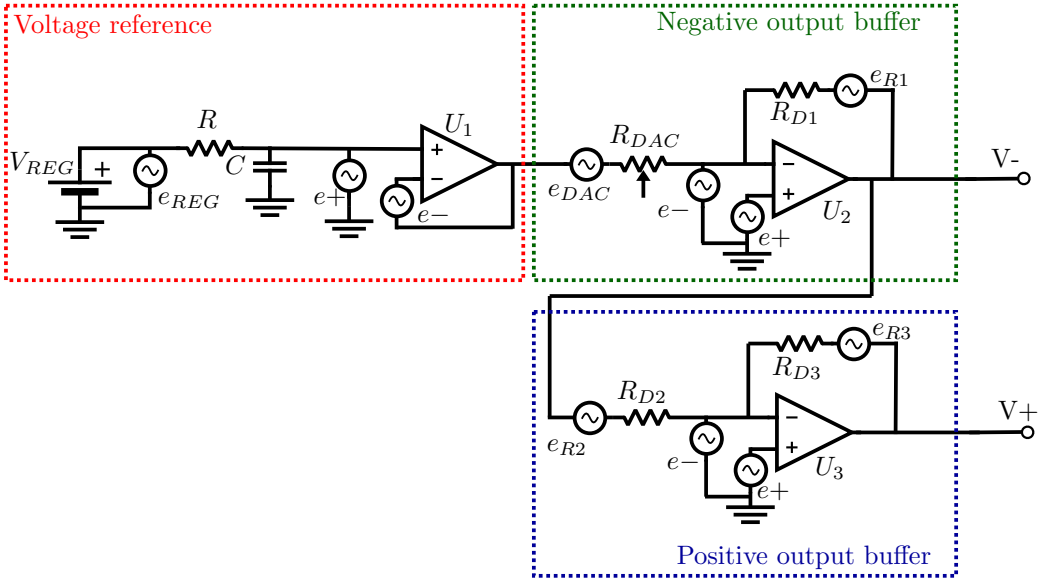

Figure 3.22: Simplified schematic of a pulser board channel. The most important noise sources are pointed out.

The second noise contribution is ascribed to the negative output buffer stage, due to the Johnson noise of the R_{DAC} and $R_{D1} = 10$ kΩ resistors and the input series noise of the OPA140 operational amplifier U_2. At $V-$, the negative output buffer noise ($e_{B\_}$) at room temperature is given by:

$$e_{B\_}\Big|_{V-} = \frac{|V\_|}{V_{REG}} e_{DAC} + e_{R1} + \left(\frac{|V\_|}{V_{REG}} + 1\right)\sqrt{e_+^2 + e_-^2} = 14 - 22\ \frac{\text{nV}}{\sqrt{\text{Hz}}} \tag{3.40}$$

Since the noise contributions of the voltage reference and the negative buffer blocks are uncorrelated, the total expected noise at the output is given by the $e_{V\_} = \sqrt{e_{REF}^2 + e_{B\_}^2}$, given from Eq. 3.40 and Eq. 3.39. Above 300 Hz, the final noise expected at $V\_$ ranges from 14 nV/$\sqrt{\text{Hz}}$ to 24 nV/$\sqrt{\text{Hz}}$ as a function of the desired output signal. The noise at the negative pulser output was measured by amplifying it with a low noise OP27 operational amplifier (in inverting configuration, close-loop gain of 20 V/V) and acquiring the final signal with an Agilent 4395A spectrum analyzer in the frequency range 10 Hz - 5 MHz. The additional amplification stage, coupled in AC through a 2200 μF capacitor, is useful to increase the noise at the output of the pulser board with respect to that due to the spectrum analyzer and the OP27 amplifier. The acquired power noise spectrum referred to the pulser output node can be easily calculated by dividing the outcomes by the close-loop gain. Figure 3.23.a shows the noise power spectra distribution observed at $V\_$ at various output static values. As expected, at low frequency the noise increases because of the contribution of the unfiltered voltage regulator up to ~ 100 nV/$\sqrt{\text{Hz}}$. This effect is also proportional to the signal amplitude since the contribution of the voltage reference is less attenuated increasing the output signal. Figure 3.23.b compares the expected and

measured RMS white noise (calculating in a bandwidth ranging form 1 kHz to 50 kHz) as a function of the signal amplitude. The expectations are in good agreement with the measurement.

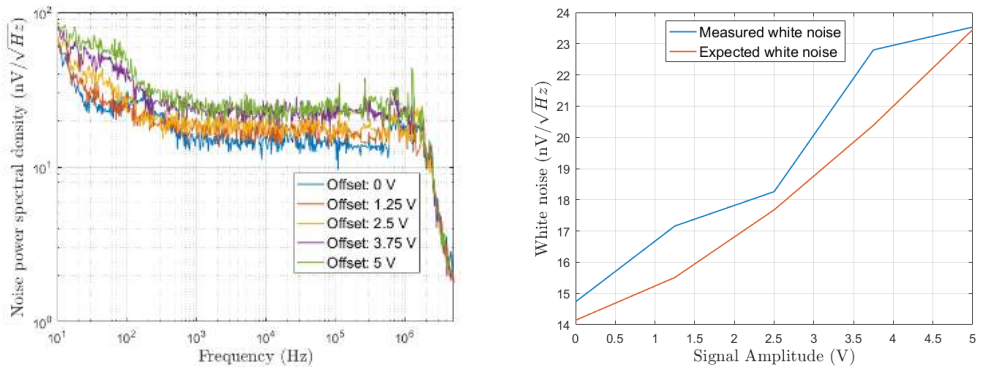

(a) (b)

Figure 3.23: On the left, noise power spectra density at different amplitude measured at node V_-. On the right, the expected and measured white noise as a function of the signal amplitude.

As well as the signal, the noise at the negative output is injected at the input of the inverting positive output buffer stage. In addition, the positive output buffer stage contributes to the total noise with the Johnson noise of the $R_{D2} = R_{D3} = 20$ kΩ resistors and the input series noise of the OPA140 operational amplifier U_3. Omitting the amplitude-dependent contribution coming from the negative output, the positive output buffer noise (e_{B_+}) at room temperature referred to the positive output is given by:

$$e_{B_+}\Big|_{V+} = \sqrt{e_{R2}^2 + e_{R3}^2 + 8e_+^2} = 29 \ \frac{\text{nV}}{\sqrt{\text{Hz}}} \tag{3.41}$$

Since the buffer works in unitary gain configuration, the total noise contribution at the positive output is given by $e_{V_+} = \sqrt{e_{B_+}^2 + e_{V_-}^2}$, so that a slight dependence on the signal amplitude is expected. The noise power spectral distribution was measured using the same setup described above. Figure 3.24 shows the acquired noise power spectral distribution at various signal amplitude and the expected and measured white noise with respect to the signal amplitude. A good agreement between real data and theoretical calculations has been verified.

In the final operative case, the two output nodes are connected to the heater resistance terminals in oder to generate a differential signal ranging from 0 to 10 V. Thus, the electrical noise measured to each node must be used to calculate the total noise referred to $\Delta V = V_+ - V_-$ signal. Since the negative output voltage is driven at the input of the inverting positive buffer stage, the noise contributions at the two output terminals are

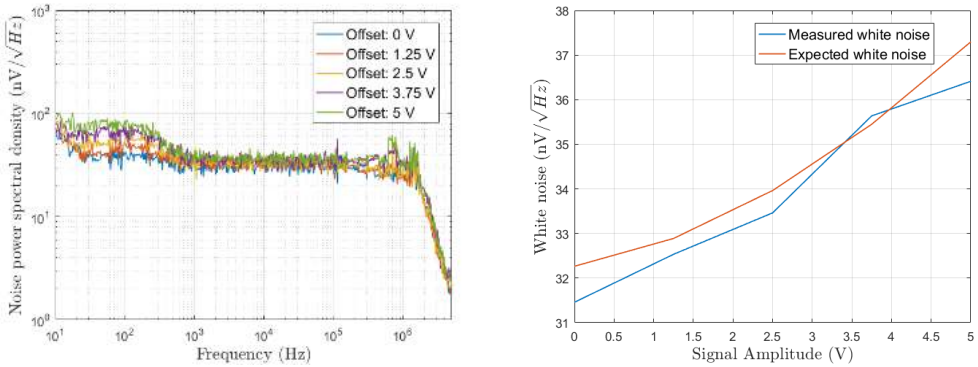

(a) (b)

Figure 3.24: On the left, noise power spectra density at different amplitude measured at node V_+. On the right, the expected and measured white noise as a function of the signal amplitude.

fully correlated. In particular the noise at $V-$ affects both terminals, thus its weight is doubled with respect to the total noise. On the other hand, the noise of the positive output buffer is independent to the other contributions and has to be quadratically summed to the variance of the negative node.

$$e_W = \sqrt{e_{B_+}^2 + 4\left(e_{REF}^2 + e_{B_-}^2\right)} = \begin{cases} 40 - 200 \text{ nV}/\sqrt{\text{Hz}} & \text{if } f < 300Hz \\ 40 - 55 \text{ nV}/\sqrt{\text{Hz}} & \text{if } f > 300Hz \end{cases}$$

where e_{REF}, e_{B_-} and e_{B_+} are given from Eq. 3.39, Eq. 3.40 and Eq. 3.41 respectively. Figure 3.25 shows the acquired noise power spectral distribution measured at various signal amplitudes. A OP27 OPAMP, mounted in differential configuration was used to amplify the noise difference between the two output pins prior the noise power spectrum acquisition. A good agreement between real data and the mathematical model has been verified.

Considering a 10 MeV calibrating pulse of $V = 10$ V and $T = 100$ μs, the most important contribution is due to the high frequency white noise, which amounts to $\sigma_W \sim 50$ nV/$\sqrt{\text{Hz}}$. Under such hypothesis, Eq. 3.37 allow us to calculate the intrinsic pulse energy resolution due to the electrical noise. In particular, substituting Eq. 3.12 in Eq. 3.37, one obtains:

$$\frac{dE}{E} = \frac{2}{\sqrt{\pi}} \frac{dV_{RMS}}{\sqrt{\omega_P}} \frac{\sqrt{\eta}}{\sqrt{e\varepsilon^2 R}} \frac{1}{\sqrt{E}} \tag{3.42}$$

where $dV_{RMS}/\sqrt{\omega_P} = \sigma_W \sim 50$ nV/$\sqrt{\text{Hz}}$ is the power spectral noise contribution. Substituting all the parameters with their typical values ($\eta = 0.20$, $e = 1.6 \cdot 10^{-19}$ C, $\varepsilon = 200$ V/V and $R = 25$ kΩ), it can be calculated that:

$$\frac{dE}{E} = \frac{2 \cdot 10^{-3}}{\sqrt{E}} \tag{3.43}$$

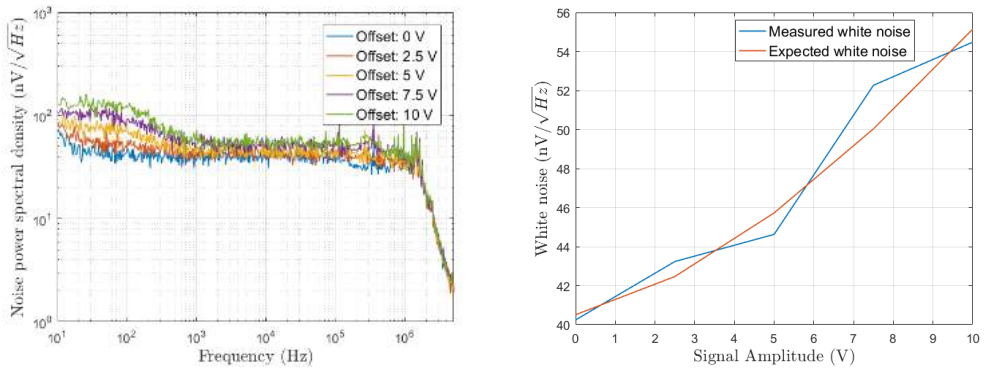

(a) (b)

Figure 3.25: On the left, noise power spectra density at different amplitude measured from the difference between V_+ and V_- terminals. On the right, the expected and measured white noise as a function of the signal amplitude. Unlike the previous plots, the differential voltage amplitude ranges from 0 to 10 V.

In this example, the calibrating pulse has an equivalent energy of 10 MeV (from Eq. 3.12) has an intrinsic resolution of ~ 0.6 ppm, or 6 eV_{RMS}. The energy resolution rises proportionally to the square root of the energy as $dE/E \sim 2$ ppm @ $E = 1$ MeV, $dE/E \sim 6$ ppm @ $E = 100$ keV and so on. In all these cases, the pulser contribution to the overall energy resolution is completely negligible with respect to that of the bolometer detectors, of the order of 2.2 keV_{RMS}.

Time fluctuation effects

According to Eq. 3.19, a fluctuation dT of the pulse width would cause an uncertainty of the energy delivered by the pulse and, consequently, a deterioration of the resolution of the calibrating peak in the acquired energy spectrum. As mentioned in Sect. 3.5.1, this signal is provided by the precise 1 MHz oscillator HC536R-1, from FXO Electronics, which feeds the fast NC7SV74K8X flip-flop from Fairchild Semiconductor. This architecture ensures both a very precise phase stability, only dependent on the oscillator performance, and fast rise and fall time transitions, limited by the output buffer stage bandwidth to $t_r \simeq t_f \sim 250$ ns. Indeed, the output buffer bandwidth is set to $\omega_P \sim 1.3$ MHz in order to ensure high phase margin and low ringing during the pulse transitions.
The time fluctuation has been estimated by acquiring a sequence of a thousand of identical pulses with the Rohde&Schwarz RTO 1044 oscilloscope (4 GHz bandwidth, 10 GHz/Ch sample frequency, 7 effective number of bits). The oscilloscope operated in High Resolution mode, so that the vertical resolution was nominally increased up to 14 equivalent bits, provided that the bandwidth is reduced to 100 MHz. The oscilloscope was set to fully exploit

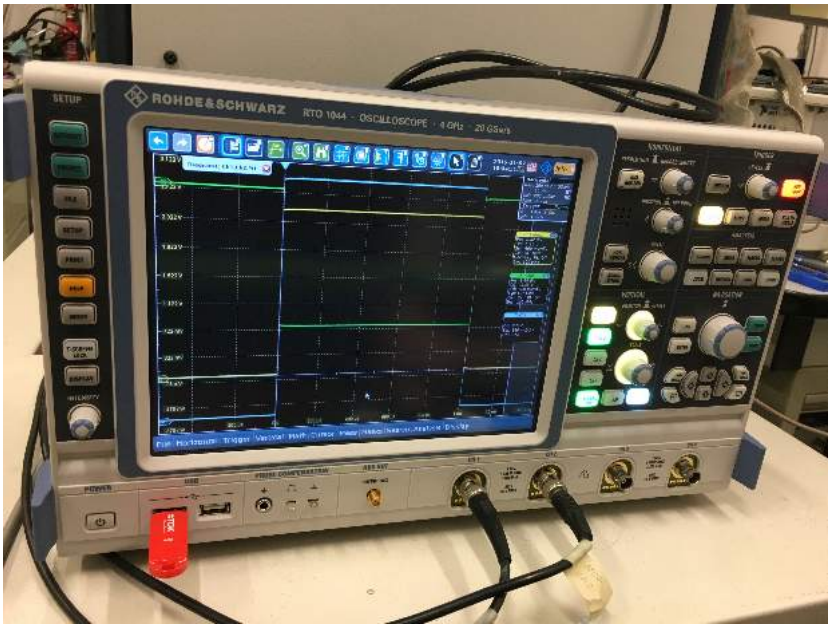

Figure 3.26: Picture of the setup used to measure the time width fluctuation. The differential signal (blue line) is obtained as the difference between the positive (yellow) and negative (green) output pins.

its recording buffer so that 10^7 samples are stored for each trigger. The acquiring window exceeded the pulse width and amplitude by 10%, in order to minimize the uncertainties related to the discrete sampling and the limited vertical resolution. The pulses can be triggered when crossing a settable threshold (V_α), equal to a desired fraction (α) of the pulse amplitude (V), so that $\alpha = V_\alpha/V$. The pulse width (T) is measured as the time difference between the two triggers during the rise and fall transitions. Since, in case of stochastic fluctuation, the pulse width distribution is described by a Gaussian function, the observed time fluctuation dT_O is obtained as the standard deviation of the pulse width distribution.

dT_O is due to two uncorrelated effects:

- dT_T is directly referred to the uncertainties affecting the time dimension. The first contribution to be taken into account is the phase stability of the reference oscillator (dT_p). According to the datasheet provided by the manufacturer, the HC536R-1 ensures a phase stability of 25 ppm with respect to the clock nominal frequency (1 MHz). The second contribution is the oscilloscope resolution on the horizontal axes (time scale). In particular, the finite record buffer length and the sample frequency limit the maximum sample frequency to the ratio between the acquiring window width and the memory buffer length. For instance, for pulse widths of 500 μs, the oscilloscope time resolution is dT_{osc} =55 ps. Note that such uncertainties affect both

transitions of the calibrating pulse, so that the total pulse width fluctuation is given by:

$$dT_T = \sqrt{2(dT_p^2 + dT_{osc}^2)} \sim 85\,\text{ps}. \tag{3.44}$$

- dT_n is related to the electric noise and the finite bandwidth of the output buffer stage. The pulse width is evaluated using a fixed voltage threshold. If the transitions were ideally vertical (infinite pulser bandwidth), then the voltage noise would have not been able to affect the measurements. On the contrary, given a finite bandwidth, the trigger time fluctuates as a consequence of the vertical position uncertainty of the trigger point due to the electric noise. A quantitative estimation of this effect is given by:

$$dT_N\Big|_\alpha = \left(\frac{dV}{dt}\right)^{-1}\Big|_{t_\alpha} dV \tag{3.45}$$

where t_α is the trigger time at the trigger threshold $V_\alpha = \alpha V$, with $0 < \alpha < 1$ and dV is the RMS noise at the oscilloscope input.
Considering the rising front of the pulse:

$$V(t) = V(1 - e^{-t/\tau}) \rightarrow \frac{dV}{dt}(t) = \frac{V}{\tau}e^{-t/\tau} \tag{3.46}$$

The trigger time on the rising edge can be calculated from Eq. 3.46, hence:

$$t_\alpha = -\tau ln(1 - \alpha) \tag{3.47}$$

Substituting Eq. 3.46 and Eq. 3.47 in Eq. 3.45, one obtains:

$$dT_{N,R}\Big|_\alpha = \frac{\tau}{V(1-\alpha)}dV \tag{3.48}$$

Equation 3.48 gives the time fluctuation of the trigger point on the rising front of the pulse. One shall use the same methodology to calculate the time fluctuation of the trigger point on the falling edge of the pulse, described by:

$$V(t \geq T) = Ve^{-(t-T)/\tau} \rightarrow \frac{dV}{dt}(t) = -\frac{V}{\tau}e^{-(t-T)/\tau} \tag{3.49}$$

One can calculate the noise effect of the falling edge trigger point as:

$$dT_{N,F}\Big|_\alpha = \frac{\tau}{V\alpha}dV_{RMS} \tag{3.50}$$

Since the noise effects on the falling and rising fronts are uncorrelated, the pulse width fluctuation is given by the square root of the sum of the variance given by Eq. 3.48 and Eq. 3.50, hence:

$$dT_N^2\Big|_\alpha = \left[\frac{(1-\alpha)^2 + \alpha^2}{(1-\alpha)^2\alpha^2}\right]\frac{\tau^2}{V^2}\,dV^2 \tag{3.51}$$

Note that $dT_N^2|_\alpha$ has a minimum for $\alpha = 0.5$. In this case, Eq. 3.51 becomes:

$$dT_N^2\Big|_{\alpha=0.5} = 8\,\frac{\tau^2}{V^2}\,dV^2 \tag{3.52}$$

Note that dV^2 is the RMS electrical noise read by the RTO 1044 oscilloscope. Thus:

$$dV^2 = dV_{RMS}^2 + dV_{Osc,pre}^2 + dV_{Osc,dig}^2 \tag{3.53}$$

where $dV_{RMS} \sim 100$ μV is the pulser RMS noise calculated over the output buffer full-bandwidth ($\tau_P = 1.3$ MHz), $dV_{Osc,pre}$ is the RMS noise if the oscilloscope analog front-end circuit and $dV_{Osc,dig}$ is the RMS voltage resolution of the oscilloscope ADC. The two latter contributions are calculated over the full oscilloscope bandwidth (up to 100 MHz) . Note that, named V the amplitude of the pulser signal, dV_{RMS} slightly increases with V (as shown in the previous section), $dV_{Osc,dig} = \gamma V$ ($\gamma \sim 400$ μV/V, according to the manufacturer specs) since the equivalent voltage step of the less significant bit is proportional to the vertical scale set up to the oscilloscope, while $dV_{Osc,pre}$ is independent of V so that its contribution becomes negligible with respect to $dV_{Osc,dig}$ at large signal amplitudes.

The two contributions are independent, so that dT_O is given by the square root of the sum of the variance related to each of them. From Eq. 3.44, Eq. 3.52 and Eq. 3.53 one obtains:

$$\begin{aligned} dT_O^2 &= dT_T^2 + dT_N^2\Big|_{\alpha=0.5} \\ &= 2dT_p + 2dT_{osc} + \frac{8\tau_P^2}{V^2}\left(dV_{RMS}^2 + dV_{Osc,pre}^2\right) + 8\tau_P^2\gamma^2 \end{aligned} \tag{3.54}$$

Equation 3.54 describes the jitter error experimentally measured at half of the pulse amplitude, univocally defined by $\alpha = 0.5$. The effective impact of such fluctuation to the pulse energy is lower (by a factor $\sim 68\%$ [63]), since the effects of one point of the pulse edge is partially compensated by the others. Moreover, dT_O decreases by increasing the signal amplitude and, neglecting all the contributions from the pulser board, has a minimum in $dT_O^2 = dT_T^2 + 8\tau_P^2\gamma^2 \sim 280$ ps, dominated by the voltage resolution of the RTO1044 oscilloscope. Thus, dT_O has to be considered as an upper limit of the intrinsic calibrating pulse fluctuation.

Figure 3.27 shows the typical pulse width distribution acquired with the RTO1044 oscilloscope generating a sequence of pulses, 10 V height, 250 ps wide. The measure was performed keeping the pulser board in a VOTSCH VT-7004 climatic camber, at a stable temperature of 20°C. The distribution is well described by a Gaussian function centered at the average measured pulse width, whose standard deviation $dT_O \sim 270$ ps describes the observed width fluctuation. Since the normal distribution fits the observed distribution, then the pulse width fluctuation is only due to random effects. In particular, neither clock transition miscounting nor missed triggers was observed. This proves the goodness of the

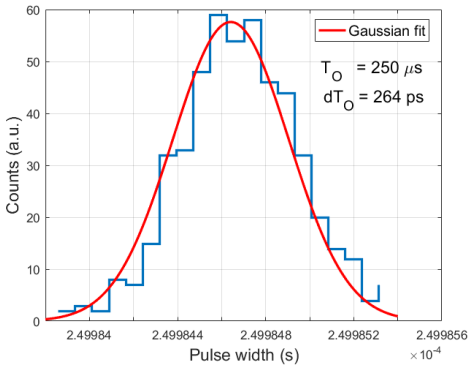

Figure 3.27: Pulse width distribution acquired recording 500 pulses, 10 V height, 250 μs wide. In red, the Gaussian function fitting the distribution. The measured average pulse width and its fluctuation is given from the center and standard deviation of the fit result.

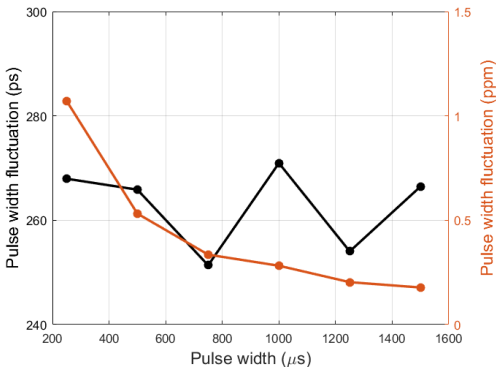

Figure 3.28: Pulse width distribution (500 pulses, 10 V height) as a function of the pulse width shown in absolute (black curve and left vertical axis) and relative (orange curve and right vertical axis) scale. For signals wider than $\sim$ 500 μs, the fluctuations stays below 0.5 ppm.

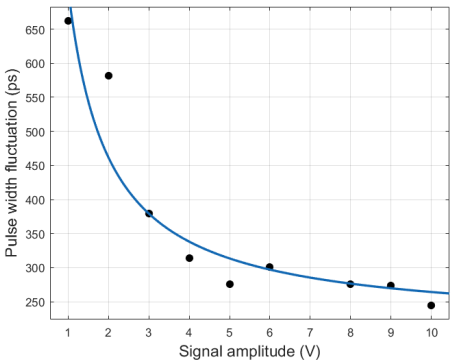

Figure 3.29: Pulse width distribution (500 pulses, 250 μs wide) as a function of the pulse amplitude. At larger amplitude value, the relative magnitude of the oscilloscope front-end noise decreases allowing to reaching enhanced sensitivities.

design hardware choice and the satisfactory operation of the firmware. This procedure has been repeated at various pulse width (T) and amplitude (V). The pulse width fluctuation as a function of T and V is shown in Fig. 3.28 and Fig. 3.29. dT_O remains constant with

respect to the pulse width and it is close to the maximum setup sensitivity, limited to ~ 280 ps by the resolution of the digital conversion. This proves that any contribution due to deterministic effects (such as reference clock instabilities) is lower than the measurement sensitivity. The observed pulse width fluctuation as a function of the signal amplitude, shown in Fig. 3.29, decreases inversely proportional to the pulse amplitude until reaching the best available sensitivity for signals larger than 4 V. The larger fluctuation at lower amplitude is due to noisy effects that are independent of the signal amplitude, such as the electric noise of the oscilloscope front-end or that of the pulser output buffer stage. Nevertheless, the contribution of the oscilloscope at low amplitudes is expected to be several times larger then that of the pulser board. A reasonable estimation of the observed pulse width fluctuation is $dT_O \sim 300$ ps, which represents the upper limit of the effective energy dispersion due to the width fluctuation. Considering a typical calibrating pulse of $T = 500$ μs, the expected contribution to the intrinsic calibrating energy resolution is:

$$\left(\frac{dE}{E}\right)_T \leq \frac{dT_O}{T} \sim 0.5\,\text{ppm} \tag{3.55}$$

3.6 Commissioning run and current state

At the end of 2015, a detector module was setup an tested in the CUORE cryostat. The prototype, called mini-tower, consisted of a 8-channel system of 2 out 13 floors of a complete CUORE tower (see Fig. 3.30). This run allowed to validate all the subsystem performance before the full detector assembly. The cryostat operation, the mechanical supports for the bolometers, the tower supper plate (TSP), most of the wires from the bolometers to the front-end electronics, the whole electronics architecture and the DAQ system were tested and commissioned.

The cryostat was capable to reach a baseline temperature of the order of 6.3 mK, allowing to acquire the first physics data using the CUORE cryogenic system. The power supply chain, the front-end electronics and the bessel filter boards were mounted and behaved satisfactorily. The optical decoupled CAN bus communication apparatus, controlled by the slow control system based on the APOLLO software, worked correctly in the complete CUORE system, even when several treads are asynchronously sanded on the bus. The small software and hardware bugs concerning the operation of the various devices in a realistic complete experimental environment were found and solved, so that a reliable and fully operational system was finally obtained. Beside the physical signals allowing to evaluate the background contribution, also the pulse generation board was tested. It was possible to use its signal to perform the stabilization of the detector response. Figure 3.31 shows the results obtained. About 500 identical pulses were delivered to each channel for every dataset and so the resolution of the pulser line in the energy spectrum can be evaluated and compared to the energy resolution of the detector baseline and of the

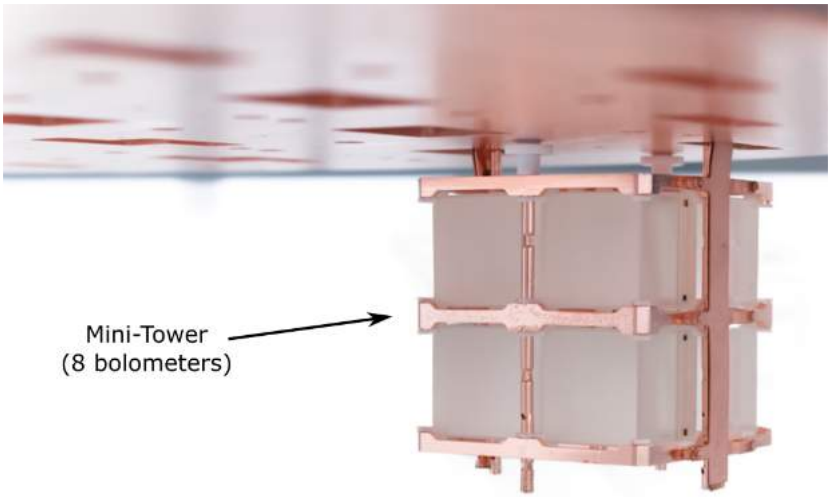

Figure 3.30: Picture of the mini-tower module hung up to the tower support plate (TSP).

background γ lines.

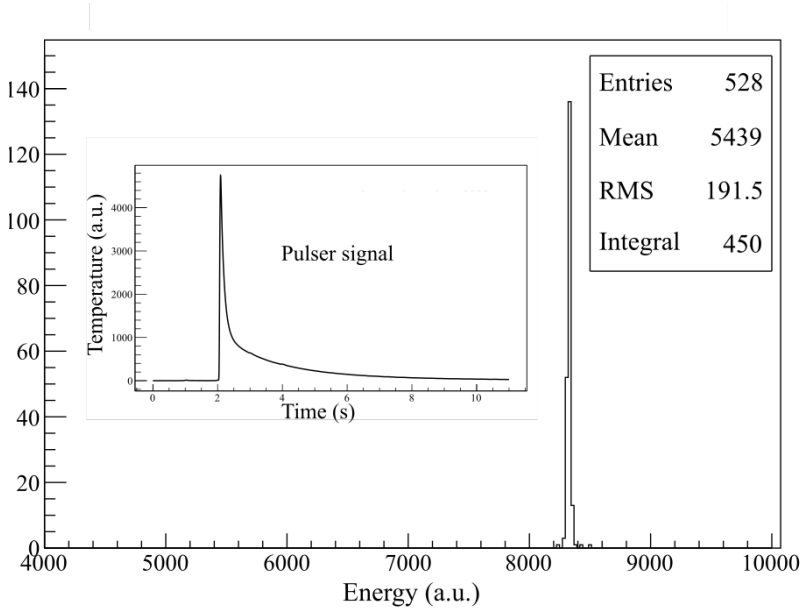

Figure 3.31: Pulser peak in the energy spectrum acquired during the commissioning run. The resolution of the line is compatible to the resolution of the baseline. The pulse waveform as a function of time is always shown. (Courtesy of M. Biassoni)

Table 3.1 shows the preliminary values of the energy resolution of the detector baseline, of the 2615 keV ^{208}Tl γ-line and the pulser, quoted as full width at half maximum (FWHM).

Channel	FWHM [keV] @ baseline	FWHM [keV] @ 2615 keV	FWHM [keV] @ pulser
01	7.5	9.2	8.3
02	8.3	9.0	9.0
03	24.7	27.6	26.3
04	10.3	14.1	12.0
05	11.8	25.4	14.0
06	14.7	16.4	17.8
07	24.7	16.6	27.3
08	26.4	30.0	35.6

Table 3.1: FWHM resolutions measured in all the mini-tower channels during the commissioning runs. Although it is larger than expected, the energy resolution of the pulser is totally dominated by that of the detector.

Except for few very noisy channels, the bolometers proved to be able to reach an energy resolution of $\sim$ 8 keV FWHM, a bit worse than that accomplished in the CUORE-0 experiment. Moreover, the energy resolution of the pulser peak is compatible with that of the baseline. We can conclude that the pulser negligibly contributes to the overall energy resolution, as expected, and can be used to stabilize the macro-bolometer response. The typical time-domain response of the detector to a calibrating pulse is shown in Fig. 3.31. The γ background turn out to be similar to that of CUORE-0. A finer analysis of the outcomes is still ongoing to evaluate the other background sources (as the signals induced from the α radiation emitted from 10 mK shield).
After this test run, the assembly and installation of all the boards of the CUORE took place and ended in the mid 2016, followed by the installation of the detector towers. The pictures shown in Fig. 3.32 were shot during the tower assembly and after getting the front-end tower in place.
Beside the towers, the mechanical components, the Faraday cage hosting the front-end electronics and the pulser boards, and all the electronics devices (including power suppliers, low-pass Bessel filters, DAQ boards and monitoring system) were set up. The communication from the slow control to the electronics board, based on the use of optical fibers, were set up and satisfactorily tested. Automatic procedures for the channel mapping and monitoring were developed and currently under commissioning. Figures 3.32 were taken from the second floor CUORE hut during the apparatus setting up. The assembly of the experiment was completed and the colling of the crystals to the baseline temperature started in December 2016.

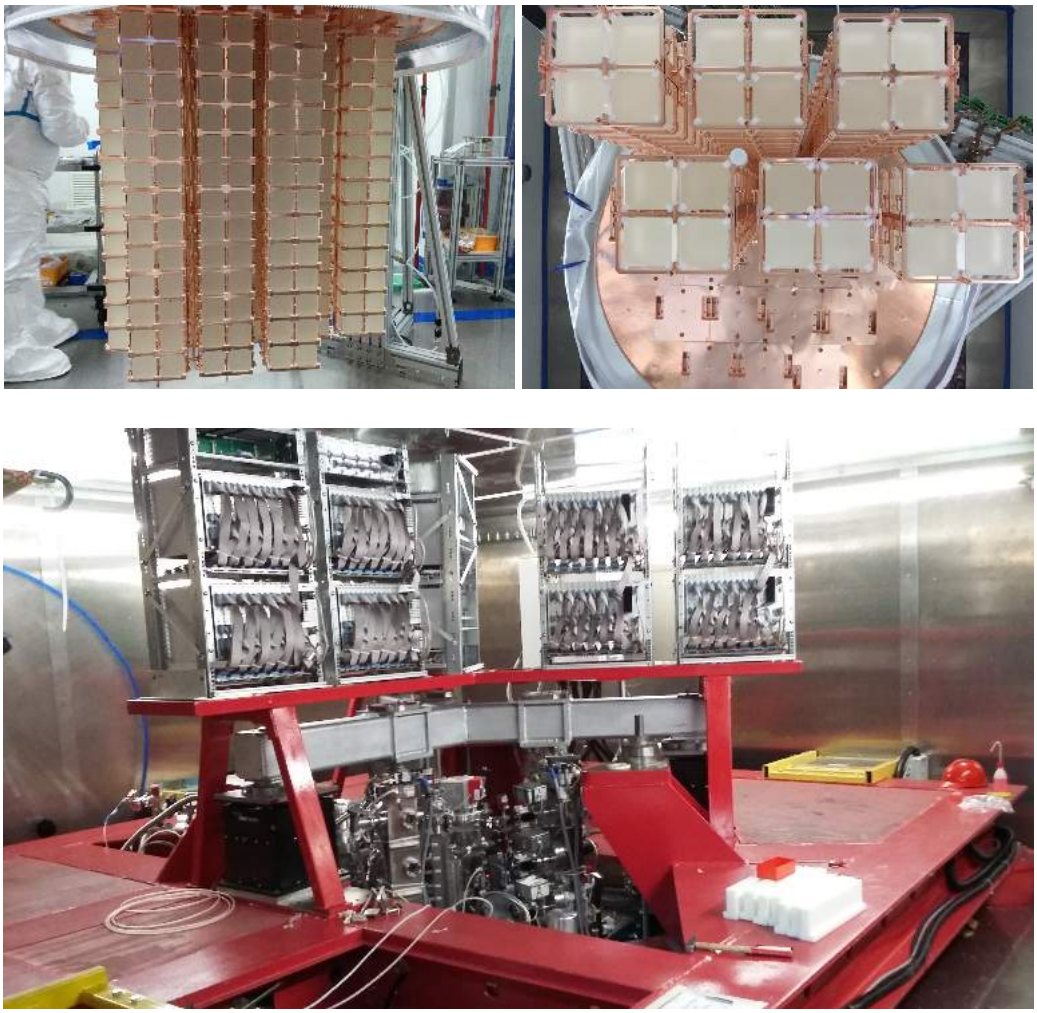

Figure 3.32: On the top, some pictures taken during the CUORE tower assembly. On the bottom, the front-end racks put in place above the cryostat and operating inside the Faraday cage.

Chapter 4

Conclusions and prospectives

Summary

The Standard Model is the most powerful theoretical architecture currently used to describe the subatomic particles and the interactions among them. Whist this structure has proved to be able to predict the majority of the detected phenomena, neutrino flavor oscillations and astrophysical observations cannot be explained without extending the Standard Model. To research for new physics, large particle physics experiments have been developed by worldwide collaborations. My PhD work has been particularly focused on the LHCb and the CUORE experiments, two examples of large scale researches for physics beyond the Standard Model.

LHCb is one of the four main detectors located at the Large Hadron Collider (LHC) at CERN. This experiment is particularly devoted to the research of CP violation and precise measurement of the Standard Model parameters in order to look for new physics by studying b and c flavor quark. In order to increase the maximum luminosity the detector is able to deal with, up to 10^{34} $\mathrm{cm}^{-2}\mathrm{s}^{-1}$ with 25 ns bunch spacing, an extensive detector upgrade is planned. My work has been focused on the upgrade of the photosensitive planes of the Ring Imaging Cherenkov (RICH) detectors. Such apparatus is a crucial tool for particle identification over a wide momentum range (from 2 GeV/c up to 100 GeV/c), since it allows to measure the speed of the high energy particles produced in the proton-proton collisions. The present RICH system uses Hybrid Photo Detectors (HPD) equipped with an encapsulated 1 MHz read-out chip. To fulfill the requirements of the upgraded detector, the HPDs will be replaced with flat panel Multi-anode Photo Multiplier Tubes (MaPMT) read out by an external Application-Specific integrated Circuit (ASIC), called CLARO, specifically designed for this purpose. The upgraded RICH photosensitive

planes will consist of ~ 3000 MaPMT grouped in a modular architecture where MaPMT and front-end electronics are arranged in 2×2 inches modules called Elementary Cells (ECs), representing the minimum autonomous and fully operational unit.

A full characterization of two MaPMT models, both produced by Hamamatsu, has been shown in this thesis. These studies took into account not only the main operational MaPMT parameters (sensitivity of single photon events, adequate gain, pixel response uniformity, low noise, moderate cross-talk and suitable quantum efficiency) but also the deterioration of the performance as a consequence of the critical environment condition expected in the final experimental setup. For such purpose the tolerance to magnetic field, including the design of shields for the field absorption, and the aging effects, due to the high pixel occupancy, were tested. These measurements drove the RICH Upgrade collaboration to the choice of using these devices as baseline photosensors for the upgraded detector. My work also included the design and test of the CLARO, the front-end ASIC chosen for the MaPMT read-out. The CLARO chip is an 8 channel custom designed ASIC realized in 0.35 μm CMOS technology from Austria Micro Systems (AMS). Such a relatively aged and inexpensive technology can still meet the LHCb requirements in terms of wide-bandwidth and low power, while ensuring a very high yield and a good tolerance to radiation. Despite its wide bandwidth, necessary to sustain a photon counting rate up to 40 MHz per channel, the power consumption in idle mode is low and amounts to about 1 mW per channel and it stays below 2 mW per channel even at a photon counting rate of 10 MHz. This feature ensures the minimization of the heat injection towards the MaPMT, avoiding the need for front-end cooling in such a closely packed system. The characterization and optimization of the circuit performance while operating in the EC has been shown in the thesis. The work included the development of two procedures which allow to calibrate on-site and in parallel all the MaPMT pixels and the electronic channels, in order to ensure the best performance during the whole data taking period. The system improvements were checked with beam tests at CERN. The setup proved the capability to detect Cherenkov rings with performance in agreement with the expectations.

CUORE (Cryogenic Undergrond Observatory for Rare Events), located at the Laboratory of Gran Sasso (LNGS), researches the neutrinoless double beta decay in ^{130}Te with a bolometric technique. Such decay, not foreseen by the Standard Model, would demonstrate the Majorana nature of the electronic neutrino, represent the first case of Leptonic number violation and allow to estimate the neutrino mass and identify its hierarchy. CUORE consists of 988 cubic crystals of TeO_2, organized in 19 towers of 4 columns and 13 floors each. Since the half-life of $0\nu\beta\beta$ decay in ^{130}Te is $\tau^{0\nu}_{1/2} > 2.9 \cdot 10^{24}$ yr, extremely low background, high energy resolution around the Q-value and high stability must be ensured over several years of data taking. This performance can be achieved not only by adopting low background techniques, but also by a proper design of the electronic equipments, from the bias power supply chain, to the signal amplification and digitalization. Considering the

large amount of channels, the electronic system should be fully controllable from remote and must be equipped with diagnostic tools, so that the operational parameters can be set and checked from the slow control system. This thesis presented my contribution to the development of such system. In particular, I took care of the design and optimization of the pulse generator board, used for the detector response stabilization. The pulser board simulates the thermal signal due to a particle interaction by exploiting the Joule effect by providing a very stable square voltage pulse across a heating resistor, thermally coupled to the crystal. Low noise and extremely high thermal stability ($\sim$ 0.5 ppm/°C) were obtained by a proper circuit design and after a thermal calibration procedure specifically developed. I also studied the communication between the whole electronic system and the unique slow monitoring center, based on the CAN-bus protocol. An HUB was designed to optically couple the remote control and the electronic system in order to prevent noise injection through the electrical ground, communicate with a desired subsystem, and easily connect the boards by means of very light optical connections thus reducing the intensity of the mechanical vibrations eventually induced in the sensitive area. My contribution also included the design of the diagnostic and protection board for the linear power supply used as reference for the thermistor bias. In all the above mentioned equipments, the operation and performance of the devices were tested in details by developing Graphical User Interface and automatic scripts. Together with the development of such electronic devices, I also actively contributed to put the whole system in place and operation at the LNGS, performing the quality assurance tests. The thesis also includes the outcomes achieved by the electronic system during the test runs at LNGS.

Prospectives

Although the systems developed for the Upgraded LHCb RICH detector and CUORE are ready to be used in the experimental context, further improvements and uses are already under study.

With the advent of the High Luminosity LHC (HL-LHC) from 2027, there is opportunity for a 50-fold increase in the luminosity at LHCb compared to the present, which would further physics goals. To cope with this challenge, the RICH system needs to be redesigned to improve the spatial resolution and reduce the occupancy. In this scenario two new upgrade phases could be foreseen: phase 1b could be introduced in Long Shutdown 3 (LS3) with a possible further upgrade in LS4, spanning a period between 2025 and 2035. In order to deal with much higher luminosities, increased mirror focal length and new photosensors with a improved granularity (pixel size $\sim$ 1 mm^2) must be considered [70]. Beside this, the Cherenkov angle resolution can be enhanced by reducing the pixel size, the chromatic dispersion of the Cherenkov medium and the photon emission point uncertainties. A possible approach consists in redesigning the optical system of the RICHs and exploiting

the photons emitted at those regions where the refractive index of the medium weakly depends on the photon wavelength ($\sim$ 550 nm). Since the number of emitted photons decreases at larger wavelengths, the new photodetectors must ensure a large photon detection efficiency. Silicon Photon Multipliers (SiPMs) are particularly promising to achieve such goals and affordable for large sensitive areas. The experience gained and the test benches developed for the MaPMT characterization will be very useful for the study of such sensors. In particular their time performance will be characterized using a pulsed laser, while dark counts can be study as a function of the temperature in a climatic chamber. Aging performance and radiation tolerance must also be carefully evaluated. An alternative solution consists in using the Micro-Channel Plate (MCPs) detectors. Such devices, whose operating principle is similar to the MaPMT, allow to achieve timing resolution of the order of few tens of picoseconds. This feature is particularly interesting since it would give the possibility to discriminate photons emitted by particles produced in two different primary vertexes of the same bunch, which would reduce the background and improve the Cherenkov angle reconstruction. Besides the photon sensors, the front-end electronics must also be upgraded. The CLARO must be adjusted to cope with the new detector granularity and the larger radiation levels. Moreover, a further improve would be the capability of discriminating among single or double photon detection. Such feature can be achieved by using a time-over-threshold technique or using a double discriminator threshold level (2-bits readout). The first approach exploits that the larger the charge collected at the CLARO input, the longer will be the digital pulse provided at the output, while the former consider the amplitude of the analog signal at the discriminator input. Further ideas and projects are currently under evaluation to cope with this challenge.

One of the most promising upgrade in the field of neutrino physics concerns the studies in the zero-background condition. Usually, such domain is achieved when only a single background event is expected in the energy region of interest during the whole life of an experiment. Background free condition would represent a huge step forward as the sensitivity to the $0\nu\beta\beta$ decay would increase proportionally to the active mass and observation time and not proportional to the square root of them. In order to run in such domain, it is necessary to discriminate the various source of background and reject them. Different approaches are currently under study and one of the most promising is based on scintillating bolometers. As in CUORE, the phonon signal is used to measure the energy spectrum. Beside this, the bolometer crystal emits light (scintillation effect) whose yield, for a fixed energy, only depends on the interacting particle. Thus, exploiting both thermal and light signals, high energy resolution and background recognition can be achieved. Several candidates are currently under investigation (for instance $CdWO_4$, $ZnMoO_4$ or Li_2MoO_4) and scintillating crystals made of ZnSe were chosen to be used in the Cuore Update with Particle IDentification (CUPID) experiment [71, 72], whose phase one will start the data taking in few months at LNGS. The high Selenium Q-value

($Q_{^{82}Se}$ = 2997 keV) and the high scintillation emission ensure a total α-background rejection as it can be discriminated from the β/γ contribution considering the shape and amplitude of the light signal. The emitted photons are detected with an intrinsic Silicon absorber, used as bolometer, located in front of the ZnSe scintillating crystal. The whole system is wrapped by a reflective foil in order to enhance the light collection efficiency. Since both light and heat signals are measured using bolometers read by NTD thermistors, the CUORE electronics represents a good starting point also for experiments such as CUPID. In particular, the flexibility of the pulser board allows not only to deliver precise squared pulse to the ZnSe crystals for their response stabilization, but also to deal with the Silicon light absorbers. In order to let them operate in optimal condition, the light detectors must be warmed up. A stable heat injection can be delivered via Joule effect by generating a constant current flowing through the NTD thermistor. Such condition can be achieved by providing an adjustable, stable and precise offset level at the pulser outputs. With few hardware and firmware upgrades, the pulser board is able to delivered both the heating offset and the calibrating pulse from a single output. The same approach can also be applied to stabilize the response of Transition Edge Sensors (TES), devices that exploit the strongly temperature-dependent resistance of the superconducting phase transition to detect particles in cryogenic experiments. The operating temperature of such sensors must be fine tuned to obtained the best sensitivity. Similarly to the light detector used in CUPID, the pulser is able to provide both a fine adjustment of the warming constant current and the reference pulse for the detector stabilization. For instance, the pulser board is currently under study for the use in the COSINUS experiment [73], which researches Dark Matter by studying nucleus recoils due to the interaction of WIMPs (Weakly Interacting Massive Particles) at LNGS. As well as CUPID, COSINUS exploits a double signal readout to disentangle β/γ events to nucleus recoils. The concept of a COSINUS detector module consisting of an undoped NaI target crystal surrounded by a beaker-shaped light detector. Both detectors, operated at milli-Kelvin temperatures, are coupled with TES. Unlike CUORE and CUPID, COSINUS uses exponentially shaped reference pulse to stabilize the detector response. The precise clock reference located in the pulser board can be used not only to generate precise squared pulses, but also to provide exponentially (or even custom) shaped pulses.

The pulser board can also be used as the core device for the operating temperature stabilization in cryogenic experiments. Indeed, bolometers do not operate at the lowest available temperature, since it is affected by unavoidable low frequency fluctuations which can spoil the system performance. A proper amount of power (of the order of few μW) is thus delivered to the system and continuously adjusted in order to compensate for the thermal drifts and keep the operating temperature stable. Such architecture commonly consists of a close loop system which monitors the temperature to be stabilized and uses it as a feedback signal for a power supply. In the domain of digital systems, a

proportional–integral–derivative (PID) controller is a mechanism widely used in industrial control systems to fulfill such a goal. A PID controller continuously calculates an error function as the difference between the desired and measured value of the process variable and applies a correction based on proportional (P), integral (I), and derivative (D) term. In the case of temperature stabilization, the extremely slow detector response usually allows to neglect the derivative term. The pulser board is equipped with all the hardware tools needed to implement a PID controller for the cryostat temperature stabilization. The on-board 24-bit ADC allows to acquire the target thermometer with high precision and uses it to adjust the voltage drop (delivered by the 12-bit DAC) across a heating resistor with a PID technique. The proper power can be calculated either by managing the pulser board from a remote computer or by exploiting the computational capability of the on-board micro-controller. Such system is under development for the use in CUORE, CUPID and COSINUS and represents a useful and promising tool for all the cryogenic experiments.

Acknowledgements

I would like to thank Yury Kolomensky and Roberto Calabrese who reviewed the thesis. It was a pleasure to be reviewed by such experts and this push me to produce a better work. Your careful and useful comments helped me a lot to improve the quality of the thesis.

Se dovessi dire l'aspetto più bello tra i tanti che hanno costellato il mio percorso di dottorato, certamente sarebbe le persone con cui ho avuto il piacere di condividere il lavoro. Ringrazio Gianluigi Pessina che mi ha accompagnato, spronato e pazientemente insegnato: è una fortuna avere un capo che ti contagia per passione ed entusiasmo. Vorrei inoltre ringraziare Marta Calvi e Clara Matteuzzi per il loro sostegno in tutti i passi compiuti nella bella esperienza di LHCb. Vorrei inoltre ringraziare i miei amici (colleghi mi sembra una definizione molto limitante) Claudio, Paolo, Andrea e Matteo: da loro ho imparato molto e condiviso gioie e fatiche di questo bellissimo cammino. Sono proprio felice dell'attenzione riservata non solo al mio lavoro, ma anche alla mia persona in questi anni e spero di poter lavorare per e con voi ancora a lungo.

Vorrei inoltre ringraziare la Magi, per tutti i caffè di quando "non funziona nulla" e tutti i compagni di Laboratorio I, Elena, Luca e Marco. Grazie a Sara e Riccardo, miei mentori nel dottorato in fisica e sempre pronti a darmi rifugio a Ginevra, a Samu e a tutti i miei amici di Muggiò, presenza costante e fortificante da sempre.

Ultimi citati, ma non per importanza, la mia famiglia che ha sostenuto i miei studi universitari e accompagnato lungo tutto il dottorato. Grazie per la fiducia e la stima che avete in me e per avermi mostrato quell'etica del lavoro da cui provengono i miei piccoli successi lavorativi. E come non menzionare la mia quasi moglie, Ester: grazie per la pazienza nelle trasferte, per aver sopportato i tanti momenti "di corsa" e per essermi stata accanto in tutto, comprese le sere o i weekend passati al lavoro. Come sai, il dottorato, oltre che essere stata una bellissima esperienza, è stato anche a servizio della nostra nascitura famiglia. La serenità e la stabilità di questi rapporti sono un pilastro che mi fa esprimere al meglio in tutto.

Bibliography

[1] Patrignani, C. and Particle Data Group, "Review of Particle Physics," *Chinese Physics C*, vol. 40, no. 10, p. 100001, 2016.

[2] Choi, S.-K. and others, "Observation of a Resonancelike Structure in the $\pi^{+-}\psi^{'}$ Mass Distribution in Exclusive $B \to K\pi^{+-}\psi^{'}$ Decays," *Phys. Rev. Lett.*, vol. 100, p. 142001, Apr 2008.

[3] Aaij, R. and others, "Observation of the Resonant Character of the $Z(4430)^{-}$ State," *Phys. Rev. Lett.*, vol. 112, p. 222002, Jun 2014.

[4] Aaij, R. and others, "Observation of $J/\psi p$ Resonances Consistent with Pentaquark States in $\Lambda_b^0 \to J/\psi K^- p$ Decays," *Phys. Rev. Lett.*, vol. 115, p. 072001, Aug 2015.

[5] Christenson, J. H. and others, "Evidence for the 2π Decay of the K_2^0 Meson," *Phys. Rev. Lett.*, vol. 13, pp. 138–140, Jul 1964.

[6] J. P. Lees *et al.*, "Observation of time-reversal violation in the B^0 meson system," *Phys. Rev. Lett.*, vol. 109, p. 211801, Nov 2012.

[7] Andrei D Sakharov, "Violation of CP invariance, C asymmetry, and baryon asymmetry of the universe," *Soviet Physics Uspekhi*, vol. 34, no. 5, p. 392, 1991.

[8] Fukuda, Y. and others, "Evidence for Oscillation of Atmospheric Neutrinos," *Phys. Rev. Lett.*, vol. 81, pp. 1562–1567, Aug 1998.

[9] Ahmad, Q. R. and others, "Direct Evidence for Neutrino Flavor Transformation from Neutral-Current Interactions in the Sudbury Neutrino Observatory," *Phys. Rev. Lett.*, vol. 89, p. 011301, Jun 2002.

[10] Eguchi, K. and others, "First Results from KamLAND: Evidence for Reactor Antineutrino Disappearance," *Phys. Rev. Lett.*, vol. 90, p. 021802, Jan 2003.

[11] Ahn, M. H. and others, "Indications of Neutrino Oscillation in a 250 km Long-Baseline Experiment," *Phys. Rev. Lett.*, vol. 90, p. 041801, Jan 2003.

[12] Pontecorvo, B., "Neutrino Experiments and the Problem of Conservation of Leptonic Charge," *Sov. Phys. JETP*, vol. 26, pp. 984–988, 1968.

[13] Redshaw, M. and others, "Masses of ^{130}Te and ^{130}Xe and Double-β-Decay Q Value of ^{130}Te," *Phys. Rev. Lett.*, vol. 102, p. 212502, May 2009.

[14] Barabash, A. S., "Experiment double beta decay: Historical review of 75 years of research," *Physics of Atomic Nuclei*, vol. 74, no. 4, pp. 603–613, 2011.

[15] Alves Jr, A. A. and others (LHCb Collaboration), "The LHCb Detector at the LHC," *Journal of Instrumentation*, vol. 3, no. 08, p. S08005, 2008.

[16] Barbosa-Marinho, P. R. and others (LHCb Collaboration), "LHCb VELO (VErtex LOcator): Technical Design Report," *CERN Document Server (CERN-LHCC-2001-011)*, 2001.

[17] Barbosa-Marinho, P. R. and others (LHCb Collaboration), "LHCb inner tracker: Technical Design Report," *CERN Document Server (CERN-LHCC-2002-029)*, 2002.

[18] Barbosa-Marinho, P. R. and others (LHCb Collaboration), "LHCb outer tracker: Technical Design Report," *CERN Document Server (CERN-LHCC-2001-024)*, 2001.

[19] Amato, S. and others (LHCb Collaboration), "LHCb magnet: Technical Design Report," *CERN Document Server (CERN-LHCC-2000-007)*, 2000.

[20] Adinolfi, M. and others (LHCb RICH Collaboration), "Performance of the LHCb RICH detector at the LHC," *The European Physical Journal C*, vol. 73, no. 5, pp. 1–17, 2013.

[21] Amato, S. and others (LHCb Collaboration), "LHCb calorimeters: Technical Design Report," *CERN Document Server (CERN-LHCC-2000-036)*, 2000.

[22] Barbosa-Marinho, P. R. and others (LHCb Collaboration), "LHCb muon system: Technical Design Report," *CERN Document Server (CERN-LHCC-2001-010)*, 2001.

[23] Antunes-Nobrega, R. and others (LHCb Collaboration), "LHCb trigger system: Technical Design Report," *CERN Document Server (CERN-LHCC-2014-016)*, 2003.

[24] Abba, A. and others (LHCb Collaboration), "LHCb PID Upgrade Technical Design Report," tech. rep., Nov 2013.

[25] Charles M. J. and Forty R., "TORCH: Time of flight identification with Cherenkov radiation," *Nuclear Instruments and Methods in Physics Research Section A: Accelerators, Spectrometers, Detectors and Associated Equipment* , vol. 639, no. 1, pp. 173 – 176, 2011. Proceedings of the Seventh International Workshop on Ring Imaging Cherenkov Detectors.

[26] Carniti, P. and others, "CLARO-CMOS, a very low power ASIC for fast photon counting with pixellated photodetectors," *Journal of Instrumentation*, vol. 7, no. 11, p. P11026, 2012.

[27] Arnaboldi, C. and others, "Crosstalk Study of the Single-Photon Response of a Flat-Panel PMT for the RICH Upgrade at LHCb," *IEEE Transactions on Nuclear Science*, vol. 57, pp. 2267–2272, Aug 2010.

[28] Calvi, M. and others, "Characterization of a Hamamatsu R7600 multi-anode photomultiplier tube with single photon signals," *Journal of Instrumentation*, vol. 8, no. 02, p. P02012, 2013.

[29] Giachero, A. and others, "Current feedback operational amplifiers as fast charge sensitive preamplifiers for photomultiplier read out," *Journal of Instrumentation*, vol. 6, no. 05, p. P05004, 2011.

[30] Sareyan, J. P. and Ischi, E., "A Study of the Physics and Non-linear Effects in Photomultipliers," *Astronomy and Astrophysics*, vol. 27, p. 183, Sept. 1973.

[31] Andrew T. Young, "Temperature Effects in Photomultipliers and Astronomical Photometry," *Appl. Opt.*, vol. 2, pp. 51–60, Jan 1963.

[32] Laustriat, Gilbert and Coche, André, "Influence de la température sur les photomultiplicateurs et les scintillateurs liquides," *J. Phys. Radium*, vol. 19, no. 12, pp. 927–929, 1958.

[33] U. Akgun, U. and others, "Afterpulse timing and rate investigation of three different Hamamatsu Photomultiplier Tubes," *Journal of Instrumentation*, vol. 3, no. 01, p. T01001, 2008.

[34] Cadamuro, L. and others, "Characterization of the Hamamatsu R11265-103-M64 multi-anode photomultiplier tube," *Journal of Instrumentation*, vol. 9, no. 06, p. P06021, 2014.

[35] Matteuzzi, C. and others, "Characterization of the Hamamatsu R11265-103-M64 multi-anode photomultiplier tube for the LHCb RICH Upgrade," *CERN Document Server (CERN-LHCb-PUB-2014-043)*, Sep 2014.

[36] Fiorini, M. and others, "Radiation hardness assurance of the CLARO8 front-end chip for the LHCb RICH detector upgrade," *Contribution to the RICH2016 Conference*, 2016.

[37] Ramos-Martos, J. and others, "Radiation characterization of the austriamicrosystems 0.35 μm CMOS technology," *in Proc. 12th RADECS European Conference*, pp. 806–811, 2011.

[38] Ramos-Martos, J. and others, "SEE Characterization of the AMS 0.35 μm CMOS Technology," *in Proc. 14th RADECS European Conference*, 2013.

[39] Poikela, T. and others, "Timepix3: a 65K channel hybrid pixel readout chip with simultaneous ToA/ToT and sparse readout," *Journal of Instrumentation*, vol. 9, no. 05, p. C05013, 2014.

[40] Frojdh, E. and others, "Timepix3: first measurements and characterization of a hybrid-pixel detector working in event driven mode," *Journal of Instrumentation*, vol. 10, no. 01, p. C01039, 2015.

[41] Arnaboldi, C. and others (CUORE Collaboration), "CUORE: A Cryogenic Underground Observatory For Rare Events," *Nuclear Instruments and Methods in Physics Research Sec.A*, vol. 518, no. 3, pp. 775 – 798, 2004.

[42] Arnaboldi, C. and others, "First results on neutrinoless double beta decay of ^{130}Te with the calorimetric CUORICINO experiment," *Physics Letters B*, vol. 584, pp. 260–268, 2004.

[43] Arnaboldi, C. and others, "New Limit on the Neutrinoless $\beta\beta$ Decay of ^{130}Te," *Phys. Rev. Lett.*, vol. 95, p. 142501, 2005.

[44] Alessandrello, A. and others, "The first step toward CUORE: CUORICINO, a thermal detector array to search for rare events," *Nuclear Physics B, Proceedings Supplements.*

[45] Alessandria, F. and others, "CUORICINO and CUORE. Neutrinoless double beta decay searches with low temperature detectors," *LNGS annual report*, vol. 1, pp. 17–38, 2006.

[46] Alessandria, F. and others, "CUORICINO and CUORE," *LNGS annual report*, vol. 1, pp. 33–52, 2007.

[47] Ahlen, S. P. and others, "Study of penetrating cosmic ray muons and search for large scale anisotropies at the Gran Sasso Laboratory," *Physics Letters B*, vol. 249, pp. 149–156, 1990.

[48] Ahlen, S. P. and others, "Muon astronomy with the Macro detector," *The Astrophysical Journal*, vol. 412, pp. 301–311, 1993.

[49] Arpesellam, C., "Background measurements at Gran Sasso Laboratory," *Nuclear Physics B, Proceedings Supplements.*

[50] Belli, P. and others, "Deep Underground Neutron Flux Measurement With Large Bf-3 Counters," *Il Nuovo Cimento A*, vol. 101, pp. 959–966, 1989.

[51] Fiorini, E. and Niinikoski, T. O., "Low Temperature Calorimetry For Rare Decays," *Nuclear Instruments and Methods in Physics Research Sec.A*, vol. 224, p. 83, 1984.

[52] Alessandrello, A. and others, "A massive thermal detector for alpha and gamma spectroscopy," *Nuclear Instruments and Methods in Physics Research Section A*, vol. 440, pp. 397–402, 2000.

[53] Zuber, K., "Summary of the Workshop on: Matrix elements for Neutrinoless Double Beta Decay," *CERN Document Server (IPPP/05/56, DCPT/05/114)*, pp. 1–20, Nov 2005.

[54] Rodin, V. A. and others, "Assessment of uncertainties in QRPA $o\nu\beta\beta$-decay nuclear matrix elements," *Nuclear Physics A*, vol. 766, pp. 107–131, 2006.

[55] Rodin, V. A. and others, "Erratum: Assessment of uncertainties in QRPA $o\nu\beta\beta$-decay nuclear matrix elements," , 2007.

[56] Barucci, M. and others, "Measurement of Low Temperature Specific Heat of Crystalline TeO_2 for the Optimization of Bolometric Detectors," *Journal of Low Temperature Physics*, vol. 123, pp. 303–314, 2001.

[57] Miller, A. and Abrahams, E., "Impurity Conduction at Low Concentrations," *Physical Review*, vol. 120, pp. 745–755, 1960.

[58] Mott, N. F. and Davies, J. H., "Metalinsulator transition in doped semiconductors," *Philosophical Magazine B*, vol. 42, pp. 845–858, 1980.

[59] Nguyen, V. D. and others, "Variable range hopping in the Coulomb gap and gate screening in two dimensions," *Physics Letters A*, vol. 349, pp. 404–410, 2006.

[60] Mather, J. C., "Bolometer noise: nonequilibrium theory," *Appl. Opt.*, vol. 21, pp. 1125–1129, Mar 1982.

[61] Arnaboldi, C. and others, "The front-end readout for CUORICINO, an array of macro-bolometers and MIBETA, an array of μ-bolometers," *Nuclear Instruments and Methods in Physics Research Sec.A*, vol. 520, pp. 578–580, 2004.

[62] Arnaboldi, C. and others, "The Programmable Front-End System for CUORICINO, An Array of Large-Mass Bolometers," *IEEE Transactions On Nuclear Science*, vol. 49, pp. 2440–2447, 2002.

[63] Arnaboldi, C. and others, "A programmable calibrating pulse generator with multi-outputs and very high stability," *IEEE Transactions On Nuclear Science*, vol. 50, pp. 979–986, 2003.

[64] Arnaboldi, C. and others, "CUORE: A Cryogenic Underground Observatory for Rare Events," *Nuclear Instruments and Methods in Physics Research Sec.A*, vol. 518, pp. 775–798, 2004. `hep-ex/0212053v1`.

[65] Arnaboldi, C and others, "Very low noise AC/DC power supply systems for large detector arrays," *Review of Scientific Instruments*, vol. 86, no. 12, p. 124703, 2015.

[66] Arnaboldi, C. and others, "The preamplifier for CUORE, an array of large mass bolometers," in *Proceedings, 2009 IEEE Nuclear Science Symposium and Medical Imaging Conference (NSS/MIC 2009): Orlando, Florida, October 25-31, 2009*, pp. 389–395, 2009.

[67] Arnaboldi, C and others, "The Design of the Input Stage for the Very Front-End of the CUORE Experiment," *Journal of Low Temperature Physics*, vol. 151, no. 3, pp. 964–970, 2008.

[68] Carniti, P. and others, "A low noise and high precision linear power supply with thermal foldback protection," *Review of Scientific Instruments*, vol. 87, no. 5, p. 054706, 2016.

[69] Arnaboldi, C. and others, "Results from a search for the $0\nu\beta\beta$-decay of ^{130}Te," *Phys. Rev. C*, vol. 78, p. 035502, Sep 2008.

[70] D'Ambrosio, C., "The Future of RICH Detectors through the Light of the LHCb RICHes," *Contribution to the RICH2016 Conference*, 2016.

[71] Artusa, D. R. and others, "First array of enriched Zn^{82}Se bolometers to search for double beta decay," *Eur. Phys. J.*, vol. C76, no. 7, p. 364, 2016.

[72] Wang, G. and others, "CUPID: CUORE (Cryogenic Underground Observatory for Rare Events) Upgrade with Particle IDentification," *arXiv: 1504.03599*, 2015.

[73] Angloher, G. and others, "The COSINUS project: perspectives of a NaI scintillating calorimeter for dark matter search," *The European Physical Journal C*, vol. 76, no. 8, p. 441, 2016.

[74] Alves Jr, A. A. and others (LHCb Collaboration), "LHCb detector performance," *International Journal of Modern Physics A*, vol. 30, no. 07, p. 1530022, 2015.

[75] Carniti, P., "Beam test results for the upgraded LHCb RICH optoelectronic readout system," *Contribution to the RICH2016 Conference*, 2016.

[76] Arneodo, F. and others, "Neutron background measurements in the Hall C of the Gran Sasso Laboratory," *Il Nuovo Cimento A*, vol. 112, pp. 819–831, 1999.

[77] Itoh, K. M. and others, "Neutron transmutation doping of isotopically engineered Ge," *Applied Physics Letters*, vol. 64, pp. 2121–2123, 1994.